HELMUT SCHMIDT
UNIVERSITÄT
Universität der Bundeswehr Hamburg

Validierung und Verbesserung von Nachlaufmodellen zur standortspezifischen Last- und Leistungsberechnung in Windparks

Von der Fakultät für Maschinenbau und Bauingenieurwesen der
Helmut-Schmidt-Universität / Universität der Bundeswehr Hamburg
zur Erlangung des akademischen Grades eines/r
Doktor-Ingenieurs/-Ingenieurin
genehmigte

DISSERTATION

vorgelegt von

Inga Reinwardt

aus Hamburg

Hamburg, 2021

Fakultät für Maschinenbau und Bauingenieurwesen
Professur für Strömungsmechanik

Univ.-Prof. Dr.-Ing. habil. Michael Breuer

Helmut-Schmidt-Universität
Universität der Bundeswehr Hamburg
Postfach 70 08 22
22008 Hamburg

Inga Reinwardt
Horner Weg 71
20535 Hamburg

E-mail: inga.reinwardt@t-online.de

Erstgutachter
Univ.-Prof. Dr.-Ing. habil. Michael Breuer
Zweitgutachter
Univ.-Prof. Dr. Jakob Mann
Tag der mündlichen Prüfung
20.12.2021

Validation and improvement of wake models for site-specific load and power calculations in wind farms

Doctoral Thesis

approved by the

Department of Mechanical and Civil Engineering

of the

Helmut-Schmidt-University

University of the German Federal Armed Forces Hamburg

for obtaining the academic degree of

Doktor Ingenieurin (Dr.-Ing.)

presented by

Inga Reinwardt

from Hamburg

Hamburg, 2021

Vorwort

Ich möchte mich ganz herzlich bei allen bedanken, die mich während der Promotion begleitet und unterstützt haben. Ich hatte das Glück, während der Zeit umgeben gewesen zu sein von vielen Menschen, die mich in ganz unterschiedlicher Weise unterstützt und zu einem Gelingen des Projektes beigetragen haben.

Die vorliegende Arbeit endstand im Rahmen einer kooperativen Promotion zwischen der Hochschule für Angewandte Wissenschaften (HAW) Hamburg und der Helmut-Schmidt-Universität (HSU). Meinem Doktorvater Prof. Dr.-Ing. Michael Breuer der HSU danke ich daher herzlich für seine vielen hilfreichen Anregungen und Korrekturen, die zu einem Gelingen der Arbeit wesentlich beigetragen haben.

Außerdem möchte ich mich bei Prof. Jakob Mann und Nikolay Dimitrov der Dänischen Technischen Universität (DTU), bedanken. Jakob Mann hat wesentlich zur Ermöglichung meines Aufenthalts an der DTU während der Promotion beigetragen und Nikolay Dimitrov hat viele hilfreiche fachliche Anregungen in unseren wöchentlichen Gesprächen gegeben. Der Aufenthalt an der DTU war für mich insgesamt sehr bereichernd. Die besondere Gastfreundschaft der DTU und damit einhergehende Förderung des wissenschaftlichen Austausches sind sehr wertvoll.

Ich möchte mich darüber hinaus bei dem ganzen Windteam der HAW bedanken. Ihr habt meinen Arbeitsalltag an der HAW jeden Tag bereichert und ich werde die gemeinsame Zeit immer in guter Erinnerung behalten. Besonders möchte ich mich bei meinem Projektpartner Levin Schilling für die fachliche und auch menschliche Unterstützung der letzten Jahre bedanken. Ich kann mir in keiner Hinsicht einen besseren Kollegen vorstellen. Außerdem möchte ich mich für das Vertrauen und die Unterstützung meines Betreuers Prof. Peter Dalhoff bedanken.

Zusätzlich möchte ich mich bei den Mitarbeitern von Nordex, die mich von industrieller Seite her unterstützt haben, ganz herzlich bedanken. Ohne Eure Hilfe bei der Umsetzung der Messkampagne sowie der fachlichen Unterstützung wäre diese Arbeit nicht möglich gewesen. Besonderer Dank gilt hier Dirk Steudel, der durch seine fachlichen Anregungen wesentlich zur Entstehung der Arbeit beigetragen hat.

Darüber hinaus möchte ich mich bei meinen Freunden und meiner Familie für die Unterstützung in den letzten Jahren bedanken. Die lange Freundschaft mit Alina Burmester und Svenne Freund hat mir immer geholfen und mich bestärkt, wofür ich sehr dankbar bin. Außerdem möchte ich mich für die Unterstützung und den Zuspruch meiner Eltern Ursula und Bernd Reinwardt sowie meines Bruders Simon Reinwardt von ganzem Herzen bedanken.

Hamburg, Juni 2021 Inga Reinwardt

Zusammenfassung

Beim Ausbau erneuerbarer Energien nimmt die Windenergie eine Führungsrolle ein. Sie ist für das Gelingen der Energiewende in Deutschland sowie in vielen anderen Ländern essentiell und lässt sich aktuell kaum durch eine andere Form nachhaltiger Energiegewinnung ersetzen. Auch wenn die Windenergie im vergangenen Jahrzehnt einen immensen Zuwachs erlebt hat, reicht die Energiemenge zurzeit noch nicht aus, um konventionelle Energieformen zu ersetzen, weshalb die Erhöhung der installierten Windenergieleistung weiterhin vorangetrieben werden muss. Gerade in dicht besiedelten Ländern wie Deutschland wird der effizienten Nutzung der zur Verfügung stehenden Flächen eine besondere Bedeutung zu Teil. Um die Flächen optimal nutzen zu können, werden Windparks möglichst dicht bebaut, was in niedrigen Anlagenabständen resultiert. Durch diese geringen Distanzen gewinnen Nachlaufeffekte an Einfluss. Sie führen zu Leistungseinbußen sowie Belastungserhöhungen durch benachbarte Windenergieanlagen. Die vorliegende Dissertation adressiert dieses Thema und validiert sowie erweitert bestehende Nachlaufmodelle für Binnenlandwindparks mit kleinen Anlagenabständen.

Bereits bestehende Nachlaufmodelle werden basierend auf Nachlaufmessungen mittels Lidarsystemen sowie Leistungs-, Belastungs- und Messmastmessungen an zwei Windparks validiert. Ein besonderer Fokus wird auf die Analyse von gondelbasierten Lidarmessungen gelegt. Darüber hinaus werden die Lidarmessungen genutzt, um das Dynamic Wake Meandering (DWM) Modell neu zu kalibrieren. Dadurch weist dieses eine deutlich höhere Genauigkeit bezüglich Windcharakteristiken sowie Betriebslasten in Nachlaufsituationen bei kleinen Anlagenabständen und flachem Terrain auf. Zusätzlich werden verschiedene Mehrfachabschattungsmodelle in Kombination mit dem DWM Modell im Hinblick auf Windcharakteristiken, Leistung und Betriebslasten validiert. Dabei stellt sich heraus, dass die Verwendung des am stärksten ausgeprägtesten Windgeschwindigkeitsdefizits aller stromaufwärts stehenden Windenergieanlagen an der jeweiligen räumlichen Position im Nachlauf besonders geeignet ist. Zudem zeigt sich, dass ähnlich gute Ergebnisse bezüglich der Belastungen und der Erträge erzielt werden, wenn nur die nächstgelegene Windenergieanlage bei der Berechnung berücksichtigt wird. Diese Methode kann daher als eine einfache Alternative mit hinreichender Genauigkeit dienen.

Abschließend wird eine Erweiterung des DWM Modells hin zu einem statischen Modell zur standortspezifischen Lastapproximation vorgestellt. Im Vergleich zum herkömmlichen Frandsen-Modell zur Berechnung der nachlaufinduzierten Turbulenz führt diese Modellerweiterung zu einer signifikanten Verbesserung insbesondere für kleine Anlagenabstände. In einer herkömmlichen standortspezifischen Lastberechnung werden rechenintensive aeroelastische Simulationen häufig vermieden und die Belastungen werden anhand bereits durchgeführter Lastsimulationen interpoliert. Die Interpolationsmethode (z. B. Response Surface Methode) ist von einer einzelnen Turbulenzintensität, welche für die gesamte Rotorfläche gilt, abhängig. Das DWM Modell hingegen liefert ein instationäres Windfeld mit einer inhomogenen Turbulenzintensitätsverteilung über den Rotor, sodass dieses Modell nicht mit der Lastapproximation kombinierbar ist. Die statische Version des DWM Modells adressiert dieses Problem und liefert eine einzelne, schädigungsäquivalente Turbulenzintensität. Darüber hinaus ist die Modellerweiterung deutlich weniger rechenintensiv als das ursprüngliche DWM Modell und ermöglicht so eine Anwendung in iterativen

Optimierungsprozessen zur Ermittlung des geeignetsten Windparklayouts.

Zusammenfassend beinhaltet die Dissertation zum einen eine rekalibrierte Version des rechenintensiven und genauen DWM Modells, welches direkt kombinierbar ist mit einer aeroelastischen Lastsimulation, zum anderen eine Methode zur Beschreibung von Mehrfachabschattungssituationen im DWM Modell und abschließend eine einfache und wenig rechenintensive statische Version des DWM Modells für Layout-Optimierungsprozesse und Lastapproximationen. Die entwickelten und validierten Modelle sind von besonderer Bedeutung für Windparks mit kleinem Anlagenabstand.

Abstract

Wind energy plays a leading role in the expansion of renewable energies. It is essential for the success of the energy transition in Germany, like in many other countries, and it can currently hardly be replaced by any other form of sustainable energy generation. Even though wind energy has experienced immense growth in the past decade, the amount of energy is currently insufficient to fully replace conventional forms of energy, which is why the increase in installed wind energy capacity must continue to be driven forward. Particularly in densely populated countries like Germany, the efficient use of available land holds special importance. In order to use the land optimally, wind farms are built as densely as possible, which results in low distances between turbines. Due to these short distances, wake effects gain influence. These lead to power losses as well as increased loads due to neighboring wind turbines. This dissertation addresses the issue and validates and extends existing wake models for onshore wind farms with dense spacing.

Current wake models are validated based on wind field measurements applying lidar systems as well as power, load, and met mast measurements in two onshore wind farms with low distances between the turbines. Special focus is devoted to the usage of nacelle-mounted lidar systems for wake model validation. Moreover, lidar measurements have been used to recalibrate the dynamic wake meandering (DWM) model. As a result, the model proves to be more accurate regarding wind characteristics and fatigue loads under wake conditions at onshore sites with small turbine distances and flat terrain.

Additionally, different methods to evaluate multiple wakes in the DWM model are evaluated regarding the wind characteristics in the wake as well as power and fatigue loads. It can be shown that taking the minimum wind speed of all upstream wakes at each point of interest in the wake is a suitable approach to approximate multiple wakes. Furthermore, the simplified method of only considering the closest turbine wake delivers very similar results regarding fatigue loads as well as power output and can be a simple alternative with sufficient accuracy.

Finally, an extension of the DWM model towards a static model for site-specific load approximations is presented and proves to be a significant improvement to the commonly used Frandsen wake-added turbulence model, especially for short turbine distances. In a common site-specific load calculation process, time-consuming aeroelastic simulations are usually avoided and the loads are estimated based on interpolations of prior-performed load simulations. The interpolation method (e.g. response surface method) depends on a single turbulence intensity value, which is assumed to be constant over the whole rotor area. Accordingly, this load estimation method is not combinable with the DWM model given that the DWM model delivers an instantaneous wind field and an inhomogeneous turbulence intensity distribution across the rotor. The static version of the DWM model addresses this issue and provides a damage-equivalent single turbulence intensity value. The extension of the model is built in such a way that the computational costs are very low, thus enabling an implementation into wind farm layout optimization processes.

In summary, this thesis provides: a recalibrated version of the high-fidelity DWM model that is directly combinable with an aeroelastic load simulation software, an appropriate suggestion to handle multiple wakes in the DWM model, and finally a simple and low-cost static DWM model version for layout optimization and load approximation

purposes. The developed and validated methods hold special importance for onshore wind farms with small turbine distances.

Contents

Nomenclature

Abbreviation

ABL	Atmospheric Boundary Layer
AOM	Acousto-Optic Modulator
BEM	Blade Element Method
CBL	Convective Boundary Layer
CFD	Computational Fluid Dynamics
CW	Continuous Wave
DBS	Doppler Beam Swinging
DTU	Danish Technical University
DWM	Dynamic Wake Meandering
ECN	Energy Research Centre of the Netherlands
EDFA	Erbium-Doped Fiber Amplifiers
EWTW	ECN Wind Turbine Test station Wieringermeer
FFR	Fixed Frame of Reference
HMFR	Horizontal Meandering Frame of Reference
LOS	Line-Of-Sight
LES	Large-Eddy Simulation
MM	Met mast
MFR	Meandering Frame of Reference
PDF	Probability Density Function
PPI	Plan Position Indicator
PRF	Pulse Repetition Frequency
RHI	Range Height Indicator
RANS	Reynolds-Averaged Navier–Stokes
RMSE	Root-Mean-square error
SCADA	Supervisory Control and Data Acquisition
SBL	Stable Boundary Layer
SNR	Signal-to-noise ratio
TI	Turbulence Intensity

VAD	Velocity Azimuth Display
WAsP	Wind Atlas Analysis and Application Program

Chapter 1

Introduction

One of the main challenges in the current century is the prevention or mitigation of global climate change. Already today, climate change has observable effects on the environment, e.g. glaciers shrunk, ice on rivers and lakes are breaking up earlier and plant and animal diversity are shifted. Climate change leads to rising sea levels and more intense heat waves, increasingly prevalent natural disasters and affects the livelihoods of many people all over the world. To mitigate climate change, a revolution and decarbonization of the complete energy sector including power and heat supply as well as the transportation sector is necessary. In Germany, 42 % of the complete electric power supply, 15 % of the heat and cooling supply and only 5.6 % of the energy needed for transportation comes from renewable energy sources in 2019 (BMWI 2020). A graphical illustration of the development of the electricity consumption in Germany over recent years is depicted in Figure 1.1. It can be seen that the percentage of renewable energy supply in the electricity sector in Germany has more than doubled in the last ten years, although most of the energy still stems from non-renewable sources. The different renewable energy sources and their share in the overall electricity production of renewable energies is illustrated in Figure 1.2. Wind energy delivers most of the renewable electricity in Germany, whereby 41.7 % of the energy originates from onshore and 10.2 % from offshore wind farms. Thus, it can be concluded that wind energy is currently one of the most important renewable energy sources. To stop climate change, renewable energy must provide all of our energy supply if likewise no nuclear power should be used. Furthermore, due to economic growth the energy demand increases, so that even more renewable energy is necessary. In industrial countries, it is assumed that the economic growth is rather slow. However, when looking at the situation from a more global perspective, in emerging countries a huge economic growth is assumed. Additionally, the world population will increase, so that the worldwide energy demand might increase by a factor of 3 to 5 (Quaschning 2019). Although renewable energies are already a well-established energy source in many countries such as in Germany, these numbers clearly reveal that a significant expansion of renewables in general as well as wind energy is still necessary. Considering that wind energy is one of the most important renewable energy sources, it is obvious that increasing the economic efficiency and thereby the installed capacity of wind turbines can significantly contribute to a more successful prevention of climate change.

The expansion of onshore wind energy in a densely populated area such as Germany is challenging and high energy output per utilized base area is crucial. The development of

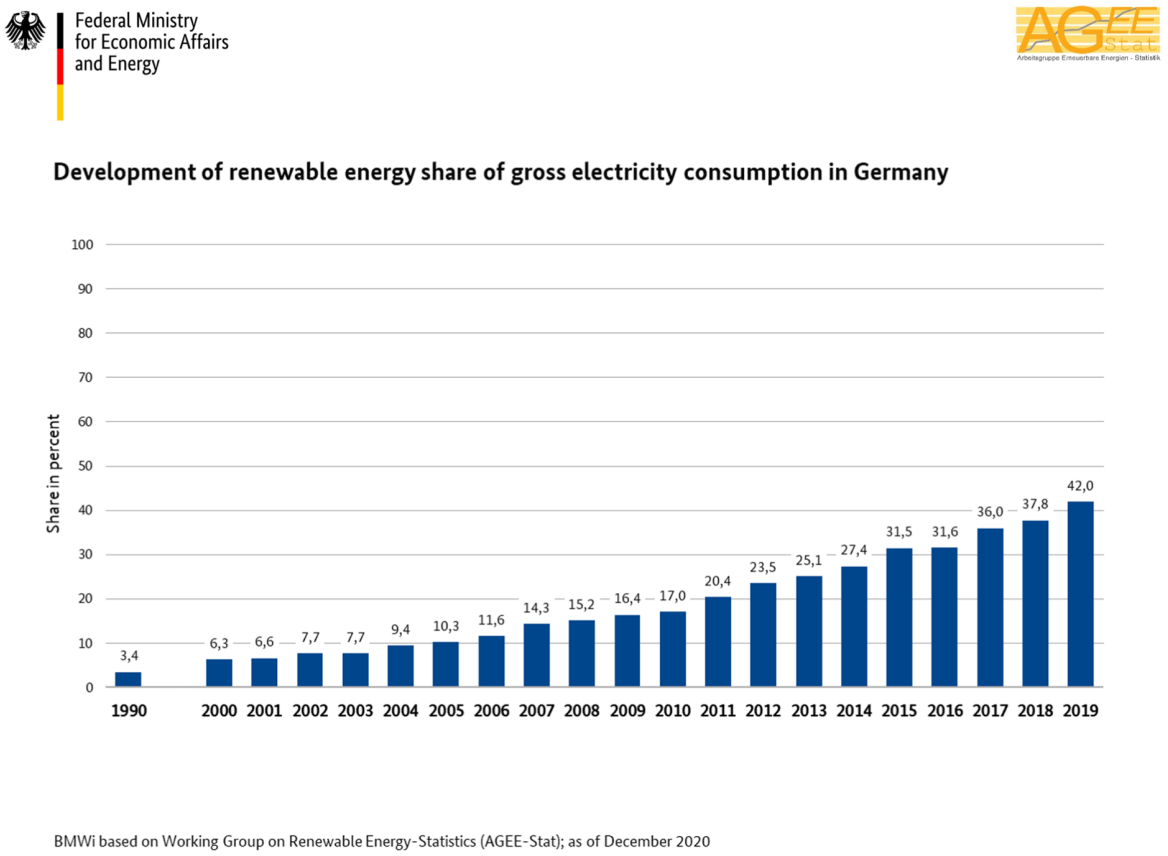

Figure 1.1: Percentage of renewable energy supply in Germany (BMWI 2020).

optimal wind farm layouts, which require detailed wake models, is essential in this regard. This thesis addresses the issue of detailed wake modeling in wind farms. It validates current wake models based on lidar, load, and met mast measurements in two onshore wind farms with low distances between the turbines. Special focus is devoted to the usage of nacelle-mounted lidar systems for wake model validation as well as recalibration. Models for single wakes as well as multiple wakes are investigated. Furthermore, the DWM model is recalibrated and extended to improve the application in layout optimization processes.

A brief overview of the current wake models for single and multiple wake calculations is provided in the subsequent literature review. Moreover, a summary of wake model validations with lidar systems is outlined. The introduction is completed by a description of the contribution of this work to the scientific community.

1.1 Literature review

1.1.1 Single wake models

The aim of wake models is to estimate both, the energy yield of the whole wind farm and loads on single turbines as accurately as possible. An overview of currently used single wake models has been published in the course of this thesis in Reinwardt et al.

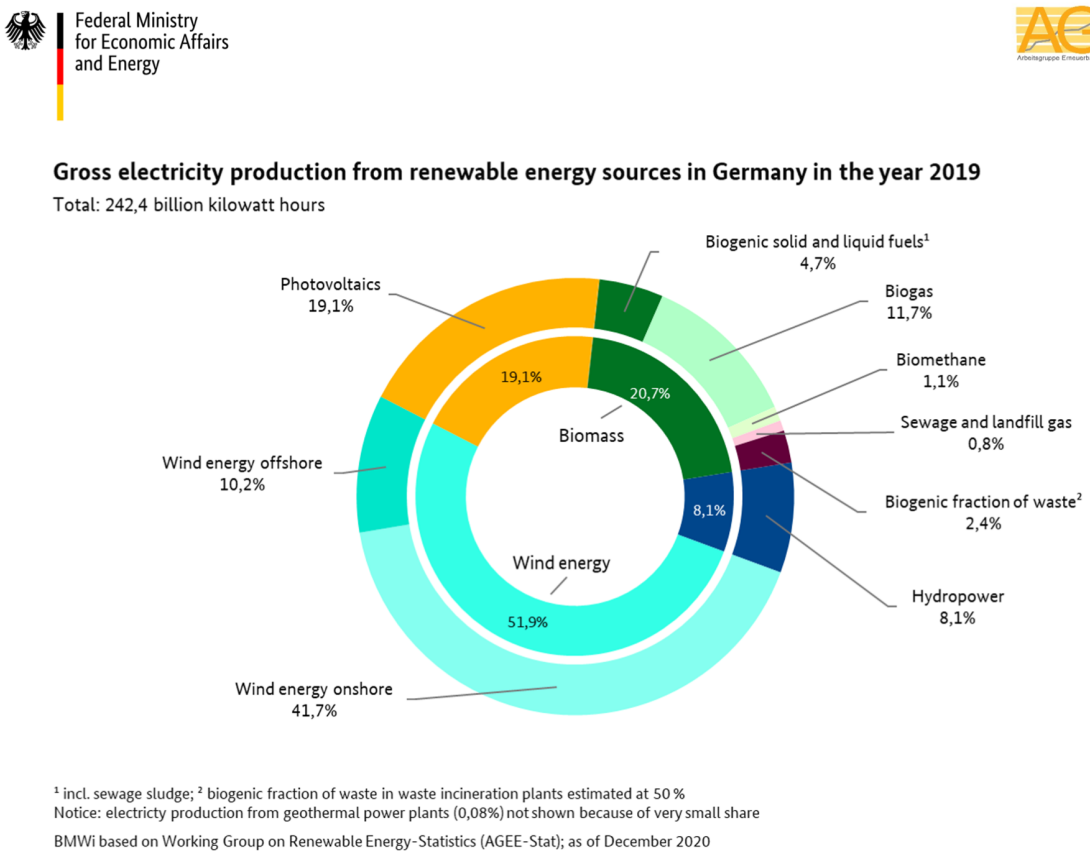

Figure 1.2: Percentage of renewable energy supply in Germany (BMWI 2020).

(2021) and Reinwardt et al. (2020a) and has been taken over in this section.

Simple analytical wake models can be divided into models estimating either the mean wind speed reduction in the wake or the wake-induced turbulence. While the former serves as a basis for power calculations, the latter is necessary to compute fatigue loads. One of the well-known models for predicting this wake-induced turbulence is the Frandsen model (see e.g. Frandsen 2007), where the total turbulence intensity (TI) at the downstream turbine is calculated by a quadratic summation of the wake-added TI and the ambient TI. Previous measurement campaigns have shown that this method delivers very conservative results for small turbine distances (Gerke et al. 2018; Reinwardt et al. 2018). This is particularly important for onshore wind farms in densely populated areas. Another simple, but less common, analytical model to calculate the wake-induced turbulence is introduced in Quarton and Ainslie (1989). The model calculates the wake-induced turbulence based on the thrust coefficient, the ambient turbulence as well as the downstream distance, which is similar to the total TI approach in the Frandsen model.

Jensen (1983) provides an analytical model to predict the wind speed reduction in the wake. This model is based on the thrust coefficient, the downstream distance and a wake decay constant. More recently developed wind speed reduction models can be found in Larsen (2009) and Bastankhah and Porté-Agel (2014). The latter is based on a Gaussian distribution for the velocity deficit in the wake. Both models depend on the

thrust coefficient of the turbines and the downstream distance. A more sophisticated model for calculating the wind speed deficit expansion in the wake is explained in Ainslie (1988), where the author suggests solving the thin shear layer approximation of the Navier-Stokes equations with an eddy viscosity closure approach.

Many research activities have recently focused on wake simulations to generate more accurate descriptions of the actual physical behavior of the wake (see, e.g., Özdemir and Bot (2018), Dimitrov (2019), Duc et al. (2019), Luzzatto-Fegiz (2018), and Göçmen and Giebel (2018)), which ultimately led to the inclusion of the DWM model in the new edition of the IEC guideline (IEC 61400-1 Ed.4 2019). The DWM model is strongly influenced by the work of Ainslie (1988). It describes the physical behavior of the wake more precisely in comparison to the purely analytical models such as the Jensen, Larsen or Bastankhah model, while it is still less time-consuming and complex than a complete computational fluid dynamic (CFD) simulation. Moreover, it is capable of estimating the wake-induced turbulence as well as the wind speed deficit. The model assumes that the wake behaves as a passive tracer, i.e. the wake itself moves (meanders) in vertical and horizontal direction (Larsen et al. 2008a). The combination of this movement and the shape of the wind speed deficit leads to an increased TI at a fixed position downstream and thus strongly influences the loads on the downstream turbine (Larsen et al. 2013). Therefore, a precise description of the meandering itself and the wind speed deficit in the meandering frame of reference (MFR) as well as a detailed validation of the wind speed deficit definition is fundamental in this model. The additional TI due to the meandering and the shape of the wind speed deficit is indirectly captured in the wake-added TI in the simple analytical models such as the Frandsen turbulence model. Based on the specific setup of the DWM model, it delivers an inhomogeneous wind field, which can be directly connected to an aeroelastic load simulation software. The model was validated and calibrated with actuator disk and actuator line simulations as outlined in Madsen et al. (2010), whereas a validation of the model with measured loads and power production was carried out in Larsen et al. (2013). Keck (2014) presents a power deficit validation of a slightly different version and extension of the model towards a stand-alone implementation. The DWM model has proved to be more accurate in load predictions than the commonly used Frandsen model (Reinwardt et al. 2018).

Further research on single wake model validation and fatigue loads in wake conditions can be found in Thomsen and Sørensen (1999) and Madsen et al. (2005). Studies related to wake model validation based on power output measurements and wind farm efficiency calculations are outlined in Barthelmie et al. (2007b), Barthelmie et al. (2007a), and Barthelmie and Jensen (2010). Furthermore, the Jensen wake model was recalibrated based on power measurements in Cleve et al. (2009) and Duc et al. (2019).

After reviewing the present research related to single wake models, it can be concluded that many research studies have been carried out for simple analytical wake models. Most research activities focus on predicting the wind speed deficit and power, whereas less research is related to wake-induced turbulence and loads. Furthermore, most of the validation has been conducted on offshore wind farms with larger turbine distances, whereas less research is carried out on onshore wind farms with small turbine spacing. A promising approach to describe the mean wind speed deficit as well as the wake-induced turbulence is given by the more recently developed DWM model. However, due to the

complexity of the model different implementations and calibrations of the model can lead to a strong variation of the results, whereby an extensive validation is necessary.

1.1.2 Multiple wake models

When considering a real wind farm not only single wakes need to be taken into account. It is often the case that multiple wakes or wake overlapping occur. Different model approaches exist to calculate multiple wakes. A commonly used approach is the summation of wind speed deficits in a quadratic or linear approach. Furthermore, energy balancing methods have been investigated.

A commonly used quadratic wake summation approach in combination with the previously mentioned Jensen wake model for single wakes is outlined in Katic et al. (1987). In this wake summation approach the wind speed deficits of all upstream turbines are added in a quadratic approach and deliver the inflow wind speed for the downstream turbine in a multiple wake situation. In the following, if the Jensen model is mentioned as a multiple wake model, it implies a quadratic summation of wake deficits. In Nygaard (2014), this quadratic summation approach has been compared to measurements from three different offshore wind farms with respect to wind speed and power measurements. Obvious discrepancies are found at lower turbulence intensities, so that the author suggests including the TI explicitly through the value of the wake decay parameter. In González-Longatt et al. (2012), the Jensen model has been extended by a shadowing factor to consider partial wakes at the rotor.

A further validation of the Jensen wake model is carried out in Gaumond et al. (2012). The model is compared to the Larsen wake model (Larsen 2009) as well as Reynolds-Averaged Navier–Stokes (RANS) simulations and power deficit measurements from the Horns Rev and Lillgrund wind farm. The Larsen model as well as the CFD simulations tend to cover the power deficit better than the Jensen model in large offshore wind farms. The Jensen model overpredicts the production of the last turbines. Another validation of engineering wake models including the Jensen model as well as slightly more complex models based on the thin shear layer equations and CFD simulations can be found in Barthelmie et al. (2009). Here, calculated wind farm losses are compared to measurements in the Horns Rev wind farm. The analysis shows that the engineering models underpredict wake losses, whereas the CFD simulations overpredict them.

A linear as well as a quadratic (energy deficit) superposition is compared to Large-Eddy Simulation (LES) predictions in Niayifar and Porté-Agel (2015). A common way to handle multiple wakes is to calculate the wind speed deficit at each upstream turbine in a row based on the ambient wind speed. If the wind speed deficits are summed up linearly, this approach can lead to negative wind speeds, whereby in the approach in Niayifar and Porté-Agel (2015) the superposition is undertaken based on the difference between the local inflow wind speed at the turbine and the wake wind speed. This leads to more reasonable results, especially for a large number of rows. The Bastankhah single wake model (Bastankhah and Porté-Agel 2014) is extended in this analysis for multiple wakes and compared to the Jensen model, as it is implemented in the commercial software Wind Atlas Analysis and Application Program (WAsP), as well as power output measurements in Horns Rev. The new analytical model fits considerably better to the measurements.

In Machefaux et al. (2015b), a comparison between four different models for multi-

ple wakes is presented. A linear as well as a quadratic superposition of wakes has been analyzed. The most pronounced wake in accordance with the DWM model definition in Larsen et al. (2013) and the linear summation of wind speed deficits taking into consideration different inflow wind speeds at each upstream turbine similar to Larsen (2009) is evaluated. All models have been validated against CFD simulations. From the analysis it could be concluded that the quadratic wake summation is in better agreement below the rated wind speed, when the deficits are most pronounced, whereas the linear summation fits better above the rated wind speed. The DWM model approach considering the most pronounced wake deficit fits best.

In Frandsen et al. (2006), a model for single and multiple wakes, based on momentum conservation and applicable to a regular grid of turbines is first introduced. In Méchali et al. (2006), the model parameters have been adjusted and compared to power measurements in Horns Rev. The analysis has shown that the model is able to predict the mean power drop from turbine 1 to turbine 2 in the row, whereas further downstream in the row the model slightly overpredicts the production. In Rathmann et al. (2006), the approach has been extended, so that irregular grids can be modeled. Two extensions are presented, namely the Mosaic-tiles model and a simple semi-linear approach. The simple semi-linear approach has been compared to wind speed measurements in Horns Rev. The first rows agree well with the measurements but in cases with strong overlapping the model tends to overpredict the deficit. In Rathmann et al. (2007), the Mosaic-tiles model is compared to measurements from Horns Rev. The comparison has shown that the model leads to better agreement than the semi-linear model but is too time-consuming in the present state and needs some adjustments of the wake expansion parameters based on more measurements.

A method to approach multiple wakes in the DWM is outlined in Larsen et al. (2013). It suggests taking the most pronounced wake of all upstream turbines. The approach has been compared to load and power measurements in the Egmond aan Zee wind farm. Measurements and simulations in wake conditions are found to be in good agreement. In Larsen et al. (2015), it is shown that this approach does not work very well for higher ambient wind speeds, so that the guideline (IEC 61400-1 Ed.4 2019) intends to use the most pronounced wake below the rated wind speed and a linear summation of the wind speed deficits above the rated wind speed. In Keck (2014), another approach to handle multiple wakes in the DWM model is proposed. The method suggests calculating the inflow at each upstream turbine successively, so that the inflow conditions change at each turbine in the row and the wake effects of all upstream turbines are included implicitly. In Jonkman et al. (2017), the National Renewable Energy Laboratory (NREL) presents a further approach to handle multiple wakes in the DWM model. It suggests using a quadratic sum of all deficits similar to the method presented in Katic et al. (1987) but utilized for the DWM model.

From the above analysis, it can be concluded that a lot of research has been carried out on calculated multiple wakes for determining power losses in large offshore wind farms, whereas similar to the single wake analysis, there is a lack of validations for dense onshore wind farms. Moreover, most of the research is focused on power instead of loads. Some recent activities of including multiple wake calculations into the DWM model have been carried out. An extensive comparison between different approaches to calculate multiple wakes in the DWM model regarding power losses as well as loads and measurements is

not available to date.

1.1.3 Wake model validation with lidar systems

Current research activities on lidar systems for wake model validation purposes have been summarized and published in Reinwardt et al. (2020a) during the thesis. This section replicates this summary.

Lidar systems are highly suitable for wake validation purposes, whereby especially the so-called scanning lidar systems offer strong potential for detailed wake analysis. These lidar systems are capable of scanning a three-dimensional wind field, so that the line-of-sight (LOS) wind speed can be measured subsequently at different positions in the wake, thus enabling detecting of the wake meandering as well as the shape of the wind speed deficit in the MFR. This is the reason why such a device is used in the measurement campaign outlined here. Several different measurement campaigns with ground-based and nacelle-mounted lidar systems have already been carried out in recent years, some of them even with the purpose of tracking wake meandering and validation of wake models.

In Bingöl et al. (2010), the horizontal meandering has been examined with a nacelle-installed continuous wave (CW) lidar. The campaign confirms the passive tracer assumption, which is essential for the definition of the meandering in the DWM model. Furthermore, the wind speed deficit in the MFR has been investigated for some distances. Given that the CW lidar cannot measure simultaneously in different downstream distances, the beam has been focused successively to different downstream distances. In Trujillo et al. (2011), the analysis has been extended to a two-dimensional scan. The measured wind speed deficit in the MFR has been compared to the Ainslie wake model (Ainslie 1988), which constitutes the basis for the definition of the deficit in the DWM model.

Additionally, in Machefaux et al. (2013) a comparison of measured lateral wake meandering based on pulsed scanning lidar measurements has been presented. Special attention is paid to the advection velocity of the wake, which is estimated by measured and low-pass filtered wind directions at the met mast (based on the assumptions of the DWM model) and the wake displacement at certain downstream distances. The analysis shows that the advection velocity calculated by the Jensen model (Jensen 1983) is in relatively good agreement. Finally, the study compares the measured expansion of the wake in the fixed frame of reference (FFR) to CFD simulations and simple analytical engineering models. The wake expansion calculated by simple analytical engineering models is mostly in line with lidar measurements and CFD simulations, but it also depicts potential for further improvements. This is the reason why a new empirical model for single wake expansion is proposed in Machefaux et al. (2015a). In Machefaux et al. (2016), a measurement campaign is presented, that involves three nacelle-mounted CW scanning lidar devices. The investigation includes a spectral analysis of the wake meandering, a comparison of the measurements to the assumptions in the DWM model as well as a comparison of the wind speed deficit profile in a merged wake situation to CFD simulations.

1.2 Contributions of the present thesis

The outlined thesis can be divided into three parts. The first part (I) deals with the validation and recalibration of the DWM model, especially for onshore wind farms with small turbine distances, which is in contrast to most of the aforementioned wake model validations. The second part (II) focuses on the application of multiple wakes in the DWM model. The final part (III) is concerned with an extension of the DWM model towards a static version to enhance the applicability in site-specific load simulations and layout optimization processes.

I. The outlined study validates the DWM model by lidar measurements, met mast as well as load and power measurements in two different wind farms and compares the DWM model to the commonly used Frandsen model. In contrast to many previously introduced measurement campaigns, the analysis is based on measurements of onshore wind farms with small turbine distances. Furthermore, the inclusion of lidar, met mast as well as load measurements and the special focus on the DWM model is unique. In the analysis of the lidar measurements, particular focus is placed on investigating the shape of the wind speed deficit in the MFR and the degradation of the wind speed deficit in downstream direction. The latter can be captured very well with the nacelle-mounted pulsed scanning lidar systems used given that it measures simultaneously at different downstream distances. Thus, a detailed comparison of the predicted degradation of the wind speed deficit between the DWM model and the measurement results is possible. Furthermore, the lidar measurements collected are used to recalibrate the DWM model, which enables a more precise modeling of the wake degradation. Consequently, the calculation of loads and energy yield of the wind farm can be improved.

Besides the validation of the recalibrated model according to power output and loads, lidar wake measurements are integrated into the load simulation to support the calculation and reduce uncertainties. This analysis has already been published in Reinwardt et al. (2021). The measured wind speed deficit in the MFR and the meandering time series are introduced successively into the load simulation. Related studies with a different approach of integrating the lidar measurements are Dimitrov et al. (2019) for wake-free inflow conditions, and Conti et al. (2020) for wake conditions. In comparison to the outlined methods the approach investigated here does not need any high frequency or raw data from the lidar system. It is purely based on the measured LOS wind speed. Furthermore, it is focused on the measured wind speed deficit and the meandering of the wake, which is successively introduced in the DWM model definition, whereas in Conti et al. (2020) special focus is given to estimating turbulence in the wake. By contrast, here the wake turbulence is only indirectly captured by the investigated wake meandering and the wind speed deficit gradient in the MFR.

II. Moreover, different methods to calculate multiple wakes in combination with the DWM model are investigated. Different commonly used approaches of multiple wakes are discussed and incorporated into the DWM model definition. Some of them have already been introduced and discussed in the literature review. The results of the different approaches are validated with lidar measurements in the MFR and FFR as well as load measurements.

III. Another aspect of the thesis is the usage of wake models for site-specific load simulations and layout optimizations. Planning a new wind farm layout is a highly itera-

tive process, where time-consuming calculations such as aeroelastic load simulations for a whole wind farm including all layout options are avoided as much as possible. A common way to counteract this problem is to estimate the loads based on interpolations between already performed load simulations, which serve as grid points of a response surface (Toft et al. 2016). This interpolation method usually only depends on a couple of site conditions (e.g. wind shear, TI, wind slope and air density). In this light it is understandable that the very simple analytical Frandsen model can be used particularly well in site-specific load simulations and layout optimization processes, whereas the physically more correct DWM model remains unusable for the industry given that the response surface requires a single TI value for the whole wind field instead of an inhomogeneous wind field, as generated by the DWM model. This issue is also addressed in this thesis. A method to extend the DWM model is presented to allow a combination with load interpolation methods. This will expand the model's scope by improving its usability for site-specific load calculation processes. Accordingly, the description of the physical behavior of the wake will be improved compared with currently used models. The analysis primarily focuses on the loads of the downstream turbine and less on the calculation of power losses due to wakes. Furthermore, the extension is defined in such a way that the computational costs of the calculation procedure are very low, thus allowing an application in wind farm layout optimization processes. This approach has been published during this thesis in Reinwardt et al. (2020b) and is subsequently called the static DWM model.

Overall, the thesis leads to an improved wake model, which holds particular interest to onshore wind farms with small turbine distances. The model deals with single as well as multiple wakes in a typical site-specific load simulation processes. The model development is based on measurements in two onshore wind farms. The outlined research enables a more accurate calculation of loads and power output in wind farms and thus leads to a more efficient wind farm operation and renewable power generation, which in turn contributes to increase the energy supply by renewable energy sources.

The remained of this work is arranged as follows. Chapter 2 summarizes the fundamentals, which build the basis for later investigations. A detailed description of the wake models used is outlined in this chapter. Subsequently, Chapter 4 and 5 describe the recalibration as well as extension of the DWM model. The wind farms used for validation purposes of the outlined models are presented in Chapter 3. In Chapter 6, the processing of the measurement data is explained in detail. The final results and comparisons with the measurements can be found in Chapter 7. Finally, all findings are concluded in Chapter 8.

Chapter 2

Fundamentals

The current chapter provides the fundamentals on which this thesis builds up. A brief introduction into atmospheric boundary layer methodology related to wind energy is given in the following. Subsequently, some fundamentals related to aerodynamics and loads of wind turbines are given. Later, an introduction into wakes of wind turbines in general followed by a description of specific wake models is outlined. Finally, some general details about lidar systems as well as different types of devices are summarized.

2.1 Atmospheric boundary layer

The atmospheric boundary layer (ABL) describes the lower part of the troposphere and is influenced by the earth's surface. The roughness of the surface (e.g. flat , complex or marine terrain), albedo, moisture content, heat emissivity and heat capacity determine the momentum and energy exchange between the surface and the atmosphere and have a large influence on the structure of the ABL (Emeis 2013). The ABL can have an expansion of 1 km to 2 km onshore and 0.5 km offshore (Foken 2016). The extension of the ABL is influenced by the generation of turbulent kinetic energy and the heat of the lower surface. Consequently, the temperature and atmospheric stability in the ABL is influenced by diurnal and annual variations. In flat terrain during daytime a convective boundary (CBL) layer is build up. During daytime the sun heats up the ground and generates thermal convection, so that vertical mixing and small vertical gradients occur. In the night the ground cools down and a stable boundary layer (SBL) develops. This implies a low TI and large vertical gradients. The remaining layer above the SBL is called residual layer. The daily variations in the vertical structure of the ABL is illustrated in Figure 2.1. The ABL is bounded by the capping inversion area, where an exchange with air from the free troposphere takes place. A neutral boundary layer arises if clouds, wind and rain disturb short-wave and long-wave radiation, so that almost no influence of diurnal variations can be recognized.

2.1.1 Vertical wind speed distribution

One of the most important atmospheric characteristics for wind turbines is the vertical shear, i.e. the vertical increase of the wind speed with the height. A schematic illustration

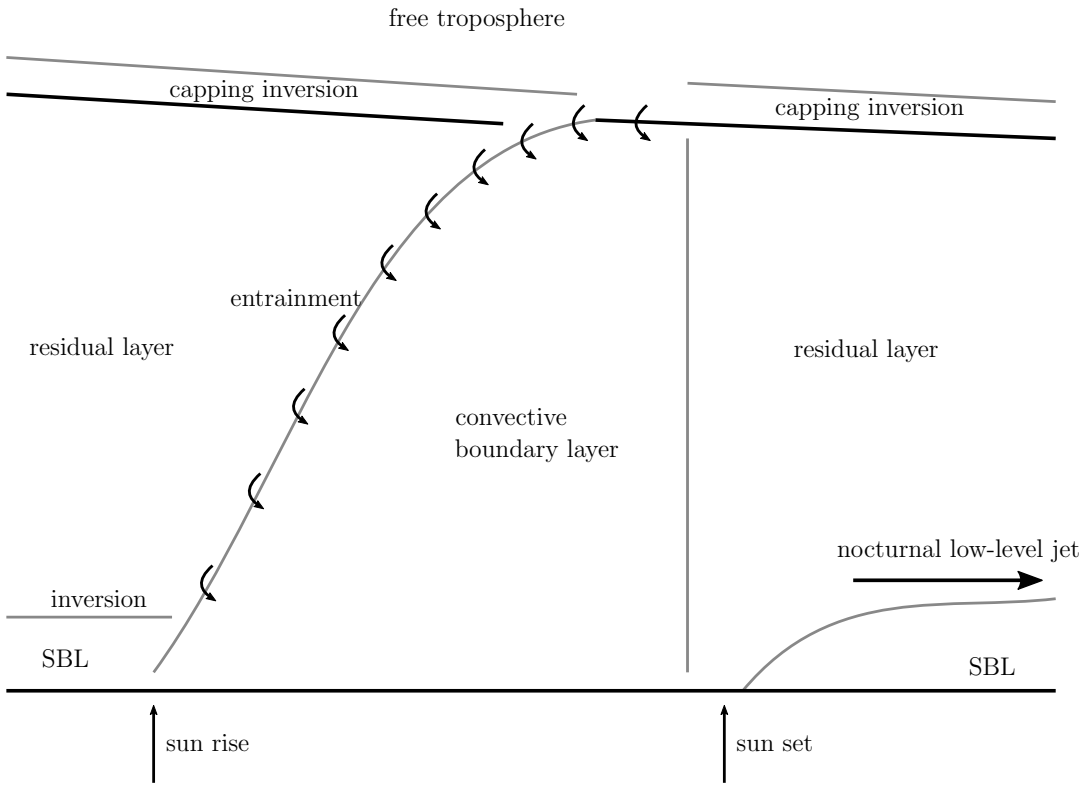

Figure 2.1: Schematic illustration of the diurnal variations in the ABL according to Emeis (2013).

of the vertical velocity distribution for stable, neutral and unstable conditions is illustrated in Figure 2.2. The wind shear can be described by either the logarithmic wind profile or the power law. The logarithmic wind profile is only valid in the surface layer, respectively the constant-flux or Prandtl layer, which is defined as the layer, where the turbulent vertical fluxes of momentum, heat, and moisture deviate less than 10 % from their surface values, and Coriolis forces are negligible (Emeis 2013). The vertical wind speed distribution according to the logarithmic wind profile is defined as follows (Emeis 2013):

$$u(z) = \frac{u_*}{\kappa}\left(\ln\left(\frac{z}{z_0}\right) - \Psi_m\left(\frac{z}{L_*}\right)\right) \quad , \tag{2.1}$$

where u_* is the friction velocity, κ the von Kármán constant of 0.4, z_0 the roughness length, Ψ_m a correction function depending on the height z and L_* the Obukhov length. The correction function Ψ_m is defined depending on whether the thermal stratification of the surface layer is stable or unstable. In neutral stratification Ψ_m is equal to zero.

Another common way to describe the distribution of the vertical wind speed is the power law, which defines the wind speed distribution as follows (Emeis 2013):

$$u(z) = u(z_r)\left(\frac{z}{z_r}\right)^{\alpha} \tag{2.2}$$

with the reference height z_r and the power law or Hellmann exponent α, which depends on the thermal stability of the surface layer and the surface roughness. The power law is often

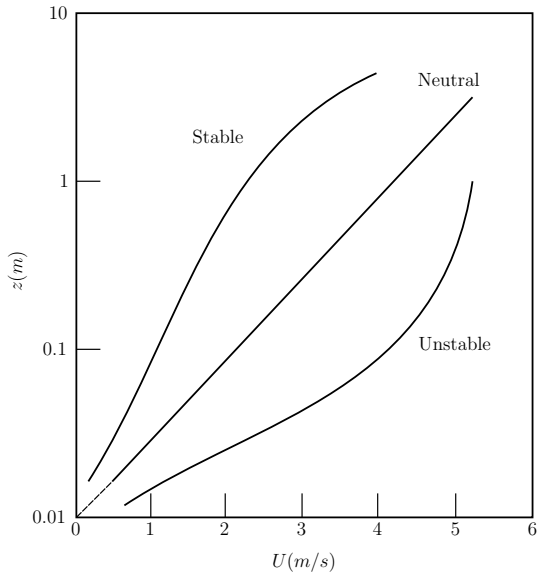

Figure 2.2: Schematic illustration of the vertical mean velocity distribution according to Kaimal and Finnigan (1994).

chosen in industry instead of the logarithmic profile due to its mathematical simplicity. Both distributions deliver similar results as long as the height range is small. However, for larger height ranges as they often occur at the current sizes of wind turbines, it is rather challenging to find a power law that fits to the logarithmic profile (Emeis 2013).

2.1.2 Atmospheric stability

The Obukhov length L_* is strongly related to the atmospheric stability and can be used to quantify the stability of the ABL. An Obukhov length lower than zero indicates unstable conditions, whereas a higher value above zero implies stable stratification (Foken 2016). Neutral conditions are indicated by an infinite Obukhov length. The Obukhov length can be derived from the Richardson number. The Gradient-Richardson number is defined as follows (Foken 2016):

$$R_i = -\frac{g}{\overline{T}} \frac{\partial T/\partial z}{(\partial u/\partial z)^2} \ , \tag{2.3}$$

where g is the gravitational acceleration, $\overline{T}$ the mean temperature, and T the temperature. The Gradient-Richardson number can also be approximated by the Bulk-Richardson number (Foken 2016):

$$R_{i,B} = -\frac{g}{\overline{T}} \frac{\Delta T \Delta z}{(\Delta u)^2} \ . \tag{2.4}$$

The Richardson number itself can be used to classify atmospheric stability. A negative Richardson number implies unstable stratification, a value around zero indicates neutral conditions and a Richardson number between 0 and the critical Richardson number of 0.2 means stable stratification (Foken 2016). The critical Richardson number is the point, where almost no turbulent flow exists and laminar flow conditions predominate.

2.1.3 Turbulence intensity

As already indicated in the last section, turbulence arises due to thermal effects and variations of the temperature, which leads to movement of masses, or friction with the earth surface, which is related to the topography. Consequently, turbulence can be classified into two categories: first, mechanically introduced turbulence due to the vertical shear, which depends on pressure gradients and the roughness of the surface; second, thermal turbulence due to thermal convection, which is mainly affected by temperature differences between the surface and the air masses above. This implies that turbulence is strongly related to time-of-day variations as well as seasonal variations. In wind energy considerations it is of major importance to classify and evaluate the turbulence at a specific site. For this purpose, a common way is to describe turbulence is based on the definition of the TI, which is defined as follows:

$$\begin{aligned} TI_u &= \frac{\sigma_u}{\overline{u}} \ , \\ TI_v &= \frac{\sigma_v}{\overline{u}} \ , \\ TI_w &= \frac{\sigma_w}{\overline{u}} \ , \end{aligned} \tag{2.5}$$

where σ_u, σ_v, and σ_w are the standard deviations of the fluctuating wind speed in the longitudinal, lateral and vertical direction. $\overline{u}$ is the mean wind speed in longitudinal direction.

2.1.4 Turbulence spectra

Additionally, to simulate fatigue loads at wind turbines a description of turbulence in the frequency domain by a turbulence spectrum is sufficient. For this purpose, the atmospheric turbulence can be described by eddies, which transport heat as well as kinetic energy. These eddies can vary in lifetime and sizes from seconds and centimeters up to days and kilometers. Larger scales are transferred to smaller scales until they dissipate and heat is released. This observation is described by the energy cascade introduced by Kolmogorov (Kolmogorov 1941a; Kolmogorov 1941b).

The characteristic distribution of the eddies is summarized in a turbulence energy spectrum, which describes the energy distribution of the eddies over the wavelength or frequency (Foken 2016). A schematic illustration of an energy spectrum is given in Figure 2.3. A scalar energy spectrum is a useful method to describe turbulence if turbulence is homogeneous in all directions and isotropic. It includes the contribution to the total kinetic energy from Fourier modes with wavenumber magnitudes from k to $k + \delta k$, where k is the magnitude of the wave number vector. The energy spectrum can be divided into three parts (Kaimal and Finnigan 1994). The first part is the energy containing part given that large eddies comprise most of the kinetic energy. In this range of wavenumbers turbulent kinetic energy is produced due to buoyancy and shear. The characteristic length scale in this range is the integral length scale Λ, which defines the maximum of the energy spectrum. The next part is the inertial subrange. In this range energy is not produced and does not dissipate, it is only transferred to smaller scales in an energy cascade as explained before. The one-dimensional spectrum of the u-component in this range can be

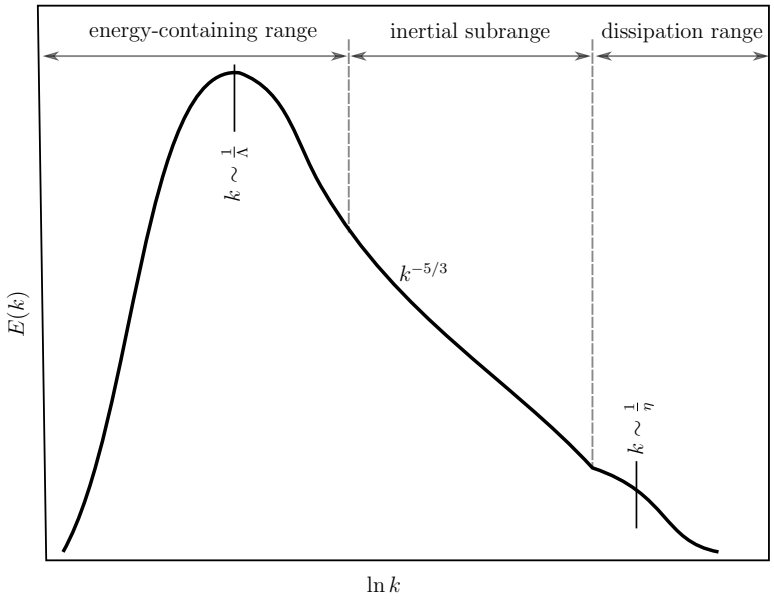

Figure 2.3: Schematic illustration of the turbulence energy spectrum according to Kaimal and Finnigan (1994).

defined as follows (Kaimal and Finnigan 1994):

$$F_u(k_1) = -\alpha_1 \epsilon^{2/3} k_1^{-5/3} \tag{2.6}$$

where α_1 is the Kolmogorov constant and ϵ the turbulent kinetic energy dissipation rate, so that the energy spectrum in the inertial subrange depicted in a logarithmic diagram has a linear slope of -5/3. The last range is the dissipation range where energy is converted into internal energy. The characteristic length scale in this range is the Kolmogorov length scale η.

Additionally, turbulence can be described by turbulent momentum fluxes or Reynolds stresses in the flow, defined as the covariance between two fluctuations (e.g. $\overline{u'w'}$ or $\overline{v'w'}$). The fundamental description of the spatial structures of turbulence is defined by the two-point covariance tensor as follows (Mann 1998):

$$R_{ij}(\mathbf{r}) = \langle u_i(\mathbf{x})\, u_j(\mathbf{x}+\mathbf{r}) \rangle \tag{2.7}$$

where $i, j = (1, 2, 3)$ are the indices corresponding to the fluctuating wind vector ($\mathbf{u}(x) = (u_1, u_2, u_3) = (u, v, w)$). $\langle\rangle$ means ensemble averaging and $\mathbf{x} = (x_1, x_2, x_3) = (x, y, z)$ is the position vector in the three-dimensional coordinate system and $\mathbf{r} = (r_1, r_2, r_3)$ the separation vector between the two points. It is often convenient to define turbulence in the Fourier domain. The Fourier transform of the covariance tensor delivers the three-dimensional spectral velocity tensor and can be calculated as follows (Mann 1998):

$$\Phi_{ij}(\mathbf{k}) = \frac{1}{(2\pi)^3} \int R_{ij}(\mathbf{r}) \exp(-i\,\mathbf{k}\cdot\mathbf{r}) d\mathbf{r} \tag{2.8}$$

where $\mathbf{k} = (k_1, k_2, k_3)$ is the wave vector. In wind energy, it is common to model second-order statistics of turbulence, such as variances or cross-spectra (definition in

Equation (2.9)). For simulation purposes, the velocity field is otherwise assumed to be Gaussian. Third-order statistics such as skewness are neglected in load calculations. All second-order statistics can be derived from the covariance tensor in Equation (2.7) or its Fourier transform, the spectral tensor in Equation (2.8). Practically, it is not possible to measure the three-dimensional velocity spectrum, whereby the cross-spectrum is defined instead (Mann 1998):

$$\begin{aligned} x_{ij}(k_1, \Delta y, \Delta z) &= \frac{1}{2\pi} \int_{-\infty}^{\infty} R_{ij}(y, \Delta y, \Delta z) \exp(-ik_1 x) dx \\ &= \int_{-\infty}^{\infty} \int_{-\infty}^{\infty} \Phi_{ij}(\mathbf{k}) \exp(-i(k_2 \Delta y + k_3 \Delta_z)) dk_2 dk_3 \ . \end{aligned} \tag{2.9}$$

The one-point spectrum $F_i(k_1) = x_{ii}(k_1, 0, 0)$ can be derived when the two indices i and j are the same and $y = z = 0$. Out of the cross spectrum the coherence can be calculated as follows (Mann 1998):

$$coh_{ij}(k_1, \Delta y, \Delta z) = \frac{|x_{ij}(k_1, \Delta y, \Delta z)|^2}{F_i(k_1) F_j(k_1)} \ . \tag{2.10}$$

In the IEC guideline IEC 61400-1 Ed.4 (2019), two different models to calculate turbulence spectra are suggested. The first one, the Mann uniform shear model, calculates the three-dimensional spectral velocity tensor based on an isotropic von Kármán energy spectrum. The spectrum is modified, so that it takes into consideration shear deformation and the life time of the eddies depending. The model is only depending on three parameters, a non-dimensional number to describe the eddy lifetime Γ, the integral length scale Λ and the Kolmogorov constant multiplied by the energy dissipation rate to the power of two-thirds $\alpha_1 \epsilon^{2/3}$.

In this thesis the second method, the Kaimal spectrum together with an exponential coherence model to account for the spatial correlation is used. Therefore, a detailed distribution of the Mann model is not outlined here but can be found in Mann (1994) or the Guideline IEC 61400-1 Ed.4 (2019).

The Kaimal model defines the velocity spectrum S_i of the velocity component i as follows (IEC 61400-1 Ed.4 2019):

$$\frac{f S_i(f)}{\sigma_i^2} = \frac{4 f L_i / U_0}{(1 + 6 f L_i / U_0)^{5/3}} \ , \tag{2.11}$$

where U_0 is the ambient mean wind speed. Equation (2.11) defines the single-sided velocity spectrum, so that only positive frequencies are considered. It should be highlighted that here the abbreviation S is used instead of F. The S indicates that the spectrum depends on the frequency f instead of the wavenumber as it is the case when using the abbreviation F. The integral scale parameters L_i are given in the guidelines (IEC 61400-1 Ed.4 2019). The standard deviations in the lateral and vertical directions σ_2 and σ_3 are given by the standard deviation in longitudinal direction scaled by 0.8 and 0.5, respectively. The coherence model to account for the spatial correlation is also defined in the guideline (IEC 61400-1 Ed.4 2019).

Overall, the section summarizes the most relevant characteristics and definitions of the ABL for this thesis. The vertical wind speed profile, the TI and the definition of a

turbulence spectra are of major importance for the load simulations conducted in this thesis, whereas the Richardson number has been used to determine the atmospheric stability during the lidar measurements. More detailed descriptions of the ABL can be found in Stull (1988), Arya (1995) and Garratt (1994).

2.2 Aerodynamics and loads

In the following, the momentum theory as well as the combination with the blade element method (BEM) is described. The BEM together with the momentum theory are the fundamental methods for the subsequently explained load simulation software.

2.2.1 Momentum theory

This section explains the simple one-dimensional momentum theory of an ideal rotor. In this model it is assumed that the rotor is a permeable disc and friction as well as the rotational velocity component in the wake are neglected. The rotor represents a drag device and slows down the wind speed from U_0 to U_w as sketched in Figure 2.4. Therefore,

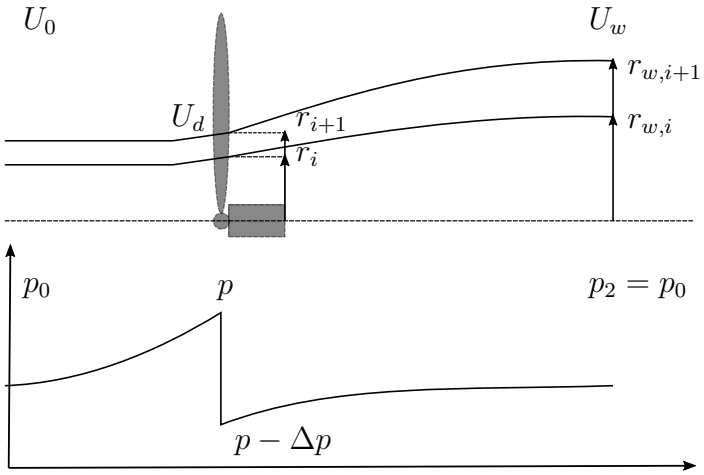

Figure 2.4: Schematic illustration of the wake expansion according to Madsen et al. (2010).

the streamlines in Figure 2.4 are expanded and accordingly the wake is expanded. In the region upstream of the rotor there is a pressure increase. A sudden pressure drop Δp is assumed over the rotor. Behind the rotor, the pressure increases again until it reaches the ambient pressure in the far wake (Hansen 2008).

Using an actuator disc model to extract energy from the wind and analytic equations for the conservation of mass, momentum and energy for incompressible flows leads to the following equations for the mass flow $\dot{m}$, the thrust on the disc T, the extracted energy E, and the power P, respectively (Sanderse 2009):

$$\dot{m} = \rho A_0 U_0 = \rho A U_d = \rho A_w U_w \,, \tag{2.12}$$

$$T = \dot{m}(U_0 - U_w) = \Delta p A \,, \tag{2.13}$$

$$E = \frac{1}{2} m \left(U_0^2 - U_w^2\right) \,, \tag{2.14}$$

$$P = \frac{1}{2}\dot{m}\left(U_0^2 - U_w^2\right) = TU_d = \dot{m}(U_0 - U_w)U_d \ , \tag{2.15}$$

where U_d is the wind speed at the rotor disc and A is the rotor area. Evaluating the last equations delivers the following expression for the velocity in the rotor plane (Froude's theorem):

$$U_d = \frac{1}{2}\left(U_0 + U_w\right) \ . \tag{2.16}$$

The velocity at the rotor plane as well as in the wake can also be described with the help of the axial induction factor a as follows (Hansen 2008):

$$U_d = (1-a)U_0 \ , \tag{2.17}$$

$$U_w = (1-2a)U_0 \tag{2.18}$$

with $a = 1 - \frac{U_d}{U_0}$. Considering that the mass flow can be calculated as $\dot{m} = \rho U A$, the following equations for the power and the thrust depending on the axial induction factor can be derived (Hansen 2008):

$$P = 2\rho U_0^3 a(1-a)^2 A \ , \tag{2.19}$$

$$T = 2\rho U_0^2 a(1-a)A \ . \tag{2.20}$$

In the wind industry, the power is often normalized by the available power due to the wind, so that a power coefficient is defined as (Hansen 2008):

$$c_P = \frac{P}{\frac{1}{2}\rho U_0^3 A} \ . \tag{2.21}$$

Similarly, the thrust coefficient is defined as (Hansen 2008):

$$c_T = \frac{T}{\frac{1}{2}\rho U_0^2 A} \ . \tag{2.22}$$

Taking into consideration Equation (2.19) and (2.20) the following equation for the power and thrust coefficients depending on the axial induction factor can be evaluated (Hansen 2008):

$$c_P = 4a(1-a)^2 \ , \tag{2.23}$$

$$c_T = 4a(1-a) \ . \tag{2.24}$$

As already mentioned and illustrated in Figure 2.4, the wake expands due to the lower wind speed in the wake. The higher the thrust coefficient, the larger is the wake expansion. The maximum value of the power coefficient is 16/27 and is reached for $a = 1/3$. This value is also known as the Betz limit (Sanderse 2009). The thrust coefficient has a value of 8/9 at the maximum power coefficient. Experiments have proven that the ideal rotor disc model leading to Equation (2.24) is only valid for an axial induction factor of less than 0.4. A higher axial induction factor would lead to a negative wake velocity, which is not feasible. Physically, at higher axial induction factors the free shear layer at the boundaries of the wake becomes unstable due to the high difference of the wake velocity and the ambient wind speed, so that eddies are formed and momentum is transported into the wake (Hansen 2008) as later on explained and illustrated in Figure 2.7.

2.2.2 Blade element theory

It is a common way in the industry to combine the momentum theory with the BEM, so that local events, which take place at the actual position of the blades as well as the actual geometry of the blades are considered (Hansen 2008). The BEM theory enables a calculation of loads and thrust as well as power of the turbine for varying wind speeds, rotational speeds and pitch angles. According to this method the streamtube behind the rotor is divided into a certain number of elements, which are delimited by streamlines as illustrated in Figure 2.4. The BEM theory assumes that there is no radial dependency, so that each element will be treated separately. Furthermore, the force of the blades on the flow at each annular element is constant, which corresponds to a rotor with an infinite number of blades. The later assumption can be corrected by Prandtl's tip loss factor to consider a rotor with a finite number of blades. Another correction is the so-called Glauert correction, which takes care of the fact that the momentum theory is not valid for high axial induction factors ($a > 0.4$).

A schematic illustration of the velocities and forces acting on a blade element is illustrated in Figure 2.5. The resultant relative velocity W is composed of an axial component

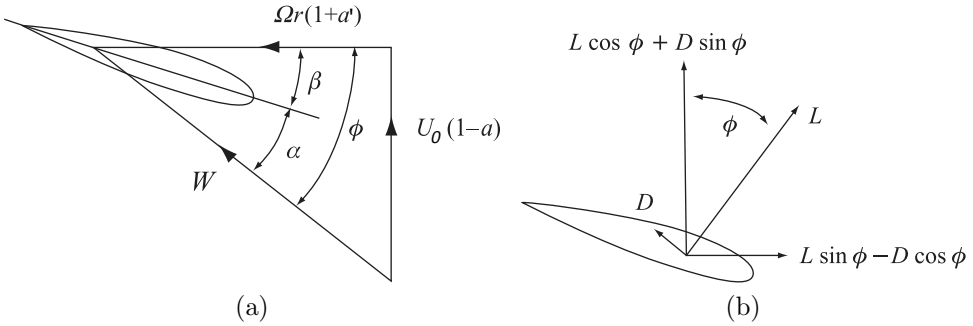

Figure 2.5: Velocities **(a)** and forces **(b)** at a blade element according to Burton (2011).

calculated by $U_0(1-a)$ and a rotational component $\Omega r(1+a')$. a' is the tangential induction factor. The exertion of torque on the rotor causes a reaction torque on the air in opposite direction, so that the wake rotates. The wake rotational velocity can be described by $a'r\Omega$. The net tangential velocity is calculated by combining the tangential velocity experienced by the blade element $r\Omega$ and the wake rotational velocity $a'r\Omega$, which delivers a total tangential velocity calculated by $\Omega r(1+a')$. The resultant velocity W relative to the chord line at a radius r can then be calculated as follows (Burton 2011):

$$W = \sqrt{U_0^2(1-a)^2 + r^2\Omega^2(1+a')^2} \ . \tag{2.25}$$

The angle ϕ between the rotor plane and the relative velocity is a combination of the angle of attack α and the local pitch β. The local pitch comprises the pitch angle of the blade and the local twist of the blade. ϕ can be calculated as follows (Hansen 2008):

$$\tan\phi = \frac{(1-a)U_0}{(1+a')\Omega r} \ . \tag{2.26}$$

Moreover, ϕ is related to the relative velocity (Hansen 2008):

$$W\sin\phi = U_0(1-a) \ , \tag{2.27}$$

$$W \cos\phi = \Omega r(1 + a') \ . \tag{2.28}$$

The rotor torque Q at a blade element is related to the power P by the rotational velocity (Hansen 2008):

$$dP = \Omega \, dQ \ . \tag{2.29}$$

Following the definition of power and thrust in Equations (2.19) and (2.20) and considering Equation (2.29) delivers the following definition for the thrust and torque on a span-wise length of dr (Hansen 2008):

$$dT = 4\pi r \rho U_0^2 a(1 - a) dr \ , \tag{2.30}$$

$$dQ = 4\pi r^3 \rho U_0 \Omega (1 - a) a' dr \ . \tag{2.31}$$

The lift force dL on the element at a chord length of c and normal to the relative velocity W can be calculated as follows (Burton 2011):

$$dL = \frac{1}{2} \rho W^2 c \, c_l \, dr \ . \tag{2.32}$$

Accordingly, the drag force dD parallel to the relative velocity is given by (Burton 2011):

$$dD = \frac{1}{2} \rho W^2 c \, c_d \, dr \ . \tag{2.33}$$

The lift and drag coefficients c_l and c_d are usually given by experimental data and can be looked up in tables. The thrust T and the torque Q on the annular section can be calculated as follows (Burton 2011):

$$dT = dL \cos\phi + dD \sin\phi = \frac{1}{2} \rho W^2 B c (c_l \cos\phi + c_d \sin\phi) dr \ , \tag{2.34}$$

$$dQ = (dL \sin\phi - dD \cos\phi) r = \frac{1}{2} \rho W^2 B c r (c_l \sin\phi - c_d \cos\phi) dr \ , \tag{2.35}$$

where B is the number of blades. Equations (2.34) and (2.35) can be simplified to:

$$dT = \frac{1}{2} \rho W^2 B \, c \, c_n \, dr \ , \tag{2.36}$$

$$dQ = \frac{1}{2} \rho W^2 B \, c \, r \, c_t \, dr \ , \tag{2.37}$$

with

$$c_n = c_l \cos\phi + c_d \sin\phi \ , \tag{2.38}$$

and

$$c_t = c_l \sin\phi - c_d \cos\phi \ . \tag{2.39}$$

Introducing Equation (2.27) into Equation (2.36) leads to (Hansen 2008):

$$dT = \frac{1}{2} \rho \frac{U_0^2 (1 - a)^2}{\sin^2\phi} B \, c \, c_n \, dr \ . \tag{2.40}$$

Similarly, introducing Equations (2.27) and (2.28) into Equation (2.41) yields (Hansen 2008):

$$dQ = \frac{1}{2}\rho \frac{U_0(1-a)\Omega r(1+a')}{\sin\phi\cos\phi} B\, c\, r\, c_t\, dr \ . \tag{2.41}$$

To consider that only a fraction of the annular area is covered by the rotor blades, the solidity σ is introduced (Hansen 2008):

$$\sigma(r) = \frac{c(r)B}{2\pi r} \ . \tag{2.42}$$

Equalizing Equations (2.30) and (2.40) and considering the solidity in Equation (2.42) delivers the following expression for the axial induction (Hansen 2008):

$$a = \frac{1}{\frac{4\sin^2\phi}{\sigma c_n} + 1} \ . \tag{2.43}$$

Similarly, equalizing Equations (2.31) and (2.41) leads to the following equation for the radial induction (Hansen 2008):

$$a' = \frac{1}{\frac{4\sin\phi\cos\phi}{\sigma c_t} - 1} \ . \tag{2.44}$$

Finally, Equations (2.43) and (2.44) are used to calculate the local induction factors at each blade element. The equations need to be solved in an iterative process due given that both equations depend on the flow angle ϕ. Moreover, c_n and c_t depend on the lift and drag coefficients c_l and c_d, which in turn are a function of the angle of attack. The angle of attack also depends on the flow angle. The following iterative procedure is used to compute the final induction factors and thereupon the local loads at the blade elements (Hansen 2008):

1. Initialize the induction factors a and a' (typically $a = a' = 0$).
2. Calculate the flow angle ϕ based on Eq. (2.26).
3. Calculate the angle of attack with $\alpha = \phi - \beta$.
4. Read $c_l(\alpha)$ and $c_d(\alpha)$ from a table.
5. Calculate c_n and c_t according to Equations (2.38) and (2.39).
6. Calculate a and a' according to Equations (2.43) and (2.44).
7. Check if a and a' have changed more than a predefined tolerance. If this is the case, the process will be repeated from step 2.
8. Calculate the local loads at the blade elements.

After calculating the thrust and torque at each blade element, the total rotor thrust as well as torque can be calculated by summing up the thrust and torque of all blade elements and multiplying them by the number of blades. Finally, the rotor power can be calculated from the rotor torque multiplied by the angular velocity.

2.2.3 Load simulation

The loads in the later outlined analysis are either simulated with the commercial software alaska/Wind (Chemnitz 2021) or Flex5. Both software packages are based on the explained BEM and momentum theory. Flex5 has been developed at the Danish Technical University (DTU) and is no longer commercially available. A comparison and explanation of alaska/Wind and Flex5 is outlined in Zierath et al. (2016) For the Curslack wind farm the loads are simulated with alaska/Wind, which is based on a flexible multibody system. The program was developed at the Institute of Mechatronics in Chemnitz, Germany. A brief description of alaska/Wind is included in Reinwardt et al. (2021) and picked up in the following.

Alaska/Wind provides an extension of the classical multibody approach, where the system comprises rigid-bodies connected by joints and force elements. The system is extended by flexible bodies with small deformations. The rigid body motions are vectorially superimposed with the deformation of the flexible body. The equations of motion are a set of ordinary differential equations. The model comprises submodels for blades, controller, nacelle, pitch system, gearbox, main shaft, high-speed shaft, generator, hub, yaw drive, and foundation. Blades and tower are reduced by a modal superposition of the first four eigenmodes. Both submodels are based on a finite-element model consisting of Timoshenko beams. The multibody model is connected to an aerodynamic code, which includes the BEM theory and delivers aerodynamic forces and moments at the individual blade sections based on the position and velocity of the blade elements provided by the multibody simulation. The classical BEM theory is extended to include dynamic inflow and dynamic stall effects. Furthermore, the multibody model is connected to a controller, which uses the generator speed and the pitch angle from the multibody simulation to calculate the generator torque and the pitch velocity and returns them to the multibody model. The controller used for the simulations is the actual controller implemented in the turbines of the analyzed wind farm. Hence, a reliable comparison with the measured loads can be achieved.

The software Flex5 is used to model the turbines in the ECN Wind Turbine Test Station Wieringermeer (EWTW). The reason for using Flex5 instead of alaska/Wind is that the wind farm comprises five N80 turbines and a model for this turbine type only exists in Flex5. Flex5 is based on a multibody formulation similar to alaska/Wind. The model has a fixed topology consisting of 28 degrees of freedom in total. The blades and the tower deformations are represented by a superposition of the first two modes in the two independent directions (Zierath et al. 2016). The aerodynamic code was developed at the DTU and is integrated directly into the multibody code. It uses also the BEM theory to calculate the aerodynamic forces and moments at the individual blade sections similar to alaska/Wind.

The inflow wind conditions can be divided into deterministic and stochastic contributions. Deterministic contributions, like the mean wind speed and the shear effects, are imposed on the turbulent wind field. The stochastic contributions are simulated based on a Kaimal spectrum and a coherence function (Veers 1988) as outlined in Section 2.1.4. To cover the stochastic influence of the turbulence on the loads, six seeds have been simulated for each ten-minute time series. The turbulent wind is modeled in both load simulation software similarly in a stand-alone in-house tool written in Python, which has

been developed within this thesis. The in-house program generates binary files containing the wind field. The wind field is described in Cartesian coordinates, which are required for the alaska/Wind simulations. However, Flex5 requires a turbulent wind field in polar coordinates, and hence a transformation of the coordinate system had to be implemented. The DWM model as well as the presented simple analytical wake models are included in the stand-alone Python tool and are uncoupled from any load simulation software. The script generates binary wind files with wake effects, which can be included in alaska/Wind or Flex5 similar to conventional stochastic wind fields for free inflow.

The analysis subsequently outlined, simulates the power, blade root flapwise and edgewise bending moments as well as tower bottom bending moments. Auxiliary sensors are added to the turbine model in alaska/Wind and Flex5 to compare the measured loads at the precise position of the strain gauges. Their locations are given in Chapter 3.

2.2.4 Fatigue load analysis

Furthermore, the analysis presented later compares measured and simulated fatigue loads quantified in damage equivalent loads (DELs). The DEL represents an amplitude that delivers the same damage as a complete load spectrum for a specified number of cycles N_r. For this purpose, a rainflow count (Radaj and Vormwald 2007) has been applied on the simulated time series, so that the number of cycles per amplitude and mean value are evaluated and a Markov matrix (Radaj and Vormwald 2007) is calculated. Usually, the rows in the matrix represent the amplitude and the columns specify the associated mean value. A summation of all columns delivers the number of cycles per amplitude and results in a load spectrum.

To support the prediction of the fatigue lifetime and evaluate the damage of a component, which has been exposed to a certain load spectrum, the Palmgren-Miner linear damage hypothesis can be applied (Palmgren 1924; Miner 1945). The hypothesis implies that the contribution to a failure due to the stress magnitudes of a spectrum is the sum of the ratio between the number of cycles per amplitude ΔN_j and the number of maximum cycles $N_{B,j}$, which would lead to a failure in accordance with the S-N curve. The S-N (Wöhler) curve illustrates the cyclic stress (S) against the cycles to failure (N) on a logarithmic scale (see Figure 2.6**(b)**. The S-N curve is determined experimentally. The following expression for the linear accumulation of damages can be applied (Radaj and Vormwald 2007):

$$D = \sum_{j=1}^{n} D_j = \sum_{j=1}^{n} \frac{\Delta N_j}{N_{B,j}} \ . \tag{2.45}$$

In accordance with the hypothesis, a failure occurs if $D > 1$. An illustration of the damage accumulation together with the Wöhler slope, which defines the number of cycles to failure $N_{B,j}$ is depicted in Figure 2.6. In the simple Palmgren-Miner approach the endurance range is neglected. Based on the linear accumulation of damages outlined in Equation (2.45) it is possible to calculate a DEL for a complete load spectrum. By introducing the constant $C = N_{B,j}\sigma_{a,j}^{m}$ into Equation (2.45) the following expression for

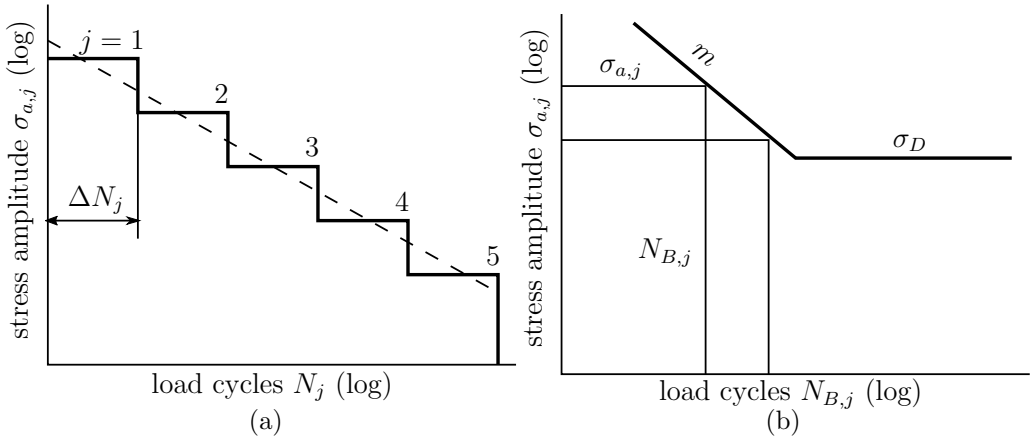

Figure 2.6: Load spectrum **(a)** and S-N slope **(b)** according to Radaj and Vormwald (2007).

the damage can be derived (Radaj and Vormwald 2007):

$$D = \frac{1}{C} \sum_{j=1}^{n} \Delta N_j \sigma_{a,j}^{m} \ . \tag{2.46}$$

In accordance with Equation (2.46) the damage from one amplitude σ_{eq} can be calculated as follows (Radaj and Vormwald 2007):

$$D = \frac{1}{C} N_{eq} \sigma_{a,eq}^{m} \ . \tag{2.47}$$

Equalizing Equations (2.46) and (2.47) gives the formula for the damage-equivalent amplitude (Radaj and Vormwald 2007):

$$\sigma_{a,eq} = \sqrt[m]{\frac{\sum_{j=1}^{n} \Delta N_j \sigma_{a,j}^{m}}{N_{eq}}} \tag{2.48}$$

Subsequently, the abbreviation DEL refers to the damage equivalent amplitude $\sigma_{a,eq}$. Furthermore, it should be highlighted that the damage or endurance limit calculated by the Palmgren-Miner hypothesis can deviate significantly from the real endurance limit and is only an estimation. It is possible to increase the accuracy by including the mean stress level and spreading in the accumulation. Nevertheless, the DEL is a helpful instrument to compare fatigue loads from different load spectra, whereby this approach is used in this thesis.

2.3 Wake of wind turbines

Single as well as multiple wake models are an essential part of the outlined thesis. Some fundamentals related to wake modeling in general as well as a description of a selection of different single as well as double wake models are outlined in the following.

The wake behind a wind turbine exhibits a lower wind velocity and a higher turbulence compared to the ambient conditions. The additional turbulence due to the wake is often

called wake-added turbulence, whereas the wind speed reduction is denoted as the wind speed deficit. Different models to describe either the wind speed deficit or the wake-added turbulence as well as wake models related to the present thesis have already been mentioned in the introduction. A general schematic illustration of the wake with different turbulence sources is depicted in Figure 2.7. The first region of the wake is dominated

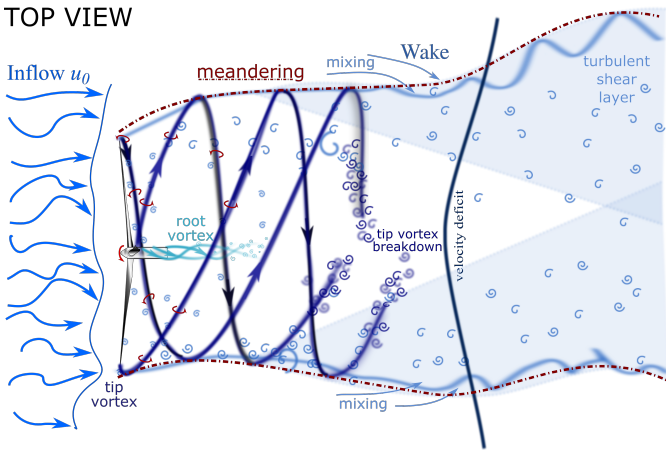

Figure 2.7: Top view illustration of the wake (Neunaber et al. 2020).

by the aerodynamics of the wind turbine itself. This region is called the near wake and extends up to two rotor diameters downstream. The wake experiences a twist counter-rotating to the rotation of the rotor (Neunaber et al. 2020). The imposed torque on the rotor leads to a reaction torque on the air in opposite direction, so that the wake rotates. Vortices arise at the blade root and the tip. The root vortices break down relatively early while the tip vortices remain longer and surround the wake in a helical path. A thin shear layer between the ambient flow and the lower wake wind speed develops. The thickness of the shear layer increases further downstream. A higher shear is generated when the differences between the wake flow and the ambient flow are higher, which implies a high thrust at the turbine. This is the case when the turbine is operating below the rated wind speed in optimal operating conditions. Subsequently, the turbulent mixing process starts, so that the low velocity in the wake mixes with the higher outer velocity and momentum is transferred into the wake. This leads to an expansion of the wake, while the velocity deficit is reduced. Turbulence in the wake increases until the shear layers merge further downstream at approximately 2 D. This area also marks the end of the near wake. Later downstream the velocity deficit becomes Gaussian shaped (Neunaber et al. 2020). This area is called the far wake and will be described by the subsequently defined wake models. Furthermore, the wake behaves like a passive tracer in the turbulent wind field, so that the wake deficit meanders based on large-scale turbulence structures. Besides, the wake recovery strongly depends on the ambient turbulence level (Sanderse 2009). A low ambient TI leads to a low wake recovery and a more pronounced deficit, while a high ambient TI leads to a faster recovery. The TI in the wake has its maximum in the shear layer as it be seen later in the results. The turbulence energy spectrum in the wake is shifted towards higher frequencies and exhibits smaller length scales in comparison to the free inflow. There might be a decrease of turbulence at low frequencies given that the turbine extracts energy in this region.

2.3.1 Single wake models

As already mentioned in the beginning of this section, wake models can be divided into models describing either the wind speed deficit or the wake-added turbulence. The most relevant models for this thesis are outlined in the following. Firstly, the Frandsen turbulence model is presented. The model provides a simple analytic definition of the wake-added TI and based on this a definition of the total TI in the wake. Subsequently, two simple analytic wake models (Jensen and Bastankhah) to calculate the wind speed deficit are introduced. The three different models have in common that they are only depending on the downstream distance and the turbine thrust coefficient, which in turn is strongly related to the amount of energy, which is extracted from the wind and consequently related to the wind speed deficit depth. After the description of the very basic wake models, the more complex Ainslie model is outlined. Similar to the Jensen and Bastankhah models, the Ainslie model calculates the wind speed deficit, but in contrast to these approaches needs to be solved numerically. Finally, a detailed description of the DWM model, which builds up on the Ainslie model is presented. The DWM model provides a definition of the wake-added turbulence as well as the wind speed deficit and is built in such a way that it can be directly connected to an aeroelastic load simulation. The loads at the downstream turbine are mainly affected by the wake-added TI, whereas the wind speed deficit leads to a power loss, so that the Frandsen model is used to calculate the loads at the turbine, whereas the Jensen, Bastankhah, and Aisnlie models are used to determine the power deficit. On the contrary, the DWM model is the only model that calculates the increased turbulence as well as the wind speed deficit, so that it can be applied to determine the increased load at the downstream turbine as well as the power deficit.

2.3.1.1 Frandsen wake-added turbulence model

The Frandsen model is a very frequently used model, which is defined in the guideline in IEC 61400-1 Ed.4 (2019). The model calculates the wake-added turbulence intensity TI_{add} as follows:

$$TI_{add} = \frac{1}{1.5 + 0.8\frac{x/d}{\sqrt{c_T}}} \tag{2.49}$$

with c_T the thrust coefficient, d the turbine diameter, and x the downstream distance. TI_{add} defined in Equation (2.49) refers to the wake-added TI at the wake center. The wake-added TI can be calculated as a function of the inflow wind direction Θ as follows (Frandsen 2007):

$$TI_{t,det.}(\Theta) = TI_0 \left(1 + \alpha_F \exp\left(-\left[\frac{\Theta}{\Theta_w}\right]^2\right)\right) \tag{2.50}$$

with

$$\alpha_F = \sqrt{\left(\frac{TI_{add}}{TI_0}\right)^2 + 1} - 1 \ , \tag{2.51}$$

$$\Theta_w = \frac{1}{2}\left(\frac{180}{\pi} \cdot \tan^{-1}\left(\frac{1}{x/d}\right) + 10^\circ\right) \ , \tag{2.52}$$

and TI_0 the ambient TI.

Furthermore, the maximum TI at the wake center (TI_t) can calculated by a quadratic summation of TI_{add} and TI_0 as follows Frandsen (2007):

$$TI_t = \sqrt{TI_{add}^2 + TI_0^2} \, . \tag{2.53}$$

In Frandsen (2007), it is stated that using the maximum, respectively the total TI at the wake center TI_t over the wake cone angle Θ_w yields approximately the same turbine response than the detailed definition of the total TI in Equation (2.50), so that the model can be simplified to a model with constant total TI in the wake calculated with Equation (2.53) and a wake cone angle calculated with Equation (2.52). Equation (2.53) uses a quadratic summation of the maximum wake-added TI calculated by Equation (2.49) and the ambient TI. In simple analytic wake-added turbulence models, it is often assumed that the ambient TI is independent of the wake-added turbulence, so that turbulent energies can be added in a quadratic approach. In the following, this simplification with a constant TI in the wake is abbreviated as "Frandsen model", whereas the detailed definition in accordance with Equation (2.50) is abbreviated as "Frandsen det. model".

A schematic illustration of the wake cone is depicted in Figure 2.8. The calculated

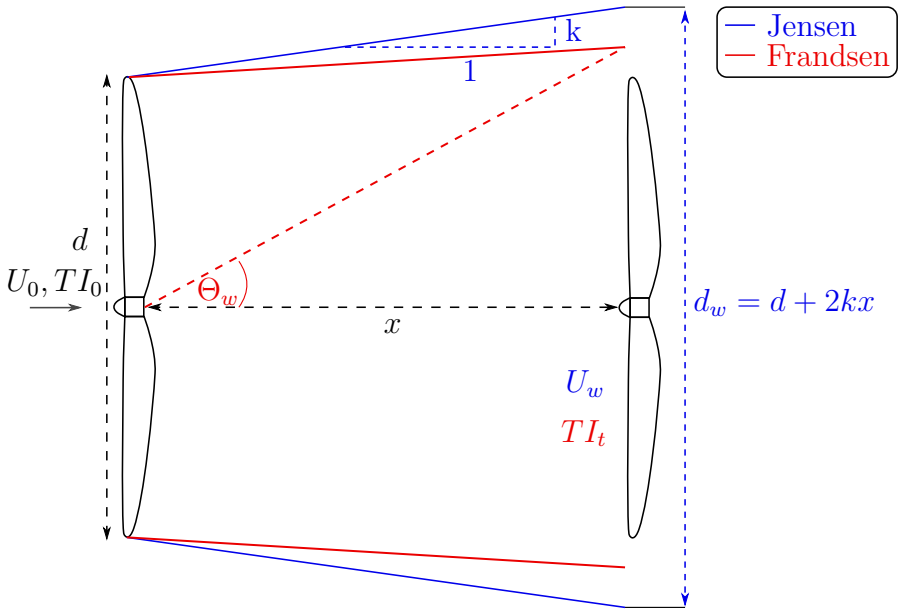

Figure 2.8: Schematic illustration of the wake cone angle and related variables in the Frandsen and Jensen wake model. Variables only related to the Frandsen model are marked in red, whereas variables related to the Jensen model are illustrated in blue.

total TI can be used to predict the loads per wind direction at the wake-affected turbine by scaling the turbulent wind field (generated by a Kaimal spectrum and outlined in Section 2.1.4).

Furthermore, in addition to the total TI Frandsen (2007) introduces the effective TI. The effective TI is a design TI and averages the total TIs for all wind directions (see Equation (2.54)). Moreover, the effective TI is an auxiliary variable to avoid many load calculations from different wind directions. The effective TI is a damage-equivalent TI,

which means that this TI results in the same fatigue damage as the total TIs from all wind directions. The effective TI can be calculated as follows (IEC 61400-1 Ed.4 2019):

$$TI_{\text{eff}}(U_0) = \left\{ \int_0^{2\pi} P_R(\Theta|U_0)\, TI_t^m(\Theta|U_0)\, \mathrm{d}\Theta \right\}^{\frac{1}{m}} \tag{2.54}$$

with $P_R(\Theta|U)$ being the probability density function of the wind direction and m being the Wöhler exponent (inverse slope of S-N curve). If it is assumed that the probability density function of the wind direction is evenly distributed, the following simplification can be applied (IEC 61400-1 Ed.4 2019):

$$TI_{\text{eff}} = \frac{\sigma_{\text{eff}}}{U_0} = \frac{1}{U_0} \left[(1 - n\,0.06)\sigma_0^m + 0.06 \sum_i^N \sigma_t^m(x_i) \right]^{\frac{1}{m}} \tag{2.55}$$

with n the number of neighboring turbines, σ_0 the standard deviation of the ambient wind speed, σ_t the standard deviation of the total wind speed, and U_0 the ambient wind speed.

Moreover, Frandsen (2007) discusses which turbines should be considered in the calculations of the effective TI. It is suggested to always take the closest turbine wakes as depicted in Figure 2.9. In a wind farm with multiple wakes as depicted in Figure 2.9 only

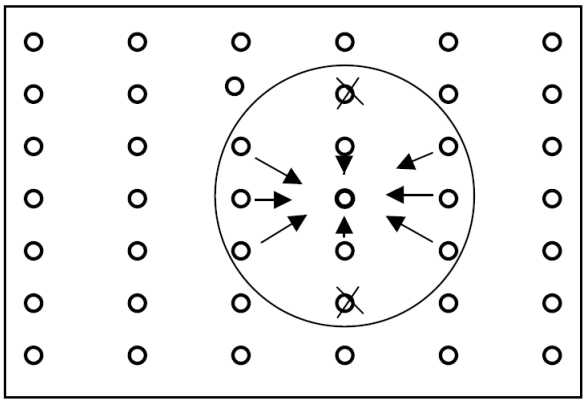

Figure 2.9: Schematic illustration of neighboring wind turbines, which are considered in the TI calculation in the Frandsen wake model (Frandsen 2007).

eight turbine wakes are considered in the calculations. Accordingly, in a wind farm with only two rows solely five neighboring turbines are considered and in a one row wind farm only two neighbors are taken into account.

2.3.1.2 Jensen model

The Jensen wake model, which was first introduced in Jensen (1983) and further developed in Katic et al. (1987), calculates the wind speed reduction in the wake. The model is described in a very ideal way, so that the velocity in the wake is constant and has no Gaussian shape as it is often assumed instead. Furthermore, it is assumed that the wake width immediately after the turbine is similar to the rotor diameter and expands linearly downstream. The wake opening angle has been adjusted to fit measurement data

further downstream than four rotor diameters, so that the model leads to large errors in the near-wake area. In accordance with the derivation of the model in Katic et al. (1987) the following mass balance can be stated:

$$d^2 U_d + (d_w^2 - d^2) U_0 = d_w^2 U_w \ . \tag{2.56}$$

In Katic et al. (1987) it is stated that the velocity deficit is derived by a balance of momentum. However, it should be highlighted that in Bastankhah and Porté-Agel (2014) it is mentioned that the mass conservation is applied in the Jensen model. This seems to be more in line with the outlined derivation.

Evaluating Equation (2.56) and considering that the velocity in the rotor plane U_d can be expressed by the axial induction factor (Equation (2.17)), the following expression for the wind speed deficit can be derived (Katic et al. 1987):

$$\frac{U_w}{U_0} = 1 - \frac{2a}{(1 + 2k\frac{x}{d})^2} \tag{2.57}$$

with k being the decay constant of 0.075. By evaluating Equation (2.24) the axial induction factor can be calculated out of the thrust coefficient c_t as follows:

$$a = \frac{1 - \sqrt{1 - c_t}}{2} \tag{2.58}$$

Finally, inserting Equation (2.58) into Equation (2.57) delivers the following expression for the wind speed in the wake cone (Katic et al. 1987):

$$U_w = \left(1 - \frac{1 - \sqrt{1 - c_T}}{\left(1 + 2k\frac{x}{d}\right)^2}\right) U_0 \tag{2.59}$$

The wake width is determined by the expression $1 + 2k\frac{x}{d}$ as depicted in Figure 2.8, so that the model is at the end only depending on the thrust coefficient, the downstream distance and the wake decay constant k.

The aim of the Jensen wake model is to calculate the energy content of the wind field at the downstream turbine, rather than to calculate the shape of the velocity deficit accurately, whereby a simple rectangular shape and the constant wind speed inside the wake cone are justified. It is a very common wake model to calculate power losses in wind farms and is also implemented in several commercial software, such as the Wind Atlas Analysis and Application Program (WAsP) (DTU 2021).

2.3.1.3 Bastankhah model

A more accurate description of the shape of the velocity deficit can be found in the Bastankhah wake model. The Bastankhah model has been developed by applying the conservation of mass and momentum to evaluate the velocity profiles downstream of the turbine and adopting a Gaussian distribution for the velocity deficit (Bastankhah and Porté-Agel 2014). Viscous and pressure terms are neglected in the momentum equations and self-similarity in the wake is assumed. Furthermore, a linear wake expansion similar

to the Jensen model is assumed. This leads to the following definition of the wind speed deficit:

$$\frac{\Delta U}{U_0} = \left(1 - \sqrt{1 - \frac{c_T}{8\left(2k^*\tilde{x} + 0.2\sqrt{\beta}\right)^2}}\right) \exp\left(-\frac{1}{2\left(2k^*\tilde{x} + 0.2\sqrt{\beta}\right)^2} 4\left((\tilde{z} - \tilde{z_h})^2 + \tilde{y}^2\right)\right) \tag{2.60}$$

with k^* being the wake growth rate, $\tilde{x}$ the downstream distance normalized by the rotor radius, $\tilde{z_h}$ the normalized hub height, $\tilde{y}$ and $\tilde{z}$ the normalized horizontal and vertical distance and

$$\beta = \frac{1}{2}\frac{1 + \sqrt{1 - c_T}}{\sqrt{1 - c_T}}. \tag{2.61}$$

The complete derivation of Equation (2.60) can be found in Bastankhah and Porté-Agel (2014).

Similar to the Jensen model a simple analytic description of the wind speed reduction based solely on the position in the wake (vertically and horizontally), the downstream distance, the thrust coefficient and the wake growth rate has been developed by this model. However, the Gaussian shape provides a suitable description of the shape of the wind speed deficit in the far wake. It should be highlighted that the Jensen wake model with the rectangular shape and a constant wind speed inside the wake delivers a suitable estimation of the overall power output over all wind directions but can lead to errors when calculating the actual power output per wind direction. Usually, at full wake the Jensen model overestimates the power output of the downstream turbine given that the velocity deficit is underestimated, whereas at partial wake the Jensen model underestimates the power due to an overestimation of the wind speed deficit (Bastankhah and Porté-Agel 2014). During the planning and optimization of a wind farm layout, this can lead to significant differences in the optimized wind farm layout. Thus, an accurate description of the wind speed deficit shape is an important issue.

2.3.1.4 Ainslie model

The models explained above are based on an empirical description of the wake, so that they do not really capture the physics of the flow field. The model developed by Ainslie (1988) describes the wake in a more physical way. First, Ainslie assumes that the wake is axisymmetric, fully turbulent, experiences no swirl and is steady state. Furthermore, it is assumed that there are no pressure gradients in the fluid outside the wake. Taking into consideration that the gradient of the mean wind speed is much higher in radial than in axial direction, and viscous terms are dropped, the thin shear layer as an approximation of the Navier-Stokes equations can be used to describe the development of the wake. The momentum equation of the thin shear layer equations expressed by the wind speed in axial and radial direction U and V_r, respectively, is defined by:

$$U\frac{\partial U}{\partial x} + V_r\frac{\partial U}{\partial r} = \frac{1}{r}\frac{\partial}{\partial r}\left(\nu_T r\frac{\partial U}{\partial r}\right). \tag{2.62}$$

Note that turbulence is taken into account by an eddy viscosity approach. The description of the eddy viscosity ν_T comprises two terms. The first describes the mixing due to

turbulence, which is related to the wake shear layer itself, and the second term is related to wake mixing due to the ambient turbulence level. This leads to the following equation for the eddy viscosity (Ainslie 1988):

$$\nu_T = l_w(\tilde{x})\, U_w(\tilde{x}) + \nu_a \ , \tag{2.63}$$

where l_w and U_w are the length and velocity scale related to the wake shear layer, and ν_a is the additional eddy viscosity based on the ambient TI. The length and velocity scales depend on the rotor radius normalized downstream distance $\tilde{x}$. The length and velocity scales are assumed to be proportional to the wake width b and the velocity difference in and outside the wake. The ambient turbulence eddy viscosity ν_a is expressed by the eddy diffusivity of momentum k_M. This leads to the following equation to define the complete eddy viscosity (Ainslie 1988):

$$\nu_T = F(\tilde{x})\left(k_1 b\left(U_0 - U_w\right) + k_M\right) \ , \tag{2.64}$$

where $k_1 = 0.015$. The eddy diffusivity of momentum k_M can be described by normal boundary layer parameters and the logarithmic wind profile for neutral conditions, which at the end leads to the following equation (Ainslie 1988):

$$\frac{\nu_T}{U_0 D} = F(\tilde{x}) k_1 \frac{b}{D}\left(1 - \frac{U_w}{U_0}\right) + \frac{F\kappa^2}{\ln\left(\frac{z_H}{z_0}\right)} \ , \tag{2.65}$$

where κ is the von Kármán constant, z_H the hub height, and z_0 the roughness length. The filter function $F(\tilde{x})$ can be calculated as follows (Ainslie 1988):

$$F(\tilde{x}) = \begin{cases} 0.65 + \left(\frac{\tilde{x}-4.5}{23.32}\right)^{\frac{1}{3}} & \text{for } \tilde{x} < 11 \\ 1 & \text{for } \tilde{x} \geq 11 \ . \end{cases} \tag{2.66}$$

The filter function $F(\tilde{x})$ is introduced to account for a lack of equilibrium between the mean velocity field and the turbulent energy content generated due to the rapid changes in mean flow gradients in the near wake. The filter function is justified and evaluated by measurements.

The initial wake parameters for solving the thin shear layer equations starting at two rotor diameters downstream are based on a Gaussian profile. It is suggested to solve the thin shear layer equations by a finite-differences scheme. Ainslie also described a method to correct the wind speed deficit for wake meandering to achieve a more suitable description of the wind speed deficit in the FFR in neutral conditions (Ainslie 1988). The terms for the correction of the wind speed deficit are based on measurements. The FFR describes the coordinate systems at a fixed position in space, such as a downstream turbine, whereas the MFR defines the coordinate system in which the steady state wind speed deficit is defined. The meandering leads to a less pronounced and broader deficit in the FFR, which should be taken into consideration with the correction. In contradiction to the subsequently explained DWM model, no meandering time series is calculated in the Ainslie model, only a transformation of the wind speed deficit from the MFR to the FFR is carried out.

2.3.1.5 Dynamic wake meandering model

In the following a detailed description of the DWM model is given. Different versions of the model are used in this thesis and defined in this section. A description of the DWM model has been published in Reinwardt et al. (2020a) and is taken over for this section. The DWM model is based on the assumption that the wake behaves like a passive tracer in the turbulent wind field. Consequently, the movement of the passive structure, i.e. the wake deficit, is driven by large turbulent scales (Larsen et al. 2007; Larsen et al. 2008a). The main components of the model are summarized in Figure 2.10 and explained in detail in the following paragraphs. The complete DWM model was programmed in-

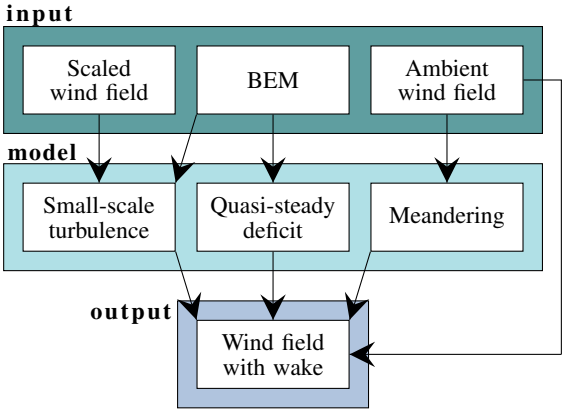

Figure 2.10: Components of the DWM model (Reinwardt et al. 2021).

house in Python and is completely independent from any commercial software.

Quasi-steady wake deficit. One key point of the model is the quasi-steady wake deficit or rather the wind speed deficit in the MFR. In this study, two calculation methods for the quasi-steady wake deficit are evaluated. The quasi-steady wake deficit is defined in the MFR and comprises a formulation of the initial deficit emitted by the wake generating turbine and the expansion of the deficit downstream (Larsen et al. 2008b). The latter is calculated with the thin shear layer approximation of the Navier-Stokes equations in their axisymmetric form (Larsen et al. 2007). This approach is strongly related to the Ainslie wake model, which has been described in the last section. The momentum equation (2.62) together with the continuity equation (2.67) build up the system of equations to solve the flow field in downstream direction.

$$\frac{1}{r}\frac{\partial}{\partial r}\left(rV_r\right) + \frac{\partial U}{\partial x} = 0 \ . \tag{2.67}$$

The notations used and coordinate system is illustrated in Figure 2.11. The first part of the quasi-steady wake deficit, the initial deficit, serves as a boundary condition when solving the equations. In both methods used to determine the quasi-steady wake deficit, the initial deficit is based on the axial induction factor a derived from the BEM theory. Pressure terms in the thin shear layer equations are neglected. The error that inherently results from this assumption is accommodated by using the wind speed deficit two rotor diameters downstream (beginning of the far-wake area) as a boundary condition for the

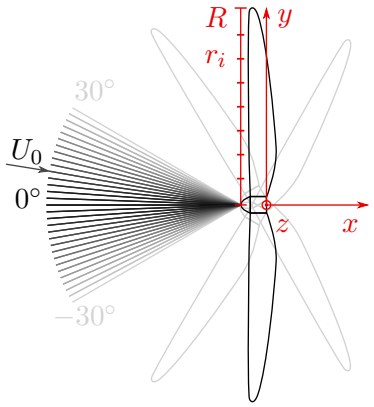

Figure 2.11: Wind directions and coordinates (Reinwardt et al. 2020b).

solution of the thin shear layer equations. Although the equations are solved directly from the rotor plane by a finite-difference method with a discretization in axial and radial direction of $0.2D$ and $0.0125D$ combined with an eddy viscosity (ν_T) closure approach. Furthermore, the eddy viscosity is calibrated in a way to balance out this simplification. The two evaluated methods for the quasi-steady wake deficit differ only in the definition of the initial deficit and the eddy viscosity formulation.

DWM-Egmond approach. For the first method, the following formulae are given to calculate the initial deficit. Hence, the boundary condition for solving the thin shear layer equations are (Madsen et al. 2010):

$$U_w \left(\frac{r_{w,i+1} + r_{w,i}}{2} \right) = U_0(1 - 2a_i) \tag{2.68}$$

and

$$r_{w,i+1} = \sqrt{\frac{1 - a_i}{1 - 2a_i} \left(r_{i+1}^2 - r_i^2 \right) + r_{w,i}^2 \, f_w} \tag{2.69}$$

with

$$f_w = 1 - 0.45\overline{a}^2 \ , \tag{2.70}$$

where $\overline{a}$ represents the mean induction factor along all radial positions i, r_i the rotor radius and $r_{w,i}$ the wake radius at the radial position i. The boundary condition of the radial velocity component is $V_r = 0$. The initial wake expansion and the corresponding radial positions as well as the pressure recovery in downstream direction are illustrated in Figure 2.4.

The eddy viscosity ν_T used in Equation (2.62), is calculated in this first approach as follows (Larsen et al. 2013):

$$\frac{\nu_T}{U_0 R} = k_1 \, F_1(\tilde{x}) \, F_{amb}(\tilde{x}) \, TI_0 + k_2 \, F_2(\tilde{x}) \frac{R_w(\tilde{x})}{R} \left(1 - \frac{U_{min}(\tilde{x})}{U_0} \right) \tag{2.71}$$

with $k_1 = 0.1$ and $k_2 = 0.008$. The eddy viscosity is normalized by the ambient wind speed U_0 and the rotor radius R. The outlined definition comprises two terms. The first is

related to the ambient turbulence intensity TI_0, whereas the second depends on the shape of the wind speed deficit itself. The single terms are weighted with the factors k_1 and k_2. The filter functions F_1 and F_2 in Equation (2.71) depending on $\tilde{x}$ (downstream distance normalized by the rotor radius) are defined by IEC 61400-1 Ed.4 (2019) as follows:

$$F_1(\tilde{x}) = \begin{cases} \left(\frac{\tilde{x}}{8}\right)^{3/2} - \frac{\sin\left(\frac{2\pi\tilde{x}^{3/2}}{8^{3/2}}\right)}{2\pi} & \text{for } 0 \leq \tilde{x} < 8 \\ 1 & \text{for } \tilde{x} \geq 8 \end{cases} \tag{2.72}$$

and

$$F_2(\tilde{x}) = \begin{cases} 0.0625 & \text{for } 0 \leq \tilde{x} < 4 \\ 0.025\tilde{x} - 0.0375 & \text{for } 4 \leq \tilde{x} < 12 \\ 0.00105(\tilde{x} - 12)^3 + 0.025\tilde{x} - 0.0375 & \text{for } 12 \leq \tilde{x} < 20 \\ 1 & \text{for } \tilde{x} \geq 20\ . \end{cases} \tag{2.73}$$

The filter functions lead to a weighting of the two terms in the eddy viscosity description depending on the downstream distance. Physically interpreted, the filter function F_2 covers the lack of equilibrium between the velocity field and the rising turbulence in the beginning of the wake as already outlined in the Ainslie model in Ainslie (1988). The eddy viscosity definition without a filter function does not describe the near-wake region probably. The filter functions as well as Equation (2.70) are calibrated against actuator disc simulations at a downstream distance of $2D$, the beginning of the far-wake area, where the wake is fully developed (Madsen et al. 2010). The actuator disk simulations have shown that already at a distance of 2D turbulent mixing has influenced the velocity deficit profile, whereby it is necessary to solve the thin shear layer equations from the beginning of the rotor although there is a pressure gradient and pressure terms are disregarded in the thin shear layer equations. The filter function F_2 is necessary to achieve a suitable low eddy viscosity in this region and align the solution with the actuator disk results. Furthermore, the comparison to the actuator disc simulations have shown that the wake expansion was too high, so that the correction in f_w has been applied in Equation (2.69). The factor k_2 is used to calibrate the eddy viscosity in the far-wake region when the filter function F_2 equals one. F_1 is introduced to include the fact that the depth of the wind speed deficit increases in the near-wake area up to $(2...3)D$ downstream of the turbine until it attenuates again in downstream direction (Madsen et al. 2010).

In Larsen et al. (2013) a comparison between the measured and simulated power based on the DWM model was carried out. The analysis has shown that the wind speed deficit degradation is too low for lower TIs and moderate to large turbine distances in the model version of Madsen et al. (2010). For this reason, another non-linear coupling function F_{amb} depending on the downstream distance was introduced into the eddy viscosity description, so that in accordance with Larsen et al. (2013) F_{amb} can be described as follows:

$$F_{amb}(TI_0) = aTI_0^{-b} \tag{2.74}$$

with $a = 0.2257$ and $b = 0.711$. This calculation method (Equations (2.68) to (2.74)) is subsequently named "DWM-Egmond model" after the site, which is used for the calibration of the eddy viscosity in Larsen et al. (2013).

DWM-Keck approach. The second investigated method defines the initial deficit by the following equations (Keck 2013):

$$U_w(r_{w,i}) = U_0\left(1 - (1 + f_u)\, a_i\right) \tag{2.75}$$

and

$$r_{w,i} = r_i \sqrt{\frac{1 - \overline{a}}{1 - (1 + f_R)\,\overline{a}}} \tag{2.76}$$

with $f_u = 1.1$ and $f_R = 0.98$. $\overline{a}$ represents the mean induction factor. The boundary condition of the radial velocity component is again $V_r = 0$. In Keck (2013) the final and recommended version of the model developed for the eddy viscosity is defined as follows:

$$\nu_T = k_1 F_1(\tilde{x})\; u^*_{ABL;\lambda<2D}\; l^*_{ABL;\lambda<2D} + k_2 F_2(\tilde{x}) \max\left(l^{*2}\left|\frac{\partial U(\tilde{x})}{\partial r}\right|, l^*\left(1 - U_{min}(\tilde{x})\right)\right) \tag{2.77}$$

with $k_1 = 0.578$ and $k_2 = 0.0178$ and the filter functions:

$$F_1 = \begin{cases} \frac{\tilde{x}}{4} & \text{for } \tilde{x} < 4 \\ 1 & \text{for } \tilde{x} \geq 4 \end{cases} \tag{2.78}$$

and

$$F_2 = \begin{cases} 0.035 & \text{for } \tilde{x} < 4 \\ 1 - 0.965 e^{-0.35(\tilde{x}/2-2)} & \text{for } \tilde{x} \geq 4\ . \end{cases} \tag{2.79}$$

In contrast to the previously mentioned model (DWM-Egmond model) atmospheric stability is considered in this final model description. Equation (2.77) involves the velocity $u^*_{ABL;\lambda<2D}$ and length scale $l^*_{ABL;\lambda<2D}$ fractions of the ambient turbulence, which is related to the wake deficit evolution (eddies smaller than $2D$). Besides the ambient turbulence intensity TI_0 the velocity scale $u^*_{ABL;\lambda<2D}$ depends on the ratio of the Reynolds stresses (normal stress in flow direction and the shear stress), which in turn are functions of the atmospheric stability. To include the atmospheric stability in the DWM model, the Mann turbulence model is adjusted to consider also unstable conditions. A detailed description of a method to introduce atmospheric stability in the DWM model can be found in Keck et al. (2014) and Keck (2013). In contrast to the recommended model in Keck (2013), atmospheric stability is not considered in the present thesis, so that a previous model in Keck (2013) without consideration of atmospheric stability is used and the numerical constants k_1 and k_2 in Equation (2.80) are changed with respect to the first least-squares recalibration in Keck (2013). Atmospheric stability in the DWM model has not been considered in this thesis due to the fact the ambient turbulence is generated by a Kaimal spectrum and a coherence function, so that the atmospheric stability in accordance to Keck et al. (2014) could not be taken into account. Furthermore, according to Keck (2013) it can be assumed that the mixing length l^* is equal to half of the wake width. This results in the following formulation of the eddy viscosity used in the present thesis:

$$\frac{\nu_T}{U_0 R} = k_1 F_1(\tilde{x}) TI_0 + k_2 F_2(\tilde{x}) \max\left(\frac{R_w(\tilde{x})^2}{R U_0}\left|\frac{\partial U(\tilde{x})}{\partial r}\right|, \frac{R_w(\tilde{x})}{R}\left(1 - \frac{U_{min}(\tilde{x})}{U_0}\right)\right) \tag{2.80}$$

with $k_1 = 0.0914$ and $k_2 = 0.0216$.

Meandering of the wake. Wake meandering is an important aspect in wake modeling and has not been treated in a physical correct manner in the previously introduced simple analytical wake models. This issue is accommodated in the DWM model. The meandering of the wake leads to a less depth wind speed deficit measured at a fixed position downstream, which thereupon leads to a higher energy output at the downstream turbine. Moreover, the wake meandering leads to increased loads at the downstream turbine, which is in the Frandsen model only indirectly captured by a higher total TI in the wake.

The DWM model assumes that the wake meandering, respectively the transportation of the wake in the ABL, can be modeled by assuming that the wake behaves as a passive tracer, which is driven by large-scale turbulent structures. Consequently, the meandering process depends on a suitable description of the transport media, the turbulent wind field, as well as an appropriate definition of large-scale turbulence. The turbulent wind field is modeled by a Kaimal spectrum and a coherence function as described in Section 2.1.4 with an ambient TI in accordance with the specific site.

The meandering process can be interpreted as a cascade of wakes emitted at the upstream turbine, which are deflected in vertical and horizontal direction during the propagation. Furthermore, by assuming that the large-scale turbulence in the ambient wind field does not change and applying Taylor's hypothesis, it is assumed that the advection velocity in downstream direction equals the ambient mean wind speed, so that no meandering in streamwise direction is considered. This simplification is made to allow a decoupling of the meandering process and the wake expansion. Based on that, it is possible to calculate the wind speed deficit propagation in the MFR in accordance with the previous section and subsequently shift the emitted wake in horizontal and vertical direction at each instant of time. Adopting Taylor's hypothesis, the meandering process can be described by the following differential equation system (Larsen et al. 2007):

$$\frac{\mathrm{d}y(t,t_0)}{\mathrm{d}t} = v(y,z,t,t_0) \ , \tag{2.81}$$

and

$$\frac{\mathrm{d}z(t,t_0)}{\mathrm{d}t} = w(y,z,t,t_0) \ , \tag{2.82}$$

where $v(y,z,t,t_0)$ and $w(y,z,t,t_0)$ are the fluctuating wind speeds at the positions y and z at the time t. t_0 is the time when the wake cascade is emitted. If it is assumed that the characteristic turbulence in the ambient wind field is homogeneous, the distinction between spatial points is meaningless and Equation (2.85) and (2.86) can be simplified to (Larsen et al. 2007):

$$\frac{\mathrm{d}y(t,t_0)}{\mathrm{d}t} = v(t_0) \tag{2.83}$$

and

$$\frac{\mathrm{d}z(t,t_0)}{\mathrm{d}t} = w(t_0) \ , \tag{2.84}$$

where $v(t_0)$ and $w(t_0)$ are the fluctuating wind speeds at hub height of the turbulent wind field related to the meandering. Given that a homogeneous turbulence is assumed the fluctuating wind speeds $v(t_0)$ and $w(t_0)$ are only depending on the time when the wake cascade is emitted. The assumption of homogeneous turbulence is acceptable for small to moderate distances as it is the case in the analyzed wind farms in this thesis. Applying

Taylor's hypothesis by correlating the time t to a specific distance x and assuming that the wake is advected with the ambient wind speed U_0, the displacement at the downstream distance x can be calculated as follows (Larsen et al. 2008a):

$$\Delta y = \frac{x}{U_0} v(t_0) \ , \tag{2.85}$$

and

$$\Delta z = \frac{x}{U_0} w(t_0) \ . \tag{2.86}$$

To define the transport media, respectively the turbulent wind field for the transportation (i.e. $v(t_0)$ and $w(t_0)$), the ambient wind field is ideally low-pass filtered. The cut-off frequency of the low-pass filter can be defined as follows (Larsen et al. 2008a):

$$f_c = \frac{U_0}{2D_w} \tag{2.87}$$

with D_w being the wake diameter. This way of defining the cut-off frequency is justified by the consideration that due to Taylor's hypothesis a displacement-wave with a period of T_p has a spatial extent of $U_0 T_p$. Half of the spatial extent is related to positive and the other half to negative displacements. That means for a spatial structure with a characteristic length of D_w, the minimum wave period that still allows a constant sign displacement of all points in the spatial structure is defined by (Larsen et al. 2008a):

$$D_w = \frac{U_0 T_p}{2} \ . \tag{2.88}$$

Thus, the selected cut-off frequency corresponds to the reciprocal of T_p. Additionally, in Larsen et al. (2013) in the recent version of the DWM model the cut-off frequency is slightly adjusted to:

$$f_c = \frac{U_0}{2D} \ . \tag{2.89}$$

Using the rotor diameter D, which is not depending on the downstream distance, instead of the wake diameter D_w simplifies the calculation of the meandering process, whereby it has also been applied in this thesis. Furthermore, the temporal resolution of the generated wind field is 0.07 s.

In addition, it should be highlighted that it is also possible to describe the transport medium by averaging the turbulent wind field over a circular area of $2D_w$, respectively $2D$, as outlined in Larsen et al. (2008a). This is of particular significance when using the Mann turbulence model to describe the transport medium. The turbulence at the grid points in a Mann turbulence box represent mean values over the grid cell, so that a turbulence box with a grid size of D_w or D can be used instead of a low-pass filtered wind field. Given that this thesis uses a Kaimal spectrum together with a coherence function and the grid points do not represent any mean values in this model definition, this approach has not been used and an ideal low-pass filter is used instead.

Small-scale turbulence. Another aspect of the DWM model is the definition of the small-scale turbulence generated through the wake shear itself as well as blade tip and root

vortices. This part of the turbulent spectrum is calculated with a scaled homogeneous and isotropic turbulent flow field also generated by a Kaimal spectrum. The wind field is generated with a length scale of one rotor diameter and a standard deviation of the turbulent fluctuations of 1 m/s. Each grid point in the turbulent wind field is multiplied by the factor k_{aw}, which is defined by IEC 61400-1 Ed.4 (2019):

$$k_{aw}(\tilde{x},\tilde{r}) = 0.6\left|1-\tilde{U}(\tilde{x},\tilde{r})\right| + 0.35\left|\frac{\partial\tilde{U}(\tilde{x},\tilde{r})}{\partial\tilde{r}}\right| \quad . \tag{2.90}$$

Equation (2.90) uses the normalized wind speed deficit $\tilde{U}(\tilde{x},\tilde{r})$ based on the calculation of the initial deficit, which itself builds on the BEM theory and the aerodynamics of the turbine.

2.3.2 Multiple wake models

The last section summarizes different approaches of the DWM model to calculate single wakes. When considering a real wind farm, it is usually the case that multiple wakes or wake overlapping occur, so that in the following different approaches to handle multiple wakes in the DWM model are outlined. The implementation of multiple wakes in the DWM model is not trivial given that the DWM model is built in such a way that requires a steady-state axisymmetric velocity field and a homogeneous TI at the wake generating turbine. However, in a multiple wake situation the second turbine in a row in downstream direction is already affected by an inhomogeneous and unsteady wind field, calculated by the DWM model for single wakes. A steady-state axisymmetric velocity field is necessary in the DWM model to calculate the boundary conditions for solving the thin shear layer equation and thereupon the steady-state wind speed deficit in the MFR. Furthermore, the eddy viscosity in the DWM model definition depends on a single ambient TI, so that an inhomogeneous TI cannot be used in the eddy viscosity calculation.

The outlined analysis compares five different methods to handle multiple wakes in the DWM model. The first method considers only the wake of the closest wake generating turbine (wct), whereas the IEC guideline provides a method (IEC-min), which always takes the minimum wind speed of all upstream wakes at each point of interest in the wake (IEC 61400-1 Ed.4 2019). Furthermore, two different wake summation approaches are analyzed. The first one sums up all upstream wakes with a quadratic summation (ws-q), whereas the second adds the wakes linearly (ws-l). Finally, Keck (2014) presents a method, which calculates the inflow at each upstream turbine successively, so that the inflow conditions change at each turbine in the row and the wake effects of all upstream turbines are included implicitly. In accordance with this method, no wake summation is necessary. All applied methods are summarized and schematically illustrated in Figure 2.12.

2.3.2.1 Wake closest turbine

The first method solely takes the wake of the closest turbine at the point of interest in the downstream direction into account, whereby the wake of all upstream turbines are calculated based on the ambient conditions. The shape of the wind speed deficit as well as the meandering and small-scale turbulence is also purely based on the wake of the closest

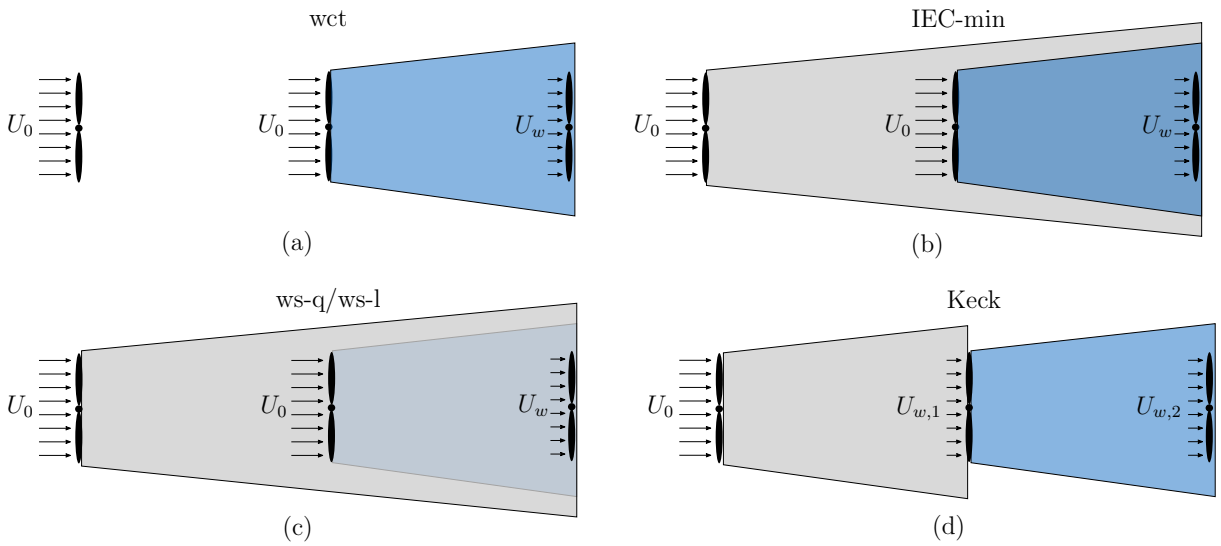

Figure 2.12: Schematic illustration of calculation assumptions in the different multiple wake models. Shown are the wake closest turbine approach (wct) in **(a)**, the IEC approach (IEC-min) in **(b)**, the quadratic and linear wake summation approach (ws-q, ws-l) in **(c)**, and the Keck approach in **(d)**.

turbine. This approach has been applied when using the Frandsen model (Frandsen 2007) in multiple wake situations, which is investigated here for the DWM model. The method is depicted in Figure 2.12 **(a)**.

2.3.2.2 International Electrotechnical Commission

The second investigated method is the one, that is recommended in the guideline (IEC 61400-1 Ed.4 2019). The guideline suggests two different methods for cases below and above the rated wind speed. For the case above the rated wind speed, it is suggested to sum up the deficits of the wake generating turbines linearly. For the case below the rated wind speed, it is recommended to take the minimum wind speed of all upstream turbine wakes at each position of interest in the wake. This yields the following description of the wind speed in the wake:

$$U(r,\theta,x) = \min_i \left(U_i\left(r,\theta,x\right)\right) \tag{2.91}$$

with U_i being the wind speed in polar coordinates at the radius r, the angle θ and the downstream distance x associated with the turbine i. This methods implies a calculation of the single wakes of all upstream turbines including the meandering and wake-added turbulence. Subsequently, the minimum wind speed is taken at each point of interest in the wake. The method is illustrated in Figure 2.12 **(b)**. In this thesis only ambient wind speeds below the rated wind speed are investigated, so that the second method, the linear summation, is not investigated when using the IEC method. However, in the next section a similar approach to sum up the wakes linearly is introduced and abbreviated as "ws-l".

2.3.2.3 Wake summation

In the third approach a summation of the wind speed deficits is carried out in the FFR. The method is depicted in Figure 2.12 **(c)**. The wakes are summed up in a quadratic (ws-q) or linear (ws-l) approach. The following formula is used for the wake summation:

$$\left(1 - \frac{U_w}{U_0}\right)^n = \sum_{i=1}^{n} \left(1 - \frac{U_{wi}}{U_0}\right)^k \tag{2.92}$$

with U_{wi} being the single wake wind speed of turbine i, U_0 the ambient wind speed and n the number of wake generating turbines. k equals 2 in case of a quadratic summation and 1 for the linear summation approach. The quadratic summation method follows the approach in Katic et al. (1987), where it is assumed that the kinetic energy of a mixed wake equals the sum of energy deficits from each single wake at the specific downstream distance. The wake of all upstream turbines is calculated based on the ambient wind speed. The wake-added turbulence is taken over from the closest turbine.

2.3.2.4 Keck model

The last investigated method to handle multiple wake situations has been introduced in Keck (2014). In contrast to the previously introduced methods this approach calculates the inflow wind speed at each single turbine in the row based on a mean wake wind speed and mean TI, so that the average effect of all upstream turbines is implicitly included in the changed inflow conditions. The method is illustrated in Figure 2.12 **(d)**. The wake at each turbine in the row is calculated successively. The issue of the necessity of a steady-state axisymmetric velocity field and a homogeneous TI at the downstream turbines is solved by calculating an averaged wind speed and a rotor-averaged TI. Note that in the previously introduced methods this problem has been solved by assuming ambient conditions at all downstream turbines, as illustrated in Figure 2.12. The average axisymmetric velocity field over an annular section can be calculated as follows:

$$U_{axisym}(r) = \frac{1}{2\pi\Delta r} \int_0^{2\pi} \int_{r-\frac{\Delta r}{2}}^{r+\frac{\Delta r}{2}} U(r,\theta)\, dr\, d\theta \tag{2.93}$$

with Δr the discretization step size in radial direction of the annular section. As already mentioned, the DWM model depends on a homogeneous inflow TI, so that it is mandatory to calculate a rotor mean TI for each downwind turbine. Keck (2014) suggests a quadratic rotor mean TI calculated as follows:

$$TI_{mean}(r) = \frac{1}{\pi R_w^2} \sqrt{\int_0^{2\pi} \int_0^{R_w} TI^2(r,\theta)\, dr\, d\theta} \tag{2.94}$$

with R_w being the width of the initial DWM wake at the downstream turbine. The wake from each turbine in the row is successively calculated in accordance with the usual single wake DWM model considering the inflow conditions calculated by Equations (2.93) and (2.94). Furthermore, it should be highlighted that in this model the meandering as well as the ABL shear are assumed to be independent of the presence of the wake, so that both are based on the ambient conditions for all turbines in the row and not on the mean wake characteristics calculated by Equations (2.93) and 2.94.

2.4 Lidar systems

One major part of this thesis is the comparison of the previously outlined single and multiple wake models with measured wind speeds in the wake of a real wind farm. The measurements are conducted with lidar (light detection and ranging) systems. Depending on the different lidar systems a variety of applications (e.g. specification of gases in the atmosphere, remote measuring of vibrations, 3D imaging or range finding) exist (Weitkamp 2005).

In wind energy Doppler lidar systems are of major importance. A Doppler lidar system is a remote sensing device that emits a laser beam, which will be reflected at the particles in the air and recorded again at the lidar device, whereby the speed of light determines the distance to the particles. The frequency shift between the emitted and reflected signal defines the travel speed of the particle in the direction of the laser beam, which in turn can be assumed to be equivalent to the wind speed in the direction of the laser beam (line-of-sight (LOS) wind speed) (Sathe et al. 2015). If the motion of the particle at which the laser light has been reflected is moving towards the lidar system, the wavelength of the laser light will be compressed and the frequency is increased, whereas if the particles move away from the device, the wavelength will be stretched and the frequency is reduced. In order to reduce the uncertainty in the measurements, several laser beams are usually averaged. Furthermore, the device delivers a mean value of the LOS wind speed along a certain laser pulse length. To determine the longitudinal, vertical or horizontal wind speed, it is necessary to combine LOS measurements at different spatial positions. Some lidar devices emit several laser beams simultaneously, whereas other devices need to measure with only one laser beam at different spatial positions successively.

Doppler lidar systems can be distinguished by the type of emitted laser (pulsed or continuous) or the detection technique of the received signal. Two different detection techniques exist: first, coherent lidar systems (heterodyne detection), which measure Doppler shifts by comparing the frequency of backscattered radiation to the frequency of the released signal; and second, direct detection lidar systems, which obtain frequency shift measurements by passing the light through an optical filter. The first category, coherent wind lidar systems, are mainly relevant for the wind industry. The frequency shift will be recognized by mixing a part of the released laser beam with the backscattered one. The mixed signal will oscillate at the frequency shift between these two signals, which thereupon can be used to calculate the speed of the moving particles (Sathe et al. 2015). Additionally, coherent lidar systems can be further distinguished according to their emission waveform, which can be pulsed or continuous (Sathe et al. 2015). A lidar system with a continuous waveform is called a CW lidar. The different lidar systems, which are mainly, relevant for the wind industry, are further explained in the next sections.

Recently, lidar systems have gained attention as a remote sensing device in wind energy, whereas traditionally met masts have been used to measure and determine atmospheric conditions. The size of wind turbines has grown significantly in the last few years, whereby it is often very expensive to install a met mast nowadays. Especially offshore installations can easily be very expensive. Additionally, the location of the met mast cannot be shifted. Hence, it is unsurprising that lidar systems are already used in industry to measure the mean wind speed and wind profiles. However, lidar systems have not yet been accepted for turbulence measurements. In industry, typically met masts are used to measure TIs. The

reason for this is that the measurement principle of lidar systems itself leads to a spatial averaging of turbulence along the LOS. Furthermore, cross-contaminations by different components of the wind vector and low sampling rates make the application challenging. Recently, a lot of research has been carried out to eliminate these side effects as much as possible. A good overview of methods to characterize turbulence with different types of lidar systems is given in Sathe et al. (2015).

In the following, the Doppler effect, which builds the fundamental method of Doppler wind lidar systems, is outlined. Subsequently, coherent pulsed as well as a cw Doppler lidar systems are explained in further detail. In the course of this, the heterodyne detection technique is explained. Finally, this sections discusses different scan techniques to determine the longitudinal wind speed component out of the LOS speed.

2.4.1 Doppler effect

The Doppler effect has been first described by the Austrian physicist Christian Doppler (1803–1853) for acoustic waves and explains the shift in frequency of radiation when the source or the receiver moves relative to one another (Weitkamp 2005). This method can directly be transferred to electromagnetic waves, so that if it is possible to measure the frequency shift, the relative speed between the source and the receiver can be determined. To use this approach in measuring wind speeds it is necessary to measure the reflected light at aerosols in the air, which is rather challenging given that the return signal is very weak. In general, the relative speed between a receiver and a emitter U_{LOS} has the following relation to the received frequency f (Weitkamp 2005):

$$f = f_0 \left(1 + \frac{U_{LOS}}{c}\right) \tag{2.95}$$

with f_0 the frequency of the emitted signal and c the speed of light. Considering that the air and aerosols itself do not emit light on their own, so that light is emitted by the lidar system itself, so that it can be reflected at the aerosols and detected again at the lidar device, leads to the following equation of the frequency of the received light (Weitkamp 2005):

$$f = f_0 + \Delta f = f_0 \left(1 + 2\frac{U_{LOS}}{c}\right) \tag{2.96}$$

where Δf is the frequency shift. Evaluating Equation (2.96) delivers the following equation for the frequency shift Δf:

$$\Delta f = 2 f_0 \frac{U_{LOS}}{c} \ . \tag{2.97}$$

The sign of the Doppler shift defines if the particle is moving towards or away from the lidar system. An example of the frequency distribution of the original and shifted signal is illustrated in Figure 2.13. The reflection of the light at the aerosols lead to a narrow peak in the distribution. Superimposed on that is a broad peak , which is related to reflections at molecules in the air. The movement of the molecules is much faster than the velocity of the aerosols due to the higher mass of the aerosols. The backscattered light from the molecules is referred to as the Rayleigh component, whereas the reflected light from the

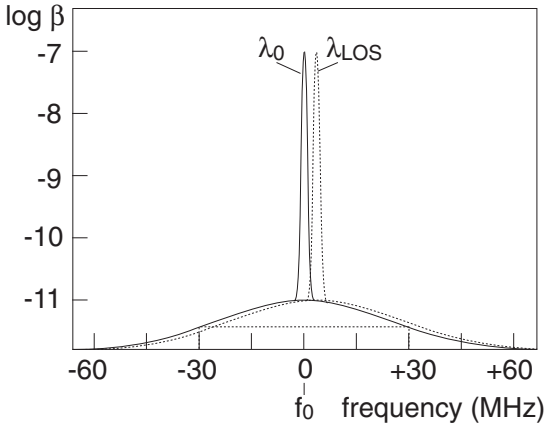

Figure 2.13: Schematic illustration of the original (solid) and the shifted (dotted) frequency distribution. Aerosols in the air lead to the narrow spike, which is superimposed onto the broad molecular peak (Weitkamp 2005).

aerosols is called Mie component. The wavelength of the original signal λ_0 and the shifted signal λ_{LOS} are depicted. The signal is shifted towards higher frequency, which indicates that the wind faces in the direction of the lidar.

2.4.2 Pulsed lidar systems

A pulsed lidar system releases a sequence of many short pulses and determines the measurement distance from the backscattered light with the speed of light. The difference between the time when the laser pulse is emitted and the time when the reflected signal is detected again together with the speed of light determines the downstream distance. This method allows almost simultaneous measurements at different distances (Peña et al. 2013). The only difference in time of the measurements at different downstream positions is the speed of light, which can obviously be neglected. The pulse length is typically 30 m. The resolution of the system is determined by the pulse width and the travel distance of the pulse while the lidar system samples the backscattered signal. The subsequent analysis uses a pulsed lidar system, which is why in the following the measurement process is explained in further detail. The complete measurement method of a coherent pulsed lidar system can be summarized into following steps:

1. Generation of laser pulses.
2. Release of laser pulses.
3. Acquisition of the backscattered light and mixing with the released signal (heterodyne detection).
4. Processing of the acquired backscattered light and estimation of the Doppler shift.

The released laser pulse has a characteristic Gaussian shape with a certain temporal pulse length and a wavelength (Vasiljevi 2014). The pulse is emitted with a specific frequency, the pulse repetition frequency (PRF). This kind of laser pulse can be generated with the

help of an acousto-optic modulator (AOM), which forms each time the AOM receives a trigger signal, a low-energy laser pulse based on an analog signal of the pulse shape and a low-energy light of a CW laser. The laser pulse frequency f_b is the sum of the CW laser frequency f_{cw} and the AOM frequency f_{AOM}. The measurement principle as well as the frequency shifts are illustrated in Figure 2.14. Out of the low energy pulse a high

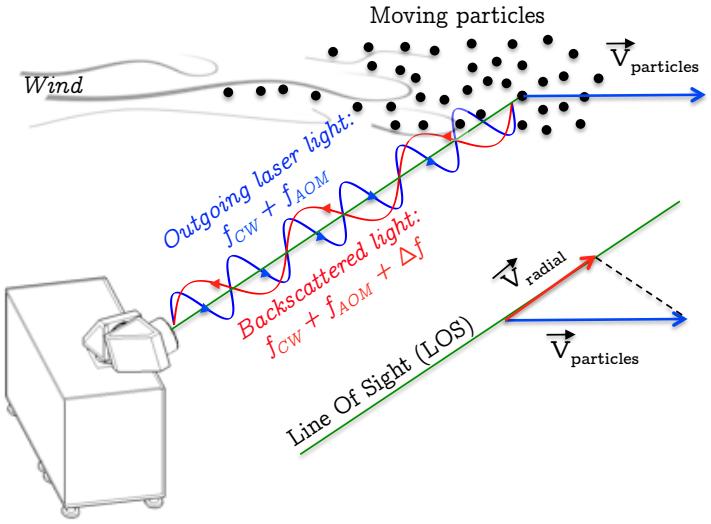

Figure 2.14: Schematic illustration of the measuring principle of a coherent lidar system (Vasiljevi 2014).

energy pulse is formed in the erbium-doped fiber amplifiers (EDFA). Subsequently, the high energy laser pulse passes an optical circulator to separate the outgoing and incoming backscattered light before the laser beam is magnified and focused to a certain distance. The laser beam is magnified to reduce the divergence in the far field, whereas the focusing is necessary to adjust the laser beam power along the LOS.

A small portion of the emitted light is reflected by the particles in the air (see Figure 2.14) (Vasiljevi 2014) and thereby, as already explained in the beginning, shifted in frequency. This frequency shift, the Doppler shift, can be calculated by Equation (2.97) and the sign of the Doppler shift defines if the particle is moving towards or away from the lidar system. The lidar system continuously receives backscattered light from particles in different distances. After receiving the backscattered light, the light is mixed with the low-energy CW laser (heterodyne detection). The mixing of the two signals with different frequencies leads to the 'beat' phenomenon, and hence the amplitude of the resulting light oscillates at the Doppler frequency. Subsequently, the mixed signal is transformed into an analog signal in a photodetector.

The radial or LOS velocity is determined out of the mean Doppler shift from a certain number of sample points. The number of sample points determines the length of a range gate and the spatial resolution. The finite discrete signal is transformed to the frequency domain and the spectrum of the frequency is calculated. With the help of a frequency estimator (e.g. maximum likelihood estimator), the frequency of the spectral peak respectively the Doppler frequency can be estimated. It is also possible to increase the Doppler shift estimation accuracy by averaging a certain number of spectra before the frequency is estimated (Vasiljevi 2014).

2.4.3 Continuous wave lidar

In contrast to a pulsed lidar system, a CW lidar focuses with the help of a telescope a continuously released laser beam at a particular distance, so that only the Doppler shift of the backscattered light from this distance can be detected (Peña et al. 2013). If more than one distance needs to be measured, the CW lidar system will adjust its telescope to focus successively to different distances. Thereby, the focal depth is proportional to the square of the distance or point of interests. The spatial resolution of the CW lidar system is determined by the focal properties of the telescope. The shorter the distance and the larger the lens, the larger is the focal depth and more volume averaging occurs. This limits the maximum range gate that can be sufficiently measured, so that current devices can measure up to 200 m, whereas for example the pulsed lidar system used here can measure in a distance up to 4000 m. The minimum range gate for a CW lidar system is very short. In principle, it would be zero but for safety reasons a minimum distance of around 10 m is used instead. In contrast to that, the here used pulsed lidar system is blind immediately after emitting the signal, so that the shortest measurable distance is 80 m. In general, CW lidar systems feature a very high spatial resolution at short distances and fast data acquisition rates, so that they are often more useful for turbulence measurements.

2.4.4 Scan techniques

As already mentioned, the lidar system measures the LOS wind speed, so that usually different measurement points are used to derive the complete wind speed vector. A common practice is to make a conical scan. In uniform flow, the measured LOS wind speed over the azimuth angle has the shape of a cosine function. The display of the LOS wind speed over the azimuth angle is called Velocity Azimuth Display (VAD). The peak of the cosine curve arises when the azimuth angle is aligned with the flow direction, whereas close to zero it is perpendicular to the flow direction (Sathe et al. 2015). If circular scans at different heights are performed, a vertical wind speed distribution (vertical wind profile) can be measured. This type of lidar system is called a profiling lidar. Besides measuring a full circle of a conically scan with very small increments, it is also possible to measure with only a few beams at the edges of the cone. This method is called Doppler Beam Swinging (DBS) and it often uses only four or five beams. To evaluate the three velocity components, both methods use the explained VAD. It is also possible to scan instead of a complete circle an arc, so that only a part of the cosine curve is presented by the scan and fitted to the cosine curve. A scan of a horizontal arc is called a Plan Position Indicator (PPI), whereas a vertical arc is called a Range Height Indicator (RHI).

Instead of a VAD method to calculate the horizontal wind speed, it is also possible to use multiple lidar systems to derive the different wind speed components. To evaluate all three wind speed components, three lidar systems are necessary. All of them need to point towards the same position. At very small elevation angles, it can be assumed that the vertical component is very small, so that it is also possible to use only two lidar systems.

The here outlined analysis performs a horizontal arc scan from the nacelle of a turbine in the wake in downstream direction. Instead of measuring continuously (speed controlled) as it is usually conducted in the above explained PPI and RHI scans, the lidar system measures in a step-stare mode. Given that the flow field is not uniform in the wake, it

is not possible to evaluate the horizontal wind speed with a cosine fit. Instead the wind speed in downstream direction is calculated from the LOS velocity and the geometric dependency of the position of the laser beam relative to the main flow direction as outlined in Machefaux et al. (2012) and later explained in Section 6.1. This method is only suitable for small scan opening angles.

Chapter 3

Wind farms

This thesis evaluates measurement results from two different wind farms. The first extensive measurement campaign in the Curslack wind farm provides met mast, lidar and load measurements and has been used to recalibrate the DWM model. The specific layout and measurement equipment allows validating loads in single as well as multiple wake situations. The second investigated wind farm, the ECN Wind Turbine Test station Wieringermeer (EWTW), serves as a reference wind farm to prove the applicability of the newly calibrated DWM model on a different turbine type as well as wind farm layout. The main characteristics of the two sites are summarized in Table 3.1. Both sites provide

Table 3.1: Comparison of the main characteristics of the Curslack wind farm and the EWTW.

	Curslack	EWTW
Number of turbines	5	5
Turbine type	N117/3.0, N117/2.4	N80/2.5
Turbine diameter	117 m	80 m
Minimal turbine spacing	2.51 D	3.8 D
Terrain	flat	flat
Mean wind speed at hub height	6.4 m/s	7 m/s
Weibull scale parameter A	7.2 m/s	7.9 m/s
Weibull shape parameter k	2.31	2.09

possibilities to evaluate wakes at close spacings of the turbines, which serves very well the subsequent analysis. Furthermore, the mean wind speed is low at both sites and the terrain is flat. In the following, both wind farms are described in further detail.

3.1 Curslack wind farm

The Curslack wind farm is located in the southeast of Hamburg, Germany. The description of the wind farm has been partly taken over from Reinwardt et al. (2020a) and Reinwardt et al. (2021). The wind rose in Curslack is depicted in Figure 3.1. The figure clearly illustrates the main wind direction sector of southwest. This wind direction

sector also has the highest mean wind speed of almost 8 m/s as depicted in Figure 3.1**(b)**. However, overall the site is a low wind speed site as visible in Figure 3.1**(b)**. The mean

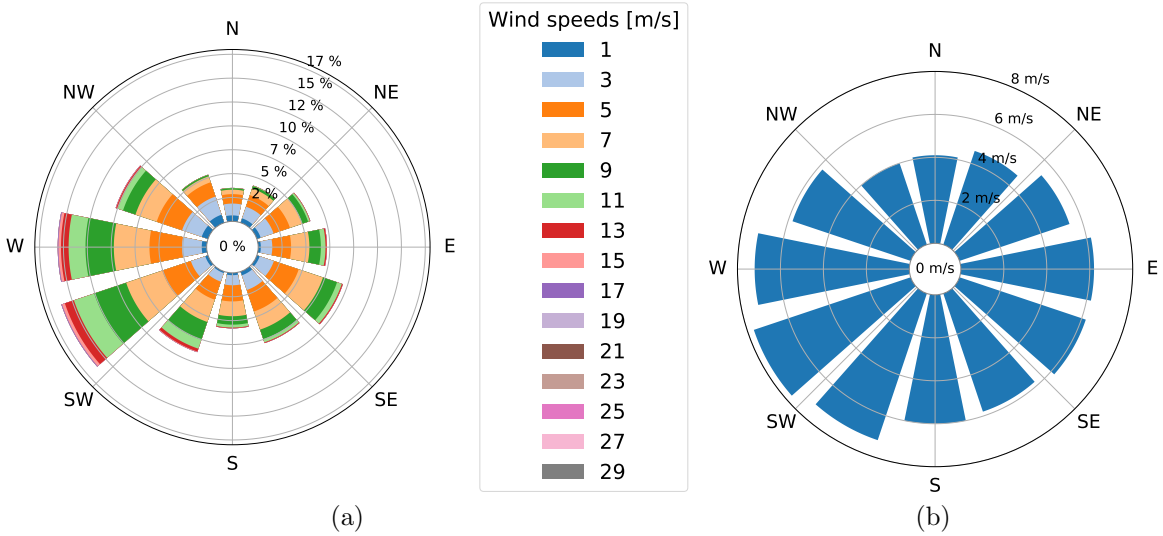

(a) (b)

Figure 3.1: Wind speed probability distribution **(a)** and mean wind speed **(b)** per wind direction sector in Curslack.

wind speed at the site is around 6.4 m/s at a height of 120 m. The terrain at the site is mostly flat and no further wind farms are located in the immediate vicinity. Only at a distance of more than 1 km the terrain becomes slightly hilly (approx. 40 m difference in altitude). The distance to the next wind farm is approximately 3 km. The wind farm layout is depicted in Figure 3.2. Looking at the closely spaced wind farm layout and the main wind direction sectors in Figure 3.1**(a)**, it is obvious that this wind farm is well suited to measure the influence of wakes at wind farms with small inner turbine distances. The wind farm includes five Nordex turbines (1x N117 3 MW and 4x N117 2.4 MW). All turbines have a hub height of 120 m. The main turbine details are given in Table 3.2. Figure 3.3 displays the thrust and power coefficient curves of both turbine types provided

Table 3.2: Specification of the wind turbine types of the Curslack wind farm.

	N117/3.0	N117/2.4
Rated power	3 MW	2.4 MW
Rotor diameter	117 m	117 m
Hub height	120 m	120 m
Cut-in wind speed	3.5 m/s	3 m/s
Cut-out wind speed	25 m/s	20 m/s
Wind turbine class	IEC IIA	IEC IIIA

by the turbine manufacturer.

An IEC compliant 120 m met mast (IEC 61400-12-1 2017) is placed in main wind direction ahead of the wind farm. It is equipped with eleven anemometers, two of which are ultrasonic devices, three wind vanes, two temperature sensors, two thermo-/hygrometers,

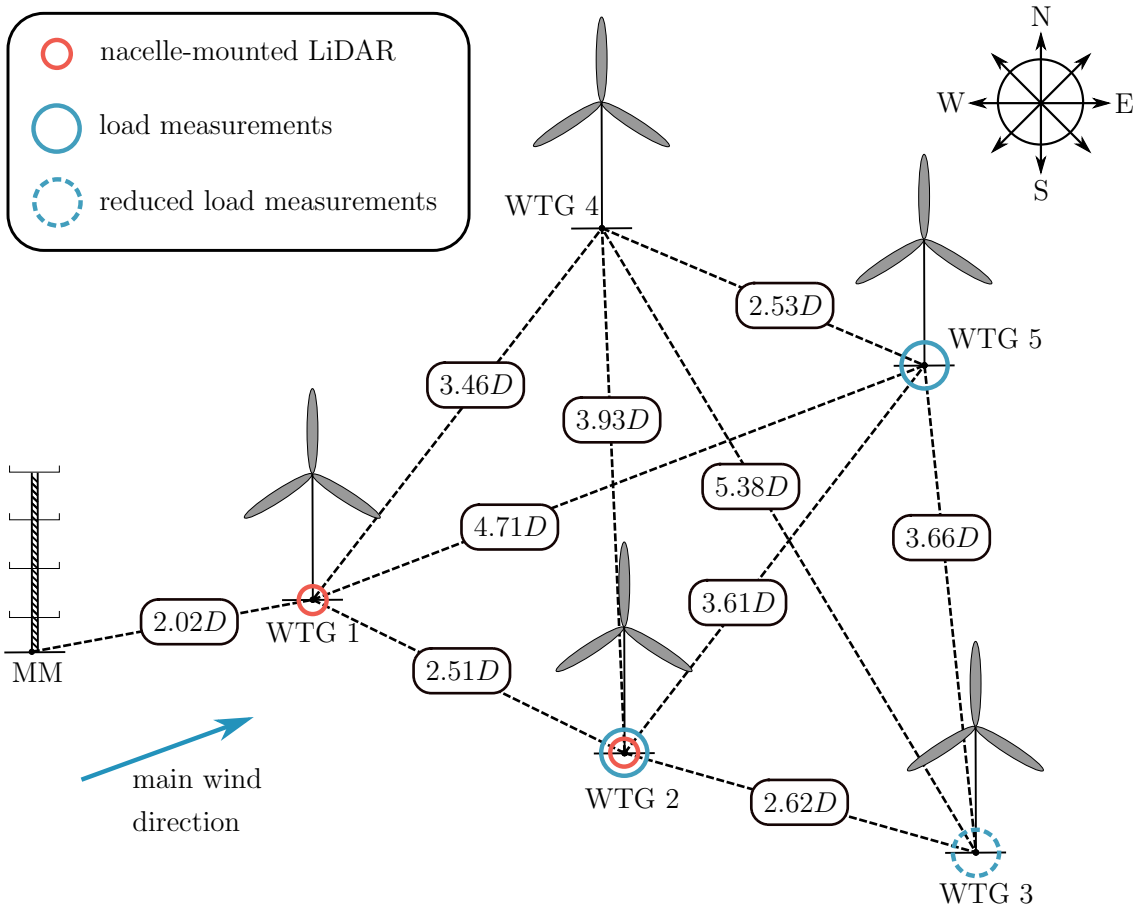

Figure 3.2: Wind farm layout of the Curslack wind farm with measurement equipment (Reinwardt et al. 2020a).

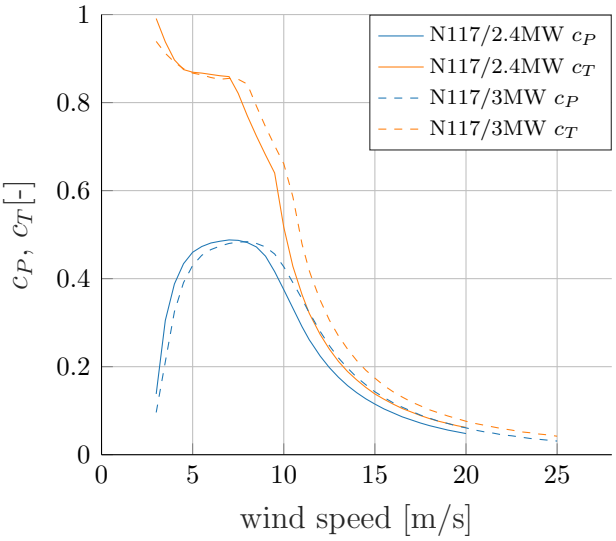

Figure 3.3: Power and thrust coefficients over the wind speed for the N117/3MW and the N117/2.4MW turbines (Reinwardt et al. 2020a).

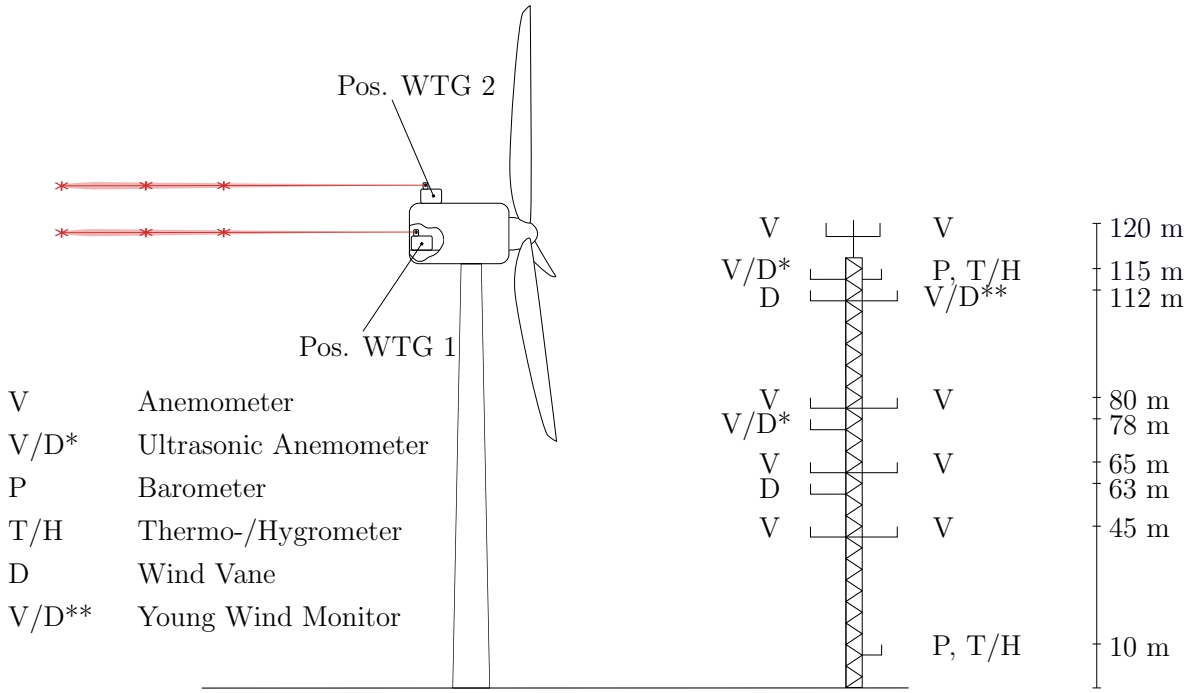

Figure 3.4: Met mast measurement equipment and lidar positions at the Curslack wind farm (Reinwardt et al. 2020a).

and two barometers. The sensors are distributed along the whole met mast as depicted in Figure 3.4. The anemometer booms are pointing towards southeast and northwest. Furthermore, the turbine nacelles of WTG 1 and WTG 2 are each equipped with a pulsed scanning lidar system (Galion G4000). The specifications of the lidar systems are summarized in Table 3.3. The lidar systems have a pulse repetition rate of 15 kHz and a ray update rate of about 1 Hz (depending on the atmospheric conditions), so that an average value of approximately 15,000 pulses is used per sample. The laser frequency is at 100 MHz. Considering the speed of light, this delivers a pulse length of 1.5 m. Hence, with a range gate length of 30 m, 20 points are used per range gate. Both lidar systems face downstream as depicted in Figure 3.4. The device on WTG 2 is installed on top of the nacelle, whereas the device on WTG 1 is installed inside the nacelle, measuring through a hole in the rear wall. The unusual location derives from the fact that a heat exchanger on top of the nacelle occupies the essential mounting area. Additionally, nacelle-mounted differential global positioning systems (GPS) help to track the nacelle's precise position with a centimeter range accuracy, so that yaw movements can be calculated.

Load measurement equipment is installed at three turbines. The tower top and bottom as well as blade flapwise and edgewise bending moments are measured with strain gauges at WTG 2 and WTG 5. WTG 3 is only equipped with strain gauges at the tower. They measure the moment at the tower in fore-aft and side-side direction as well as the tower torsion. The strain gauges at the tower top are installed 3.4 m below the nacelle and the strain gauges at the tower bottom are placed 1.5 m above the floor panel. The edgewise and flapwise moments are measured at a distance of 1.5 m from the blade root. Besides the installed measurement equipment, the turbine's Supervisory Control and Data Acquisition (SCADA) system is used to determine the operational conditions of the turbines. In the

Table 3.3: Specification of the lidar system Galion G4000.

Property	Specification
Measurement range	80 m to 4000 m
Range gate length	30 m
Laser frequency	100 MHz
Pulse repetition rate	15 kHz
Ray update rate	up to 1 Hz
Accuracy of LOS velocity	$< \pm 0.1$ m/s
Maximum / Minimum LOS velocity	$\pm$ 38 m/s
Azimuth range	0 ° to 360 °
Elevation range	−17 ° to 90 °
Angular accuracy	< 0.1 °
Angular speed	30 °/s

night the turbines are working in a reduced mode for noise reduction purposes, which can be determined by the SCADA system. Later on, 10-min measurement statistics as well as measurement data with a frequency of 1 Hz have been used for the analysis.

3.2 ECN Wind Turbine Test Station Wieringermeer

The EWTW site is placed at the polder Wieringermeer, which is located northeast of the province North-Holland (Bergman et al. 2016). In total, the site has six prototype locations as well as five locations on which a research wind farm has been built. The area is a flat agricultural land at an altitude of 5 m below the sea level. In the immediate vicinity are only small trees and farmhouses. The IJsselmeer lake is located at a distance of 2 km in easterly direction from the wind farm. The mean wind speed at the site is about 7 m/s at a height of 71.6 m. The wind rose and wind speed distribution are illustrated in Figure 3.5. The main wind direction is southwest.

The wind farm layout is depicted in Figure 3.6. The wind farm comprises of five Nordex N80/2.5MW turbines in a row. The row is nearly oriented in east-west direction. The spacing between the turbines is 304 m (3.8 D). All turbines have a hub height of 80 m and are numbered from 5 to 9 beginning at the west end of the wind farm. Further details regarding the turbine type are given in Table 3.4. The thrust as well as power coefficients of the N80/2.5MW turbine can be found in Figure 3.7.

A met mast is located south of the wind farm in between WTG 5 and WTG 6 (see Figure 3.6). The distances between the met mast and WTG 5 and WTG 6 are 3.5 D and 2.5 D, respectively. The met mast is equipped with 3D ultrasonic anemometers at three different heights (52 m, 80 m and 109.1 m). The anemometer booms are pointing towards the north. Furthermore, cup anemometers and wind vanes are installed at a height of 79.2 m and 51.2 m. The air temperature, the humidity as well as the pressure has been measured at 80 m, so that the air density can be determined. The met mast

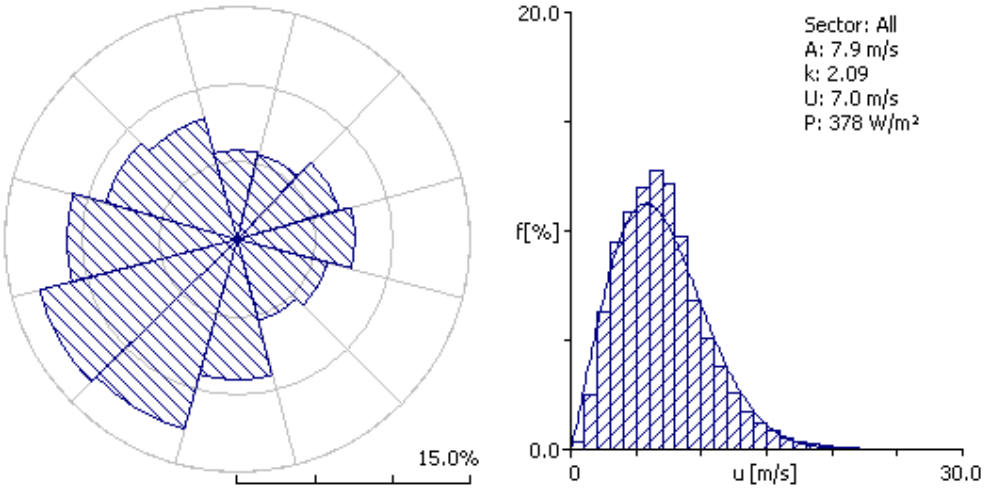

Figure 3.5: Wind rose and wind speed distribution at the ECN wind turbine test station Wieringermeer (Verhoef et al. 2009).

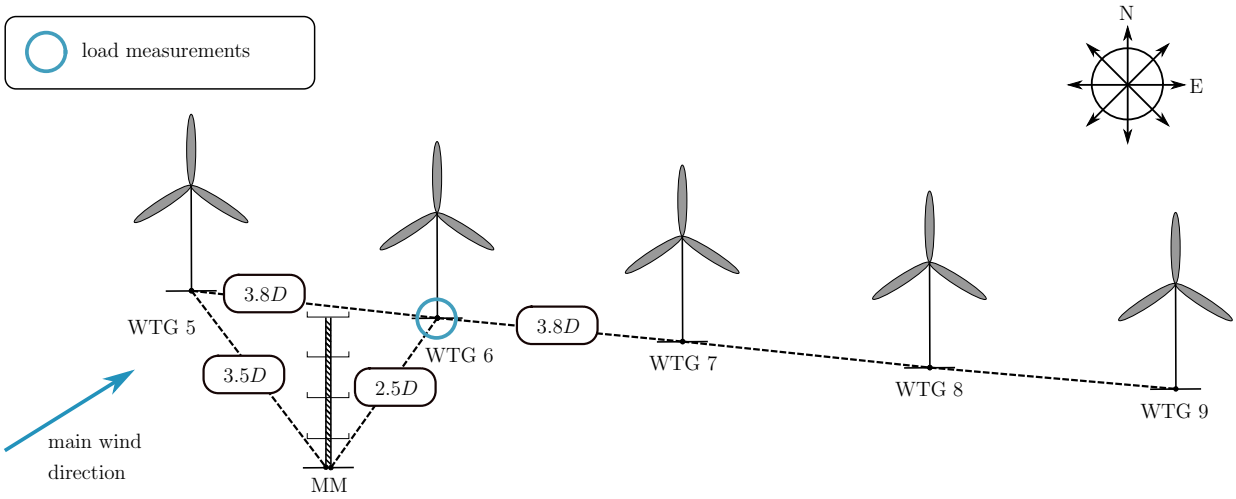

Figure 3.6: Wind farm layout of the ECN wind turbine test station Wieringermeer with measurement equipment.

Table 3.4: Specification of the wind turbine type in the ECN wind turbine test station Wieringermeer.

	N80/2.5
Rated power	2.5 MW
Rotor diameter	80 m
Hub height	80 m
Cut-in wind speed	3 m/s
Cut-out wind speed	25 m/s
Wind turbine class	IEC IA

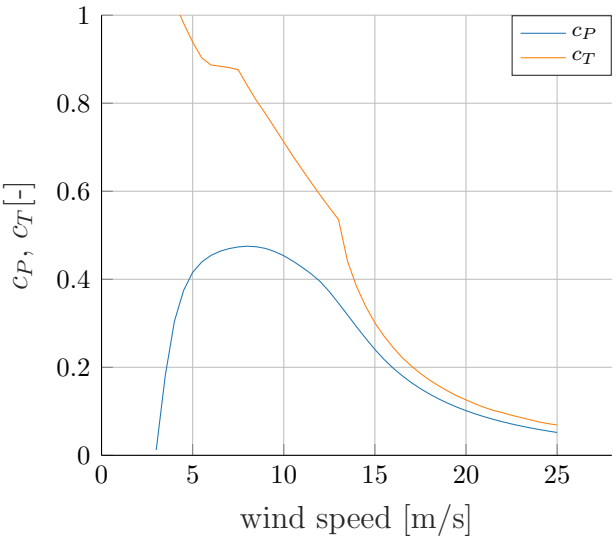

Figure 3.7: Power and thrust coefficients over the wind speed for the N80/2.5MW turbine.

measurement equipment is marked in Figure 3.8. The ultrasonic anemometer data at the hub height of 80 m have been used to determine the ambient wind speed. Furthermore, the measurements at the hub height have been used to determine wind speeds and TIs in the wake of WTG 5 and WTG 6 as shown in Section 7.2.1. In this case, the ambient wind speed has been determined with the anemometer measurements from the turbines itself and a nacelle transfer function has been implemented to exclude the rotor influence. The nacelle transfer function is defined as follows (Machielse 2007):

$$U_0 = 0.0131\, U_{nac}^2 + 0.7355\, U_{nac} + 1.3133 \tag{3.1}$$

Moreover, WTG 6 is equipped with strain gauges at the blade root, main shaft as well as tower top and bottom. The blade edgewise and flapwise moment at a distance of 1.33 m from the blade flange is measured (Poodt and Wouters 2016). The tower torsion is measured 1.61 m below the tower top and the tower bottom bending moments in fore-aft and side-side direction are measured 7.31 m above the foundation. The operational conditions of the turbines are tracked by the SCADA system of the turbines. 10-min measurement statistics from the SCADA system and the met mast as well as the DEL of a 10-min time series have been used in the subsequent analysis.

V	Anemometer
V/D*	Ultrasonic Anemometer
P	Barometer
T/H	Thermo-/Hygrometer
D	Wind Vane

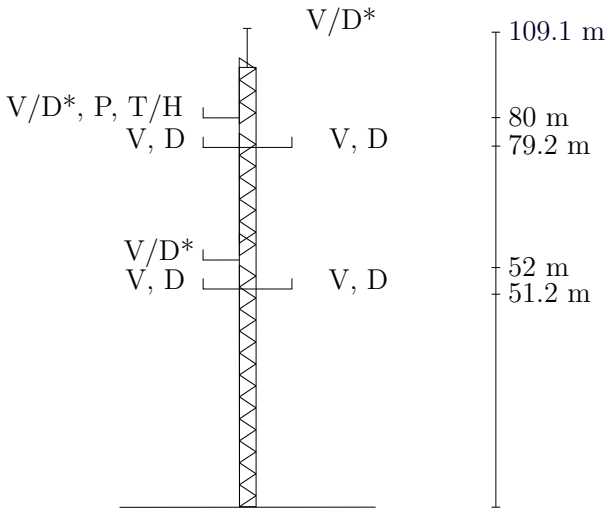

Figure 3.8: Met mast with measurement equipment at the ECN wind turbine test station Wieringermeer.

Chapter 4

Calibration of the dynamic wake meandering model

The following chapter represents the recalibrated version of the DWM model, which has been derived based on the lidar measurements in the Curslack wind farm. The results of the lidar measurements will be presented in the subsequent sections. The recalibration process as well as the final version has been published in Reinwardt et al. (2020a). Parts from this publication have been taken over in this chapter. The wind speed deficit in the HMFR measured by the lidar systems in the Curslack wind farm has been used to recalibrate the wake degradation in the downstream region. To be more precise, the eddy viscosity description in the DWM model is revised. In Larsen et al. (2013) a recalibration was already achieved by introducing a non-linear coupling function F_{amb} into the ambient TI term of the eddy viscosity definition (see Equation (2.71)). The validation of the DWM model in Larsen et al. (2013) showed that the wind speed deficit degradation is too low for low TIs and moderate to large turbine distances in the model version of Madsen et al. (2010). Thus, the ambient TI dependent function F_{amb} was introduced into the eddy viscosity description (Larsen et al. 2013).

A similar behavior but even more pronounced can be seen in the results in Section 7. Following the approach of Larsen et al. (2013), a function based on a least-squares calibration using the acquired lidar measurements is developed. This function is incorporated into the normalized eddy viscosity description in Eq. (2.80), whereby it changes to (Reinwardt et al. 2020a):

$$\frac{\nu_T}{U_0 R} = k_1 F_{amb}(TI_0) F_1(\tilde{x}) TI_0 + k_2 F_2(\tilde{x}) \max\left(\frac{R_w(\tilde{x})^2}{R U_0}\left|\frac{\partial U(\tilde{x})}{\partial r}\right|, \frac{R_w(\tilde{x})}{R}\left(1 - \frac{U_{min}(\tilde{x})}{U_0}\right)\right) \tag{4.1}$$

with the constants $k_1 = 0.0924$ and $k_2 = 0.0216$ and the coupling function:

$$F_{amb}(TI_0) = a TI_0^{-b}, \tag{4.2}$$

where the constants are $a = 0.285$ and $b = 0.742$. These parameters are the results of the least-squares calibration. The non-linear coupling function multiplied by the constant k_1 for the original (DWM-Keck) and the recalibrated (DWM-Keck-c) version of the model are illustrated in Figure 4.1 as a function of the ambient TI. The original version of the

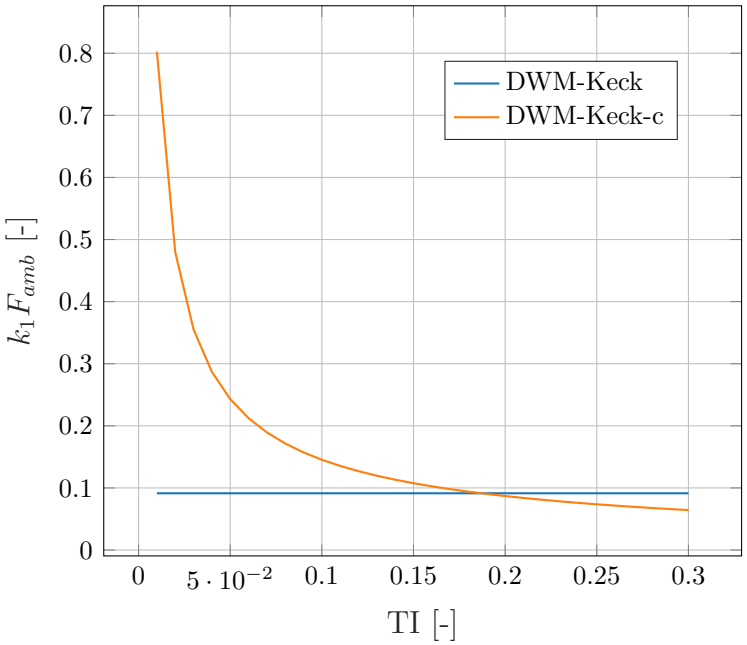

Figure 4.1: Recalibrated weighting function of the ambient TI term of the eddy viscosity over the ambient TI. The non-linear coupling function F_{amb} has been adjusted to improve the wind speed deficit description in the DWM model with respect to the ambient TI.

model does not use a non-linear coupling function, so that $F_{amb} = 1$ in the DWM-Keck model. Furthermore, it should be noted that the constant k_1 was also slightly adjusted by the recalibration, which relies on the normalized eddy viscosity definition of Keck (2013). The reason for improving the eddy viscosity definition of the DWM-Keck model instead of using the DWM-Egmond model, which is also outlined in the guideline, results from the fact that this model is already in good agreement with the measurement results in most TI bins as demonstrated in Section 7 and Reinwardt et al. (2018), so that less adjustments have to be made. Both models are explained in detail in Section 2.3.1.5. For the recalibration, the minimum normalized wake wind speed has been used, measured by the lidar systems. A least-squares fit between the minimum measured and simulated wind speed of the wake of all collected downstream distances has been used to optimize the wake degradation in downstream direction.

Figures 4.2 and 4.3 compare results of the recalibrated final DWM model to the original DWM-Keck model as well as the DWM-Egmond model. Figure 4.2 shows the minimum normalized wind speed in the MFR and Figure 4.3 depicts the wind speed at the wake center in the MFR over downstream distances between 0 D and 10 D for a low and a high TI case of 6 % and 16 %, respectively. The wind speed deficit in the wake has a w-shape instead of a Gaussian shape at close distances due to the low induction close to the nacelle, so that the minimum wind speed differs in this region from the wind speed at the wake center.

Observing the wind speed at the wake center, higher wind speeds can be seen at lower distances, which derives from the mentioned w-shape of the wind speed at these downstream distances. The comparison of the DWM-Keck model (orange curve) and

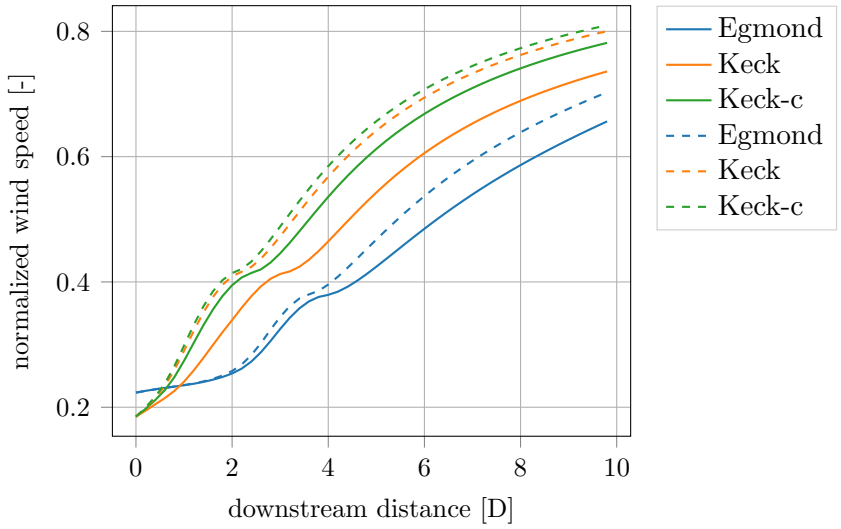

Figure 4.2: Simulated minimal normalized wind speed in the MFR over the downstream distance for a TI of 6 % (solid curves) and 16 % (dashed curves). The recalibrated model is denoted DWM-Keck-c (Reinwardt et al. 2020a).

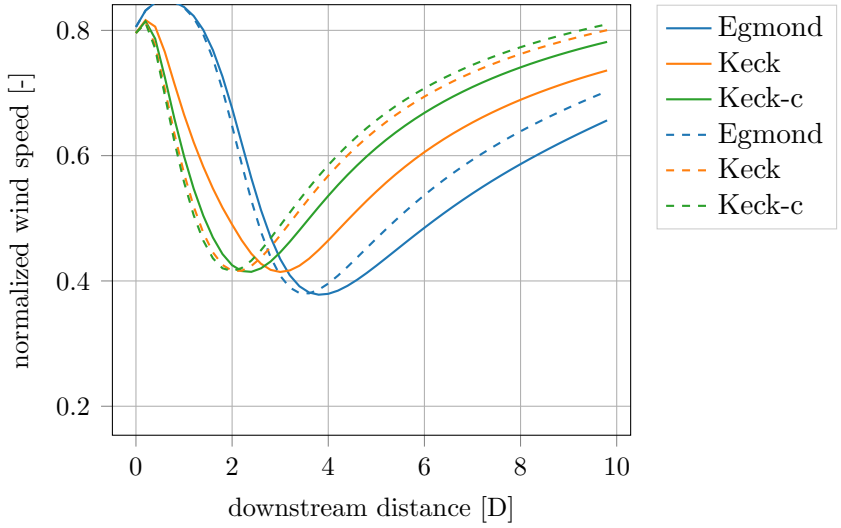

Figure 4.3: Simulated normalized wind speed at the wake center in the MFR over the downstream distance for a TI of 6 % (solid curves) and 16 % (dashed curves). The recalibrated model is denoted DWM-Keck-c (Reinwardt et al. 2020a).

the recalibrated DWM-Keck-c model (green curve) demonstrates that the recalibration leads to a shift of the curve towards lower distances. This shift is more pronounced for the low TI, leading to a faster degradation of the wind speed deficit. For the high TI, both curves, orange and green, are very close to each other over all distances. The faster degradation of the wind speed deficit in the recalibrated model version is caused by introducing the function F_{amb} in the eddy viscosity definition in Equation (4.1) as explained before. The function increases the eddy viscosity for low TIs and thus increases the wind speed deficit degradation in downstream direction. The DWM-Egmond model delivers in both cases the slowest wake recovery. Later on, Section 7.1.1.1 compares the measured minimum wind speed in the horizontal meandering frame of reference (HMFR) to the original and calibrated DWM model for downstream distances up to 8 D. The lidar system performs only a horizontal scan, so that no vertical meandering is determined, whereby the measurements are transformed to the HMFR instead of the MFR as it could be conducted for the simulation results in Figures 4.2 and 4.3. A more detailed explanation of the lidar scan and the transformation is given in Section 6.1.2. The comparison to measurements and the recalibration of the DWM model with the help of a least-squares fit is based on the minimum wind speed in the HMFR instead of the wind speed at wake center in the HMFR. The reason for this is that if the transformation of the wind speed deficit from the FFR to the HMFR is not completely accurate, the wake center cannot be predicted correctly. Consequently, the minimum wind speed in the wake is assumed to be less biased and more suitable for a comparison with the lidar measurements.

Contemplating the curves of the minimum wind speed in Figure 4.2, small steps are formed in the curves between $2D$ and $4D$ (depending on the model used and the TI). These steps correspond to the minima of the curves in Figure 4.3 and are thus related to the transition from the w-shape of the wind speed deficit towards the Gaussian profile and are consequently caused by the resolution in downstream direction. These steps were also found in some measurements and could likewise be related to the implied cross-over zone between the two shapes.

Chapter 5

Extension of the dynamic wake meandering model towards a static model

In the following chapter an extension of the DWM model towards a static model version for site-specific load calculations is presented. The extension of the DWM model has been published in Reinwardt et al. (2020b) and parts from the publication have been taken over in this chapter. The extension is developed in a way that it provides a fast alternative to the often used Frandsen model and can be combined with response surface methods to interpolate site-specific loads. Thus, a complete aerodynamic load simulation can be avoided, which is in particular interesting for layout optimization purposes. The outlined method, denoted *static DWM model*, can be divided into three parts. The single parts of the model are summarized in Figure 5.1. The first part (blue box) comprises

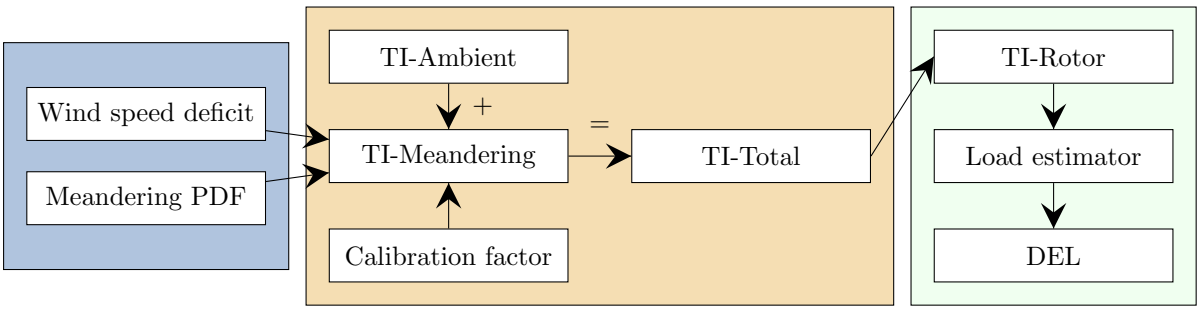

Figure 5.1: Overview of the components of the *static DWM model* (Reinwardt et al. 2020b).

the description of the meandering as well as the downstream expansion of the wind speed deficit. The description of the latter is fully adopted from the DWM model. In the second step (yellow box), the added TI induced by the meandering of the wake itself is determined and superimposed on the ambient TI leading to TI-Total. The last step (green box) is the calculation of a rotor-averaged TI (TI-Rotor), which subsequently serves directly as an input for the load simulation software, so that the DEL can be calculated. In the following, the different substeps are explained in further detail.

5.1 Wind speed deficit

In the DWM model, the downstream expansion of the wind speed deficit is calculated by the thin shear layer equations. This method has been explained in detail in Section 2.3.1.5. For the present analysis, the recalibrated eddy viscosity definition, provided in Chapter 4, is used. The eddy viscosity definition and the calculation of the steady wind speed deficit in the MFR is not influenced by the model extension, so that the general approach can be transformed to all DWM model versions. Although the expansion of the wind speed deficit is solved numerically in the DWM model definition, the computational costs are very low, making it still applicable in an optimization process, as long as the axial induction factor has been calculated in advance for several different wind speeds and stored in a database or look-up table. Alternatively, it is possible to simply replace the wind speed deficit definition by an entirely analytical model (see, e.g. Bastankhah and Porté-Agel (2014) and Larsen (2009) and the explanation in Section 2.3).

5.2 Meandering of the wake

The meandering in the DWM model is based on the assumption that the wake behaves as a passive tracer in the turbulent wind field. Consequently, the movement of the passive structure, i.e. the wake deficit, is driven by large turbulent scales (Larsen et al. 2007; Larsen et al. 2008a). In the proposed extension of the model the meandering is described by a probability density function (PDF), which characterizes the probability of the position of the wind speed deficit in horizontal and vertical direction at a specific downstream position. The approach of using a PDF to describe the meandering is adopted from Keck (2014). The PDF is defined as a normal distribution with the standard deviation of the deflection in horizontal σ_y and vertical direction σ_z, respectively. Thus, the probability of the horizontal and vertical position y_i and z_i of the wind speed deficit is defined as follows (Reinwardt et al. 2020b):

$$PDF(y_i, z_i) = \frac{1}{2\pi\sigma_y\sigma_z} \exp\left[-\frac{1}{2}\left(\frac{(y_i-\mu_y)^2}{\sigma_y^2} + \frac{(z_i-\mu_z)^2}{\sigma_z^2}\right)\right] , \tag{5.1}$$

where μ_y and μ_z are the mean positions of the wind speed deficit (e.g. $\mu_y = 0$ and $\mu_z = 0$ in full wake). This description of the meandering is in contrast to the original model definition described in Section 2.3.1.5, since due to this adjustment the meandering only depends on two parameters, σ_y and σ_z, which can be calculated from the integral of the single-sided velocity spectrum of the component k of the ambient wind field. The index k refers to the considered velocity component (longitudinal, lateral, or vertical). A Kaimal spectrum is used in this analysis, which can be derived from Equation (2.11):

$$S_k(f) = \frac{4(L_k/U_0)\sigma_k^2}{(1+6fL_k/U_0)^{\frac{5}{3}}} . \tag{5.2}$$

Equation (5.2) incorporates the velocity integral scale parameter L_k, the frequency f, the standard deviation σ_k of the velocity component, and the ambient wind speed U_0. Integrating the single-sided spectrum of the velocity component k delivers the standard

deviation σ_k of the velocity component, whereas integrating only up to the cut-off frequency f_c delivers the standard deviation of the lower frequency part of the fluctuating wind speed $\sigma_{k,M}$, which is correlated to the meandering (M) itself (Reinwardt et al. 2020b):

$$\sigma_{k,M}^2 = \int_0^{f_c} S_k(f)df \ . \tag{5.3}$$

The cut-off frequency defines the large-scale turbulence that is correlated to the meandering and has been defined in Equation (2.89). After calculating the standard deviation of the lower frequency part of the fluctuating wind speed, the PDF of the meandering can be determined directly (Reinwardt et al. 2020b):

$$PDF(y_i, z_i) = \frac{1}{2\pi\sigma_{v,M}\sigma_{w,M}} \exp\left[-\frac{1}{2}\left(\frac{((y_i-\mu_y)U_0/x)^2}{\sigma_{v,M}^2} + \frac{((z_i-\mu_z)U_0/x)^2}{\sigma_{w,M}^2}\right)\right]\left(\frac{U_0}{x}\right)^2 \ . \tag{5.4}$$

where x is the downstream distance. Equation (5.4) depends on the standard deviation of the fluctuating wind speed $\sigma_{v,M}$ and $\sigma_{w,M}$, which can be calculated by Equation (5.3). Given that the PDF of the meandering is based on the standard deviations of the deflections in horizontal and vertical directions (σ_y and σ_z), the term U_0/x is introduced into Equation (5.1) leading to Equation (5.4).

The original DWM model suggests a low-pass filtered turbulent wind field to describe the horizontal and vertical deflection of the wake (see Section 2.3.1.5). However, calculating a turbulent wind field requires considerable computational power. The aim of the model extension proposed here is to increase the usability of the DWM model in site-specific load calculations and wind farm layout optimization processes. Thus, the purely analytical PDF along with the Kaimal spectrum is more suitable and used instead. Furthermore, it should be highlighted that this approach uses only a single-point spectrum and neglects any spatial coherence. Further analyses have shown that this simplification has only negligible influence on the overall results and therefore seems to be acceptable in this model approach. A comparison of the PDFs using either the Kaimal spectrum or the complete wind field is depicted in Figure 5.2. The horizontal meandering predicted by both methods agree very well, whereas there is a slight difference in the less dominant vertical meandering. However, since the turbine loads are mainly affected by the horizontal meandering, this deviation is acceptable.

5.3 Total turbulence intensity

The next step is the calculation of the added TI induced by the meandering, which is based solely on the combination of the meandering PDF and the shape of the wind speed deficit and thereupon the calculation of the TI-Total. According to Keck (2014), the meandering TI can be calculated from the squared difference of the wind speed deficit

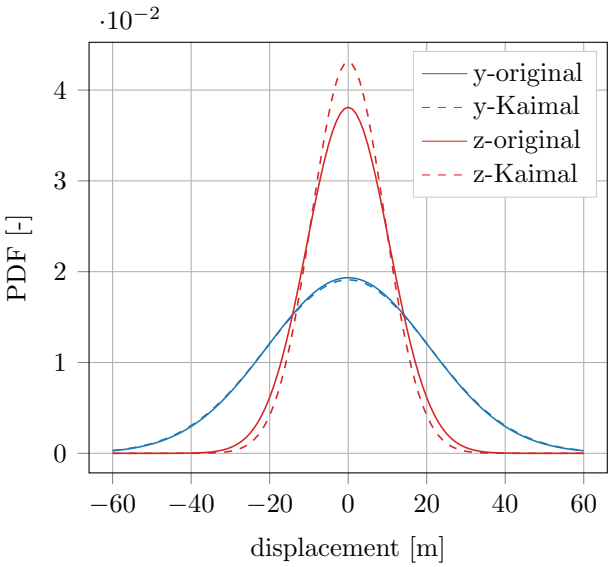

Figure 5.2: PDFs of the horizontal (y) and vertical (z) meandering based on the original DWM model with a complete wind field (Section 2.3.1.5) and the newly proposed model (Reinwardt et al. 2020b).

in the MFR and the FFR. This results in:

$$TI_M(y_i, z_i) = \sqrt{\iint (U(y_i - y_M, z_i - z_M)_{MFR} - U(y_i, z_i)_{FFR})^2 \, PDF(y_M, z_M) \, dy_M \, dz_M} \ , \tag{5.5}$$

where $U(y_i - y_M, z_i - z_M)_{MFR}$ is the mean wind speed in the MFR at the position y_i and z_i. The integral needs to be solved over the complete area of the PDF, which deviates from zero. In the example illustrated in Figure 5.2 it is necessary to integrate from $-60\,\mathrm{m}$ to $60\,\mathrm{m}$ in y-direction and from $-40\,\mathrm{m}$ to $40\,\mathrm{m}$ in z-direction. The wind speed deficit $U(y_i, z_i)_{FFR}$ in the FFR can be calculated in a similar way and is consequently based on the convolution of the wind speed deficit in the MFR and the PDF of the vertical and horizontal deflection (Keck 2014):

$$U(y_i, z_i)_{FFR} = \iint U(y_i - y_M, z_i - z_M)_{MFR} \, PDF(y_M, z_M) \, dy_M \, dz_M \ . \tag{5.6}$$

The calculated meandering turbulence intensity TI_M is subsequently added to the ambient turbulence intensity TI_0 in a quadratic summation as follows (Reinwardt et al. 2020b):

$$TI(y_i, z_i)_{total} = \sqrt{(k_M \cdot TI_M(y_i, z_i))^2 + TI_0^2} \ . \tag{5.7}$$

This method is adopted from Keck (2014), where it is applied to calculate power losses of wind farms. The calibration factor k_M for the meandering is added in this context. It is necessary to introduce a calibration factor here given that a damage-equivalent mean rotor TI needs to be calculated. The calibration factor depends on the downstream distance and the ambient wind speed. The procedure to determine the factor k_M and a summary of the values used are outlined in Section 7.3. Furthermore, no small-scale turbulence is

modeled in the static DWM model version given that this model version does not include any time-consuming wind field simulations. In the original DWM model the small-scale turbulence is based on scaled wind field generated by a Kaimal spectrum and a coherence function as outlined in Section 2.3.1.5. The small-scale turbulence has only a marginal influence in the TI in FFR as later on outlined in Section 7.3. Additionally, the calibration factor k_M includes indirectly the influence of the small-scale turbulence.

5.4 Rotor-averaged turbulence intensity

The outcome of the previous step is the aforementioned inhomogeneous wind field, which leads directly to the final step, the calculation of a load-equivalent homogeneous TI. The purpose of this final step is to find a TI that correlates for all wake conditions with the turbulence-driven loads of the downstream turbine. Wake conditions could be that only one half of the rotor is in the wake (partial wake) or the full rotor is in the wake (full wake). A TI that is averaged over the whole rotor with respect to the Wöhler coefficient shows a good correlation with the turbulence-driven loads. It follows the approach of the effective TI introduced by Frandsen (Frandsen 2007) and outlined in Section 2.3.1.1. He identified a linear correlation between TI and DELs and introduced a weighted design TI over different wind directions. This effective TI should damage the structure equivalent to the sum of the damage contributions of all single wind directions. In consequence of this investigation and the fact that the rotor-averaged TI calculated here should be correlated to the DEL, the Wöhler coefficient is also considered in the calculation. Accordingly, the rotor-averaged TI is defined as (Reinwardt et al. 2020b):

$$TI_{rotor} = \frac{1}{\pi R^2} \left(\int_0^{360°} \int_0^R TI_{total}(r,\alpha)^m \, r \, dr \, d\alpha \right)^{\frac{1}{m}} , \tag{5.8}$$

where R is the rotor radius and m the Wöhler coefficient. Finally, the rotor-averaged TI can be used as an input for a response surface to calculate DELs. Given that the Wöhler exponent is introduced in Equation (5.8), the homogeneous rotor-effective TI depends on the material of the evaluated load component, so that different TIs for different materials need to be calculated similar to the approach of Frandsen.

Chapter 6

Data processing

The following chapter describes the scan pattern definition as well as the procedure for evaluating the lidar data. Parts of these sections are taken over from Reinwardt et al. (2020a). The lidar data are used to determine the meandering time series and based on this the mean longitudinal wind speed in the MFR. Moreover, this chapter outlines the evaluation and filtering of the load measurements. To evaluate the load simulation itself without any wake model influence, a comparison between measured and simulated loads is presented. Furthermore, the procedure of incorporating the measured lidar data into the wake and load simulations is described. Parts of these sections have been published in Reinwardt et al. (2021).

6.1 Lidar data

6.1.1 Longitudinal wind speed calculation

As already explained in Section 2.4 lidar systems measure the LOS velocity, so that either multiple lidar systems are necessary to evaluate the three-dimensional wind velocity vector, the VAD method is applied or the geometric dependency of the position of the laser beam relative to the main flow direction is used to determine the wind speed in longitudinal direction. The latter is used in this analysis. Accordingly, the wind speed in downstream direction is calculated from the LOS velocity of the lidar system and the position of the laser beam relative to the main flow direction is determined as outlined in Machefaux et al. (2012). Thus, the horizontal wind speed is defined as:

$$U(t) = U_{LOS} \cdot \frac{1}{\cos(\theta) \cdot \cos(\phi)} \ , \tag{6.1}$$

where θ is the azimuth angle and ϕ the elevation angle of the lidar scan head. This is a suitable approach for small scan opening angles like in the measurement campaign presented here. The largest opening angle in the scan pattern is 20°. Nevertheless, if the turbine is not correctly oriented towards the main flow direction (yaw misalignment), this could have an impact on the overall results. The misalignment would lead to larger discrepancies between the direction of the laser beam and the main flow direction, so that the method to calculate the horizontal wind speed by Equation (6.1) might be more

biased. To reduce the uncertainties based on yaw misalignments, the measurement data have accordingly been filtered and no data with misalignments greater than 6° are used as outlined in the next section. The yaw misalignment has been determined by the difference between the nacelle position determined by the nacelle-installed GPS systems and the measured wind direction from the met mast. The yaw misalignment has the strongest impact at the largest scan opening angles, i.e. a misalignment of 6° at an opening angle of 20° leads to an overestimation of the wind speed by about 5 %.

6.1.2 Transformation to the meandering frame of reference

The meandering time series and the horizontal displacement of the wake are determined with the help of a Gaussian fit. Trujillo et al. (2011) assume that the probability of the wake position in vertical and horizontal direction is completely uncorrelated, so that the two-dimensional fitting function can be expressed as follows:

$$f_{2D} = \frac{A_{2D}}{2\pi\sigma_y\sigma_z} \exp\left[-\frac{1}{2}\left(\frac{(y_i-\mu_y)^2}{\sigma_y^2} + \frac{(z_i-\mu_z)^2}{\sigma_z^2}\right)\right] , \tag{6.2}$$

where σ_y and σ_z are the deficit widths in terms of the standard deviations in horizontal and vertical direction and μ_y and μ_z are the mean horizontal and vertical displacements. In the analysis presented here, only results from a horizontal line scan are analyzed, so that the vertical meandering could not be eliminated from the wind speed deficit and the deficit's depth is less pronounced in comparison to the real MFR. To denote that the vertical meandering is not eliminated in the present investigation, but included in the wind speed deficit, the abbreviation HMFR (horizontal meandering frame of reference) is introduced and henceforth used instead of MFR. A comparison of the wind speed deficit simulated with the DWM model in the complete MFR and the HMFR is illustrated in Figure 6.1. The simulations were carried out for a small downstream distance of $2.5D$ and a high TI of 16 %. There are only small discrepancies around the center of the wake, which validates the present assumption.

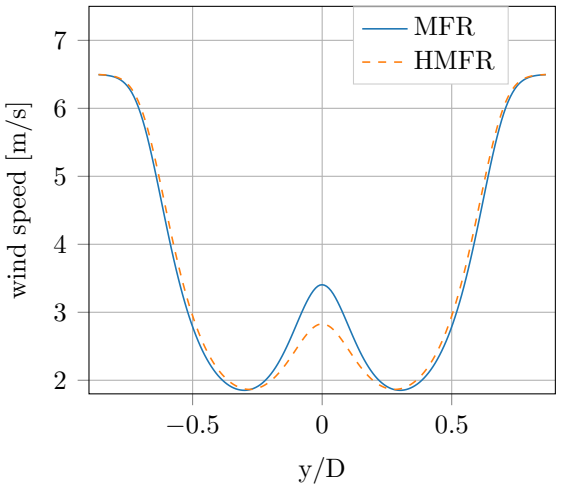

Figure 6.1: Wind speed deficit at a downstream distance of $2.5D$ and an ambient TI of 16 % (Reinwardt et al. 2020a).

Since the vertical meandering is neglected, the measured wind speed deficit from the horizontal line scan is fitted to a one-dimensional (1D) Gaussian curve defined as follows:

$$f_{1D} = \frac{A_{1D}}{\sqrt{2\pi}\sigma_y} \exp\left(-\frac{1}{2}\frac{(y_i - \mu_y)^2}{\sigma_y^2}\right) , \tag{6.3}$$

where A_{1D} represents a scaling parameter. The measured wind speeds are fitted to the Gaussian shape via a least-squares method. The result of the fitting procedure is the horizontal displacement μ_y. Thereby, only fitted horizontal displacements between $-200\,\mathrm{m}$ and $200\,\mathrm{m}$ are used for further validations of the mean wind speed in the HMFR. A horizontal displacement of more than $200\,\mathrm{m}$ cannot be represented by the Gaussian fit due to a lack of measurement points. However, such an event is highly improbable (e.g. the DWM model predicts the wind speed deficit's probability at the horizontal position of $200\,\mathrm{m}$ to be $2 \cdot 10^{-22}$ for an ambient wind speed of $6.5\,\mathrm{m/s}$ and an ambient TI of $8\,\%$).

The entire method of calculating the wind speed deficit in the HMFR is illustrated in Figure 6.2 and can be described as follows: the lidar system takes measurements from the

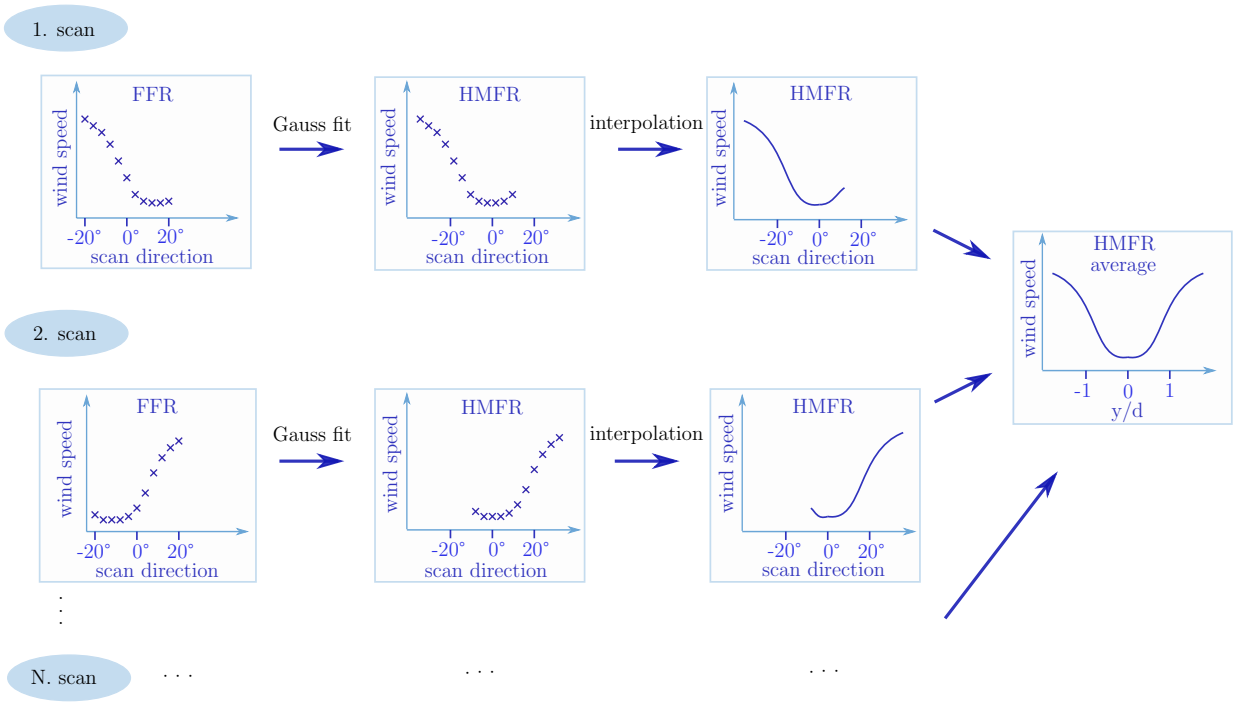

Figure 6.2: Method for the determination of the mean wind speed deficit in the HMFR (Reinwardt et al. 2020a).

nacelle of the turbine in downstream direction, which deliver the wind speed deficit in the nacelle frame of reference or even in the FFR (see left side of Figure 6.2) if the turbine is not moving (this is ensured by the GPS systems). A Gaussian curve is then fitted into the scanned points as explained previously. It provides the horizontal displacement of the wake, so that each scan point can be transferred into the HMFR with the calculated displacement (see middle diagrams in Figure 6.2). The last step illustrated in the diagrams is the interpolation to a regular grid. These three steps are repeated for a certain number of scans N (e.g. approx. 37 for a 10-min time series). Finally, the mean value of all single

measurement results in the HMFR is calculated. It should be noted that it is mandatory to interpolate to a regular grid; otherwise, it would not be possible to take the mean of all scans since the horizontal displacement differs at each instant in time and, thereupon, the measurement points are transmitted to a different location in the HMFR. After averaging, the plausibility of the results is inspected. If the calculated minimum mean wind speed in the HMFR is higher than the minimum mean wind speed in the FFR, it is assumed that the Gaussian fit failed and the results are no longer considered. In theory, the wind speed deficit in the HMFR should be more pronounced than those measured in the FFR, whereby this fundamental plausibility check is added.

6.1.3 Lidar simulation and scan pattern definition

To capture the meandering time series and thereupon calculating the mean wind speed in the HMFR as outlined in the last section, it is necessary to ensure a certain scan time. Accordingly, the most challenging part of the lidar measurement campaign is the low ray update rate of the lidar system. The ray update rate of the installed lidar system is considerably smaller than those of similar measurement campaigns outlined in Bingöl et al. (2010) and Trujillo et al. (2011). To ensure that the meandering as well as the wind speed deficit in the HMFR can be captured despite of the low ray update rate, lidar and wind field simulations have been conducted in advance. The simulations incorporate lidar specifications (e.g. beam update rate and scan head angular velocity) and wind farm site conditions (ambient TI and wind shear). The simulations assume perfect lidar measurements, where no probe volume averaging is considered and the lidar system measures the horizontal wind speed directly. The wind field is simulated at halfway of the range gate. The simulated lidar system "takes measurements" in a simulated wind field that is generated by the DWM model and includes wake effects as well as ambient turbulence. The in-house code is written in Python. From these "measured" wind speeds the meandering is determined via Gaussian fits as previously explained and implemented in the real measurement campaign. Simulations are performed for different scan patterns, ambient conditions, and downstream distances to test the scan patterns. For this purpose the one-dimensional scans comprises only eleven scan points scanned in a horizontal line from $-20°$ to $20°$ in $4°$ steps. The "measurement" results of the simulated meandering time series are shown in Figure 6.3(a, c, e), whereas the corresponding wind speed deficit in the HMFR is presented in Figure 6.3(b, d, f). Simulations with three different ambient wind speeds (5.5 m/s, 6.5 m/s and 7.5 m/s) are depicted. The results are compared to the original meandering time series and the simulated wind speed deficit. The "measured" wind speed deficit in the simulated environment reproduces the simulated wind speed and its underlying meandering time series very well (the coefficient of determination R^2 is approximately 0.93 at an ambient wind speed of 6.5 m/s). Although only eleven scan points are used for these plots, the curve of the wind speed deficit is very smooth. The reason for this behavior is the previously mentioned interpolation process. The distribution generated by the meandering process provides many scan points around the center of the wind speed deficit and only a few at the tails. Therefore, the influence of turbulence at the tails is much higher, leading to a somewhat coarse distribution at the boundaries of the deficit. It should also be noted that since this is a one-dimensional scan, the simulated lidar system "measures" the wind speed deficit only horizontally neglecting the wake's less

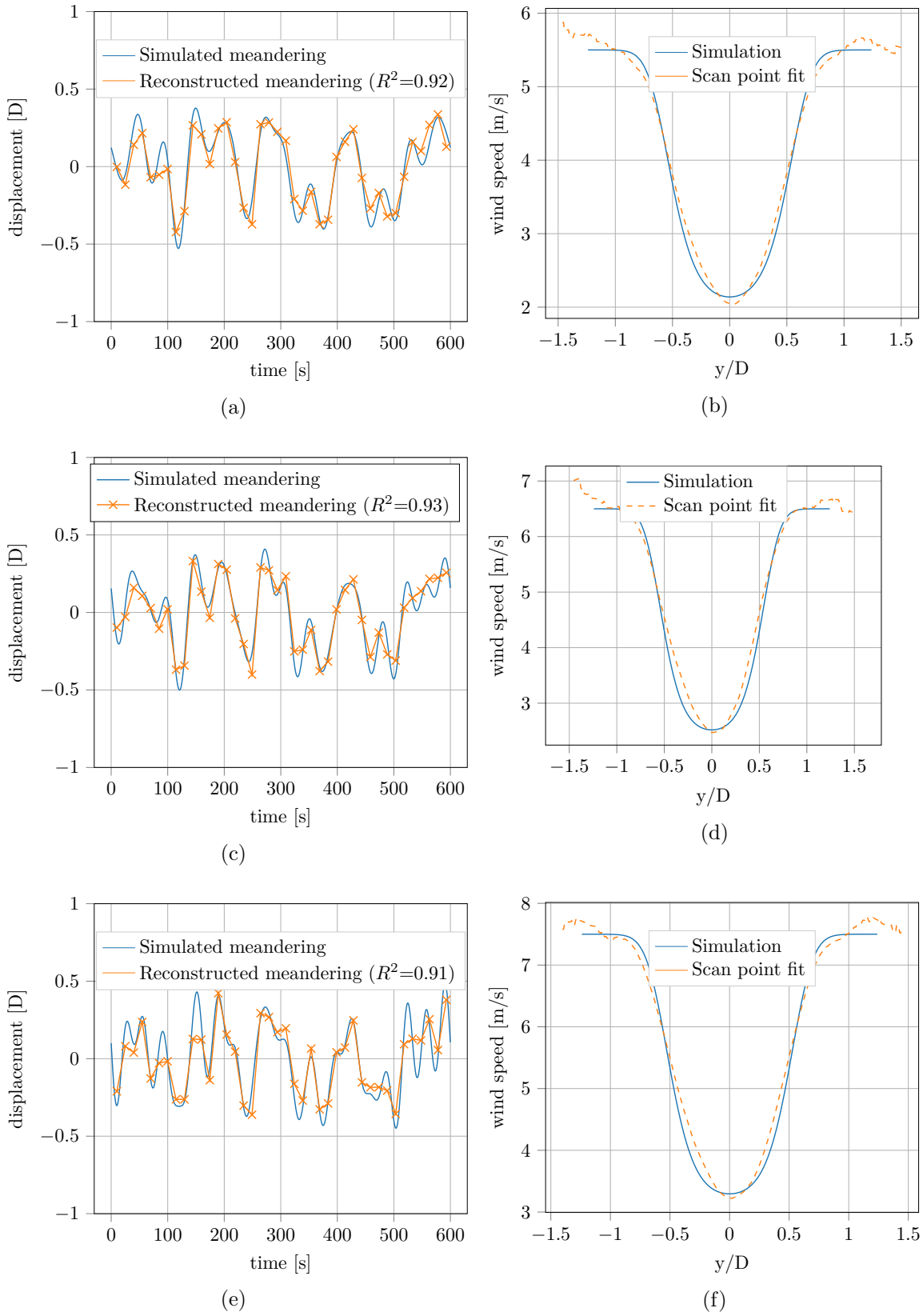

Figure 6.3: Simulated and simulated "measured" meandering time series (a, c, e) and wind speed deficit in the HMFR (b, d, f) at a downstream distance of 3.61 D, an ambient TI of 12 % and an ambient wind speed of 5.5 m/s (a, b), 6.5 m/s (c, d) and 7.5 m/s (e, f).

dominant vertical movement. Whenever the wind speed deficit in the HMFR is mentioned in subsequent validations, it implies the neglection of eliminating the vertical meandering from the wind speed deficit, which has only a marginal impact on the shape of the wind speed deficit in the real MFR (see Figure 6.1).

The lidar simulations indicate that the Gaussian fit works more reliably under optimal operating conditions, i.e. at optimal tip speed ratio, when the wind speed deficit is most pronounced and the power coefficient c_P has its maximum (see Figure 3.3). For the turbines examined, this applies to a range of 5 m/s up to 8 m/s, so that only measurement results with ambient wind speeds in this interval are analyzed. Simulations for the wind speed bins 4.5 m/s, 8.5 m/s and 9.5 m/s are depicted in the appendix in Figure A.1. The figure shows that up to 8.5 m/s the fit works reliable, whereas at higher wind speeds (e.g. 9.5 m/s) the Gaussian fit tends to fail and the complete meandering time series could not be captured. Furthermore, simulations for different downstream distances as well as ambient TIs are illustrated in the appendix in Figure A.2 and A.3. Both figures prove that the fit works reliable for different downstream distances as well as ambient TIs.

The first lidar simulations have shown that it is even possible to capture the wake by a scan with only 9 points and an opening angle of 16°. However, in the beginning of the real measurement campaign it emerged that a horizontal line scan with only nine points scanned from $-16°$ to 16° in 4° steps does not capture the wake reliably given that a small misalignment of the turbine leads to wake deflections, so that the scan pattern had to be enlarged. Moreover, it has been recognized that the measurement time increases with the number of range gates, because the internal data processing time increases. Thus, to decrease the measurement time, the number of range gates has been limited, so that the farthest scan point is 750 m downstream.

Furthermore, simulations for a two-dimensional scan have also been carried out. These simulations have clearly demonstrated that a determination of the wake meandering in both directions (vertically and horizontally) is very challenging with the lidar device used due to the long scan time. It emerged that it is not possible to measure sufficient scan points on a two-dimensional wind field by keeping an adequate scan time, whereby this approach has not been further investigated.

6.1.4 Data filtering

This section describes the filtering procedure, which has been applied to the lidar data used to recalibrate the DWM model. For the recalibration of the model, lidar data from a measurement period of half a year (January until July 2019) have been evaluated. The data are filtered in accordance with the wind direction, so that lidar data without free inflow of the wake generating turbine as well as lidar measurements in the induction zone of another turbine are rejected. This leads to the remaining wind direction sectors listed in Table 6.1. The remaining sectors are relatively small, especially for the lidar system on WTG 2, which reduces the amount of usable measurement data drastically. Additionally, the measured lidar data are sorted into TI bins for the further validation and recalibration of the DWM model. The ambient conditions are determined by 10-minute time series statistics from the met mast, and hence only measurement results with free inflow at the met mast are usable. Only situations with normal power production of the wake generating turbine are considered. The turbine operation mode is identified

Table 6.1: Considered wind direction sectors per wake generating turbine in the measurement campaign. Wind direction sectors without free inflow of the met mast and the turbine as well as measurements in the induction zone of another turbine are omitted.

	lower limit [°]	upper limit [°]
WTG 1	160	190
	320	350
WTG 2	150	160
	240	250

through the turbine's SCADA system. The statistics of the 10-minute time series are applied to identify the operational mode. Furthermore, the data have been analyzed according to yaw misalignments, so that no data with turbine misalignments greater than 6° are considered in the analysis. The misalignment is determined by the GPS systems and the met mast wind direction. Moreover, the lidar data are filtered by the power intensity of the measurement results, which is closely related to the signal-to-noise ratio (SNR) of the measurements. Results with an intensity lower than 1.01 have been discarded. Additionally, the scanning time of each complete horizontal line scan is verified by the timestamp of each scan to ensure that the meandering can really be captured. In summary, this leads to the following filtering procedure for the measured lidar data:

1. Filtering according to the wind direction determined by the met mast (free inflow at met mast and wind turbine and no induction zone from other turbines).
2. Filtering according to the ambient wind speed determined by the met mast.
3. Filtering according to the normal power production determined by the SCADA system of the turbines.
4. Filtering according to yaw misalignment determined by the GPS system and met mast wind direction.
5. Filtering according to the SNR of the lidar measurements.
6. Filtering according to the scan time.
7. Grouping all data sets in TI bins with a bin width of 2 % according to the measured ambient TI at the met mast.

The filtering procedure leads to a high decrease of usable lidar data sets, so that only 155 10-minute data sets fulfill the filtering criteria in the measurement period of seven months.

6.2 Load data

6.2.1 Data filtering

For the load validation at free inflow and under the influence of the wake, measurement results from April 2019 to May 2020 have been used. The data are filtered and sorted in accordance with the ambient conditions (e.g. ambient wind speed, TI and wind direction) determined by the met mast and the operational states of the turbine tracked by the SCADA system, so that all filtering is based on 10-minutes statistics from the met mast or the SCADA system. Only measurement results, where the turbines operate under normal power production are included in the analysis. This procedure is in analogy to the filtering used for the lidar data. In the night, the turbines work in a reduced mode for noise reduction purposes, so that no data could be gathered during the night. The procedure of filtering the load data can be summarized as follows:

1. Filtering according to the wind direction determined by the met mast to match the wind direction sector with wake-free inflow or wake inflow at the evaluated turbine.
2. Sorting the data into wind speed and TI bins determined by the met mast.
3. Filtering according to the normal power production of both the wake generating and wake-affected turbine determined by the SCADA system of the turbines.
4. Grouping all data sets into wind speed bins with a bin width of 1 m/s and for the wake sectors in wind direction bins with a bin width of 4°.

The wind direction sectors for free inflow and wake conditions are summarized in Table 6.2. The filtering procedure leads to a strong reduction of available data sets, so that for

Table 6.2: Considered wind direction sectors for wake-free inflow and analyzed wake sectors.

	lower limit [°]	upper limit [°]
Wake-free inflow at met mast & WTG 2	140	260
Wake at WTG 2 generated by WTG 1	259	335
Wake at WTG 5 generated by WTG 2	193	237
Wake at WTG 5 generated by WTG 1	228	268

example at a TI of 6 % and an ambient wind speed of 6 m/s only about 100 10-minute data sets could be collected when WTG 2 is placed in the wake of WTG 1. Considerably more data sets could be collected for wake-free inflow conditions. In total around 370 samples could be collected at a TI of 12 % for the analysis presented in the next section.

6.2.2 Validation of the load simulations

In order to validate the aerodynamic load simulations, the following section compares measured and simulated loads under wake-free inflow conditions. The section shows results from WTG 2 under normal operating conditions. The met mast as well as WTG 2 are

exposed to wake-free inflow conditions. Thus, the met mast is suitable to determine all ambient conditions. The mean value of the measured and simulated normalized power curve is depicted in Figure 6.4**(a)** for a TI of 12 %.

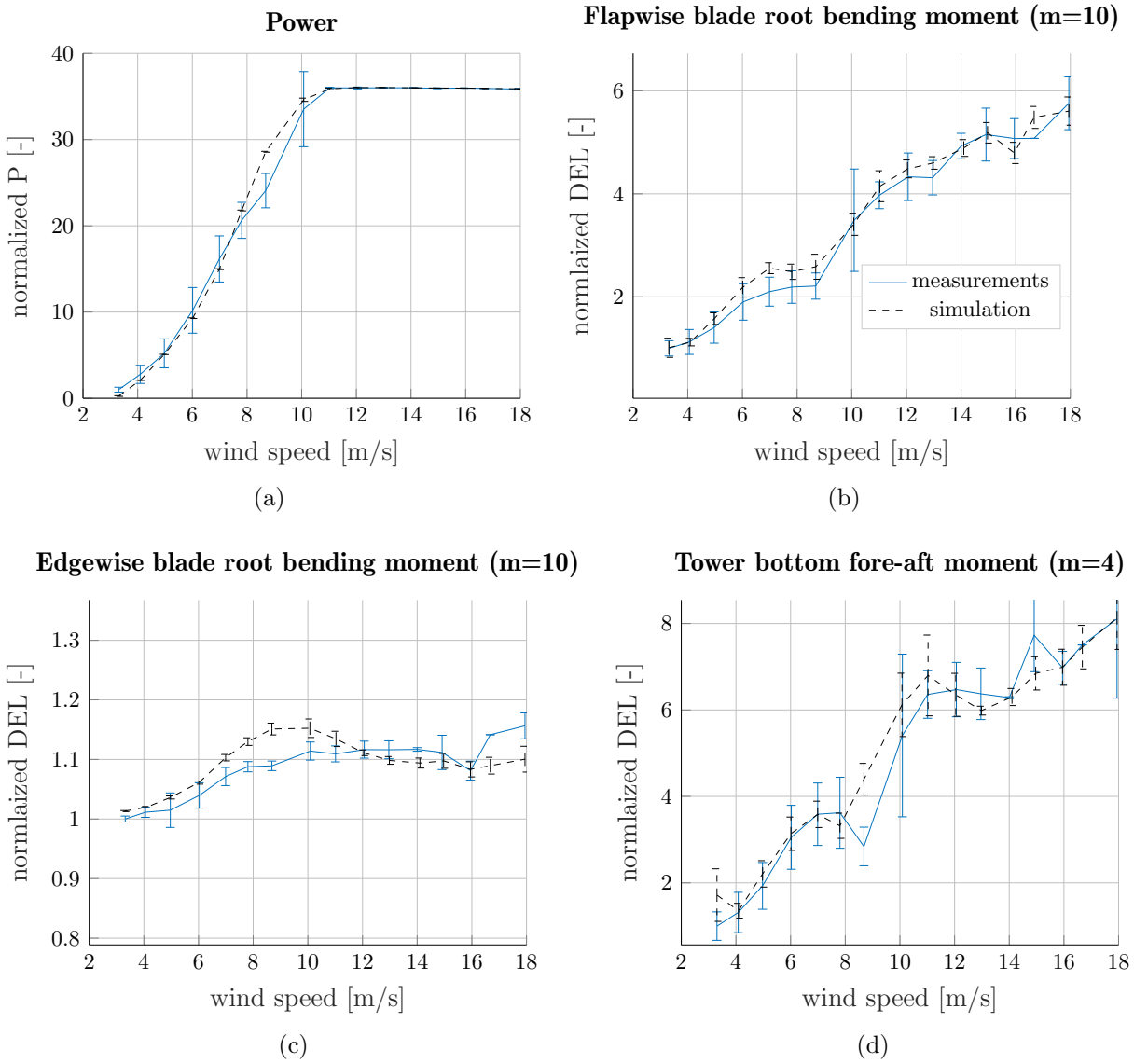

Figure 6.4: Measured and simulated power **(a)**, flapwise blade root moment **(b)**, edgewise blade root moment **(c)** and tower bottom fore-aft moment **(d)** at WTG 2 at an ambient TI of 12 % and wake-free inflow. The Wöhler exponent m is given in the title.

The power curve is normalized by the measured power in the smallest wind speed bin. The error bars in the figures illustrate the standard deviation in each wind speed bin. All data sets are divided into wind speed bins with a width of 1 m/s. The mean values of wind speed, TI, wind shear, and air density of each wind speed bin determine the input parameters of the load simulations. Each simulation is conducted six times with different seeds, so that the simulation results are likewise shown as mean values with standard deviations. In summary, the simulated power agrees very well with the

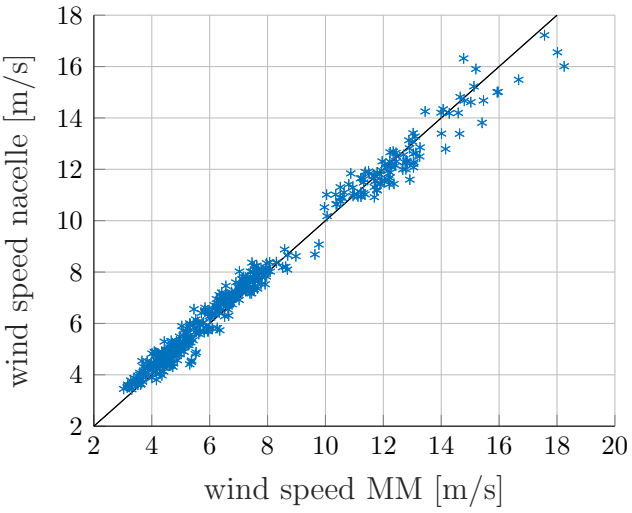

Figure 6.5: Measured nacelle anemometer wind speed at WTG 2 over the met mast wind speed.

measured power. Some discrepancies between measurements and simulations occur solely close to the rated wind speed of 11 m/s. In this area only a few measurement points can be extracted due to the chosen filtering criteria. As a result, the measurements show an extraordinarily high standard deviation. A direct comparison of the measured wind speed of the nacelle anemometer and the met mast has indicated some discrepancies in this range (see Figure 6.5). Thus, it is very likely that the deviation arises due to a momentarily different inflow wind speed at the turbine and the one measured at the met mast and used in the simulations. The measured wind speed at the nacelle anemometers is corrected by a nacelle transfer function, so that the current inflow wind speed at the turbine can be estimated. Given that the number of data sets is very low in this wind speed range, the momentarily different inflow wind speed at these data sets is not averaged out as it is the case in other wind speed ranges. The very low number of data sets in this range is assumed to be related to the filtering of the operational state of the turbine. The signal, which determines normal power production, might behave different in this region.

The results of the measured and simulated flapwise blade root bending moment are illustrated in Figure 6.4**(b)**. It displays the normalized 1 Hz DEL. The Wöhler coefficient (inverse slope of S-N curve) is given in the title of the figure. The development of the measured flapwise fatigue load as a function of the wind speed can be reproduced very well by the simulations. Only some slight discrepancies occur between 6 m/s and 9 m/s, where the simulation overestimates the loads slightly. These discrepancies are assumed to be related to the inaccuracy of the load simulation software itself.

The measured and simulated DELs of the edgewise blade root bending moment is depicted in Figure 6.4**(c)**. The simulations of the edgewise moment show a local maximum just below the rated wind speed of 11 m/s. This observation could not be verified by the measurements. The measured and simulated power deviate in this wind speed range, which can be explained by differences between the nacelle anemometer and the met mast anemometer in the estimated wind speeds and the low number of measurements in this wind speed range. It is most likely that the load discrepancies in this range derive from the same issue. The differences in the edgewise moment and the power around the rated

wind speed as well as the illustration of the measured nacelle wind speed and the met mast supports the hypothesis that the turbine experiences a different inflow wind speed during the few measured data sets in this wind speed range and explains the discrepancies. Furthermore, due to the low amount of data points in this region, the measured wind speed might be biased. However, since the differences between measurements and simulations in the edgewise moment are still below 5 %, the overall agreement is reasonable for this load component. The edgewise moment is mainly driven by the rotational speed of the rotor and the gravity. The dependency of the edgewise moment on the wind speed is less pronounced in comparison to the flapwise moment.

The simulated DELs of the tower bottom bending moment are depicted in Figure 6.4**(d)**. For the tower bottom bending moment a Wöhler exponent of 4, which is appropriate for a steel tower, is applied. The DELs of the blade sensors have been calculated with a Wöhler exponent of 10, which is suitable for composite materials. The measured tower bottom bending moment can be predicted very well by the simulation, although there are similar discrepancies around the rated wind speed. Results of the tower torsion, tower top fore-aft, side-side (lateral) as well as tower bottom side-side moments are depicted in the appendix in Figure A.4. The tower torsion can be represented over all wind speed bins very well, whereas the other sensors show discrepancies above the rated wind speed. Especially the measured side-side moment deviates from the simulated one above the rated wind speed. Given that the overall load in side-side direction is much smaller than the one in fore-aft direction, outliers have a major impact on the overall results, so that in the area with only a few measurement points these discrepancies can occur.

Further results of the measured and simulated loads at WTG 3 and WTG 5 can be found in the appendix in Figures A.5 to A.8. A similarly good agreement between simulations and measurements has been observed for WTG 3. Only some outliers above the rated wind speed and at the side-side moments could be detected. WTG 3 is only equipped with strain gauges at the tower, so that no blade moments are illustrated. The measurement results at WTG 5 deviate slightly more from the simulations. The reason is that only very few data sets could be detected, where WTG 5 and the met mast experience free inflow due to the specific wind farm layout.

Nevertheless, the accuracy of the load simulation software used in combination with the turbine model for load simulations is presumed to be appropriate for a further analysis of the wake sectors, since for the wake analysis only results below the rated wind speed are analyzed and the most relevant load components for wakes such as the blade root flapwise moment as well as the tower fore-aft moments are in good agreement with the simulations in this wind speed range.

6.3 Lidar-assisted load simulation

In Chapter 4, a recalibrated version of the DWM model has been introduced. The lidar systems have been used to recalibrate the DWM model to decrease the uncertainties of load simulations in wake conditions. Another approach to decrease uncertainties in the load simulation under wake conditions is described in this section. A method to incorporate lidar measurements successively into the wake simulation is explained. The measured lidar data for this application are similarly filtered as explained in Section 6.1.4. The

data are filtered by the power intensity of the returned laser beam of the measurements. Furthermore, the scan time is observed, so that only results with a sufficient scan time to track the wake meandering are considered. In contrast to the filtering in the last section, measurements in the induction zone of the turbines have been explicitly taken to determine the inflow wake characteristics and incorporate these in the DWM model.

A schematic illustration of the process for lidar-assisted load simulations is illustrated in Figure 6.6. First, the lidar-measured mean wind speed deficit is used to replace the

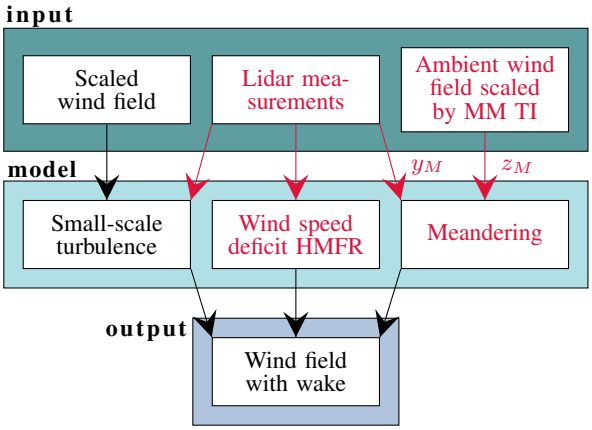

Figure 6.6: Incorporation of lidar measurements into the DWM model; y_M is the horizontal and z_M the vertical meandering component (Reinwardt et al. 2021).

quasi-steady deficit in the DWM model definition (see also Figure 2.10). Since only a horizontal line is scanned, no vertical meandering can be captured (see Section 6.1.2). In a second step, the measured horizontal meandering is included in the DWM model.

The lidar system measures in the induction zone of the downstream turbine, where the wind speed is reduced due to the upstream effect of the subsequent turbine. However, its influence must be excluded from the measurement results to use the measured wind speed deficit in the wake model. The simple induction model defined in Troldborg and Meyer Forsting (2017) is applied to account for this effect. The two-dimensional model defines the wind speed in the induction zone as follows:

$$U = U_0 \left[1 - a_0 \left(1 - \frac{\tilde{x}_u}{\sqrt{1+\tilde{x}_u^2}} \right) \left(\frac{2}{\exp(+\beta\epsilon) + \exp(-\beta\epsilon)} \right)^{\alpha_i} \right], \tag{6.4}$$

where $\tilde{x}_u$ is the positive upwind distance normalized by the rotor radius, a_0 is the induction factor at the rotor center area defined as $a_0 = 0.5(1 - \sqrt{1-\gamma c_t})$, $\epsilon = \tilde{r}/\sqrt{\lambda(\eta + \tilde{x}_u^2)}$, $\tilde{r}$ is the radial distance from the hub normalized by the rotor radius, and c_t is the thrust coefficient. The other parameters are $\gamma = 1.1$, $\beta = \sqrt{2}$, $\alpha_i = 8/9$, $\lambda = 0.587$ and $\eta = 1.32$. The model has already been used to correct lidar measurements in the induction zone by Dimitrov et al. (2019) and Conti et al. (2020).

The time series of the meandering and the horizontal displacement of the wake are determined with the help of a Gaussian fit in accordance with Trujillo et al. (2011) and explained in detail in Section 6.1.2. Determining the measured mean wind speed deficit in the HMFR for lidar-assisted load simulation can be summarized as follows:

1. Correction of the measured wind speed by the induction zone model according to Troldborg and Meyer Forsting (2017).

2. Fitting of a Gaussian curve to the wind speed distribution along the horizontal direction determined by a measured horizontal line scan and determination of the horizontal displacement of the wake.

3. Transfer of the measured wind speed deficit to the HMFR by shifting the scan points according to the determined displacement.

4. Interpolation of the scanned wind speed deficit in the HMFR to a regular grid.

5. Repetition of steps 1 to 4 until a certain number of scans is reached (e.g. approx. 37 for a 10-minute time series).

6. Calculation of the mean wind speed deficit in the HMFR from all scans.

7. Fitting of the measured mean wind speed deficit to the Bastankhah wake model described in Bastankhah and Porté-Agel (2014).

It should be highlighted that always the closest available measured range gate, which is still outside the rotor area of the downstream turbine, is used to determine the inflow wind speed deficit. Furthermore, the fourth step of interpolating the wind speed deficit to a regular grid is mandatory given that the horizontal displacements differ at each instant in time and, thereupon, the measurement points are transmitted to a different location in the HMFR, so that the sixth step of calculating a mean wind speed deficit over all scans is only possible after interpolating all scans to the same regular grid (Section 6.1.2).

An example of the measured and simulated time series of the meandering is shown in Figure 6.7. It depicts the measured time series of the meandering as well as the one simulated with the Keck-c model and a random turbulence seed. To incorporate the time series of the meandering in the wake and load simulations, the time series has been cubically interpolated, so that a smooth meandering could be included in the wake model and the turbine loads are not increased by an immediate change of the position of the wind speed deficit. The interpolated time series of the meandering is denoted as DWM-meas. The comparison of simulations and measurements shows that the amplitude of the measured time series is slightly more pronounced. Furthermore, at the low frequency part the energy content from the measurements is higher as illustrated in the power spectrum of the meandering in Figure 6.8. A reason could be that the meandering is modeled based on the ambient wind speed although the wind speed in the wake is reduced. Applying a reduced mean wake wind speed in the meandering calculation procedure would lead to a higher deflection of the wake. It should also be highlighted that only a certain measurement frequency could be reached due to the lidar specifications outlined in Table 3.3, so that it might be the case that some parts of the meandering could not be captured by the measurements.

An example of a measured wind speed deficit over the radial distance from the hub center in the HMFR in comparison to the simulated one with the recalibrated DWM model is illustrated in Figure 6.9. The ambient conditions (ambient wind speed U_0, ambient TI I_0, wind shear α and wind direction θ) are defined in the title of the figure. The edges of

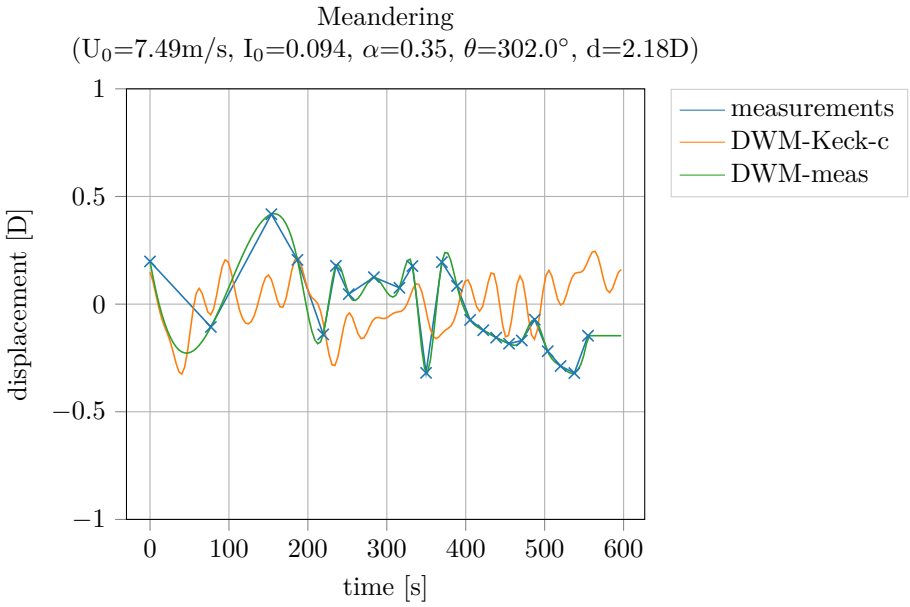

Figure 6.7: Time series of the meandering; measured and simulated with the calibrated DWM-Keck-c model as well as the interpolated time series (DWM-meas) (Reinwardt et al. 2021).

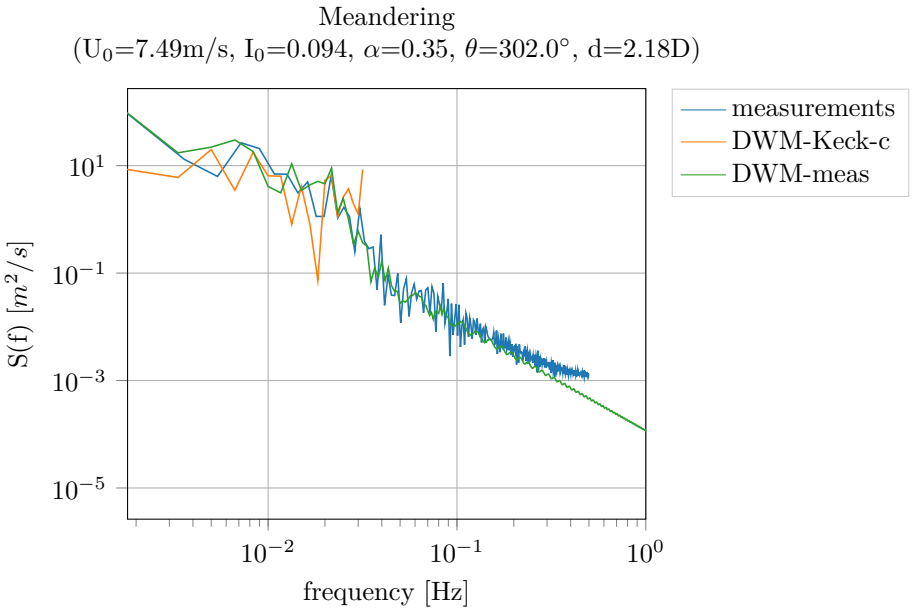

Figure 6.8: Power spectrum of the meandering; measured and simulated with the calibrated DWM-Keck-c model as well as the interpolated time series (DWM-meas) (Reinwardt et al. 2021).

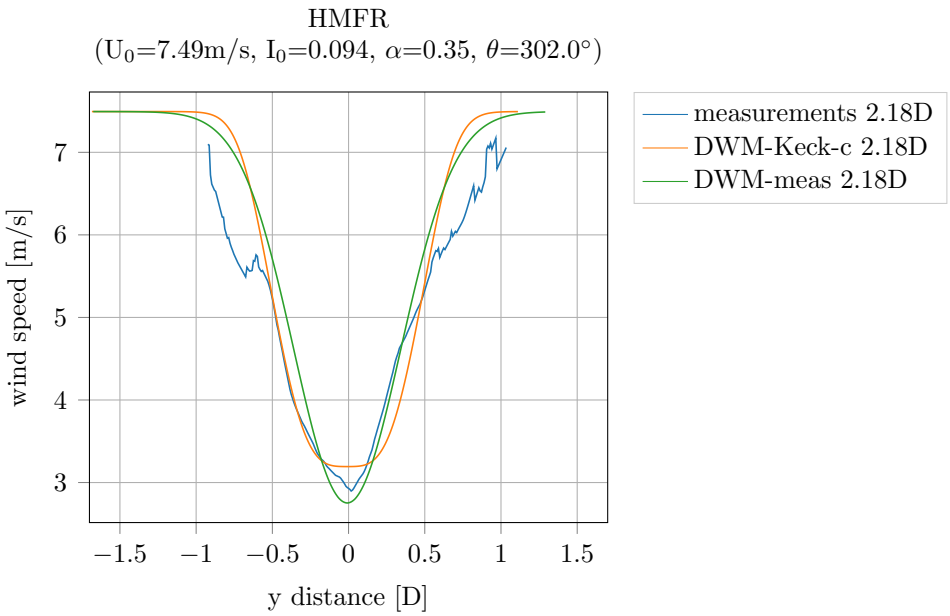

Figure 6.9: Wind speed deficit in the HMFR; measured and simulated with the calibrated DWM-Keck-c model as well as fitted to a Gaussian shaped wake model (DWM-meas) (Reinwardt et al. 2021).

the measured deficit are coarser than the area close to the center of the deficit given that many scan points are gathered around the center of the wind speed deficit and only a few at the tails, so that the influence of turbulence at the tails is much higher. Thus, the measured wind speed deficit shows a coarse distribution at the boundaries of the deficit. Using this coarse curve and replacing the wind speed deficit description in the DWM model directly by the measured one leads to increased loads in the simulation, which are not feasible, whereby the measured wind speed deficit has to be fitted to a smooth curve before applying it in load simulations. Furthermore, the lidar system only measures an opening angle of $-20°$ to $20°$. Hence, particularly for short distances the deficit is not captured exhaustively. Even the ambient wind speed is not reached at the edges of the curve, thus it is necessary to extrapolate the wind speed to smoothly meet the ambient wind speed. As a result of these issues, the measured deficit has been fitted to a simple Gaussian shaped wake model (Bastankhah model) outlined in Bastankhah and Porté-Agel (2014). A description of the model can be found in Section 2.3.1.3. The wake growth rate k^* in the model definition has been adjusted to fit the model to the measured deficit in the HMFR. The fitted model is labeled “DWM-meas” in Figure 6.9.

Chapter 7

Validation of wake models

The following chapter presents a validation of different versions of the DWM model. The original model definition as well as the recalibrated one are compared to lidar as well as load measurements at the two analyzed wind farms. Furthermore, different approaches to handle multiple wakes in the DWM model definition are evaluated and compared to measurements. Finally, the extension of the DWM model towards a static model version is compared to the recalibrated DWM model as well as the Frandsen model.

7.1 Curslack wind farm

7.1.1 Single wakes

7.1.1.1 Comparison with lidar measurements

The following section compares the measured wind speed in the wake to the modeled one. Some of the results in this section have been published in Reinwardt et al. (2020a). Parts of this publication are taken over in this section. Both lidar systems, introduced in Section 3.1, were used to collect the data. The results of the meandering time series over 10 minutes are exemplarily shown in Figure 7.1**(a)**. The maximum displacement of the wake is about $0.5D$, which is equivalent to 58.5 m. The results are derived from a 10-min. time series with an ambient wind speed of 6.44 m/s and an ambient TI of 11.7 %. Some of the met mast detected ambient conditions (wind speed U_0, TI_0, wind shear α and wind direction θ) are given in the title of the figure. The corresponding mean wind speed deficit is illustrated in Figure 7.1**(b)**. The wind speed decreases to less than 3 m/s in full wake situations. As already seen in the lidar simulations and explained in Section 6.1.3, the tails of the curve are relatively coarse since fewer scan points were gathered. It can also be seen that the ambient wind speed is not even reached at the edges of the curve. The opening angle of the scan appears too small to capture the whole wake at this distance. Towards the left part of the wind speed deficit (at negative y distances) a larger part of the wake is captured. This arises from the fact that the horizontal displacement of the wake is more often positive than negative and, therefore, more measurement results are collected towards the left part of the wind speed deficit curve.

The lidar system used is capable of simultaneously measuring several range gates in 30 m intervals. The results of all detected range gates for the data set presented in

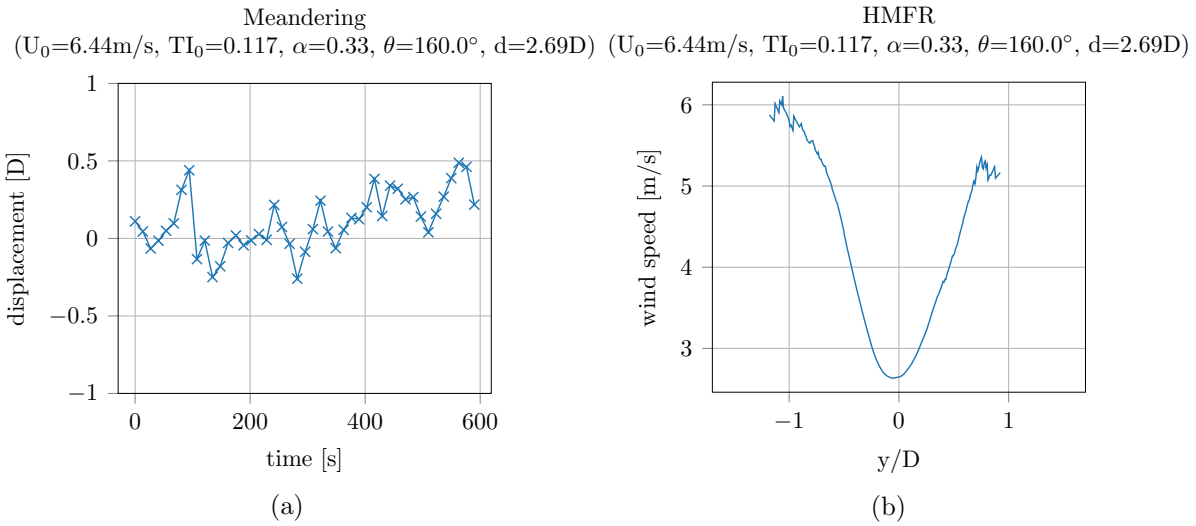

Figure 7.1: Meandering time series **(a)** and wind speed deficit in the HMFR **(b)** at $2.69D$ downstream of the turbine (Reinwardt et al. 2020a).

Figure 7.1 are shown in Figure 7.2**(a)**. The closest distance is $1.92D$ downstream and the farthest is $6.28D$. The degradation of the wind speed deficit in downstream direction is clearly identifiable. As for the single distance case (Figure 7.1), for most range gates a broader database is captured at the left part of the wind speed deficit, resulting in smoother curves. The presumption of an insufficient opening angle of the scan proves correct, as previously stated. With increasing downstream distances, the wind speed deficits captured reach closer to integrity. A broader scan angle would result in more detailed wind speed deficits for close downstream distances at the expense of far distances, where the scan points might not capture a sufficient number of points inside the deficit and thereby prevent a successful Gaussian fit. Furthermore, additional scan points at the edges can lead to a better representation of the deficit, but would also increase the scan time. According to Equation (2.89), the meandering corresponds to frequencies lower than approximately 0.028 Hz considering a wind speed of 6.5 m/s and a rotor diameter of 117 m. This means that, considering the Nyquist–Shannon sampling theorem, the scan frequency must be higher than twice the meandering frequency of 0.028 Hz, which results in a necessary scan time of less than 18 s. The scan time for the current usage of eleven scan points is already at about 16 s (depending on the visibility conditions), which is close to the limit of 18 s. Thus, with an increased number of scan points it is no longer ensured that the meandering can be captured.

Figure 7.2**(b)** illustrates the wind speed deficit in the HMFR measured under different ambient conditions. The corresponding meandering time series and wind speed deficit for this measured time series at a distance of $2.69D$ downstream of the turbine is given in Figure B.1 in the appendix. The wind shear is fairly high ($\alpha = 0.7$) and the ambient TI is very low ($TI_0 = 2.4$ %), which indicates stable atmospheric conditions. Due to the low TI it remains possible to see the w-shape of the wind speed deficit at closer distances. The typical w-shape is caused by the low axial induction in the area of the nacelle. Further downstream, the wake becomes more Gaussian shaped. At a horizontal distance of about

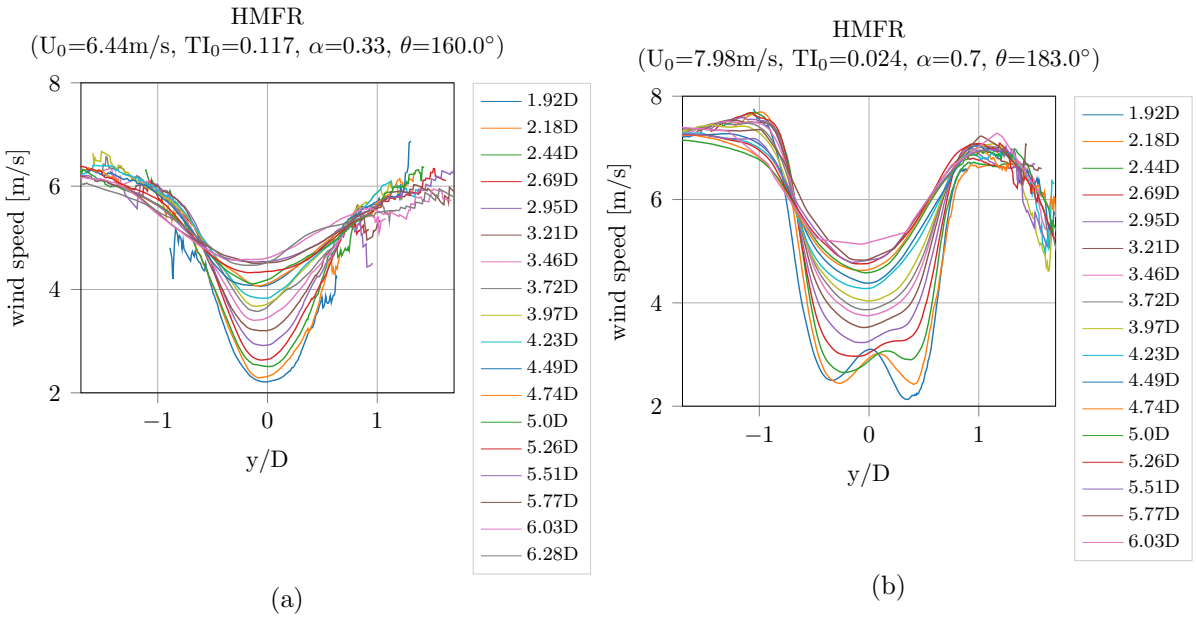

Figure 7.2: Wind speed deficit in the HMFR for an ambient TI of 11.7 % **(a)** and an ambient TI of 2.4 % **(b)** (Reinwardt et al. 2020a).

$1.5D$ from the wake center, the wind speed decreases on the right side. The reason is the wake of other turbines in the wind farm. The mean wind direction in this time series is 183° and the measurements are taken at WTG 1, so it could be either the influence of the wakes of WTG 2 or WTG 4. The associated results of the mean wind speed deficit in the FFR are illustrated in Figure 7.3. The curves in the FFR are less smooth than the wind speed deficit in the HMFR, simply because only eleven points are scanned and no interpolation is necessary when calculating the mean wind speed over the whole time series. Comparing Figures 7.2 and 7.3, it becomes apparent that the wind speed deficit in the FFR is less pronounced. Furthermore, for the lower TI the w-shape of the wind speed is not visible, since it vanished due to the meandering.

Similar results as exemplarily shown in Figures 7.2 and 7.3 have been collected for a multitude of different ambient conditions. The number of measured time series per TI and wake generating turbine, on which the lidar system is installed, is listed in Table 7.1. The TI is binned in 2 % steps. Column 1 of Table 7.1 specifies the mean values for each bin. Most of the measurement results are collected at low to moderate TIs ($TI_0 = (4-10)$ %). Only a few results could be extracted at higher TIs. The results include time series with an ambient wind speed of 5 m/s to 8 m/s. In this range, both turbines operate under optimal and most efficient conditions resulting in maximum energy output from the wind. The thrust coefficient is constant in this region (see Figure 3.3). Therefore, the axial induction and the wind speed deficit normalized by the turbine's inflow wind speed are also expected to be constant for similar ambient conditions over this wind speed range. For the single TI bins and both turbine types, simulations with different DWM models are carried out applying the same axial induction over the whole wind speed range. A scatterplot of the shear exponent and the ambient TI determined by the met mast is given in Figure 7.4. It includes all used datasets. At lower TIs, the shear spreads quite a lot,

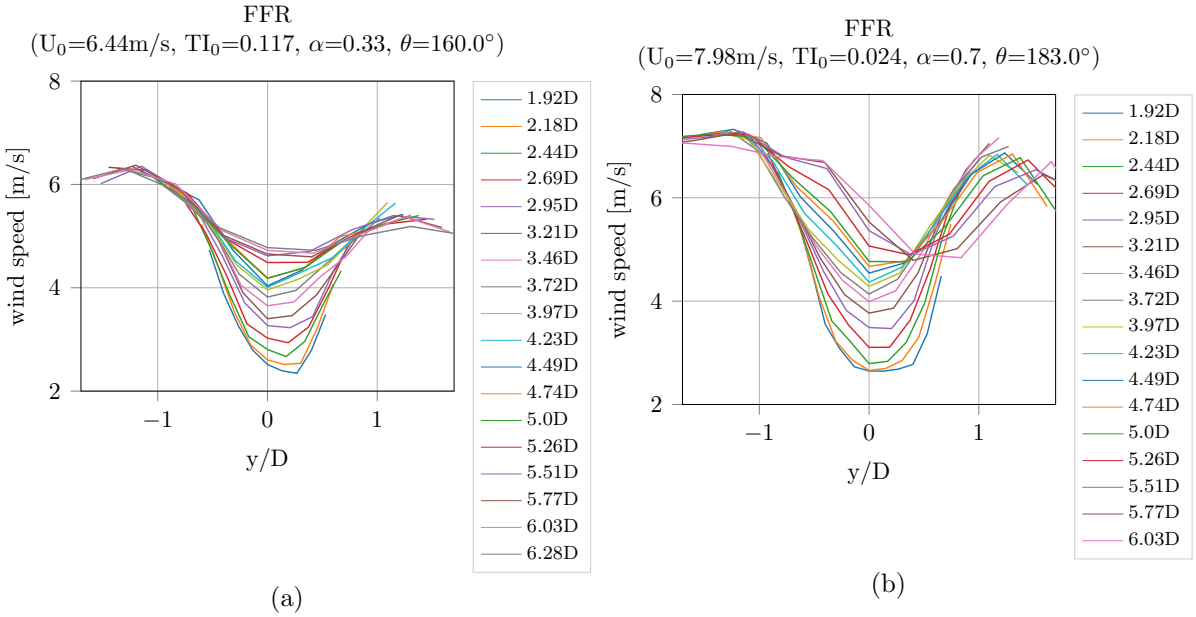

Figure 7.3: Wind speed deficit in the FFR for an ambient TI of 11.7 % **(a)** and an ambient TI of 2.4 % **(b)** (Reinwardt et al. 2020a).

Table 7.1: Number of measured and considered data sets per ambient TI for the lidar systems on WTG 1 and WTG 2 (Reinwardt et al. 2020a).

TI_0 [%]	WTG 1	WTG 2
4	23	28
6	8	11
8	23	14
10	11	9
12	13	4
14	0	0
16	1	1
18	1	2
20	1	3
22	0	2

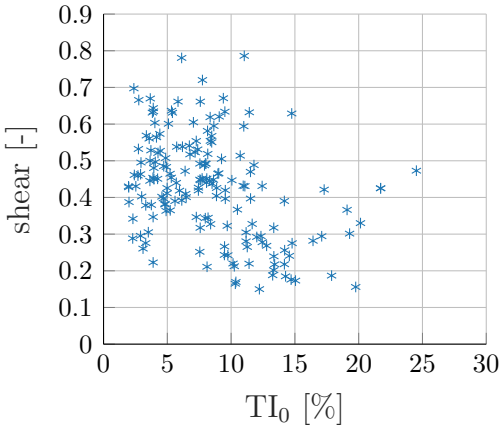

Figure 7.4: Shear exponent over the ambient TI for all considered data sets (Reinwardt et al. 2020a).

whereas towards higher TIs the shear decreases as expected.

Figure 7.5 summarizes all measured wind speed deficits in the HMFR. It demonstrates

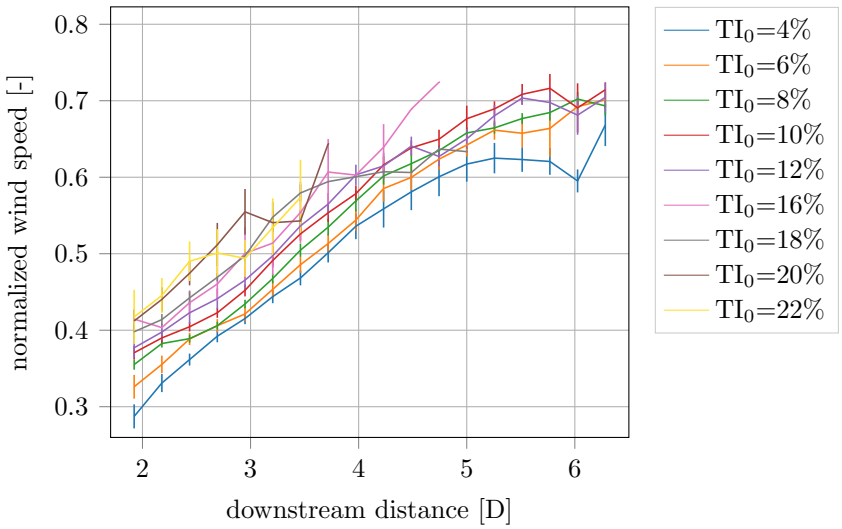

Figure 7.5: Measured mean value (line) and standard deviation (bar) of the mean value of the minimal wind speed in the HMFR for different TI bins with a bin width of 2 % (Reinwardt et al. 2020a).

the mean value and the standard deviation of the mean for all captured turbulence bins plotted against the downstream distance. Each value is related to the minimum value of the wind speed deficit, which itself is normalized by the inflow wind speed. It should be noted that in some distances only one value satisfies the filtering and plausibility checks (see Section 6.1.4), whereby the error bar is omitted. Additionally, it is highlighted that the plotted values always refer to the minimum value of a wind speed curve and not necessarily to the velocity in the wake center. Therefore, no increase of the wind speed at low downstream distances on account of the w-shape is visible as it could be seen in Figure 4.3. Figure 7.5 illustrates very well that the lowest degradation of the wind speed deficit occurs at the lowest TI. Up to a TI of 10 %, the degradation of the wind speed deficit continuously rises, leading to increasing minimum wind speeds at nearly all downstream distances. Above 10 % TI, the case is less clear. Especially at larger downstream distances, the measured normalized minimum wind speed is observed to fall below the corresponding lower TI bin. A possible explanation is the reduced number of measurement results in these bins and the higher uncertainty that comes along with it (expressed as error bars). Furthermore, discrepancies in the determined ambient TI at the met mast location and the actual TI at the wake position could lead to a misinterpretation of the lidar measurements. The farthest distance between the met mast and the location measured by the lidar system that occurs in the analyzed sectors is about 1200 m. With an ambient wind speed of 6.5 m/s, this leads to a wake advection time of 185 s. Thus, even at worst conditions, the measured ambient conditions at the met mast should be valid for the measured wakes from the lidar system most of the time. Furthermore, there is no complex terrain at the site, so it can be assumed that the conditions do not change with the wind direction. In addition, the agreement between measurements and simulations of the original DWM-Keck model is already good in the higher TI bins (see Figure 7.6).

Thus, the recalibration of the DWM model has been developed in a way that it affects only the lower TI bins, while the influence of the calibration on higher TIs is negligible (see Figure 7.6). This in turn means that the regions with low amount of data sets have a negligible influence on the recalibration of the model. Therefore, even though there are some discrepancies, the faster recovery of the wind speed deficit due to the higher ambient TI can be verified and the measurements are reliable for the outlined investigation. Thus, it is valid to use these measurement results for comparisons with DWM model simulations and the recalibration of the DWM model.

Figure 7.6 compares the measured normalized minimum wind speed in the wake to DWM model simulations for different TI bins, starting at a low TI of 4 % and ending at 22 %. The simulations were carried out for a specific downstream distance, which corresponds to the center of the range gate of the lidar system. It should be noted that the wind speeds measured by the lidar system can be interpreted as a mean value over the whole range gate. However, the wind speed gradient in axial direction is low and the wind speed distribution in this direction almost linear at the observed downstream distances. Furthermore, in the DWM model, the discretization step size in downstream direction is 23.4 m (equivalent to $0.2D$), which is in the same order as the range gate of 30 m. Therefore, a valid comparison between simulations and measurements is carried out. The wind speed deficit simulations in the HMFR obtained by the DWM models also include the vertical meandering to ensure a correct comparison between measurements and simulations. Three different simulation results with varying definitions of the initial deficit and eddy viscosity description are illustrated. The method called "DWM-Egmond" is based on the definitions of Madsen et al. (2010) and Larsen et al. (2013) and the "DWM-Keck" method is adopted from Keck (2013) (see Section 2.3.1.5).

Figure 7.6 shows that the DWM-Egmond method strongly overestimates the wind speed deficit for all downstream distances and all TIs. The simulated minimum wind speed with the DWM-Keck method is in better agreement with the measurement results. This confirms the results in Reinwardt et al. (2018). Especially at higher TIs (Figure 7.6**(e-i)**) the results of the DWM-Keck model agree very well with the measurements. For lower TIs and larger distances (greater than $3D$) there is a relatively large discrepancy between measurements and simulations. A similar observation was made in Larsen et al. (2013) with the model version of Madsen et al. (2010). The recalibrated DWM model is called "DWM-Keck-c" (see Figure 7.6).

The recalibration of the DWM model and accordingly the normalized eddy viscosity definition in the DWM model are based on a least-squares fit of the minimum of the simulated normalized wind speed to the minimum of the measured normalized wind speed for several downstream distances. The definition of the eddy viscosity along with the recalibrated parameters are explained in detail in Section 2.3.1.5 and Chapter 4. For the recalibration, the measurement results are divided into 2 % TI bins. All measurement results from Figure 7.5 containing data sets from two different turbines are used for the recalibration. The first turbine is a N117 turbine with 3 MW and the second one is a N117 with 2.4 MW. DWM model simulations were carried out for both turbine types, since the axial induction of both turbines is slightly different under partial load conditions. To calculate a mean value of the simulated minimum wind speed and thus allow a comparison with the results in Figure 7.5, simulations are carried out for each TI bin and weighted in

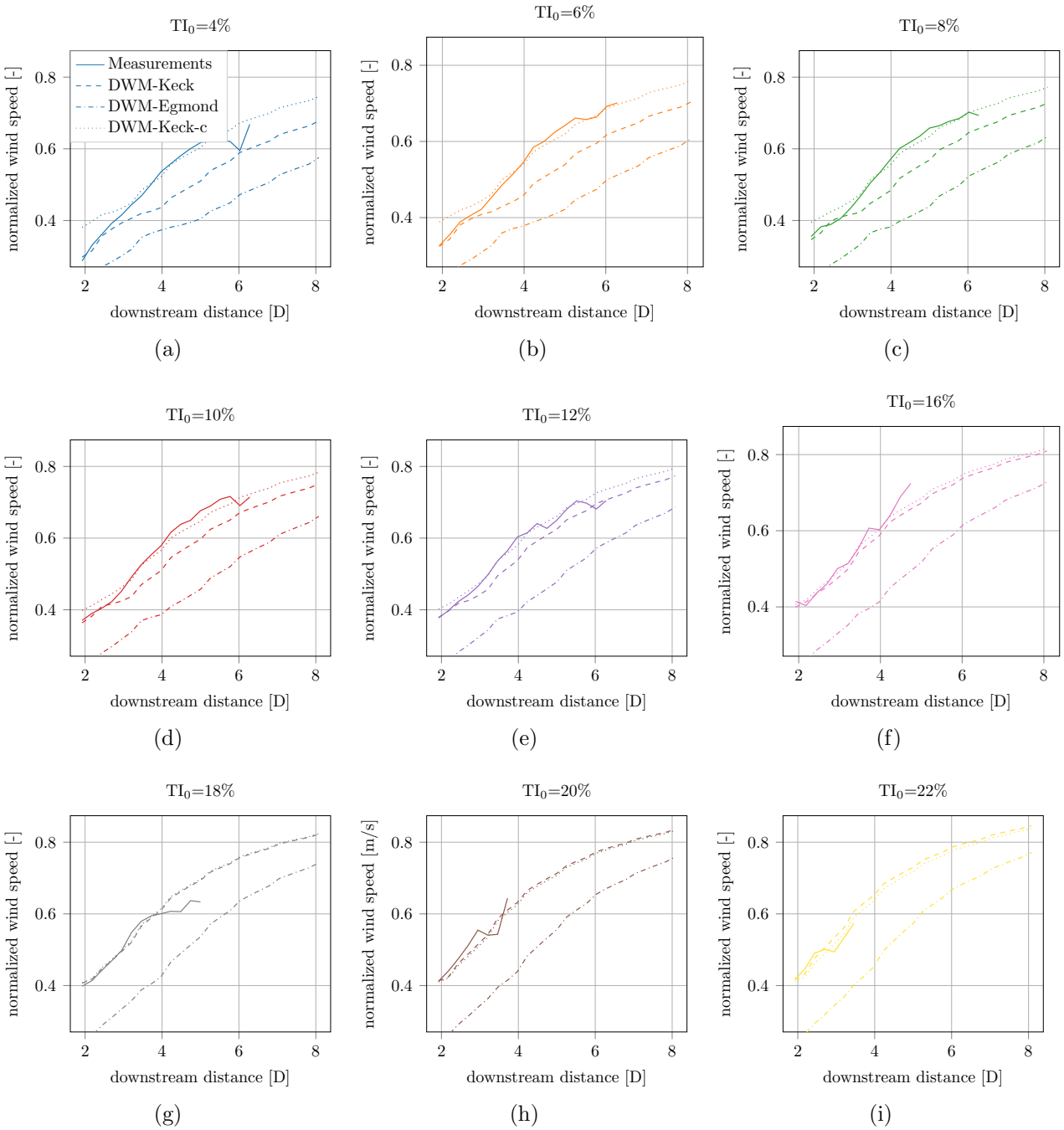

Figure 7.6: Comparison of measurements and simulations of the minimum wind speed deficit in the HMFR for different TIs according to Reinwardt et al. (2020a). The solid, the dashed and the dashed dotted line reflect the measurement, the results of the DWM-Keck model and those of the DWM-Egmond model, respectively. The recalibrated model is denoted DWM-Keck-c and depicted as dotted line.

accordance with the number of measurement results per turbine listed in Table 7.1. Thus, for example at the ambient TI bin of 4 %, the mean value of the simulated minimum wind speed comprises the sum of the simulated minimum wind speeds weighted by 0.451 and 0.549, the weighting factors for WTG1 and WTG2, respectively. Nonetheless, this weighting has only a marginal influence on the overall results, because the axial induction in the considered wind speed range (5 m/s to 8 m/s) is very similar for these two turbine types (see also thrust and power curves in Figure 3.3).

The results of the recalibrated DWM model coincide very well with the measurements. In particular, the results for lower TIs could clearly be improved (see Figure 7.6**(a-d)**). For higher TIs, the influence of the recalibration is less significant and the already good agreement between simulation and measurement results remains unchanged (see Figure 7.6**(e-i)**). Only at the lowest downstream distances and TIs up to 12 %, the recalibrated model delivers higher deviations than the original model. For downstream distances larger than $3D$, the recalibrated model leads to more than 10 % lower deviations from the measurements than the original model. For TIs higher than 16 %, the deviation between the recalibrated and original model is smaller than the uncertainties in the measurements. Hence, no further conclusions about improvements can be made. The uncertainties due to misalignments could be up to 6 % (see also the data filtering in Section 6.1). Furthermore, the LOS accuracy of the lidar system itself is about 1.5 % at a wind speed of 6.5 m/s (see Table 3.3). The root-mean-square error (RMSE) between the measured and simulated normalized minimum wind speed is collected for all analyzed TI bins in Figure 7.7. A clear improvement of the results due to the recalibrated model version up to an

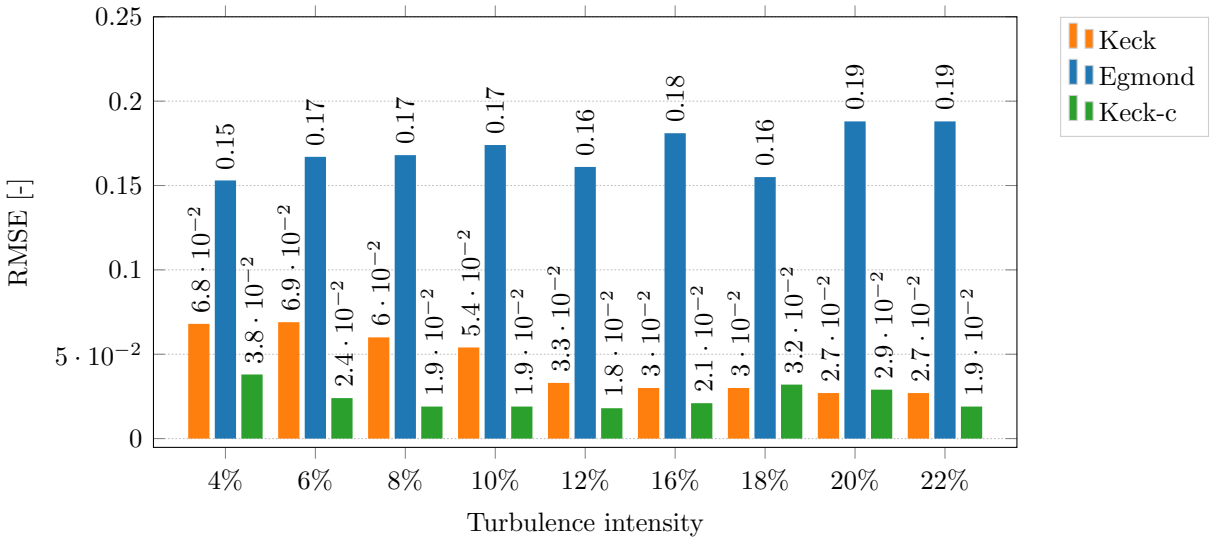

Figure 7.7: RMSE between the lidar-measured and the simulated normalized minimum wind speed in the wake (Reinwardt et al. 2020a).

ambient TI of 16 % is visible. For higher TI bins, the RMSE of the recalibrated and the original DWM-Keck model version are similar. The DWM-Egmond model delivers significantly higher RMSEs than the other model versions for all TI bins.

To compare the complete curve of the simulated and measured wind speed deficit in

the HMFR, two examples of a high and a low TI case are illustrated in Figure 7.8 and 7.9. The measurement results of these two 10-min time series have already been depicted as

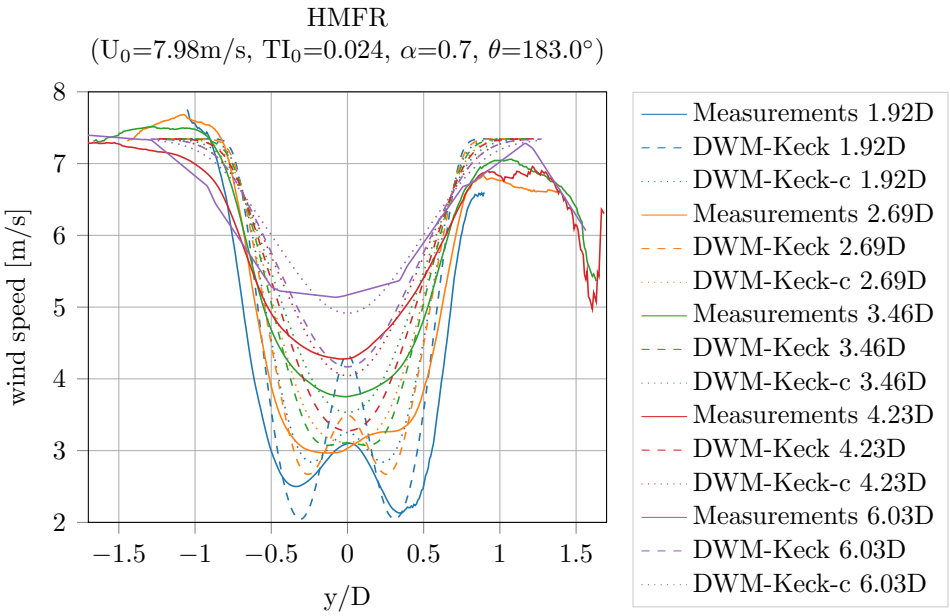

Figure 7.8: Comparison of the measured and simulated wind speed deficit in the HMFR for an ambient TI of 2.4 %.

an example in Figure 7.2. Measurements and simulations for five different downstream distances are shown. The simulations were carried out with the original DWM-Keck and the recalibrated DWM model. Both figures prove a very good agreement between the measurements and the results predicted by the DWM-Keck-c model. The wind speed gradient in radial direction, which is together with the meandering highly relevant for the loads of the downstream turbine, is estimated well. In the case of a low ambient TI the w-shape at close distances is well predicted. For the higher TI case there is no significant difference between the two model versions over the complete wind speed deficit curve.

Another possibility to compare the different model versions over the complete wind speed deficit curve and quantify the performance over all data sets is to calculate a rotor-averaged mean wind speed, as undertaken in Figure B.2 in the appendix. A comparison between the simulated and measured mean wake wind speed over the rotor area is illustrated. The corresponding RMSE of all TI bins is depicted in Figure B.3 in the appendix. The improvement of the mean wind speed due to the model recalibration is less clear in comparison to the normalized minimum wind speed (compare Figure 7.7). Nonetheless, there is an improvement or results of equal quality are obtained in almost all TI bins. Since, at the tails of the wind speed deficit, the curves are coarse, less scan points are gathered and the influence of turbulence is much higher (see Figure 7.2). This leads to an error in the rotor-averaged mean wake wind speed but not in the minimum wind speed. This is the reason why the illustration of the minimum wake wind speed is more meaningful and the recalibration is based on the minimum wake wind speed instead of the rotor-averaged mean wind speed.

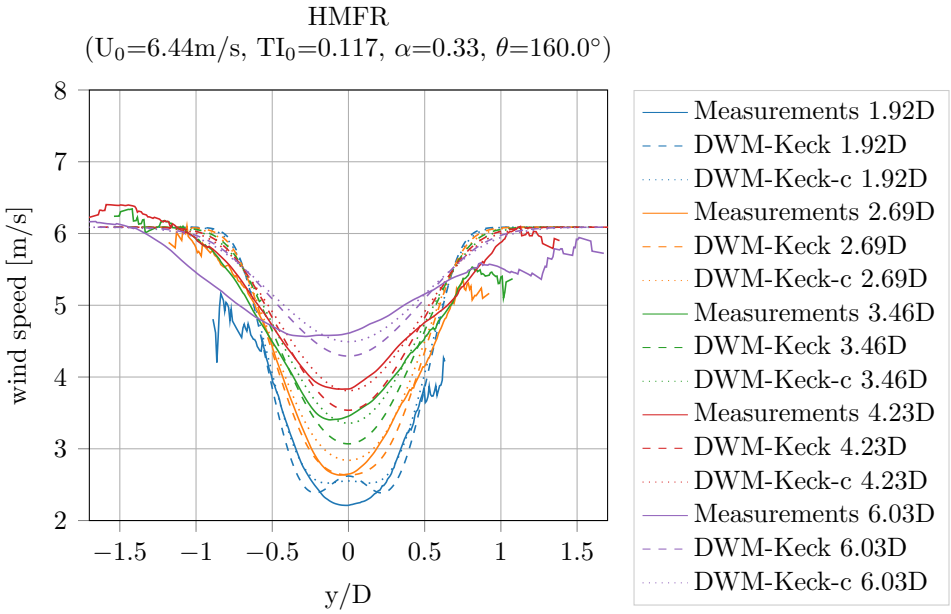

Figure 7.9: Comparison of the measured and simulated wind speed deficit in the HMFR for an ambient TI of 11.7 %.

7.1.1.2 Comparison with load measurements

The following section summarizes the measured and simulated fatigue loads under normal operating conditions for different wake sectors. A comparison of the original and newly calibrated DWM model regarding loads and power productions is outlined. The results of this section have been published in Reinwardt et al. (2021) and partly taken over. The ambient conditions for the simulations are determined by the met mast, so that only results with wake-free inflow at the met mast are included in the evaluation. The results of the measured and simulated normalized power deficit, where WTG 2 experiences the wake of WTG 1, are shown in Figure 7.10**(a)**.

The results are normalized by the measured power at wake-free inflow on the left side of the power deficit curve. The measurements were gathered during an ambient wind speed of 6 m/s and an ambient TI of 6 %. The number of measured 10-min time series in each wind direction bin is illustrated in the bar graph. The mean values and their corresponding standard deviations are illustrated for each wind direction bin, along with the number of considered measurements and simulations. Close to full wake, only a few measurement points could be collected, whereas towards the edges of the deficit more points could be gathered. The reason is that the deficit towards full wake is very pronounced and thus the inflow wind speed at the wake-affected turbine is often below the cut-in wind speed. All simulated power deficits agree very well with the measured deficit. There is a slight overestimation of the power deficit calculated by the DWM-Egmond model. Its predicted deficit is so pronounced that in full wake conditions the turbine often does not operate in the simulations. There is a slight decrease of the power above 320°, which marks the beginning of the wake of WTG 4.

The DELs of the flapwise blade root bending moment under wake conditions are illustrated in Figure 7.10**(b)**. The Wöhler coefficient is given in title of the figure. The

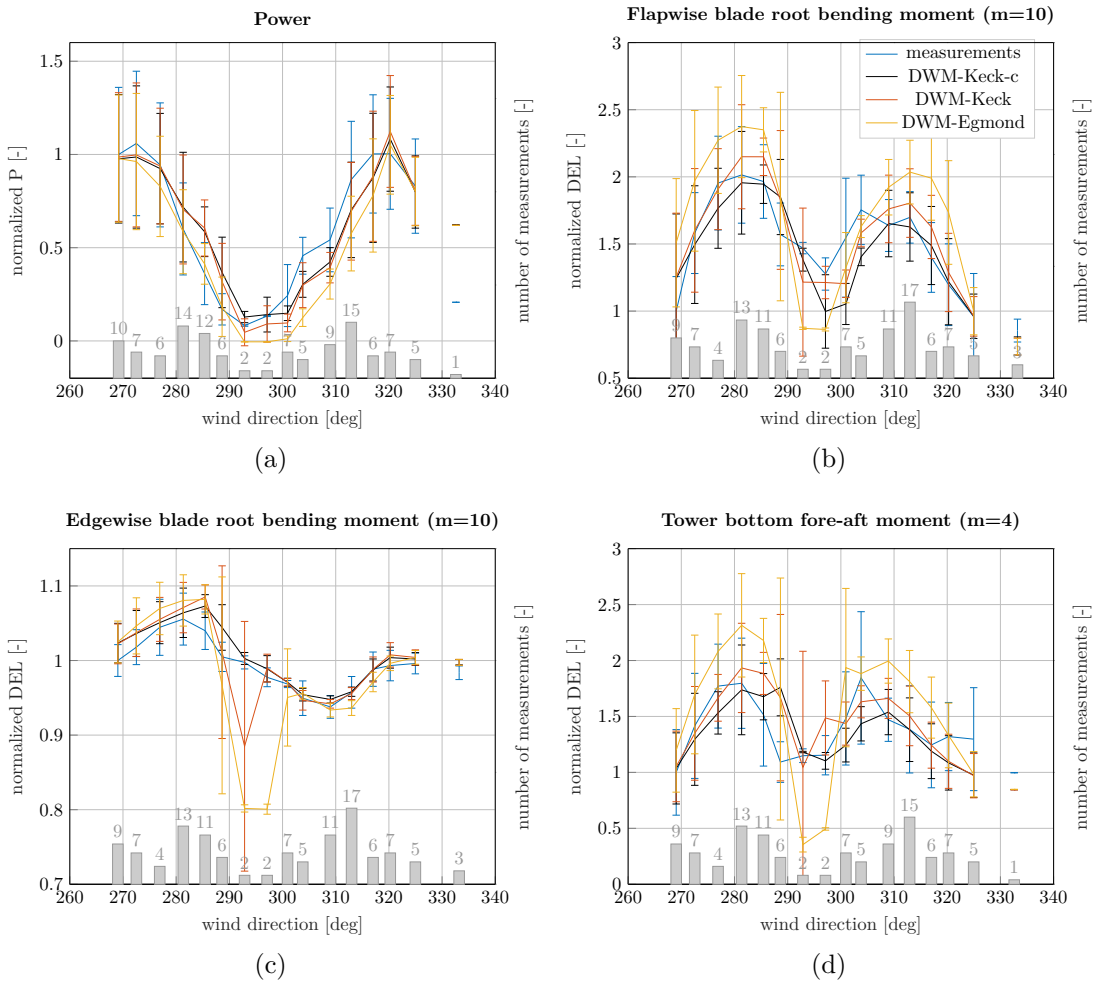

Figure 7.10: Measured and simulated power deficit **(a)**, flapwise blade root bending moment **(b)**, edgewise blade root bending moment **(c)** and tower bottom fore-aft bending moment **(d)** at WTG 2 at an ambient wind speed of 6 m/s and an ambient TI of 6 %. WTG 2 is exposed to the wake of WTG 1. The number of measured 10-min time series in each wind direction bin is illustrated on the secondary axis (Reinwardt et al. 2021).

flapwise fatigue loads agree very well with the measurements when using the DWM-Keck-c and DWM-Keck model, so that even the two maxima at partial wake conditions are in close agreement. The DWM-Egmond model overpredicts the loads especially at partial wake conditions. At partial wake, the wind speed deficit only affects a section of the rotor, so that in combination with the meandering and the horizontal shear of the wind speed, the blade experiences a highly alternating load at each rotation.

The two maxima are differently pronounced, which derives from the aerodynamic force and the rotor tilt. The aerodynamic forces on a blade segment are a function of the apparent wind velocity, which is a vector composed of the motion of the blade and the incoming wind. Due to the turbine tilt, the apparent wind velocity is slightly lower during the upward movement, and thus the aerodynamic force is reduced. The blade faces slightly away from the wind direction during the upward movement, whereas during the downward movement, the blade faces slightly more towards the wind direction, which results in an increase of the aerodynamic force. At wake conditions, the increase is stronger when the wind speed deficit coincides with the upward movement of the rotor, so that a higher alternating load at the blade occurs and the maximum is more pronounced in comparison to the case, in which the wind speed coincides with the downwind movement of the rotor. In order to explain this behavior, a schematic illustration of the phenomenon is depicted in Figure B.4 in the appendix.

The results of the edgewise blade root bending moment are depicted in Figure 7.10**(c)**. All models agree similarly well with the measurements. The edgewise moment depends significantly on the blade weight force, while the wake only has a marginal impact on the loads, so that the highest increase of the edgewise moment in comparison to wake-free inflow is merely about 5 %. Towards full wake, several outliers in the results of the DWM-Keck and DWM-Egmond model can be recognized. These are related to the simulations, where the turbine does not operate as a result of the low wake wind speed predicted by the models. The rotation of the rotor largely influences the alternating load of the edgewise moment. Hence, the fatigue load is drastically reduced when the turbine turns off. The simulations as well as the measurements show an increase of the load in comparison to the wake-free inflow at about 280° and even a decrease of the load at about 310°. The influence of the wind speed is not only related to the rotational speed of the rotor. There is an additional influence due to the tilt of the rotor. The load is defined in the rotating frame of reference, so that the weight force switches its sign with each rotation, whereas the influence of the aerodynamic force on the edgewise moment does not change the sign. Thus, at one side of the rotor the forces level each other out, while on the other side of the rotor they accumulate. If the deficit is on the side, where the forces level each other out, the alternating load increases in comparison to a situation without wake, whereas when the wind speed deficit is on the side, where both aerodynamic and weight forces are facing in the same direction, the alternating load is reduced. To clarify this explanation, a schematic illustration is provided in Figure B.5 in the appendix.

The tower bottom bending moment is illustrated in Figure 7.10**(d)**. The two maxima at partial wake conditions that derive from the higher alternating load observed in Figure 7.10**(b)** are also clearly visible for the tower bottom bending moment. At full wake conditions, the load is only slightly increased in comparison to wake-free inflow. Despite being similar to the flapwise bending moment, the tower bottom bending moment is al-

most doubled at partial wake conditions. The results of all three models agree well with the measurements. Only the DWM-Egmond model overestimates the loads as it could already be seen in the blade flapwise and edgewise bending moments.

A similar analysis as the one presented in Figure 7.10 is carried out for different TI bins and summarized in Figure 7.11. A comparison of the results of the flapwise bending moment over all TI bins is shown in Figure 7.11**(a)**. It illustrates the bias of the accumulated DEL over all wind directions. A negative value implies a lower value of the simulated accumulated DEL than the measured DEL. The accumulated DEL over all wind directions is calculated with respect to the Wöhler coefficient. A Wöhler coefficient of 10 is used for the blades and 4 for the tower loads as specified in the titles. The results for an ambient TI of 4 %, 8 %, and 12 % are based on the curves illustrated in Figure B.6 and B.7 in the appendix. Of all models, the recalibrated DWM-Keck-c model coincides best with the measurements over all TI bins. At small TIs, the DWM-Keck-c model underestimates the accumulated DEL slightly. The DWM-Egmond model overestimates the accumulated DEL drastically, especially at high TIs. The RMSE of the flapwise bending moment between the simulations and the measurements over the wind directions is given in Figure 7.11**(b)**. The RMSE of the DWM-Keck and the recalibrated DWM-Keck-c model are very similar, while the DWM-Egmond model delivers the highest RMSE. The reason for illustrating the deviation ΔDEL between measurements and simulations as well as the RMSE is that the deviation of the accumulated DEL expresses how accurate the models perform in a site-specific load calculation procedure. Additionally, it allows a comparison with the Frandsen wake-added turbulence model, whereas the RMSE represents the overall capability of predicting the distribution of the DELs over the wind direction. Note that the Frandsen model overestimates the DELs significantly throughout all TIs.

Figure 7.11**(c)** depicts the bias of the accumulated DELs of the edgewise blade root bending moment. The smallest deviation between the accumulated DELs is achieved with the DWM-Egmond model, but the difference between the models is very small, so that even the highest deviation with the DWM-Keck-c model is only about 1.4 %. The RMSE of the DWM-Keck-c model is the lowest (see Figure 7.11**(d)**). However, it should be highlighted that also the RMSE is very low in all cases. The results over different TI bins of the tower bottom fore-aft bending moment are shown in Figure 7.11**(e-f)**. Similar to the flapwise bending moment, the accumulated DELs over all wind directions calculated by the DWM-Keck-c model agree very well with the measurements. Again, only a slight underestimation occurs at small TIs. The DWM-Egmond model as well as the Frandsen wake-added turbulence model overestimate the accumulated DEL substantially. The RMSE of the recalibrated and the original model are low and have similar magnitudes. The DWM-Egmond model delivers the highest RMSE over all TI bins.

To evaluate the model behavior at different downstream distances further, load results at WTG 5 at an ambient wind speed of 8 m/s and an ambient TI of 10 % are analyzed. Considering the wind farm layout in Curslack, the following three wake situations including the wake at WTG 2 can be analyzed:

- WTG 2 in the wake of WTG 1 $\rightarrow$ turbine distance $= 2.51D$
- WTG 5 in the wake of WTG 2 $\rightarrow$ turbine distance $= 3.61D$

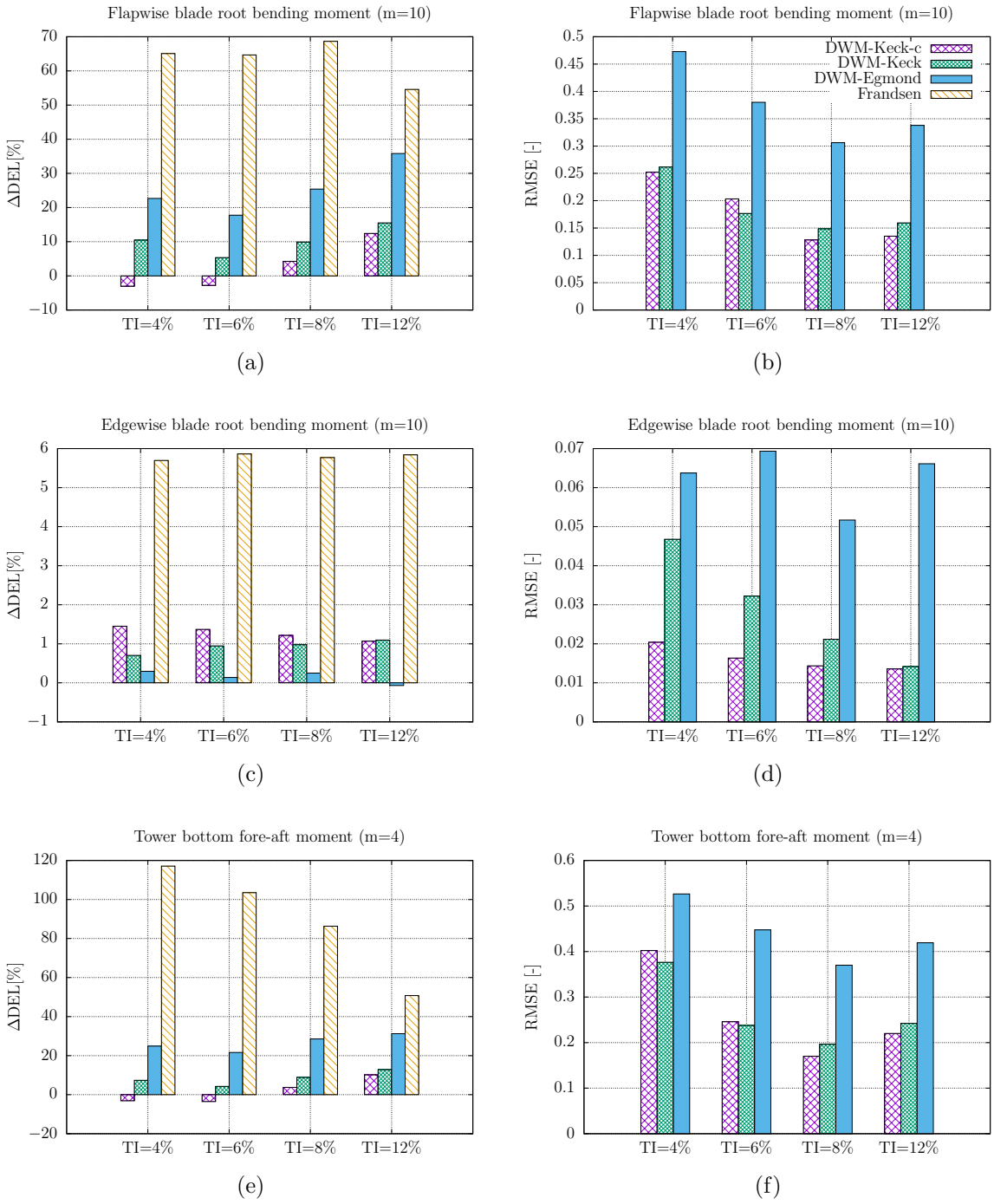

Figure 7.11: Bias between the measured and simulated fatigue loads and RMSE for the flapwise blade root bending moment **(a)** and **(b)**, the edgewise blade root bending moment **(c)** and **(d)** as well as the tower bottom fore-aft bending moment **(e)** and **(f)** at an ambient wind speed of 6 m/s. WTG 2 is exposed to the wake of WTG 1 (Reinwardt et al. 2021).

- WTG 5 in the wake of WTG 1 $\rightarrow$ turbine distance = $4.71D$

The results of the power deficit as well as the flapwise bending moment over the wind directions for these three different distances are shown in Figure 7.12. The plots display the mean value in each wind direction bin accompanied by the corresponding standard deviation as an error bar. The same DWM model versions as previously discussed are compared. The closest turbine distance of $2.51D$ shows the most pronounced deficit and vice versa. The predicted results of all models agree very well with the measurements, except the DWM-Egmond model overestimates the deficit, especially at the largest distance of $4.71D$.

The results of the edgewise blade root bending moments and the tower bottom bending moments are shown in Figure 7.13. The results of the recalibrated and original DWM-Keck-c models agree very well with the measurements over all distances. The DWM-Egmond model on the other hand mostly overestimates the loads, particularly at the highest distance of $4.71D$. The reason is that the degradation of the wake over the downstream distance is underestimated by this model.

The bias of accumulated DELs over all wind directions as well as the RMSE are depicted in Figure 7.14. The recalibrated DWM-Keck model delivers the lowest deviation and RMSE over all distances for the flapwise bending moment and the tower bottom fore-aft bending moment, whereas the edgewise blade root bending moment is not improved by the recalibration. However, as previously mentioned, the difference between the results of the single variations of the DWM model is very low for this load component, so that all models agree very well with the measurements of the edgewise moment with the exception of the Frandsen wake-added turbulence model. The reason for this is that no wind speed deficit is considered in Frandsen's model, so that the alternating load at the edgewise moment is higher due to the higher wind speed and the rotational speed of the rotor. The DWM-Egmond model overestimates the loads over all downstream distances. Towards greater downstream distances, the improvement due to the recalibration increases. Finally, the Frandsen model overestimates the loads over all distances, in particular for close distances.

Subsequent to the comparison between the different DWM model versions, the recalibrated DWM model is compared to a constrained simulation with lidar measurements of the meandering and the wind speed deficit. The method to incorporate the wind speed deficit in the HMFR as well as the meandering itself is explained in Section 6.3. Figure 7.15**(a)** shows the measured power deficit at WTG 2, when the turbine is exposed to the wake of WTG 1 at an ambient wind speed of 8 m/s and an ambient TI of 10 %. The blue solid curve with error bars is the measured mean power deficit with all measurement results that comply with the requirements for ambient conditions and the filtering criteria. Lidar measurements were not available for all collected data sets. The blue circles illustrate the 10-min time series, where lidar measurements are available. The stars denote the simulated 10-min series using the recalibrated version of the DWM model (DWM-Keck-c). The crosses represent the results when incorporating only the measured wind speed deficit in the HMFR fitted to the Gaussian shaped wind speed deficit model (DWM-Lidar), whereas the squares consider both the measured meandering and the wind speed deficit in the HMFR (DWM-Lidar-m). The RMSE between measurements (blue circles) and simulations are given in the legend. The recalibrated DWM model and the

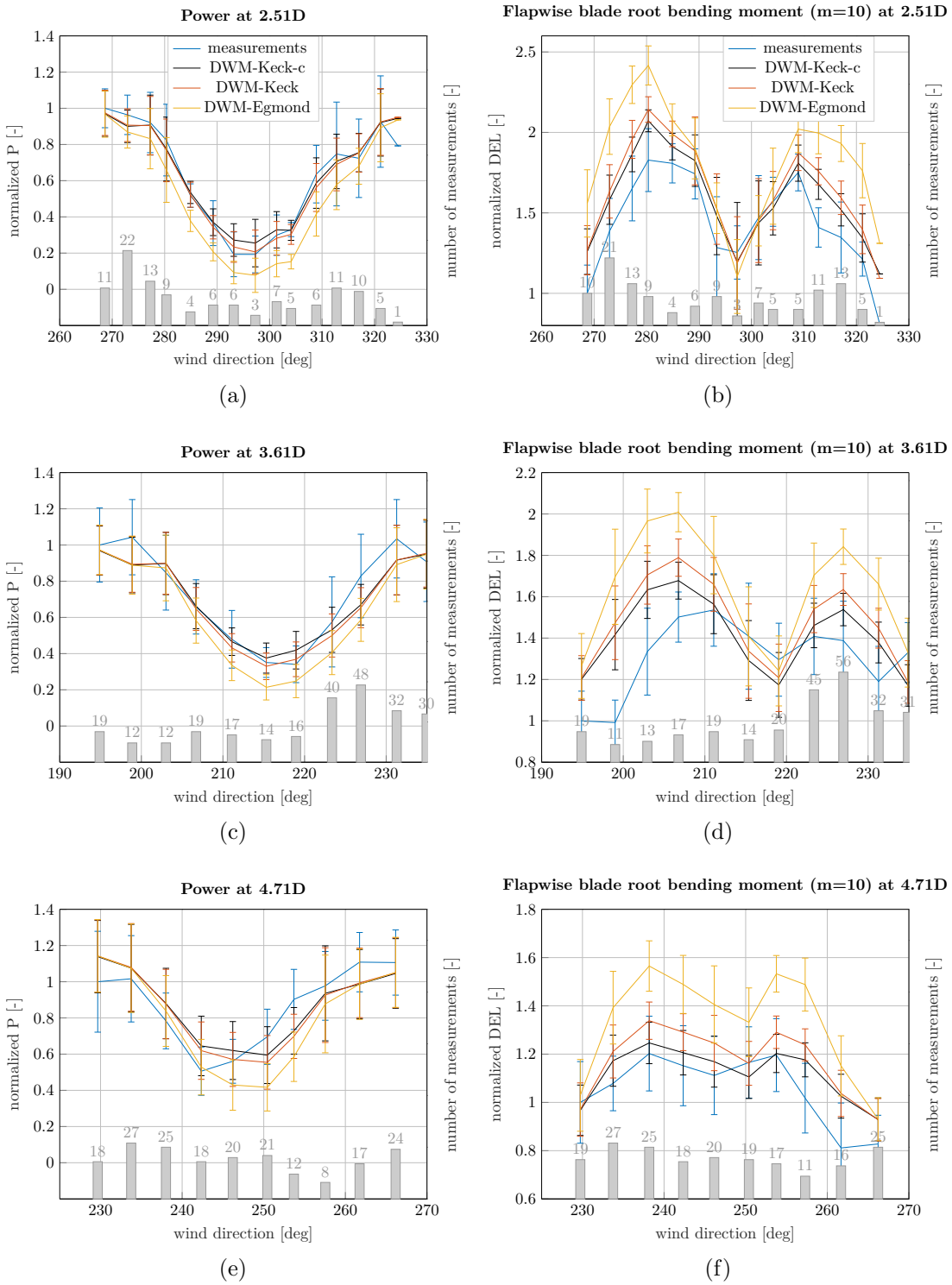

Figure 7.12: Measured and simulated power **(a)**, **(c)** and **(e)** as well as flapwise blade root bending moment **(b)**, **(d)** and **(f)** at an ambient wind speed of 8 m/s and an ambient TI of 10 % when WTG 2 is exposed to the wake of WTG 1 **(a)** and **(b)**, WTG 5 is exposed to the wake of WTG 2 **(c)** and **(d)**, and WTG 5 is exposed to the wake of WTG 1 **(e)** and **(f)**. The number of measured 10-min time series in each wind direction bin is illustrated on the secondary axis (Reinwardt et al. 2021).

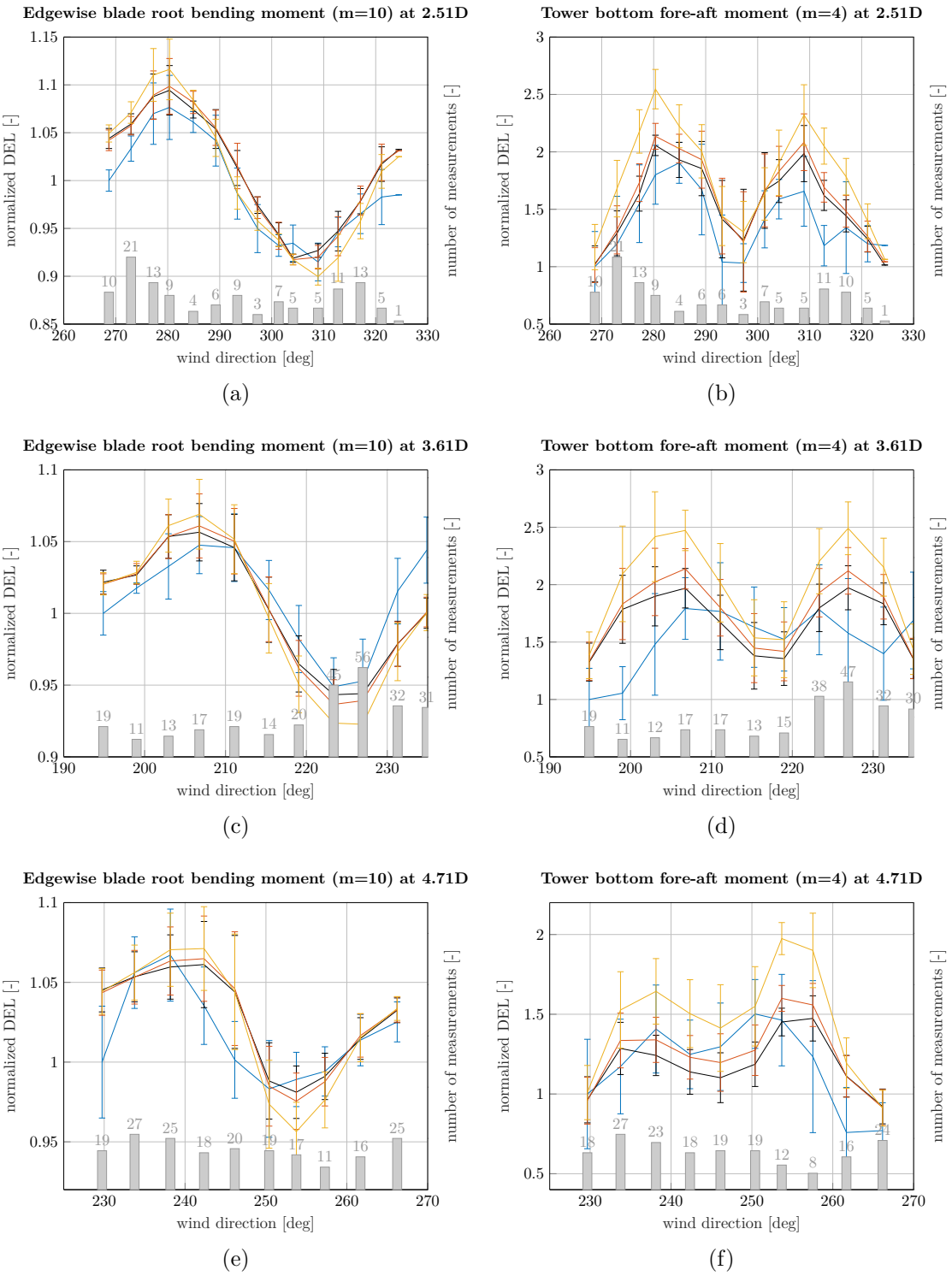

Figure 7.13: Measured and simulated edgewise blade root bending moment **(a)**, **(c)** and **(e)** as well as tower bottom fore-aft bending moment **(b)**, **(d)** and **(f)** at an ambient wind speed of 8 m/s and an ambient TI of 10 % when WTG 2 is exposed to the wake of WTG 1 in **(a)** and **(b)**, WTG 5 is exposed to the wake of WTG 2 in **(c)** and **(d)**, and WTG 5 is exposed to the wake of WTG 1 in **(e)** and **(f)**. The number of measured 10-min time series in each wind direction bin is illustrated on the secondary axis (Reinwardt et al. 2021).

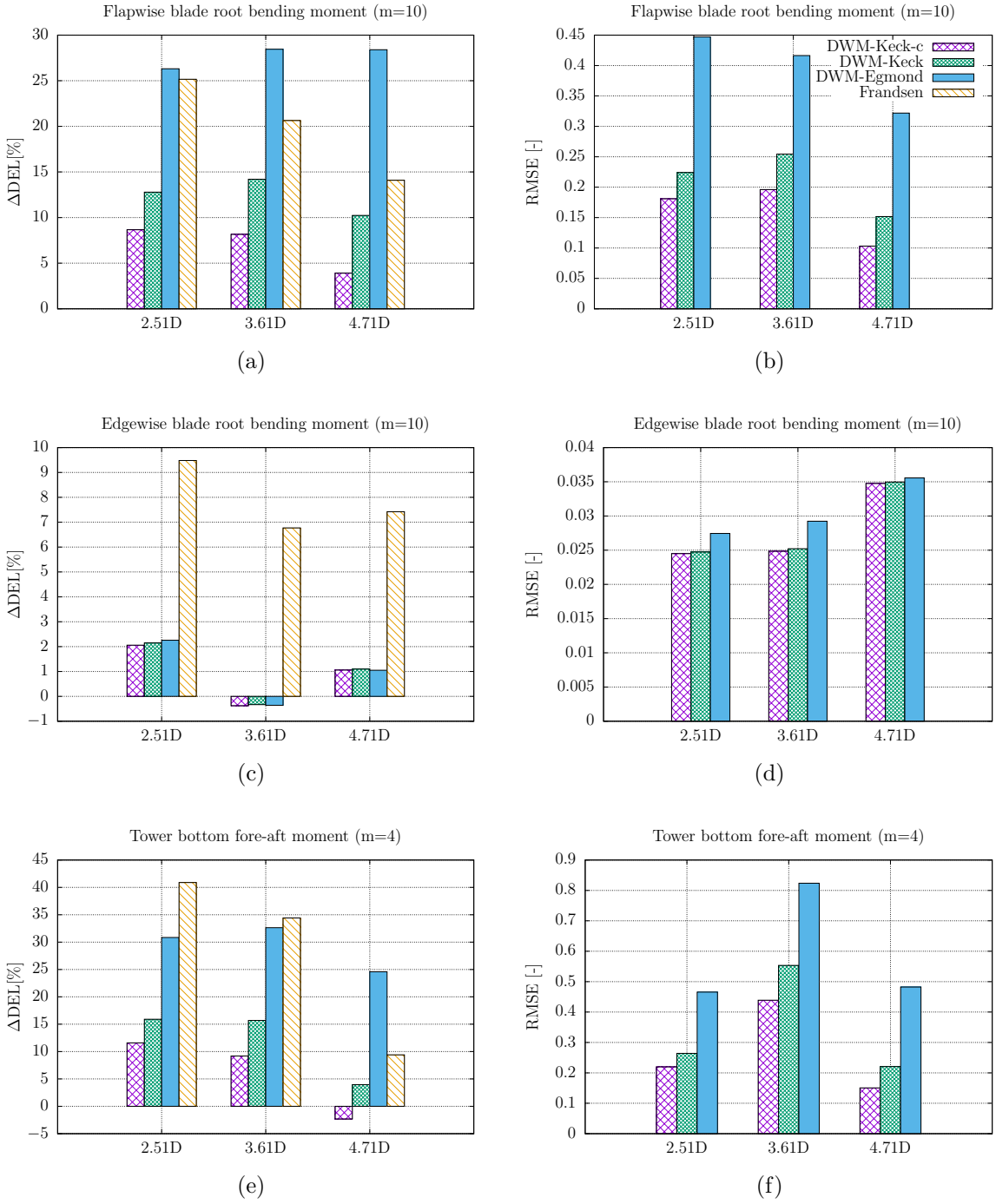

Figure 7.14: Bias between the measured and simulated fatigue loads and RMSE for the flapwise blade root bending moment **(a)** and **(b)**, the edgewise blade root bending moment **(c)** and **(d)**, as well as the tower bottom fore-aft bending moment **(e)** and **(f)** at an ambient wind speed of 8 m/s and an ambient TI of 10 % (Reinwardt et al. 2021).

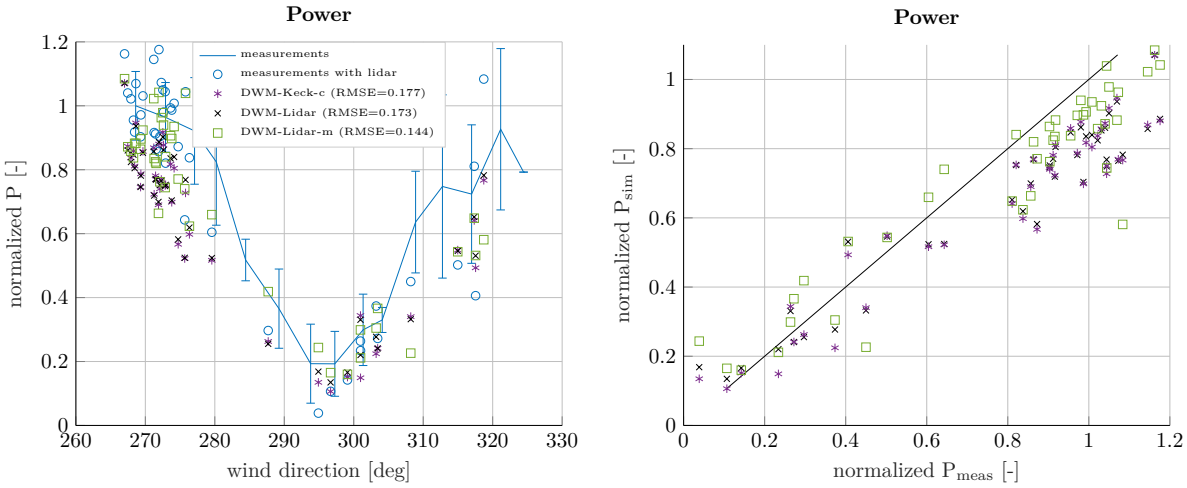

(a) (b)

Figure 7.15: Measured and simulated power over the wind direction **(a)** and simulated power over measured power **(b)** at an ambient wind speed of 8 m/s and an ambient TI of 10 %, when WTG 2 is exposed to the wake of WTG 1 (Reinwardt et al. 2021).

constrained simulations, which only uses the measured wind speed deficit shape, agree similarly well with the measurements, but the results based on the incorporation of the measured meandering (DWM-Lidar-m) fit considerably better to the measurements, especially towards the left part of the curve. It has been observed that the meandering is more pronounced in the measurements than in the DWM model simulations as it could already be seen in Figure 6.7. Thus, especially at the edges of the wake, when the downstream turbine is almost out of the wake, the amplitude of meandering becomes more important. If the meandering is more pronounced in this region, the wake-affected turbine experiences wake-free inflow conditions more often. Furthermore, if there is a slight misalignment of the wake generating turbine, it is indirectly captured in the determination of the meandering.

The normalized simulated power over the normalized measured power is illustrated in Figure 7.15**(b)**. The plotted straight black line has a slope of one and serves as a reference. The underestimation of the power deficit in the simulations is clearly visible in the upper part of the figure. Furthermore, the improvement when considering the measured meandering is obvious.

The results of the flapwise blade root bending moment are detailed in Figure 7.16. A clear overestimation of the loads can be seen in the flapwise bending moment. Consequently, a higher influence of the wake on this quantity is found in the simulations. The incorporation of the wind speed deficit (DWM-Lidar) leads to a slightly better agreement between measurements and simulations compared to the pure application of the recalibrated DWM model. Including the time series of the meandering (DWM-Lidar-m) leads to even better coincidences between measurements and simulations. However, the simulations overestimate the loads towards the edges of the curve. Similar behavior can be seen for the edgewise bending moment as well as the tower bottom bending moment (see Figures 7.17 and 7.18), although the differences between simulations and measurements are

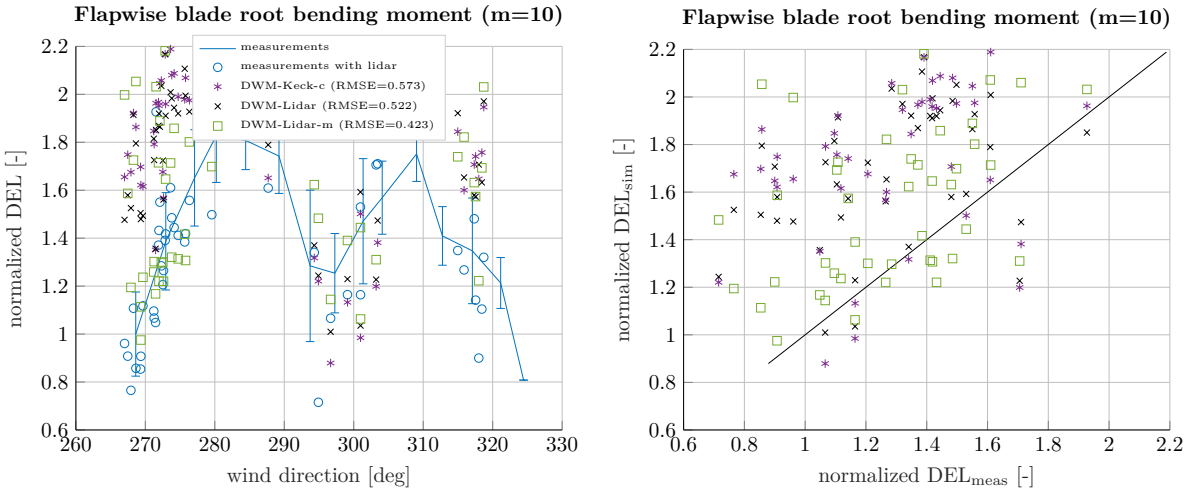

(a) (b)

Figure 7.16: Measured and simulated flapwise blade root bending moment over the wind direction **(a)** and simulated loads over measured loads **(b)** at an ambient wind speed of 8 m/s and an ambient TI of 10 %, when WTG 2 is exposed to the wake of WTG 1 (Reinwardt et al. 2021).

smaller for these load components. An explanation for the differences and uncertainties can be found in the different downstream distance, which is used in the simulations. For the comparison, measurements at the closest available lidar range gate that is still outside the rotor area of the downstream turbine are used. Thus, it happens that the downstream distance used in the simulations is slightly too low. The lidar system specifically measures in 30 m range gates, so that no measurements are available at the exact position of the downstream turbine. To achieve a suitable comparison with the DWM-Keck-c model, the measurement distance has also been used in the model. However, the influence should be rather small due to the small gradient of the wind speed in downstream direction, and hence it does not completely explain all differences. Especially an overestimation of the power cannot be explained by the insufficient downstream distance, whereby it is assumed that some discrepancies are related to a bias in the determination of the ambient conditions and/or the load simulation itself. Furthermore, it should be highlighted that the vertical meandering is neglected, when the measured meandering is used, given that no vertical meandering is captured by the lidar systems. The vertical movement is less pronounced than the horizontal meandering and has only a small influence on the shape of the wind speed deficit in the fixed FFR and on the loads. Hence, this simplification barely affects the overall results.

It can be concluded that the recalibrated DWM-Keck-c model predicts the measured wind characteristics and loads in the wake very well for the analyzed downstream distances as well as TIs and wind speeds. Improvements in the prediction of the loads can be achieved by incorporating lidar measurements in the load simulations. After obtaining a valid single wake model, the next step is the analysis and evaluation of methods to handle multiple wakes in the DWM model definition.

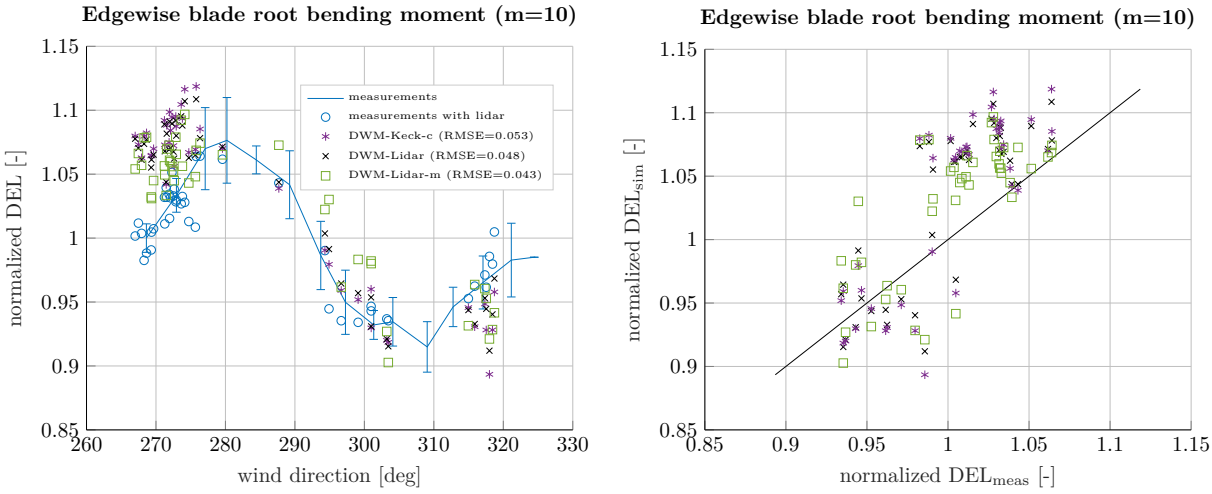

(a) (b)

Figure 7.17: Measured and simulated edgewise blade root bending moment over the wind direction **(a)** and simulated loads over measured loads **(b)** at an ambient wind speed of 8 m/s and an ambient TI of 10 %, when WTG 2 is exposed to the wake of WTG 1 (Reinwardt et al. 2021).

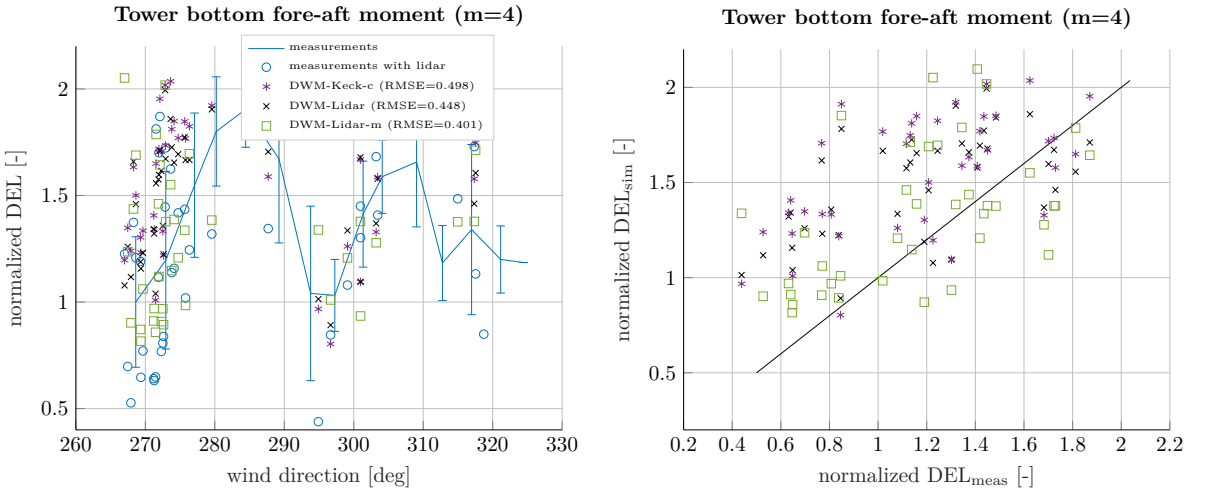

(a) (b)

Figure 7.18: Measured and simulated tower bottom fore-aft bending moment over the wind direction **(a)** and simulated loads over measured loads **(b)** at an ambient wind speed of 8 m/s and an ambient TI of 10 %, when WTG 2 is exposed to the wake of WTG 1 (Reinwardt et al. 2021).

7.1.2 Multiple wakes

The following section compares multiple wake measurements at the Curslack wind farm. First of all, lidar results from WTG 1 are analyzed, when the lidar system measures the double wake of WTG 2, WTG 4, or WTG 5. In a next step, the loads at WTG 3 are investigated when WTG 3 is affected by the wakes of WTG 1 and WTG 2.

7.1.2.1 Comparison with lidar measurements

This section presents results of the wind speed deficit in the HMFR as well as the FFR in a double wake situation. Given that the wake has been superimposed in the FFR for several of the outlined multiple wake approaches, the meandering series of the superimposed wake is no longer accompanied with the modeled meandering of the single wakes. Thus, even in the simulations a Gaussian curve according to the method outlined in Section 6.1.2 is fitted to the wind speed deficit in the FFR to recalculate the meandering.

Two examples of the mean minimum wake wind speed in the HMFR for all recorded distances are illustrated in Figure 7.19. Figure 7.19**(a)** depicts a high TI case of 15.1 %,

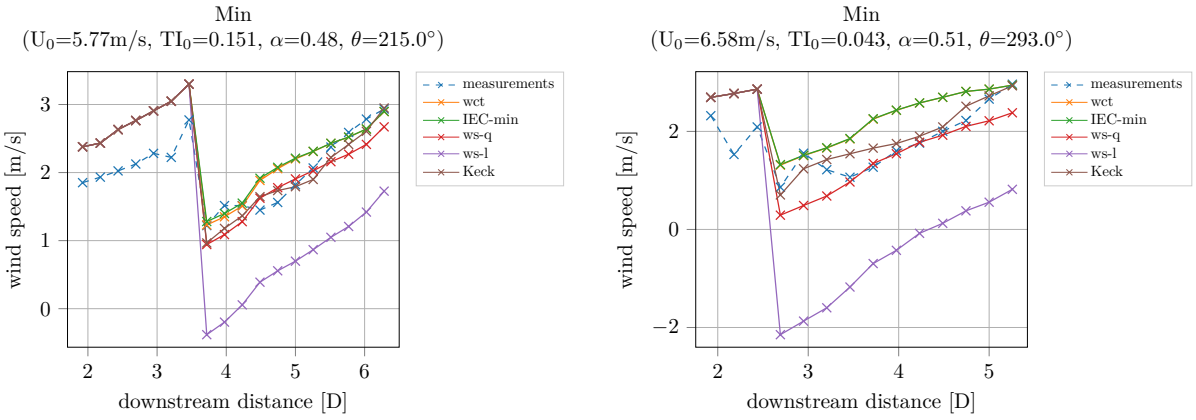

Figure 7.19: Minimum normalized wake wind speed in the HMFR over the downstream distance at a high ambient TI of 15.1 % **(a)** and a low TI of 4.3 % **(b)**. A double wake is simulated and measured at 3.46 D **(a)** and at 2.51 D **(b)**.

whereas the results in Figure 7.19**(b)** have been measured at an ambient TI of 4.3 %. The resulting ambient conditions such as the ambient wind speed, the vertical shear and the wind direction are given in the titles of the figures. The results in Figure 7.19**(a)** illustrate the single wake of WTG 1 until a distance of about 3.46 D. There are discrepancies between the single wake measurements and simulations. These are very likely related to the induction zone of the second turbine in the row in downstream direction, which is not accurately represented by the simulations. However, given that the focus in this chapter is on the performance of multiple wake models, these inconsistencies can be neglected for the outlined analysis. Downstream of 3.46 D the double wake of WTG 1 and WTG 4 is measured. The measurements are compared with the five methods previously introduced in Section 2.3.2. The first method denoted ”wake closest turbine” (wct) considers only

the wake of the nearest turbine, whereas the IEC-min method calculates the minimum wind speed of all upstream wakes. Two different wake summation approaches, a quadratic summation (ws-q) as well as a linear summation (ws-l) are depicted. The last illustrated method (Keck) calculates a rotor mean wind speed and TI at each downstream turbine in the row, so that the wake is calculated successively and multiple wakes are considered by the changed inflow conditions at each downstream turbine in the row. The comparison shows that the linear wake summation (ws-l) clearly overestimates the wind speed deficit depth. It even delivers a slightly negative wind speed, which is an artifact of the wake summation approach. The predicted data of the remaining models fit considerably better to the measurement results. In the area between 4 D and 5.5 D the quadratic summation approach (ws-q) and the Keck method are in better agreement with the measurements, whereas at the farthest distance the wct and IEC-min approach agree better. The wct and IEC-min approach deliver very similar results for the minimum wake wind speed as expected. Only directly after the second rotor (3.46 D) small discrepancies are detected. In this area the wake is usually not Gaussian shaped, so that the wake tracking method and the calculation of the meandering tends to fail. Similar results could be predicted for the low TI case in Figure 7.19**(b)**. It illustrates the wakes of WTG 1 and WTG 2. The double wake area begins after 2.51 D.

It should be highlighted that the DWM model is only valid in the far wake after 2 D, which corresponds to the area where an accurate predictions of wakes for downstream turbines becomes relevant. Thus, in the following figures only results of the farthest measured distance are analyzed. The DWM model neglects the pressure terms in the thin shear layer equations (see Section 2.3.1.5). Consequently, the model is only valid in the area, where the pressure has reached again ambient conditions, which in turn is assumed to be the case after 2 D. The ambient conditions of all evaluated data sets are summarized in Table 7.2. Overall, 29 10-min time series fulfilled the filtering criteria for the double wake measurements. The ambient wind speed of all data sets is between 5.47 m/s and 7.71 m/s. Data sets in an ambient TI range of 3.6 % to 15.3 % could be collected, whereas the wind shear varies between 0.38 and 0.62. Figure 7.20 illustrates the bias between the measurements and the simulations of the minimum wake wind speed at the farthest distance of all collected data sets, whereby a negative bias indicates that the simulated wind speed deficit is less pronounced than the measured one. In all data sets the linear summation approach overpredicts the wind speed deficit depth drastically, whereas all other models fit considerably better. The best agreements could be achieved with the wct, IEC-min and Keck model. The wct and IEC-min method deliver at this distance the same minimum wind speed, so that the wct model results are covered by the IEC-min results. The quadratic summation also overpredicts the wind speed deficit in most of the cases. Only at the data sets 12, 13, and 14 the quadratic model predicts the wind speed deficit depth more accurately.

Figure 7.21 depicts the complete wind speed deficit at hub height in the HMFR. All results are evaluated for the farthest measured downstream distance, where the DWM model has proven to be valid. Figure 7.21**(a)** shows the results for the high TI case, whereas Figure 7.21**(b)** depicts the results of the low TI situation. The gradient of the wind speed deficit can be predicted in both cases accurately with the wct, IEC-min and Keck model. The IEC-min model agrees better with the measurements in the transition

Table 7.2: Ambient wind speed U_0, ambient TI and wind shear α of all used data sets to evaluate double wakes. The ambient conditions have been determined by the met mast.

data set	U_0 [m/s]	TI_0 [%]	α [-]
1	5.86	9.5	0.50
2	5.54	11.2	0.49
3	5.77	15.1	0.48
4	5.47	11.2	0.54
5	5.79	10.4	0.56
6	7.04	9.3	0.59
7	7.05	9.2	0.51
8	7.60	9.0	0.41
9	7.71	10.6	0.38
10	6.48	8.4	0.38
11	6.01	13.4	0.38
12	6.75	9.2	0.49
13	6.17	7.3	0.50
14	6.78	3.6	0.52
15	6.30	4.3	0.62
16	6.51	4.8	0.45
17	6.58	4.3	0.51
18	7.21	15.3	0.45
19	7.02	11.4	0.39
20	7.59	8.5	0.44
21	6.10	11.0	0.43
22	6.47	8.0	0.40
23	6.20	9.2	0.52
24	6.42	11.0	0.56
25	6.68	10.0	0.52
26	6.92	8.8	0.51
27	6.9	12.0	0.51
28	6.6	9.4	0.4
29	6.42	10.0	0.49

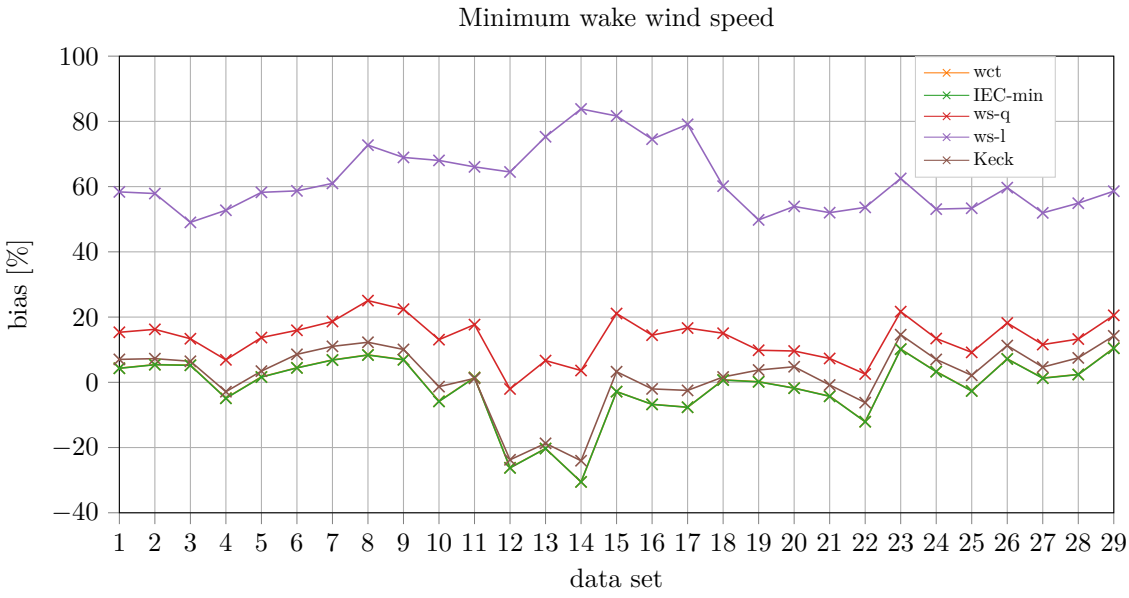

Figure 7.20: Bias of the minimum wake wind speed in the HMFR of all collected data sets at the farthest distance in a double wake situation. The wct and IEC-min method deliver at this distance the same results.

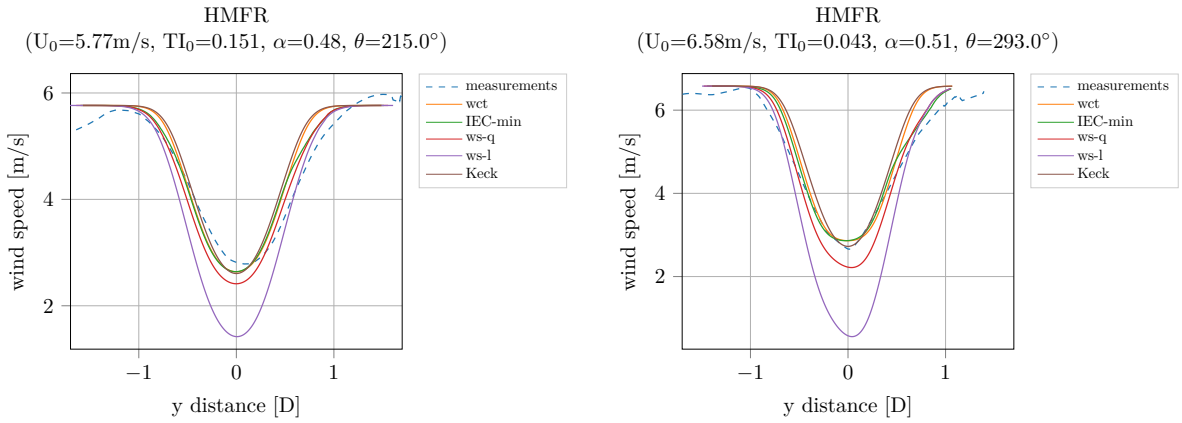

(a) (b)

Figure 7.21: Wind speed in the HMFR at the farthest distance of all collected data sets at a high ambient TI of 15.1 % (6.03D) **(a)** and a low TI of 4.3 % (5.0D) **(b)**.

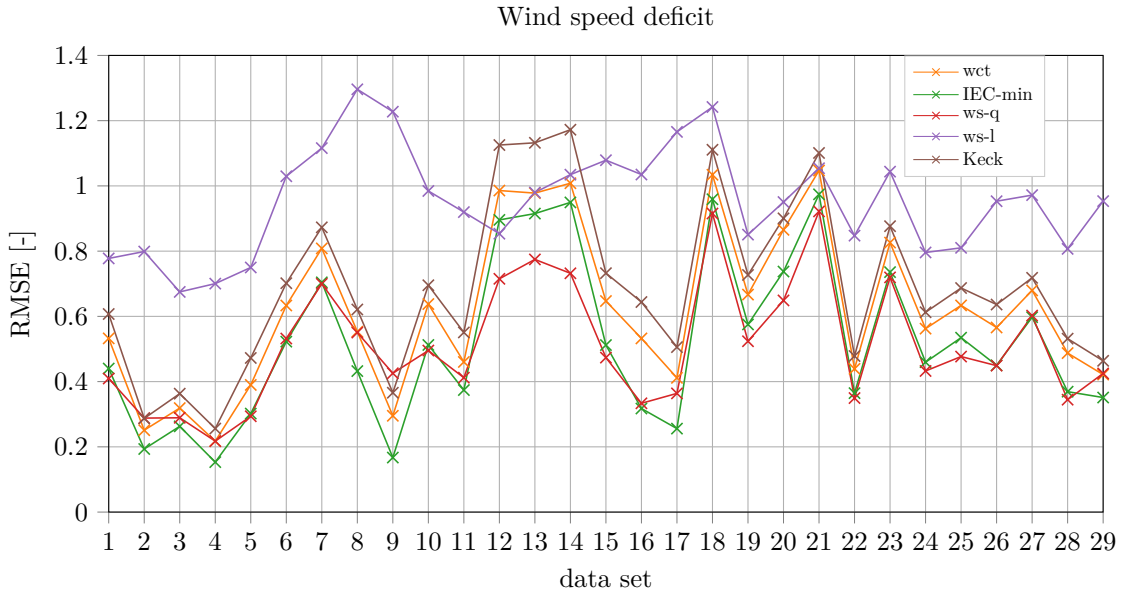

Figure 7.22: RMSE of the wind speed deficit in the HMFR of all collected data sets at the farthest distance in a double wake situation.

zone towards the ambient wind speed. In contrast to the wct method, where only the closest turbine wake is considered, the IEC-min takes the minimum wind speed at each point of interest in the wake. Close to the wake center this is usually in line with the wct model, whereas towards the edges of the curve the wake of the further upstream turbine is more pronounced. The reason for this is that, the wake of the closest turbine is less expanded, so that the IEC-min model differs in this area from the wct model and is in better agreement with the measurements. In the Keck model, the wind speed deficit is calculated successively, so that the wake width is also dominated by the closest turbine wake. The quadratic wake summation approach ws-q overpredicts the wake depth slightly but agrees better with the measurements in the transition zone towards ambient conditions than the wct method given that it also considers the broader wakes from all upstream turbines. The ws-l approach overpredicts the wind speed deficit drastically almost over the complete wake sector as it could already be seen in the results of the minimum wake wind speed.

The RMSE between the measured and simulated wind speed deficit in the HMFR, as shown in Figure 7.21, is illustrated in Figure 7.22. Figure 7.22 summaries the results of all evaluated data sets. Overall, the IEC-min is in good agreement with the measurements. Similar good results are delivered by the ws-q method, which is related to the more accurate description of the wind speed deficit gradient in the transition zone towards ambient wind speed. The wct and Keck method deliver slightly higher deviations from the measurements, whereas huge discrepancies can be identified for the linear summation approach. Only at the data sets 12 to 14 a better agreement could be achieved.

Figure 7.23 illustrates the mean wind speed deficit in the FFR for the low and the high TI case. Similar to the analysis in the HMFR, the wct, IEC-min, ws-q and Keck models coincide better with the measurements than the linear wake summation. Towards

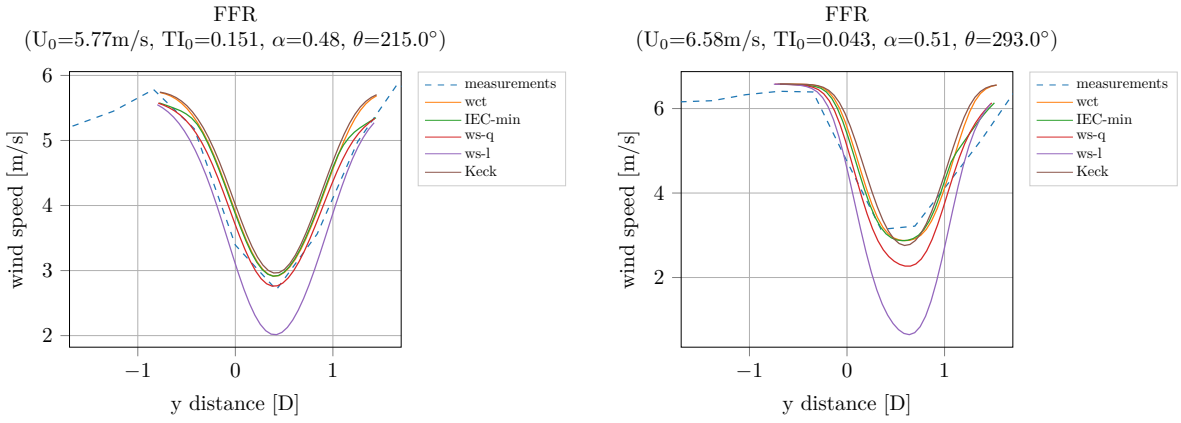

(a) (b)

Figure 7.23: Wind speed in the FFR at the farthest distance of all collected data sets at a high ambient TI of 15.1 % (6.03D) **(a)** and a low TI of 4.3 % (5.0D) **(b)**.

ambient wind speed a better agreement can be achieved by the IEC-min and the ws-q method, so that the wind speed gradient is predicted more accurately.

The RMSE of the measured and simulated wind speed deficit in the FFR is illustrated in Figure 7.24. The difference between the wct, IEC-min, ws-q and Keck model is more obvious in the FFR than in the HMFR. The best agreement could mainly be achieved by the quadratic summation. The IEC-min is also in good agreement with the measurements, whereas the wct and Keck model deliver slightly higher errors. The different performances of the models in the analysis based on the HMFR and FFR indicate that the meandering is not modeled correctly, whereby subsequently, a more detailed analysis of the meandering time series has been carried out.

The standard deviation of the horizontal wake meandering for a single wake situation and all collected data sets at a downstream distance of 2.44 D is illustrated in Figure 7.25. The standard deviation of the simulated meandering with the DWM model is compared to the measurements. The simulations and measurements have some discrepancies but the overall estimation of the behavior of the meandering is captured. However, when looking at the double wake situation (see Figure 7.26) major discrepancies could be detected. The standard deviation of the meandering found in the measurements tends to be higher than the simulated one. The meandering is equally calculated by the wct and Keck model. The same is true for the wake summation approaches. In case of the wct and Keck method, the meandering is only determined by the closest turbine wake, whereas when using the IEC-min or the wake summation methods the meandering has been recalculated from the merged wakes with a Gaussian fit. In general, the wakes from further upstream turbines exhibit a more pronounced wake meandering due to the higher wake travel distance. This influences the overall meandering in the summation models as well as in the IEC-min model and thereupon leads to slightly higher standard deviations of the time series of the meandering. Nevertheless, even in these models the meandering is not sufficiently pronounced, so that it can be concluded that the meandering path is more affected by the further upstream turbines. The wake of the further upstream turbines has larger

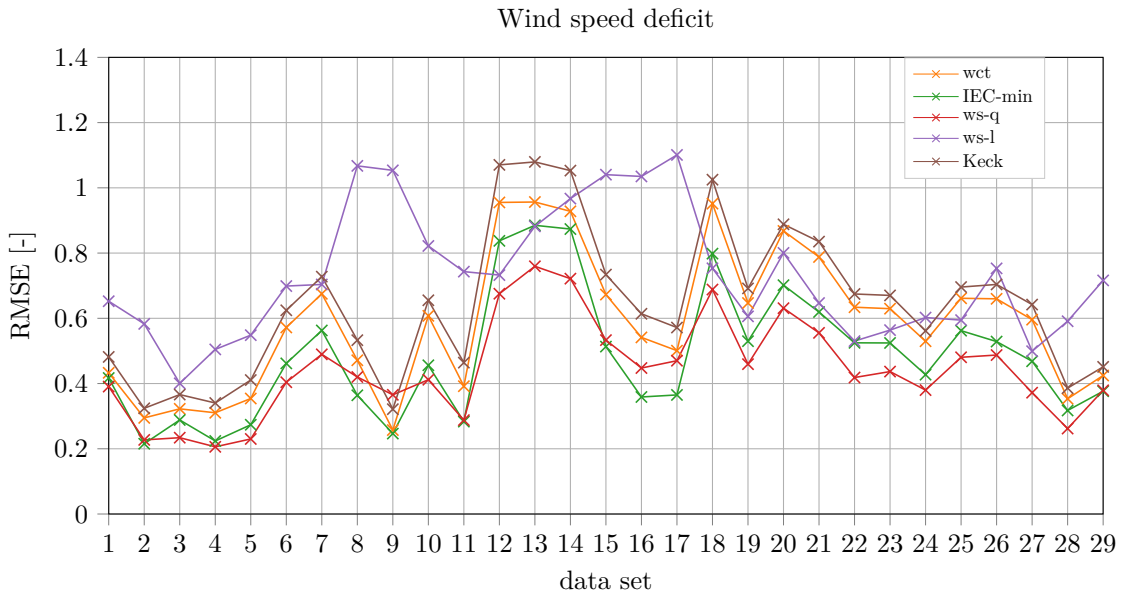

Figure 7.24: RMSE of the wind speed deficit in the FFR of all collected data sets at the farthest distance in a double wake situation.

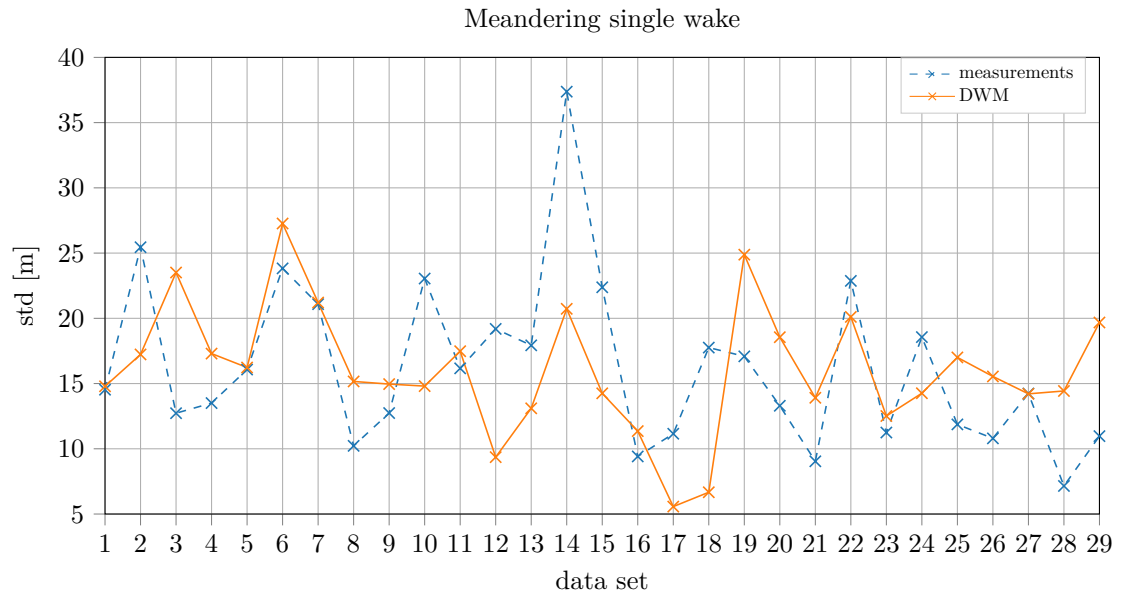

Figure 7.25: Standard deviation of the single wake horizontal meandering of all collected data sets at a downstream distance of 2.44D.

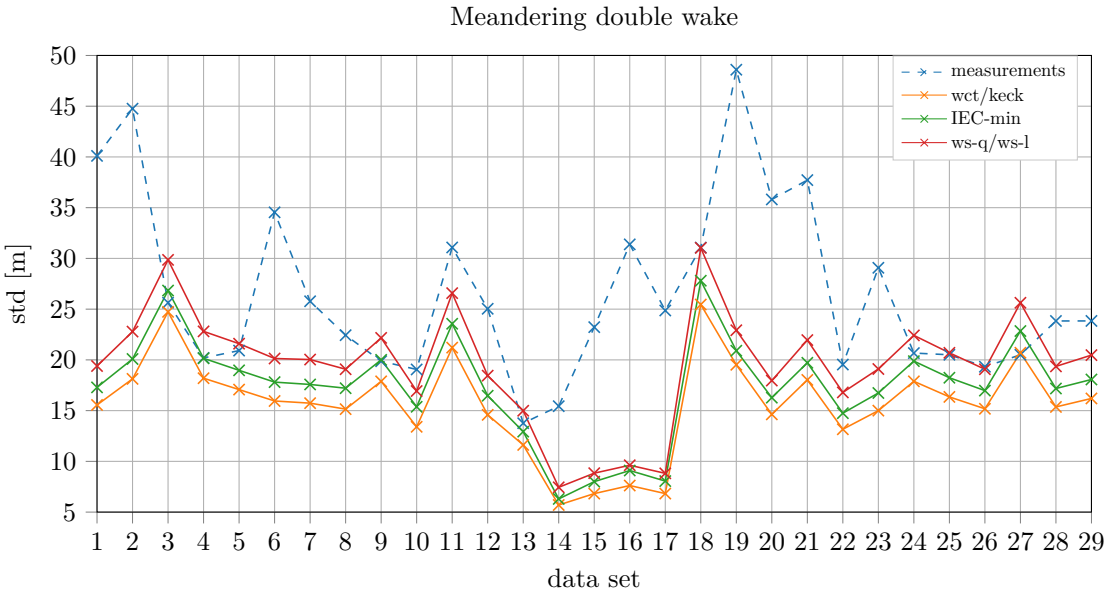

Figure 7.26: Standard deviation of the double wake horizontal meandering of all collected data sets at the farthest distance.

deflections given that the wake travel distance is longer. This explains the different model behavior in the FFR and HMFR analysis and reveals that the meandering in a double wake situation needs to be investigated further.

7.1.2.2 Comparison with load measurements

This section evaluates the measured loads at WTG 3 under double wake conditions. Only a few measurement results could be collected, when all three turbines (WTG 1, WTG 2 and WTG 3) are operating under normal conditions. To collect a reasonable amount of data, all data sets up to an ambient wind speed of 12 m/s and an ambient TI of 20% have been used in the subsequent analysis. To achieve a suitable comparison with the simulated loads, each 10-min time series has been simulated, whereby the ambient conditions (wind speed, TI, and wind shear) for each 10-min time series have been used in the simulations.

Figure 7.27 illustrates the mean power of all collected data sets. Figure 7.27**(a)** depicts the measured power at WTG 2, when WTG 2 is affected by the wake of WTG 1. The secondary axis illustrates the number of measurements. The measured power under single wake conditions agrees also very well with the DWM model for the here analyzed data sets, which is in line with the results of the last section. The corresponding measurement and simulation results at WTG 3, when WTG3 is affected by the wake of WTG 1 and WTG 2 are illustrated in Figure 7.27**(b)**. The four different multiple wake approaches are compared to the measurements. There are only slight differences in the predicted data of the different models under partial wake conditions. All models agree well with the measurements.

Figure 7.28 depicts the mean tower bottom fore-aft DEL of all collected data sets. The curve of the tower bottom bending moment looks rather coarse. The reason for this

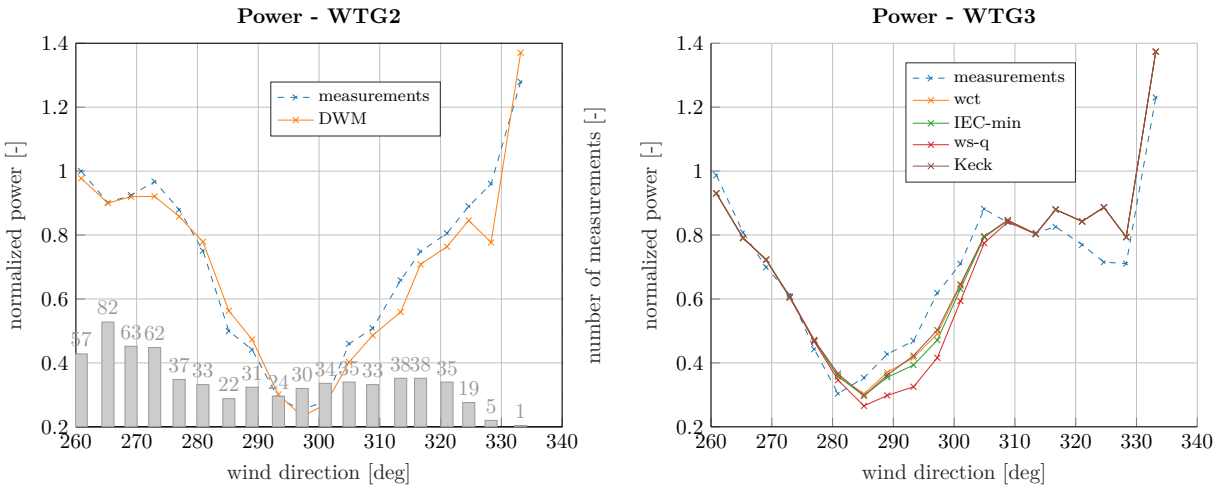

(a) (b)

Figure 7.27: Measured and simulated power over the wind direction when WTG 2 is exposed to the wake of WTG 1 **(a)** and WTG 3 is exposed to the wake of WTG 1 and WTG 2 **(b)**.

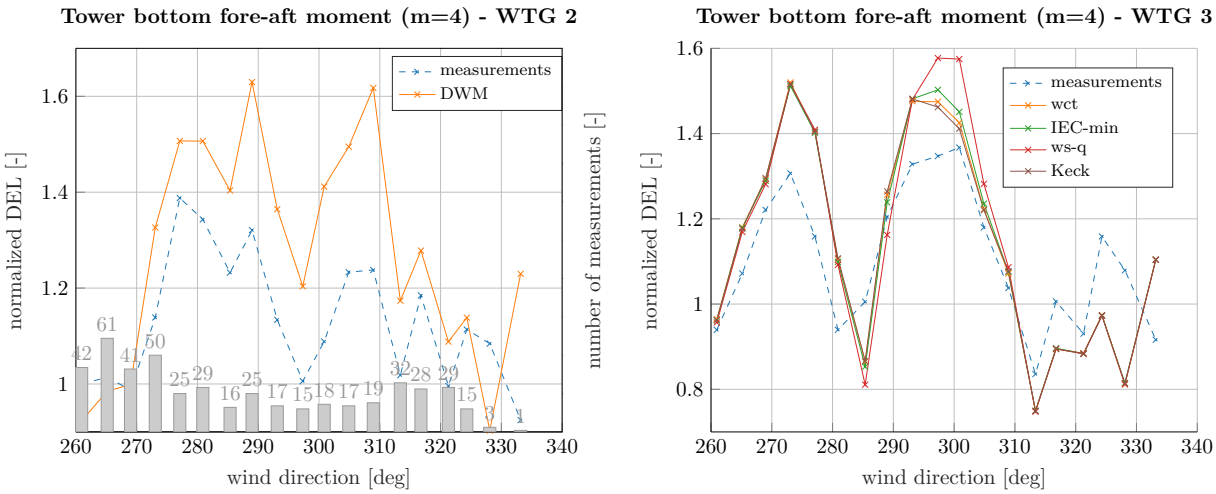

(a) (b)

Figure 7.28: Measured and simulated tower bottom fore-aft moment over the wind direction when WTG 2 is exposed to the wake of WTG 1 **(a)** and WTG 3 is exposed to the wake of WTG 1 and WTG 2 **(b)**.

is that results over a broad range of ambient conditions are analyzed. However, the loads measured under single wake conditions could be predicted well with the DWM model (see Figure 7.28**(a)**). The simulated loads are higher than the measured ones. The corresponding measurement and simulation results at WTG 3 are illustrated in Figure 7.28**(b)**. All four models predict very similar results and agree well with the measurements. Similar to the measured power, there are only slight discrepancies between the different multiple wake models at partial wake conditions.

It can be concluded that the IEC-min method agrees in most of the evaluated situations best with the measured wind speed deficit in the HMFR. It should also be highlighted that the very simple method wct, which only considers the closest turbine wake, coincides also very well with the measured wind speed deficit and deviates only slightly from the IEC-min method. Different results can be seen, when comparing the wind speed deficit in the FFR. This is very likely related to the different approaches to handle the wake meandering in a double wake situation. Some deviations between the modeled and measured wake meandering could be identified, whereby there is potential for improvements in the definition of the meandering in a merged wake situation. Nevertheless, when comparing the power output and the fatigue loads at a turbine in a double wake situation all models agree well with the simulations and only small difference can be recognized.

7.2 Wieringermeer wind farm

In the last section the measured wind speed deficit at the Curslack wind farm has been used to recalibrate the DWM model. The measured wind speed deficit has been transformed to the MFR to directly recalibrate the eddy viscosity definition in the DWM model. A good agreement between the measured and simulated wind speed deficits over all analyzed ambient TIs could be achieved. Furthermore, the recalibrated model has been evaluated with respect to the measured and simulated power and loads in Curslack. A good conformity of the results of the recalibrated model could be achieved in the analysis. Although this proves the applicability of the model for the simulation of the Curslack wind farm, it remains unclear whether the recalibrated model can be applied to other wind farms with different turbine types. This issue is investigated in this section. Comparisons of the measured wind speed deficit in the FFR and the measured loads under wake conditions are evaluated in this section.

7.2.1 Comparison with met mast measurements

The EWTW site comprises five Nordex N80/2.5 turbines aligned in a row and a met mast in a distance of 2.5 D and 3.5 D to the first two turbines in the row (see wind farm layout in Figure 3.6). The met mast offers the possibilities to measure the wind speed deficit in the FFR, when either the met mast is in the wake of WTG 5 or WTG 6, so that the two distances of 2.5 D and 3.5 D can be analyzed. The measured and simulated wind speed deficit as well as the TI in the FFR are depicted in Figure 7.29 over the distance to the nacelle in rotor diameters. The measured mean values and their corresponding standard deviations are illustrated. The measurements were gathered during an ambient wind speed of 9 m/s and an ambient TI of 10 %. The ambient wind speed as well as

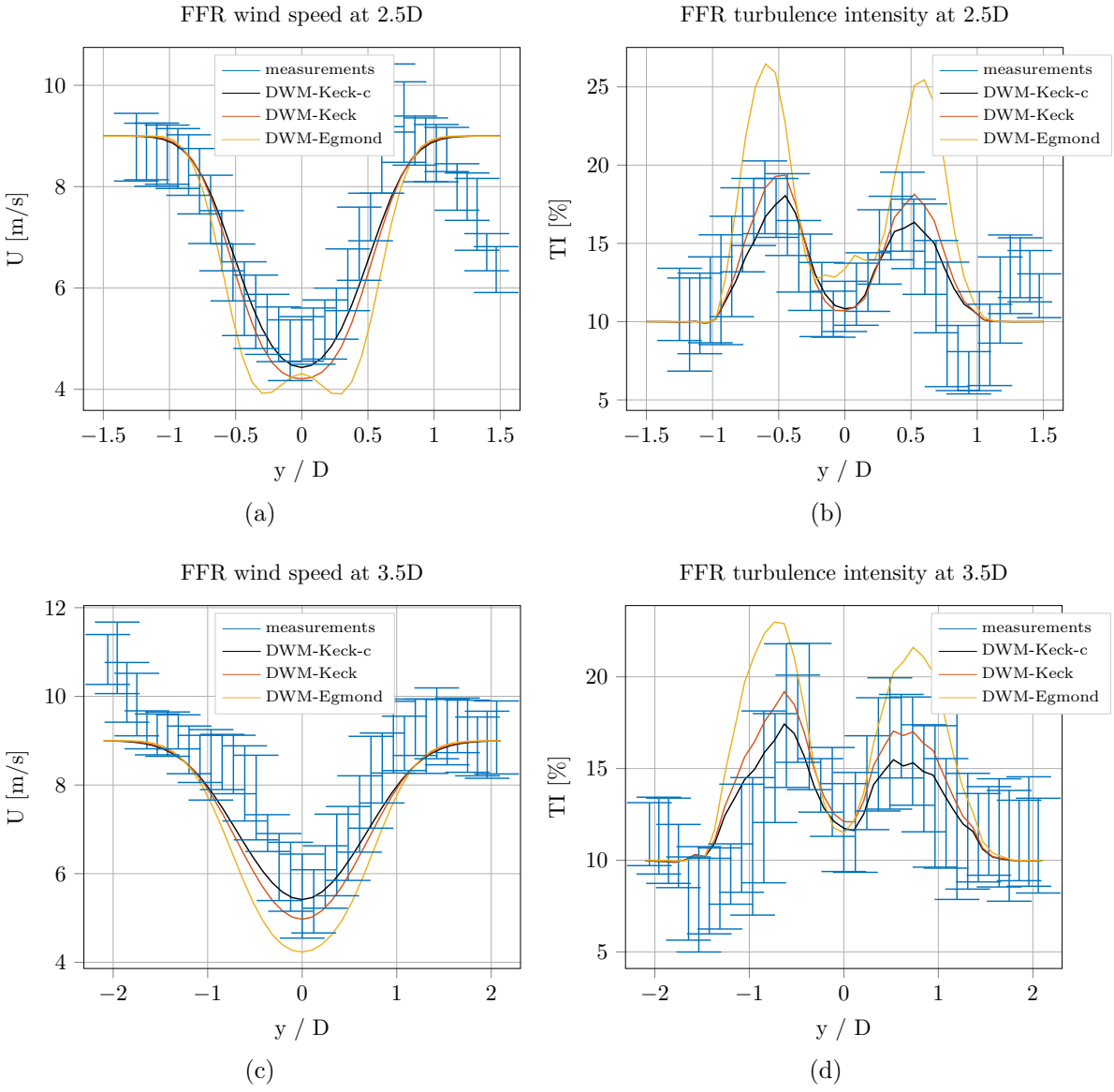

Figure 7.29: Measured and simulated wind speed deficit **(a, c)** and TI **(b, d)** over the distance from the hub at an ambient wind speed of 9 m/s and an ambient TI of 10 % at the wind farm Wieringermeer.

the ambient TI are determined with the turbine's SCADA system and a nacelle transfer function as outlined in Section 3.2. The three different DWM model variants from the last section are analyzed.

The recalibrated version of the DWM model is denoted as DWM-Keck-c. The wind speed deficit could be predicted with the newly calibrated model very well for both turbine distances, whereas the DWM-Egmond model overestimates the deficit drastically. This confirms the findings of the last section. The TI in the wake is drastically overestimated at the maxima of the TI curve, in the wake region of the turbines with the strongest velocity gradients. The DWM-Keck as well as the recalibrated model match the measurement results considerably better. For the lower distance, the DWM-Keck-c model agrees best with the measured TI, whereas at the larger distance of 3.5 D the TI is partly underestimated. There is only a slight difference between the results of the DWM-Keck and the recalibrated DWM-Keck-c model. The reason is that the ambient TI is relatively high and the recalibration has only a slight influence on the overall results. Unfortunately, it was not possible to gather a sufficient number of measurement samples at lower TIs. Nevertheless, an improvement by the recalibration is identifiable.

7.2.2 Comparison with load measurements

The turbine WTG 6 in the EWTW site is equipped with load measurement devices, so that results when WTG 6 is affected by the wake of WTG 5 can be analyzed. The distance between the turbines is 3.8 D. The measured and simulated power are depicted in Figure 7.30. The loads are simulated with the commercial software Flex5 (see

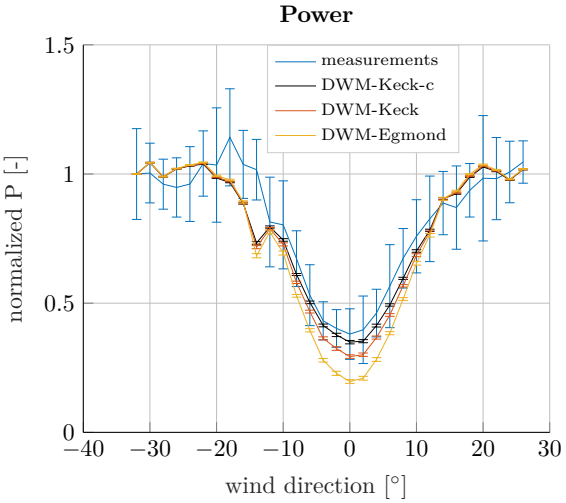

(a)

Figure 7.30: Measured and simulated power over the wind direction at an ambient wind speed of 9 m/s and an ambient TI of 10 % at the wind farm Wieringermeer.

Section 2.2.3). The simulations were carried out with six different seeds to cover the stochastic influence of turbulence on the loads. The mean value of the results of all seeds as well as the mean value of all gathered measurement results are illustrated with their corresponding standard deviations as error bars. The measurements were also collected

during an ambient wind speed of 9 m/s and an ambient TI of 10 %. The power deficit is captured very well with the newly recalibrated DWM-Keck-c model. Similar good agreements could be achieved with the DWM-Keck model. The DWM-Egmond model overpredicts the power deficit, which is in line with the measurement results of the wind speed deficit from the previous section.

The flapwise blade root bending moments as well as the tower bottom bending moment are depicted in Figure 7.31. The fatigue loads in Figure 7.31 are summarized in DELs.

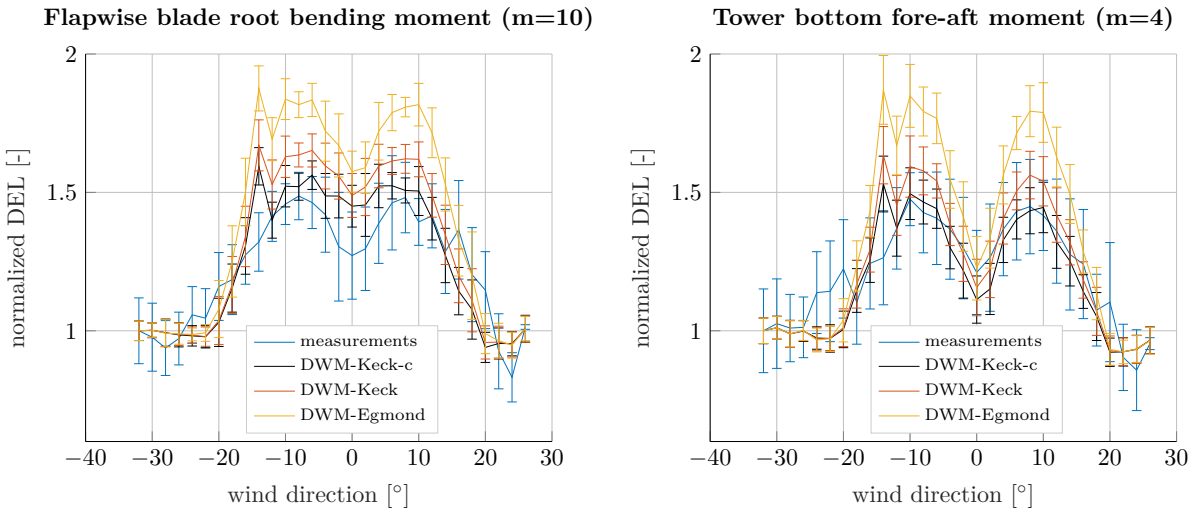

Figure 7.31: Measured and simulated flapwise blade root bending moment **(a)** and tower bottom fore-aft moment **(b)** over the wind direction at an ambient wind speed of 9 m/s and an ambient TI of 10 % at the wind farm Wieringermeer.

All values are normalized by the ambient conditions. The DWM-Keck-c model predicts the DEL of the tower bottom bending moment as well as the measurements of the flapwise blade root bending moment very well. The DWM-Egmond model as well as the DWM-Keck model overpredict the tower bottom bending and blade root flapwise fatigue loads.

A comparison between the measured and simulated bias of the flapwise blade root bending moment (MYB1) and the tower bottom bending moment (MYTb) determined with the DWM models and the Frandsen model is depicted in Figure 7.32**(a)**. The bias between the accumulated DELs over all wind directions, which are illustrated in Figure 7.31, are depicted. The Frandsen model overestimates the DEL of both load components drastically, whereas the recalibrated DWM model predicts the accumulated DEL very well. However, the tower bottom bending moment is slightly underestimated with the recalibrated DWM model. The RMSE between the entire measured and simulated curves in Figures 7.30 and 7.31 are depicted in Figure 7.32**(b)**. The lowest RMSE can be achieved by the recalibrated DWM model.

Overall, the comparison of the measurements at the EWTW has strengthened the findings of the last section, which are based on the measurements at the Curslack wind farm. The evaluation in this section has shown that the recalibration delivers similar good results at the EWTW wind farm, although a different turbine type is installed

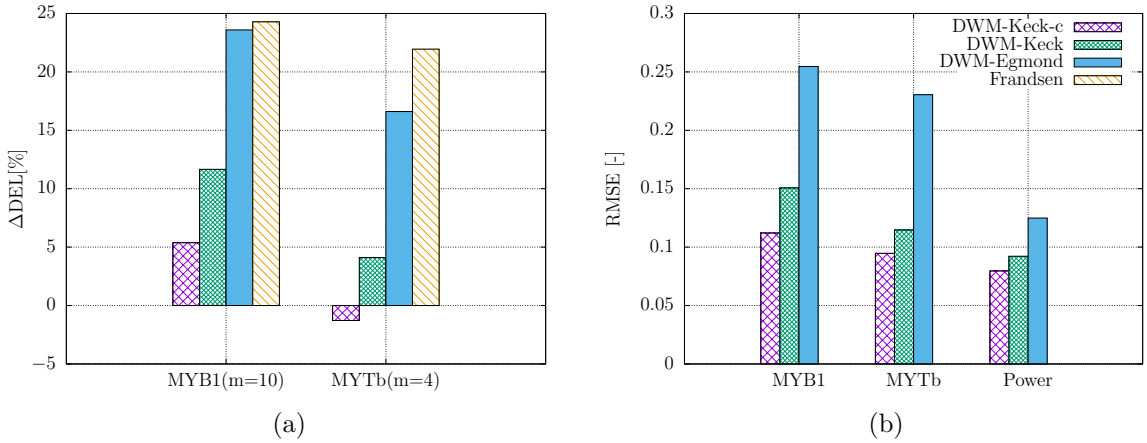

Figure 7.32: Bias between the measured and simulated fatigue loads **(a)** and the RMSE **(b)** for the flapwise blade root bending moment (MYB1) and the tower bottom bending moment (MYTb) as well as the power at an ambient wind speed of 9 m/s and an ambient TI of 10 % at the wind farm Wieringermeer.

at this site. Furthermore, the Curslack site has demonstrated that Frandsen's model is very conservative, especially at short turbine distances (see Figure 7.14). This could be replicated by the EWTW (see Figure 7.32). Nevertheless, it should highlighted that only results for one ambient TI could be evaluated and a further analysis of different ambient TIs should be conducted. Moreover, similar small turbine distances have been evaluated in both analyses given that the focus of this study on wake modeling is on onshore turbines with small turbine distances.

7.3 Validation of the extension of the dynamic wake meandering model towards a static version

In the last sections a recalibrated version of the DWM model has been evaluated. This recalibrated version has proven to predict the wind characteristics in the wake as well as the simulated power and loads very well. Furthermore, it has been seen that the Frandsen model is very conservative, especially for short distances, so that the DWM model has proven to be much more accurate in predicting fatigue loads.

However, despite the fact that the DWM model predicts the fatigue loads in the wake very well, the model mostly remains unusable for the industry given that it delivers an inhomogeneous and instantaneous wind field, which can be directly connected to an aeroelastic load simulation tool. In a common site-specific load calculation process this time-consuming aeroelastic simulations are usually avoided and the loads are estimated based on interpolations of already performed load simulations. The interpolation method (e.g. response surface methods) only depends on a couple of site conditions (e.g. wind shear, TI, wind slope and air density). Unfortunately, such a load estimation method is not combinable with the DWM model, since it requires a single TI value for the whole wind field instead of an inhomogeneous wind field as generated by the DWM model. This

section addresses this problem and presents the results of an extension of the DWM model towards a static model version as outlined in Chapter 5. First, this section compares the modeled wind characteristics in the FFR, when using a PDF to describe the meandering with the one from the original DWM model. The static DWM model is built in a way that it does not require any wind field simulations, so that a PDF together with a Kaimal spectrum is used to calculate the meandering in the model. This simplification is applied to avoid time-consuming wind field simulations. In the original DWM model the ambient wind field, generated by a Kaimal spectrum together with a coherence function, is low-pass filtered to determine the meandering. Second, this section presents the calculated calibration factors and discusses their necessity. Finally, the results are compared with the Frandsen model regarding effective TIs and fatigue loads. The extension of the DWM model has been published in Reinwardt et al. (2020b) and parts of this publication are taken over in this section.

7.3.1 Validation of the meandering PDF approach

Figure 7.33**(a)** illustrates the wind speed deficit at hub height over the horizontal distance to the hub. The shown wind speeds correspond to a rotor diameter of 117 m, a downstream distance of $3.61D$, an ambient wind speed of 8 m/s, and an ambient TI of 8 %. The original DWM model is compared to the PDF approach in the new static DWM

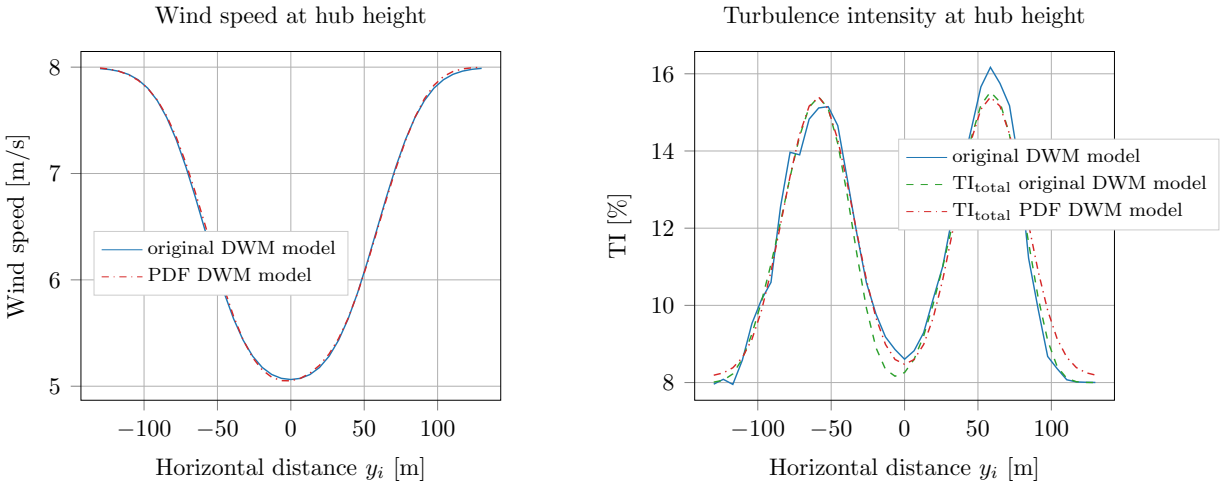

Figure 7.33: Wind speed deficit **(a)** and TI **(b)** at full wake conditions. The simulations are performed with an ambient wind speed of 8 m/s, an ambient TI of 8 %, a rotor diameter of 117 m, and a downstream distance of $3.61D$ (Reinwardt et al. 2020b).

model version outlined in Chapter 5. It is apparent that both approaches match very well. The corresponding TIs at hub height are depicted in Figure 7.33**(b)**. Besides the overall TI of the original DWM model (solid blue curve), the total TI (dashed green curve), which is the combination of the meandering TI and the ambient TI of the original DWM model, as well as the PDF approach of the total TI (dashed dotted red curve) are illustrated. In the PDF approach no small-scale turbulence is included in the model version given that

this model does not include any time-consuming wind field simulations. In the original DWM model the small-scale turbulence is based on a scaled wind field generated by a Kaimal spectrum and a coherence function as outlined in Section 2.3.1.5. To avoid this wind field simulation, the small-scale turbulence is neglected in this PDF approach and later on in the static DWM model version. The comparison clarifies that the influence of the small-scale TI, which is only considered in the overall TI of the original model version, is rather low. Furthermore, the PDF approach also agrees very well with the combined TI of the original model. Based on the illustrated total TI, the rotor-averaged TI can be calculated. This delivers a rotor-averaged TI of 12.88 % for the PDF approach, which agrees very well with the rotor-averaged TI derived from the original model of 12.90 % (solid blue curve). Overall, the outlined figures of the wind speed deficit and TI in the FFR prove that the PDF approach to determine the wind speed and TI is a very good approximation. The TI in Figure 7.33**(b)** refers to the inhomogeneous TI-Total in the schematic illustration of the model extension in Figure 5.1.

7.3.2 Determination of the calibration factors

The next step in the static DWM model is to calculate the a calibrated rotor-averaged TI (TI-Rotor), which is a homogeneous damage equivalent TI. This implies that the rotor-averaged TI shall correlate with the fatigue loads of the downstream turbine. The correlation between the rotor-averaged TI and the normalized DEL of the tower bottom fore-aft moment is displayed in Figure 7.34**(a)**. Simulations based on the original DWM

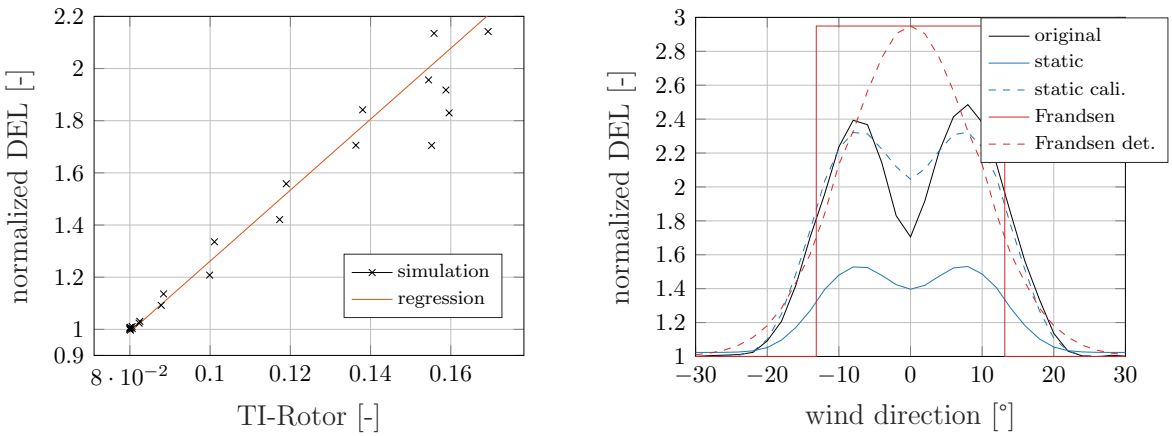

Figure 7.34: Normalized tower bottom fore-aft DEL over the rotor-averaged TI **(a)** and over the wind direction **(b)** according to Reinwardt et al. (2020b). The DELs are calculated with a Wöhler coefficient of 4, an ambient wind speed of 8 m/s, an ambient TI of 8 %, and a downstream distance of 3.61D.

model for wind directions from −30° to 30° are illustrated as crosses together with a linear regression between these points. The simulations are based on a turbine model with a turbine diameter of 117 m and a hub height of 120 m. The simulations were carried out with the commercial load simulation software alaska/Wind (see Section 2.2.3). The wake generating turbine and the wake-affected turbine are of the same type. The simulations were

carried out at a downstream distance of $3.61D$ and are valid for an ambient wind speed of 8 m/s and an ambient TI of 8 %. Figure 7.34**(a)** proves a linear correlation between the rotor-averaged TI and the DEL of the tower bottom bending moment. Furthermore, it shows clearly that the slope of the regression line is different from unity and thus indicates that a calibration of the extended DWM model is necessary. Simulations reveal that the slope is different for each load component (see Figures 7.34**(a)**, 7.36**(a)**, and 7.37**(a)**). Moreover, the calibration factor is a function of the downstream distance and the ambient wind speed. A summary of all calibration factors per downstream distance and ambient wind speed is depicted in Figure 7.35. Figure 7.35**(a)** illustrates the factor at an ambient

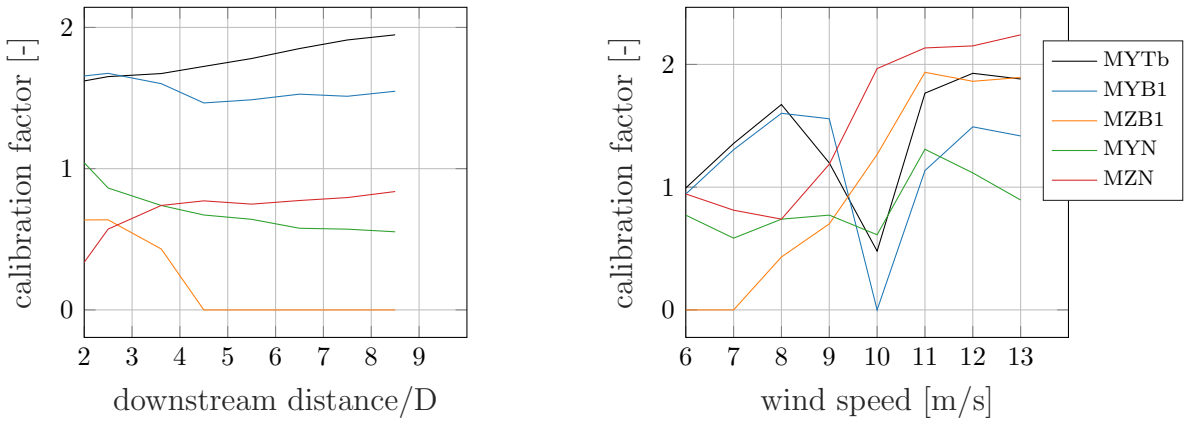

Figure 7.35: Calibration factor k_M as a function of the downstream distance for a wind speed of 8 m/s **(a)** and as a function of the wind speed at a downstream distance of 3.61 D **(b)**. The tower bottom fore-aft bending moment (MYTb), the flapwise (MYB1) and the edgewise (MZB1) blade root bending moment, the main bearing fore-aft bending moment (MYN) and the main bearing torque (MZN) are depicted.

wind speed of 8 m/s over different downstream positions, whereas Figure 7.35**(b)** presents the results over different wind speeds at a downstream distance of 3.61 D. A collection of the main load components distributed over the turbine is presented. For wind speeds from 6 m/s up to 8 m/s the highest calibration factor is found for the tower bottom bending moment (MYTb), whereas at higher wind speeds the main bearing or rotor torque (MZN) shows the highest calibration factors. The behavior of the different load components are strongly related to the operational conditions of the turbine. Depending on the ambient wind speed the operating conditions may significantly differ inside and outside the wake. For example, at an ambient wind speed of 10 m/s the turbine is operating above the rated wind speed outside the wake, whereas inside the wake the wind speed is considerably reduced, so that the turbine is very likely operating in the region, where the turbine's thrust possesses its maximum, which is relevant for the thrust-depending loads. This might change with higher or lower ambient wind speeds. Furthermore, below the rated wind speed, the wind speed deficit is very pronounced and the alternating load at partial wake conditions is very high, so that the load components, which are affected by alternating loads due to partial wakes (e.g. blade root flapwise and tower bottom fore-aft bending moment), deliver very high fatigue loads inside the wake and considerably lower

loads outside the wake resulting in a high calibration factor for lower wind speeds as it can be seen for the sensors MYB1 and MYTb in Figure 7.35**(b)**. Furthermore, at low wind speeds (6 m/s and 7 m/s) the wake-affected turbine is operating close to the cut-in wind speed of 4 m/s. Thus, in the DWM model simulation, the turbine has been frequently turned off in the full wake region, which has a different effect on each load component and is indirectly captured in the calibration factor. To achieve conservative results, the highest calibration factor of all load components for each downstream distance and ambient wind speed is taken to calibrate TI-Rotor in the static DWM model.

It should be highlighted that it is only necessary to calibrate the TI related to the meandering itself, which leads to the previously mentioned calibration factor k_M introduced in Equation (5.7). The calibration factor is specified by a least-squares fit between the simulated static DWM model fatigue loads and the original model loads. This leads to the calibration factor depicted in Figure 7.35. Simulations for different ambient TIs have proven that this factor is independent of the ambient TI.

The normalized DEL of the tower bottom bending moment over the simulated wind directions is illustrated in Figure 7.34**(b)**, in which a wind direction of 0° represents a full wake. It shows the simulation results based on the original DWM model, the developed static model as an extension of the original model as well as the calibrated static DWM model with the introduced calibration factor k_M. The calibrated static version of the DWM model is in very good agreement with the original model over all wind directions. Additionally, two versions of the Frandsen turbulence model are displayed. The first considers a characteristic view angle, which leads to the rectangular shape of the turbulence distribution over the wind direction, while the second model version assumes a bell-shaped turbulence distribution (see Section 2.3.1.1). Both versions lead to significantly higher loads, especially at full wake conditions.

Simulation results for the flapwise blade root bending moment are depicted in Figure 7.36. The flapwise moment shows a similarly good linear correlation between the

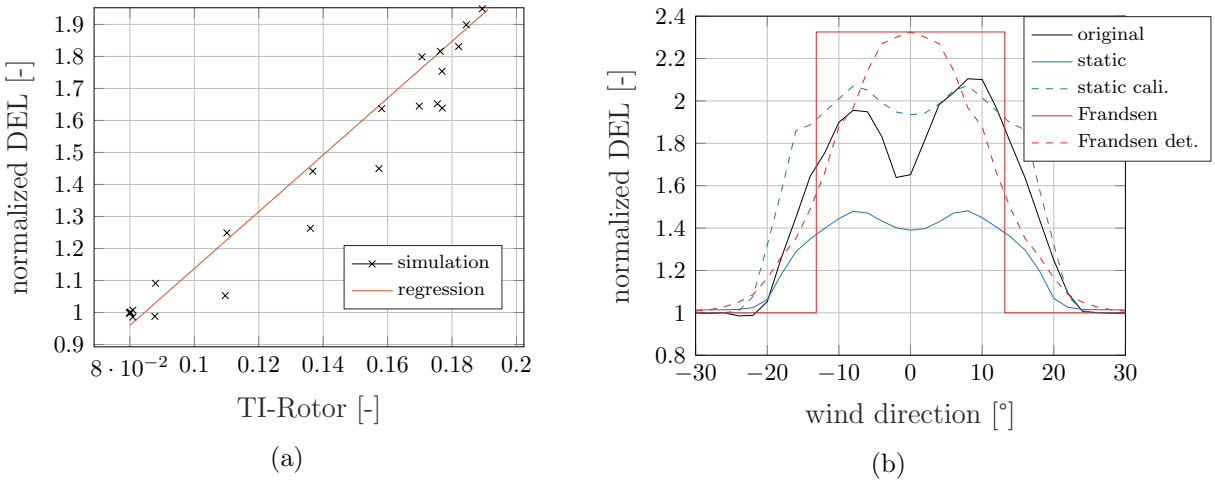

Figure 7.36: Normalized flapwise blade root bending DEL over the rotor-averaged TI **(a)** and over the wind direction **(b)** according to Reinwardt et al. (2020b). The DELs are calculated with a Wöhler coefficient of 14, an ambient wind speed of 8 m/s, an ambient TI of 8 %, and a downstream distance of 3.61D.

rotor-averaged TI and the DEL (see Figure 7.36**(a)**). The comparison of the simulated DEL of the flapwise moment of the static DWM model and the Frandsen model to the original DWM model is depicted in Figure 7.36**(b)**. The static model is in good agreement with the original DWM model but the discrepancies are higher than for the tower bottom bending moment. This is caused by the fact that the highest calibration factor is determined by the tower bottom bending moment and subsequently applied to all other turbine components. The Frandsen model overestimates the DEL again, especially at full wake situations. However, the overestimation of the blade root bending moment is less pronounced than for the tower bottom bending moment, which seems to be reasonable taking into account that the model is validated based on this component (Frandsen 2007).

A suboptimal correlation arises for the edgewise blade root bending moment (see Figure 7.37). The edgewise moment is mainly driven by the weight of the blades and has

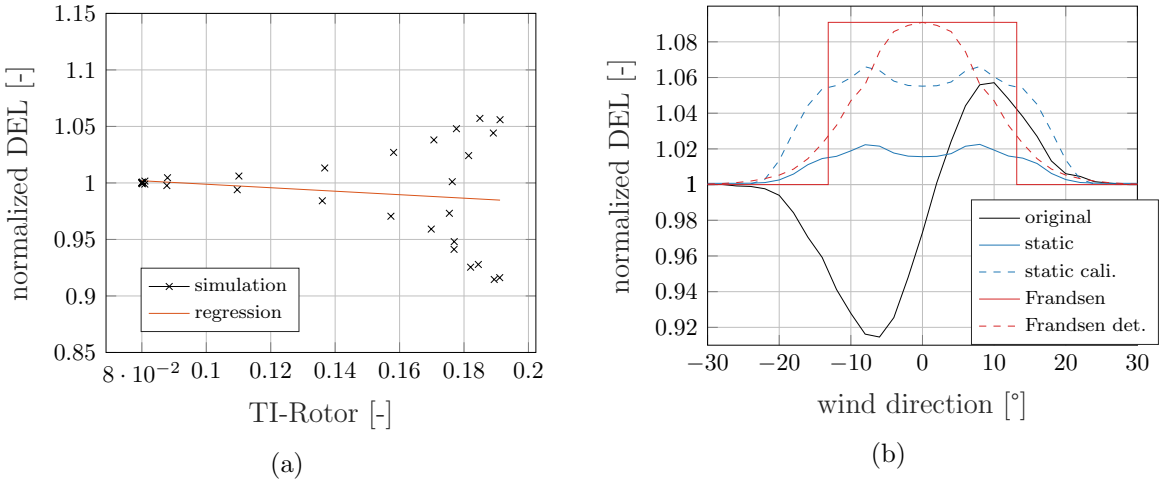

Figure 7.37: Normalized edgewise blade root bending DEL over the rotor-averaged TI **(a)** and over the wind direction **(b)** according to Reinwardt et al. (2020b). The DELs are calculated with a Wöhler coefficient of 14, an ambient wind speed of 8 m/s, an ambient TI of 8 %, and a downstream distance of 3.61D.

only a weak dependency on the turbulence, whereas the flapwise moment and the tower bottom fore-aft moment strongly correlate with the fluctuating wind. Therefore, the linear regression generates an appropriate linear correlation of the rotor-averaged TI with DELs of the turbulence-dependent loads, but not with weight-driven loads. Nonetheless, even though there is no linear correlation, the static DWM model still predicts the edgewise fatigue loads superior to the Frandsen model. Its only disadvantage is the behavior at negative wind directions, where it is not possible to establish the decrease of the DEL. It should also be highlighted that the maximum increase of the edgewise moment in wake conditions is less than 6 % (see maximum in Figure 7.37**(b)** at a wind direction of 8°), whereas the flapwise moment is more than doubled at partial wake conditions, so that all together the static model seems to be an acceptable approach, even for the edgewise moment. Results of the main bearing fore-aft bending moment and the rotor torque are depicted in Figures B.8 and B.9 in the appendix. Similar to the blade root flapwise as well as tower bottom bending moment, the main bearing bending moment depends on the fluctuating wind, so that a correlation to the rotor-averaged TI can be determined.

The rotor torque also depends on the fluctuating wind but is also strongly influenced by the mean wind speed.

7.3.3 Comparison with Frandsen's model

A comparison of the effective TI predicted by the calibrated static DWM model and the two different Frandsen models is depicted in Figure 7.38. The accumulated effective

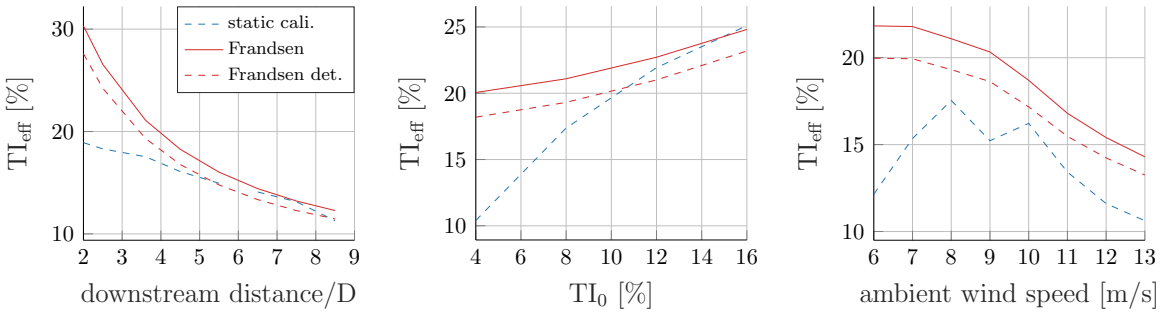

(a) (b) (c)

Figure 7.38: Effective TI of the static DWM and the Frandsen models. The simulations were carried out with an ambient wind speed of 8 m/s and an ambient TI of 8 % for varying downstream distances **(a)**, for a fixed ambient wind speed of 8 m/s, but varying ambient TIs **(b)**, and for a fixed ambient TI of 8 %, but varying ambient wind speeds **(c)**, both of the latter at a downstream distance of $3.61D$. The effective TI is calculated with a Wöhler coefficient of 14.

TI over the wind direction range of $-30°$ to $30°$ is depicted. The same ranges as depicted in the previous Figures 7.34, 7.36 and 7.37 are applied. Figure 7.38**(a)** depicts results over different downstream distances with an ambient wind speed of 8 m/s and an ambient TI of 8 %. At lower distances the effective TIs predicted by the static DWM model is considerably lower than those of the Frandsen model, whereas towards higher distances the models deliver similar results. Downstream of a distance of 6.5 D the static DWM model delivers slightly higher effective TIs than the Frandsen detailed model. A similar comparison over different ambient TIs with a constant downstream distance of 3.61 D is illustrated in Figure 7.38**(b)**. For small TIs, the static DWM model predicts lower loads, whereas at higher TIs the model becomes more conservative. The effective TI over different ambient wind speeds is depicted in Figure 7.38**(c)**. The static DWM model delivers lower effective TIs over all ambient wind speeds. The effective TI over different ambient TIs for downstream distances from 2.0 D to 8.5 D is depicted in Figure B.11 in the appendix. The simulations were carried out for an ambient wind speed of 8 m/s. The figures support the fact that the static model delivers lower effective TIs towards close distances as well as small ambient TIs, whereas towards higher downstream distances and higher ambient TIs the model delivers similar effective TIs as the Frandsen model and reveals sometimes slightly higher effective TIs. Up to a downstream distance of 2.5 D the static DWM model delivers lower loads than both Frandsen model variants over all analyzed ambient TIs. Furthermore, at ambient TIs lower than 8 % the static model delivers also significantly lower effective TIs. A comparison of the effective TI over the

ambient TI for different ambient wind speeds is depicted in Figure B.12 in the appendix. A similar behavior towards small ambient TIs can be investigated over all ambient wind speeds. Moreover, over all ambient wind speeds the static DWM model delivers lower effective TIs or similar effective TIs as the Frandsen model except for simulations at an ambient wind speed of 10 m/s. This behavior can be explained by the high calibration factor of the rotor torque at 10 m/s (see Figure 7.35**(b)**), which is in this case used to determine the effective TI.

A comparison of the bias between the DELs calculated by the static model as well as the Frandsen model and the original DWM model is summarized in Figure 7.39. The first row shows the deviation over different downstream distances, whereas the second row shows the deviation over different ambient TIs similar to the curves in Figure 7.38. In all cases, the deviations between the accumulated DELs over all inflow conditions from −30° to 30° are illustrated. The Frandsen model delivers significantly higher loads towards lower downstream distances, which is in agreement with the findings in Figure 7.38 and also the study of Gerke et al. (2018). The deviations between the static model and the original DWM model are less pronounced in this region. The Frandsen model and the static model converge towards larger downstream distances as well as higher TIs, leading to slightly higher loads of the static DWM model at larger distances and higher TIs than the bell-shaped Frandsen model (Frandsen detailed). Furthermore, towards higher distances the static DWM model delivers higher loads than the Frandsen model.

The deviation between the static DWM model and the two Frandsen models for varying ambient wind speeds is illustrated in the last row of Figure 7.39. At low wind speeds the static DWM model delivers significantly lower loads than the Frandsen models and agrees very well with the original DWM model, whereas the Frandsen model overpredicts the loads. One reason for the deviation at low wind speeds, i.e. 6 m/s and 7 m/s, is that the wake-affected turbine is operating close to the cut-in wind speed of 4 m/s. Thus, in the DWM model simulation the turbine has been frequently turned off in the full wake region. The Frandsen models do not consider the wind speed deficit, which is why no turbine shutdown cases are included in the load simulations, resulting in large discrepancies at low wind speeds. In the static model this phenomenon is indirectly covered by the calibration factor. At higher wind speeds, i.e. in the range of 9 m/s to 10 m/s, the deviation shows a clear peak in the flapwise as well as the tower bottom bending moment. Again, the presumed reason is the disregarded wind speed deficit. In this region, the turbine's thrust possesses its maximum, whereas in the original DWM model the thrust is substantially lower due to the wind speed deficit. This explanation is encouraged by the fact that at higher wind speeds, where the turbine starts to pitch and the turbine's thrust decreases, the Frandsen model converges towards the original DWM model. The static DWM model seems to be capable of eliminating this phenomenon by adjusting the rotor-averaged TI with the calibration factor, even though, the real physical reason of the load decrease, i.e. the wind speed deficit, is not considered. Overall, it can be stated that compared to the original DWM model, the static DWM model delivers higher loads at almost all conditions. Only at low TIs around 4 % and 6 %, the tower bottom and flapwise moments result in lower loads than those of the original DWM model. Finally, it should be mentioned that the tower bottom bending moment coincides best with the original model, which predicates on the fact that the calibration factor is in most cases

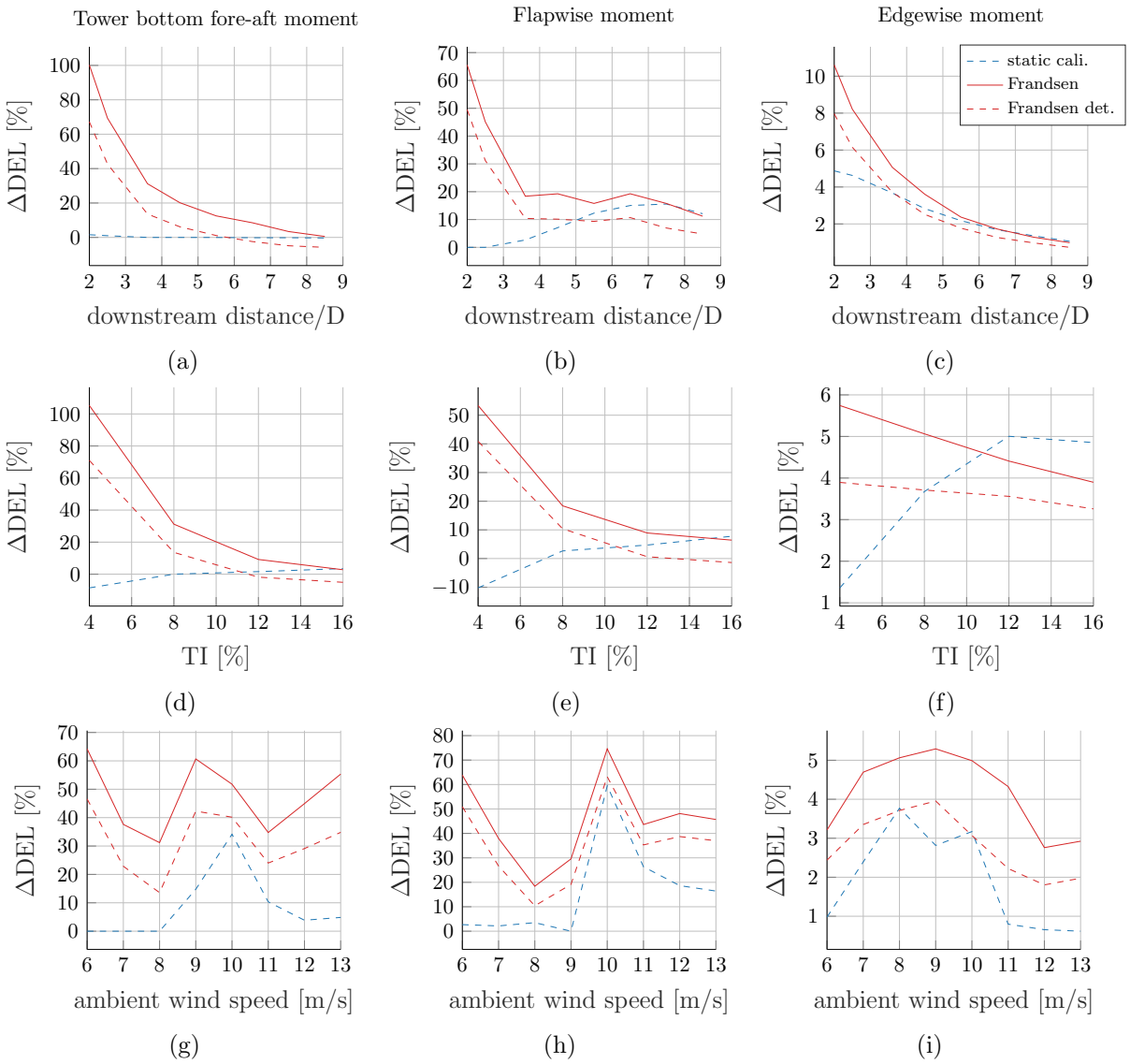

Figure 7.39: DEL deviations of the static DWM and the Frandsen model with respect to the original DWM model. The simulations were carried out with an ambient wind speed of 8 m/s and an ambient TI of 8 % for varying downstream distances (**(a)** to **(c)**), for a fixed ambient wind speed of 8 m/s, but varying ambient TIs (**(d)** to **(f)**), and for a fixed ambient TI of 8 %, but varying ambient wind speeds (**(g)** to **(i)**), both of the latter at a downstream distance of $3.61D$ (Reinwardt et al. 2020b).

derived from this load component.

This section provides an extension of the DWM model towards a static model with a homogeneous TI over the whole wind field, enabling its application for load approximation methods, which are commonly used in site-specific load calculation processes. Furthermore, the computational costs of the developed model are very low, making it a valid alternative to the Frandsen model, when implemented in wind farm layout optimization processes. For this purpose, the utilization of a PDF to describe the meandering together with a single-point spectrum has been applied as outlined in Chapter 5. It has been shown that the rotor-averaged TI (TI-Rotor) correlates with the turbulence depending loads. Based on this correlation, the calibration factor has been determined as a function of the downstream distance and the ambient wind speed to adjust TI-Rotor. The calibration factor has been determined to match the fatigue loads of the turbulence-depending loads calculated by the original DWM model. The effective TI calculated by the new static DWM model and the Frandsen model has been evaluated. The effective TI calculated by the new static model is less conservative for low TIs and small downstream distances. Furthermore, a comparison of the new static DWM model with the Frandsen and the original DWM model regarding fatigue loads has been carried out. Overall, a good agreement between the loads based on the calibrated static DWM model and those based on the original model is achieved. At low downstream distances the Frandsen model predicts significantly higher loads than the DWM model. Especially in this region, the new static DWM model confirms to be an improvement to the commonly used Frandsen model.

Chapter 8

Conclusions and outlook

8.1 Conclusions

The outlined thesis can be divided into three parts and summarized as follows. The first part (I) focuses on the validation and recalibration of the DWM model. Special attention is given to onshore wind farms with small turbine distances. The second part (II) investigates the application of the DWM model to multiple wakes. The last part (III) presents and evaluates an extension of the DWM model towards a static version to enhance the applicability for site-specific load simulations and layout optimization processes.

I. In this thesis, the DWM model has been recalibrated with lidar measurements at the Curslack wind farm. The measurement campaign in Curslack includes two nacelle-mounted lidar systems. The lidar measurements were prepared by lidar and wind field simulations to determine a suitable scan pattern. The one-dimensional scan worked reliably in the field campaign delivering lidar data for a multitude of different ambient conditions. These measurements have been compared to the simulated wind speed deficits in the HMFR. The comparison has led to the conclusion that the simulation result of the DWM-Keck model is in good agreement with the measurements, whereas the DWM-Egmond model yields an insufficient degradation of the wind speed deficit. Furthermore, even the DWM-Keck model shows some discrepancies to the measurements at low turbulence intensities, so that a recalibration of the model has been carried out. The recalibrated model (DWM-Keck-c) improves the correlation with measurements at low turbulence intensities and leads to an agreement at high turbulence intensities. The results are as good as those of the original model, thus resulting in a very strong overall conformity with the measurements.

In a next step, measured and simulated loads have been compared under wake conditions to evaluate the performance of different DWM model versions regarding fatigue loads. Special focus has been put on the newly calibrated DWM model. Additionally, a comparison with the commonly used Frandsen wake-added turbulence model has been performed. The evaluation has proven that the outcome of the newly calibrated DWM model fits very well to measured fatigue loads, whereas the Frandsen model delivers very conservative results for small turbine distances. Furthermore, constrained wake model simulations based on the lidar measurements have been presented. The measured wind speed deficit in HMFR as well as the measured time series of the meandering have been

incorporated into the wake simulations. The incorporation of the wind speed deficit has led to insignificant improvements, which supports the finding that the shape of the wind speed deficit in the HMFR could already be largely reproduced by the recalibrated DWM model. The incorporation of the meandering time series, on the other hand, resulted in a better agreement with the measurements.

Moreover, to evaluate whether the findings based on the measurement campaign at the Curslack wind farm are applicable at different sites, measurements at the Wieringermeer site have been analyzed. Met mast measurements of the mean wind speed deficit and the TI in the FFR have been used to validate the different DWM models including the newly recalibrated version. Additionally, measured and simulated fatigue loads have been assessed and a comparison with the Frandsen model has been conducted. The evaluation of the measurements at the EWTW has strengthened the findings from the analysis of the Curslack wind farm and supports the assumption that the recalibration is applicable to other onshore wind farms with small turbine distances. However, only a limited data set could be evaluated at the EWTW site, so that no broad investigation over different ambient conditions was carried out.

II. In the second part of the thesis, different methods to handle multiple wakes in the framework of the DWM model have been investigated. Overall, it could be stated that the implementation of multiple wakes in the DWM model is far from trivial, as the DWM model is built in a way that requires a steady-state axisymmetric velocity field and a homogeneous TI at the wake generating turbine. However, in a multiple wake situation the second turbine in a row in downstream direction is affected by an inhomogeneous and unsteady wind field. In the DWM model, a steady-state axisymmetric velocity field is necessary to calculate the boundary conditions to solve the thin shear layer equation and predict the steady-state wind speed deficit in the MFR.

In the thesis, five different methods to handle multiple wakes in the DWM model have been investigated. The first method considers only the wake of the closest wake generating turbine (wct), whereas the second always takes the minimum wind speed of all upstream wakes at each point of interest in the wake (IEC-min) into account. Additionally, two different wake summation approaches have been analyzed. The first aggregates all upstream wakes with a quadratic summation (ws-q), whereas the second adds the wakes linearly (ws-l). The last method (Keck) calculates the inflow at each upstream turbine successively, so that the inflow conditions change at each turbine in the row and the wake effects of all upstream turbines are included implicitly. In accordance with this method, no wake summation is necessary. The different methods have been compared to lidar measurements of the mean wind speed deficit in a double wake situation. Moreover, measured and simulated fatigue loads have also been evaluated in a double wake situation. All measurements were conducted in the Curslack wind farm.

It could be concluded from the multiple wake analysis that the IEC-min method agrees best with the measured wind speed deficit in the HMFR in most of the evaluated situations. The IEC-min model is recommended in the guideline. Furthermore, the very simple method wct, which only considers the closest turbine wake, also delivers results that coincide well with the measured wind speed deficit and deviate only slightly from the IEC-min method. The analysis has revealed a different validity of the methods when comparing the wind speed deficits in the FFR instead of the HMFR, which is very likely related to

the approach to handle the wake meandering in a double wake situation. Some deviations between the modeled and measured wake meandering could be identified. Nevertheless, it has been observed that both the modeled power output and the fatigue loads at a turbine in a double wake situation agree well with the simulations. Only small differences were obtained over all model variants.

III. The last part of the thesis is the extension of the DWM model towards a static version for site-specific load simulations. Although the newly recalibrated DWM model predicts the fatigue loads in the wake very well, it is not applicable in a standard site-specific load calculation procedure, as it delivers an inhomogeneous and instantaneous wind field. The DWM model is built in such a way that it can be directly connected to an aeroelastic load simulation tool. However, in a common site-specific load calculation process, time-consuming aeroelastic simulations are usually avoided and the loads are estimated based on interpolations of already performed load simulations. The interpolation method (e.g. response surface method) depends on a single TI value, which is assumed to be constant over the whole rotor area, so that this load estimation method is not combinable with the DWM model. The static version of the DWM model addresses this issue and provides a single TI value, hence enabling its implementation into simple load estimation procedures.

Additionally, the extension of the model is built in a way that the computational costs are very low, making an implementation in a wind farm layout optimization process possible. For this purpose, the utilization of a PDF to describe the meandering together with a single-point spectrum has been applied. Based on this approach, the mean wind speed and TI in the FFR can be calculated. Comparing the results to the original DWM model provided a very good agreement. The simplification has proven to be a fast and appropriate alternative.

Another important part of the model extension is the definition of a rotor-averaged TI, which is supposed to correlate with turbulence-dependent loads of the turbine. It has been demonstrated that a rotor-averaged TI, which is calculated with respect to the Wöhler coefficient (S/N slope), correlates very well with the turbulence-dependent fatigue loads. Based on the correlation, calibration factors have been determined as a function of the downstream distance and the ambient wind speed to match the fatigue loads calculated by the original DWM model.

The extension of the DWM model has been evaluated by a comparison of the effective TI calculated by the new static DWM model and the Frandsen wake-added turbulence model. The analysis has demonstrated that the effective TI calculated by the new static model is less conservative for low TIs and small downstream distances than the Frandsen model. Moreover, the fatigue loads calculated by the new static DWM model and the Frandsen model have been compared to the calculated fatigue loads from the original DWM model. Overall, a good agreement between the loads based on the calibrated static DWM model and those based on the original model has been achieved. At low downstream distances, the Frandsen model predicts significantly higher loads than the static DWM model, albeit which, is slightly more conservative than the original DWM model.

In summary, this thesis provides a recalibrated version of the DWM model, which has proven to be more accurate regarding wind characteristics and fatigue loads under wake conditions at onshore sites with small turbine distances and flat terrain. An extension of

the DWM model towards a static model for site-specific load approximations has been developed and exhibited to be an improvement to the commonly used Frandsen model, especially for short turbine distances. Additionally, different methods to evaluate multiple wakes in the DWM model have been evaluated. The outcome suggests that taking the minimum wind speed of all upstream wakes at each point of interest in the wake (IEC-min) is a good approximation of the merged wake. Furthermore, the very simple method of only considering the closest turbine wake delivers similar results as the IEC-min method regarding fatigue loads and might be a simple alternative with sufficient accuracy, whereby it is suggested to be applied in the new static version of the DWM model.

8.2 Outlook

As summarized in the previous section, the outlined recalibration of the DWM model has only been validated based on measurements from two wind farms so far. Thus, future work should include a broader evaluation of the recalibrated model versions at more sites with different turbine types and distances. Furthermore, it is suggested to validate the performance of the model against a more comprehensive collection of ambient conditions. The model has only been sufficiently validated against low to moderate ambient TIs. Moreover, the mean wind speed deficit could only be evaluated in the HMFR and not in the MFR, as only a line has been scanned. Therefore, future work can include an analysis of lidar measurements from two-dimensional scans, so that the vertical meandering can also be investigated. Additionally, lidar measurements with more range gates and a higher spatial resolutions might be worth to analyze. Increasing the number of range gates and scan points will lead to longer scan times. However, this would prevent further analysis of the wind speed deficit in the HMFR and the determination of the meandering time series due to the high scan time of the pulsed scanning lidar system used. Nevertheless, a validation of the wind speed deficit in the FFR with higher resolutions and more distances seems reasonable to prove the validity of the outlined calibration also for further distances. Another possibility would be to repeat the analysis with a different lidar device with a shorter scan duration.

Another part of the thesis was the incorporation of the lidar measurements, respectively, the measured mean wind speed in the HMFR and the meandering time series, in the load simulation. The constrained simulations with lidar measurements have verified that the conformity between measured and simulated loads can be enhanced by incorporating the measured meandering as well as the wind speed into the aeroelastic load simulation. Up to now, only a horizontal line with only a few scan points has been measured with the lidar system. Thus, a more detailed scan of the wake with a higher temporal resolution might even lead to a further decrease of the uncertainties in the load and power predictions. By incorporating the measured meandering time series into the load simulation, a better agreement with the measurements could be achieved, which indicates that there remains room for improvements in the physical description of the meandering. Furthermore, the significance of further research on wake meandering is underlined.

The analysis of multiple wakes offers potential for more investigations. Multiple wakes have been evaluated only at one wind farm with a limited data set, so that it is recommended to repeat the investigation at different wind farms and ambient conditions. Especially for the evaluation of loads, only a very limited data set could be used, so that future investigations of the predicted loads with the DWM model in a multiple wake situation and a comparison with measurements would be a valuable investigation. Additionally, this study has only analyzed loads in a double wake situation, so that future work should include an analysis and comparison of fatigue loads in wind farms with several turbines in a row. The multiple wake analysis has shown that there are some discrepancies between the measured and simulated wake meandering in a double wake situation. This should also be addressed in the future. Considering only the closest turbine wake or the minimum wake of all upstream turbines leads to a meandering path, which is not sufficiently pronounced, as the influence of the further upstream turbines in the meandering process is not dominant enough.

The presented extension of the DWM model towards a static version delivers an applicable alternative to the commonly used Frandsen model as it could be demonstrated in the outlined investigation. Nevertheless, the calibration of the model is strongly related to the turbine type and needs to be repeated for every type. Hence, it is recommended to derive more generally accepted calibration factors to achieve an easier application of the model extension. Furthermore, to date no reduction of the wind speed has been included in the model definition. The influence of the wind speed reduction on the fatigue loads is only indirectly captured by the calibration factor. Thus, it is worth investigating this issue in a physically more correct manner to include the wind speed reduction in the static DWM model definition. A solution for the incorporation of the wind speed deficit could be achieved by a rotor-averaged wind speed calculation, which in turn can be calculated from the mean wind speed deficit in the FFR.

Overall, future work, should be mainly related to a broader investigation of the performance of the recalibrated DWM model at different wind farms as well as the derivation of a more generally accepted calibration factor of the static DWM model version.

Appendix A

Data processing

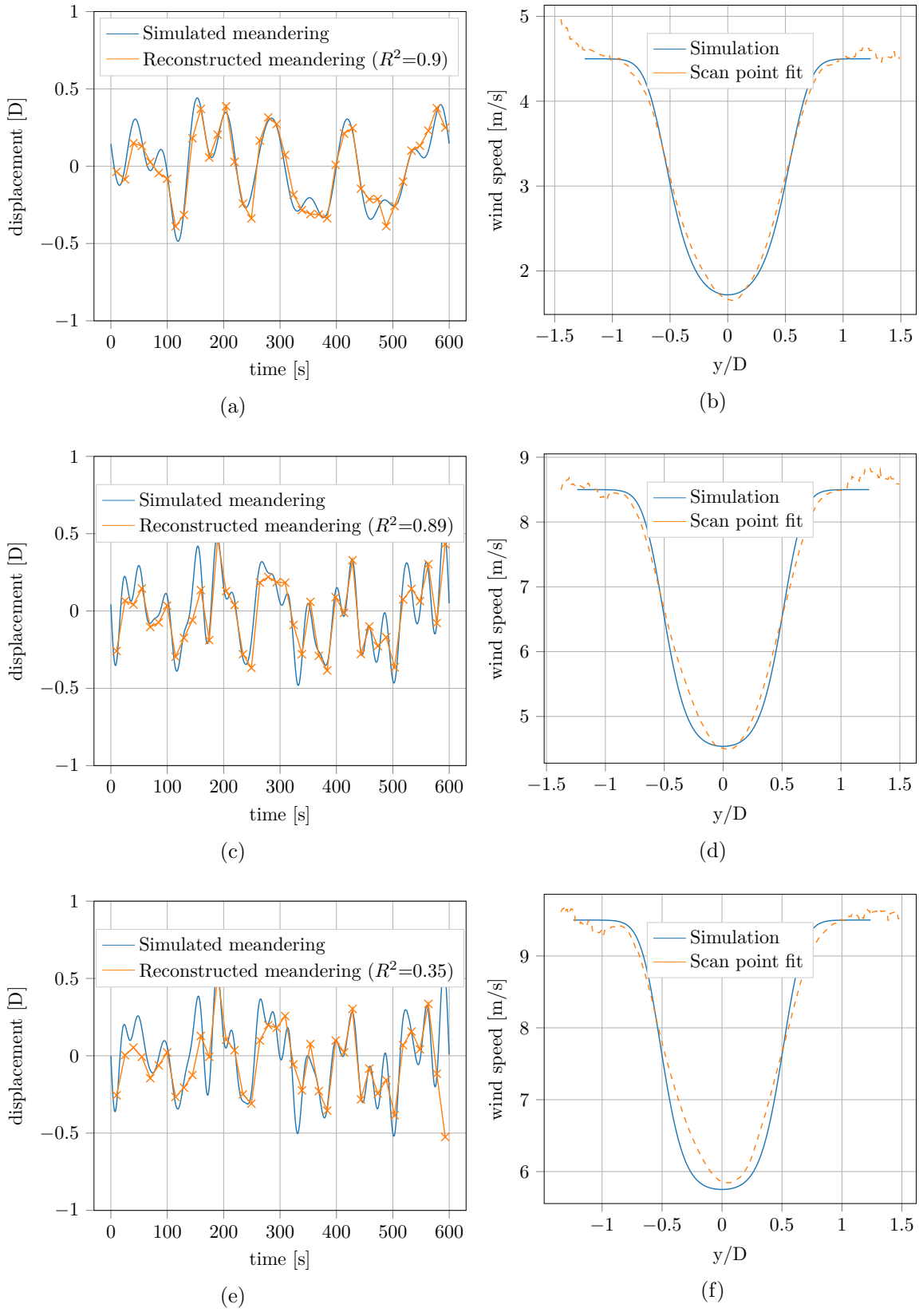

Figure A.1: Simulated and simulated "measured" meandering time series **(a, c, e)** and wind speed deficit in the HMFR **(b, d, f)** at a downstream distance of 3.61 D, an ambient TI of 12 % and an ambient wind speed of 4.5 m/s **(a, b)**, 8.5 m/s **(c, d)** and 9.5 m/s **(e, f)**.

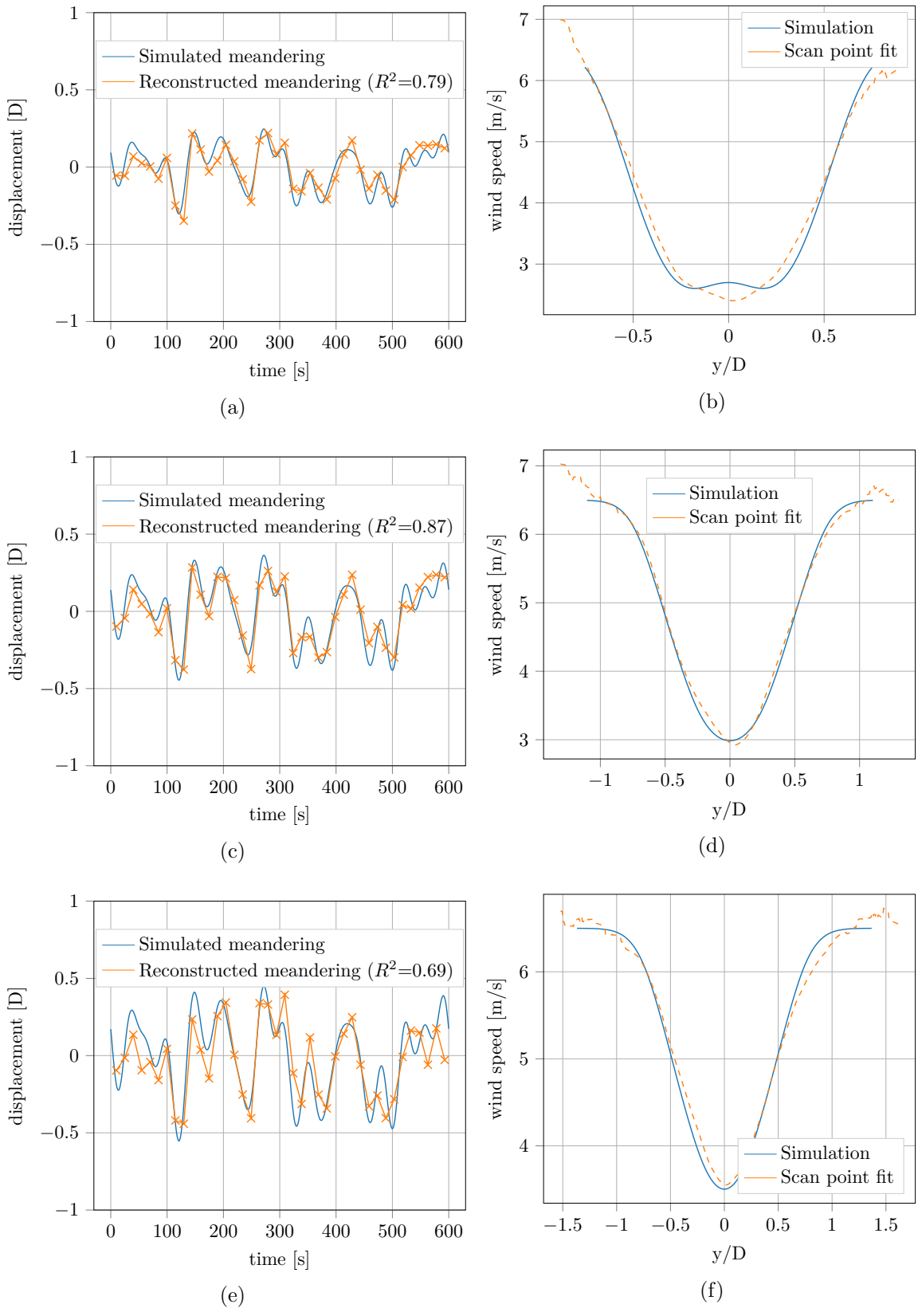

Figure A.2: Simulated and simulated "measured" meandering time series **(a, c, e)** and wind speed deficit in the HMFR **(b, d, f)** at an ambient wind speed 6.5 m/s, an ambient TI of 12 % and a downstream distance of 2.18 D **(a, b)**, 3.21 D **(c, d)** and 3.97 D **(e, f)**.

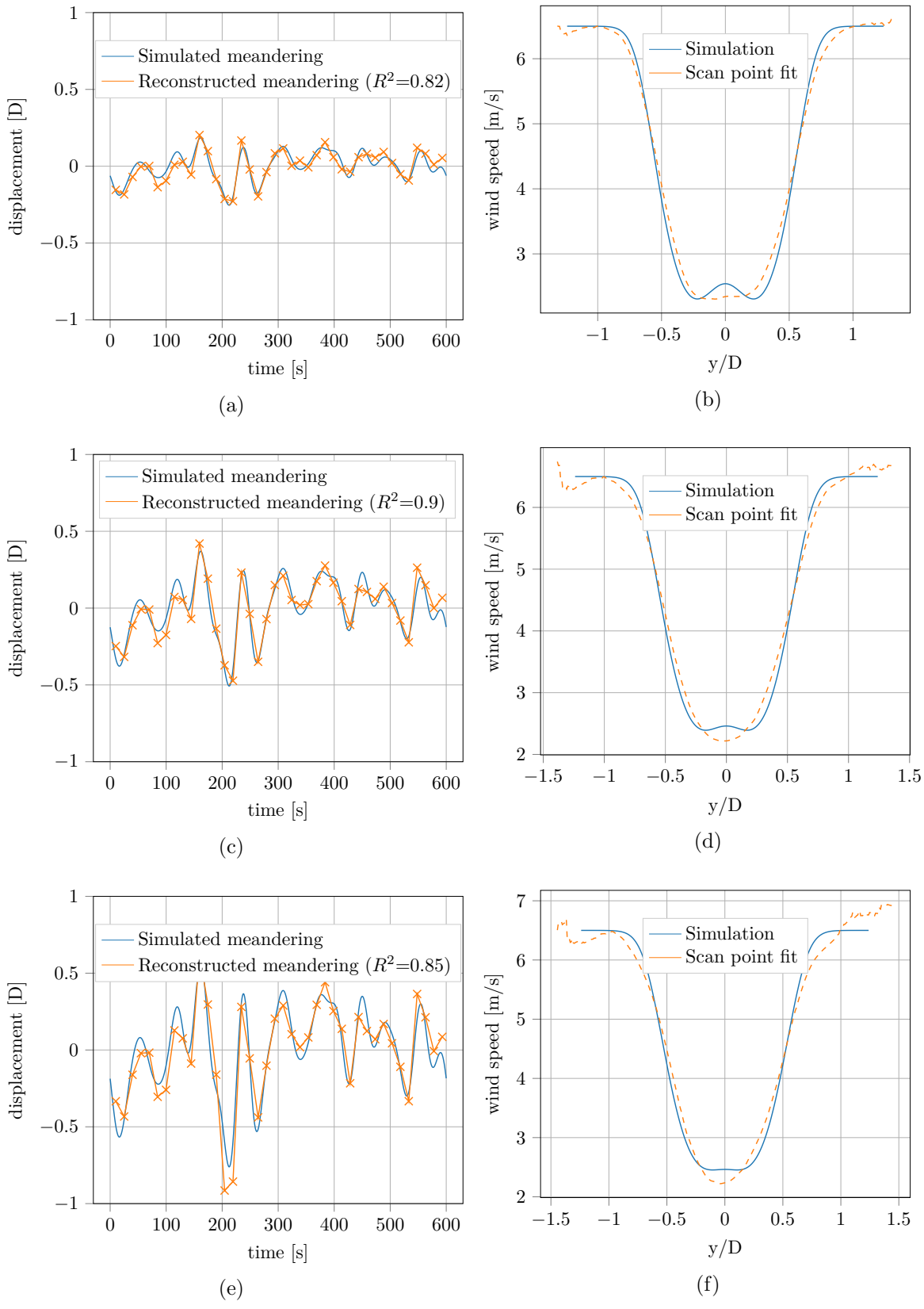

Figure A.3: Simulated and simulated "measured" meandering time series (a, c, e) and wind speed deficit in the HMFR **(b, d, f)** at a downstream distance of 3.61 D, and an ambient wind speed of 6.5 m/s and an ambient TI of 5 % **(a, b)**, 10 % **(c, d)** and 15 % **(e, f)**.

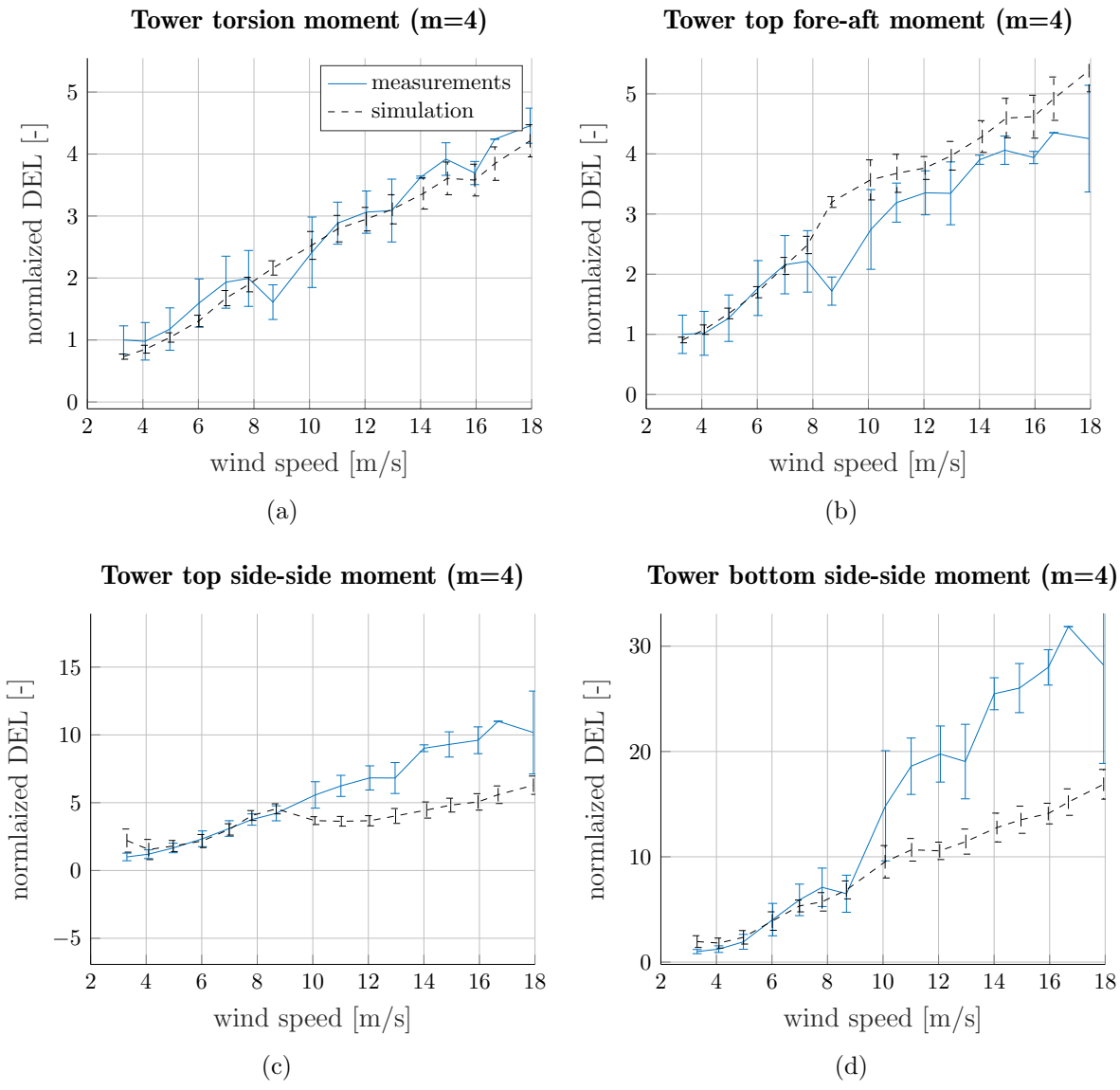

Figure A.4: Measured and simulated tower torsion **(a)**, tower top fore-aft moment **(b)**, tower top side-side moment **(c)** and tower bottom side-side moment **(d)** at WTG 2 at an ambient TI of 12 % and wake-free inflow.

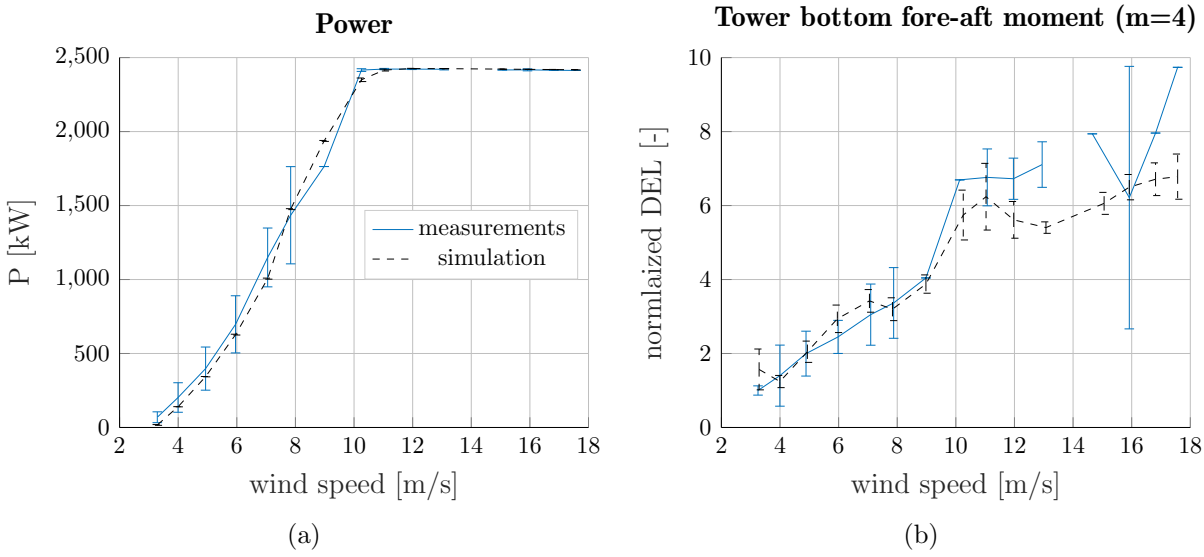

Figure A.5: Measured and simulated power **(a)**, and tower bottom fore-aft moment**(b)** at WTG 3 at an ambient TI of 12 % and wake-free inflow.

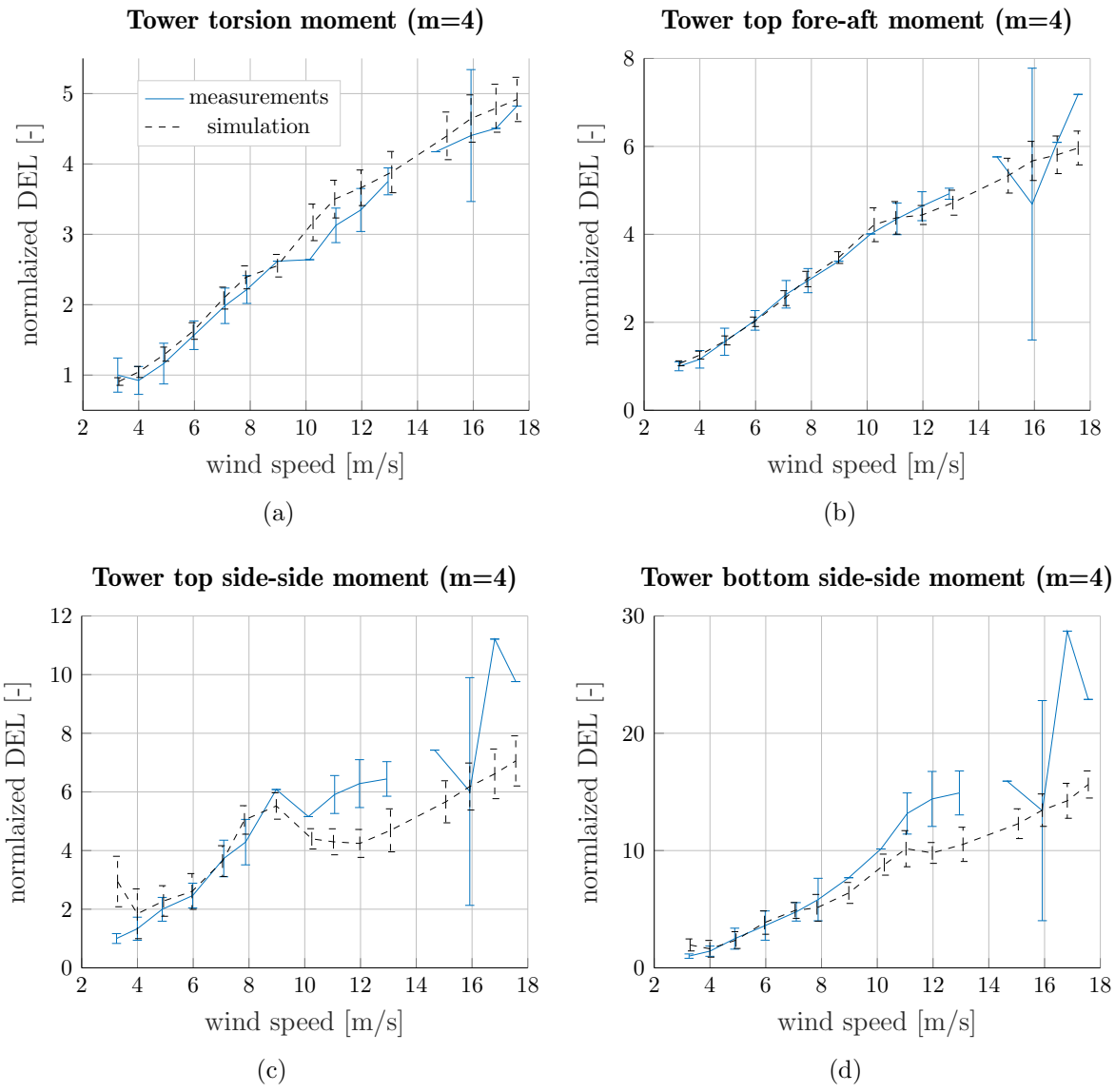

Figure A.6: Measured and simulated tower torsion **(a)**, tower top fore-aft moment **(b)**, tower top side-side moment **(c)** and tower bottom side-side moment **(d)** at WTG 3 at an ambient TI of 12 % and wake-free inflow.

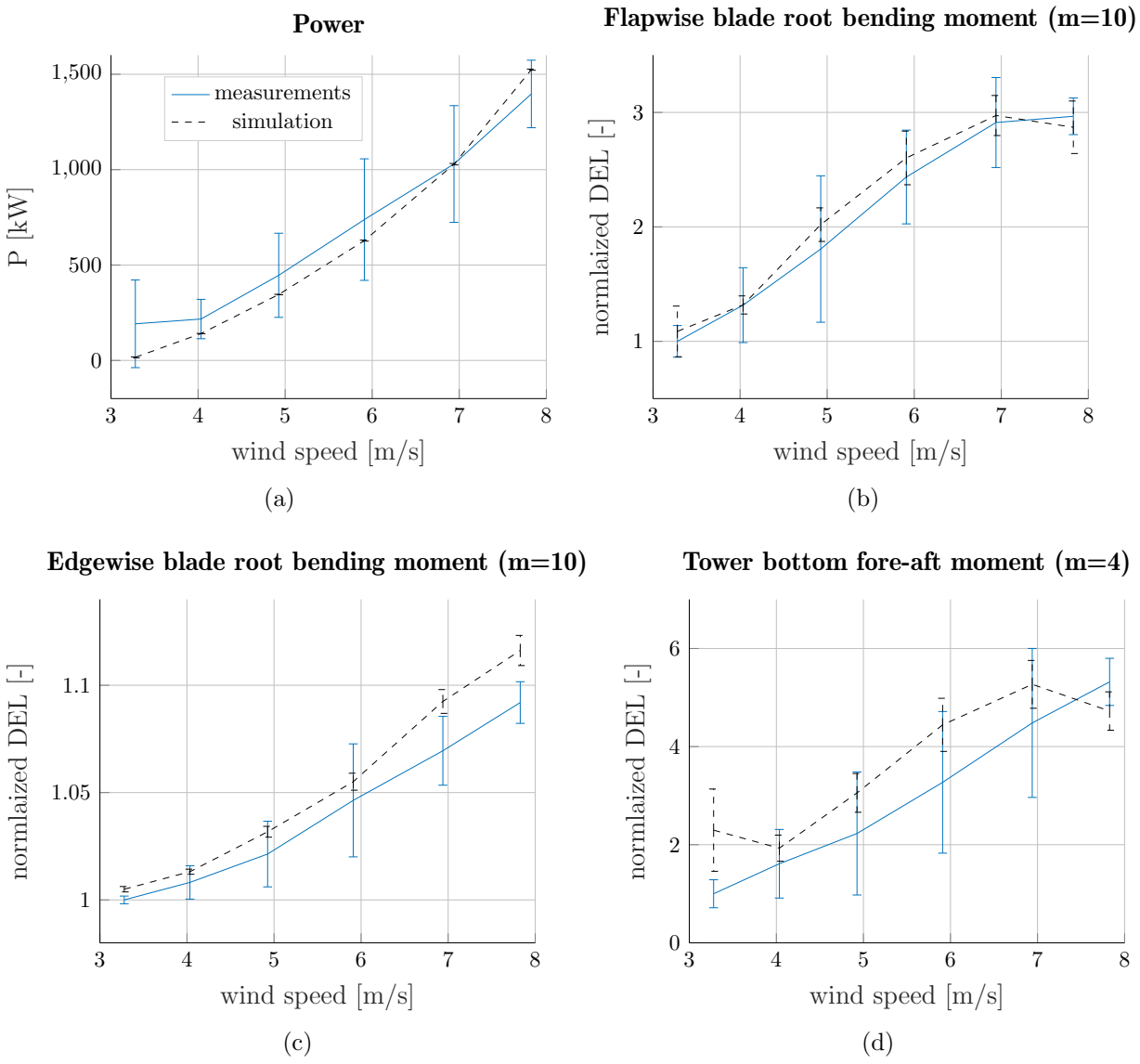

Figure A.7: Measured and simulated power **(a)**, flapwise blade root moment **(b)**, edgewise blade root moment **(c)** and tower bottom fore-aft moment **(d)** at WTG 5 at an ambient TI of 12 % and wake-free inflow.

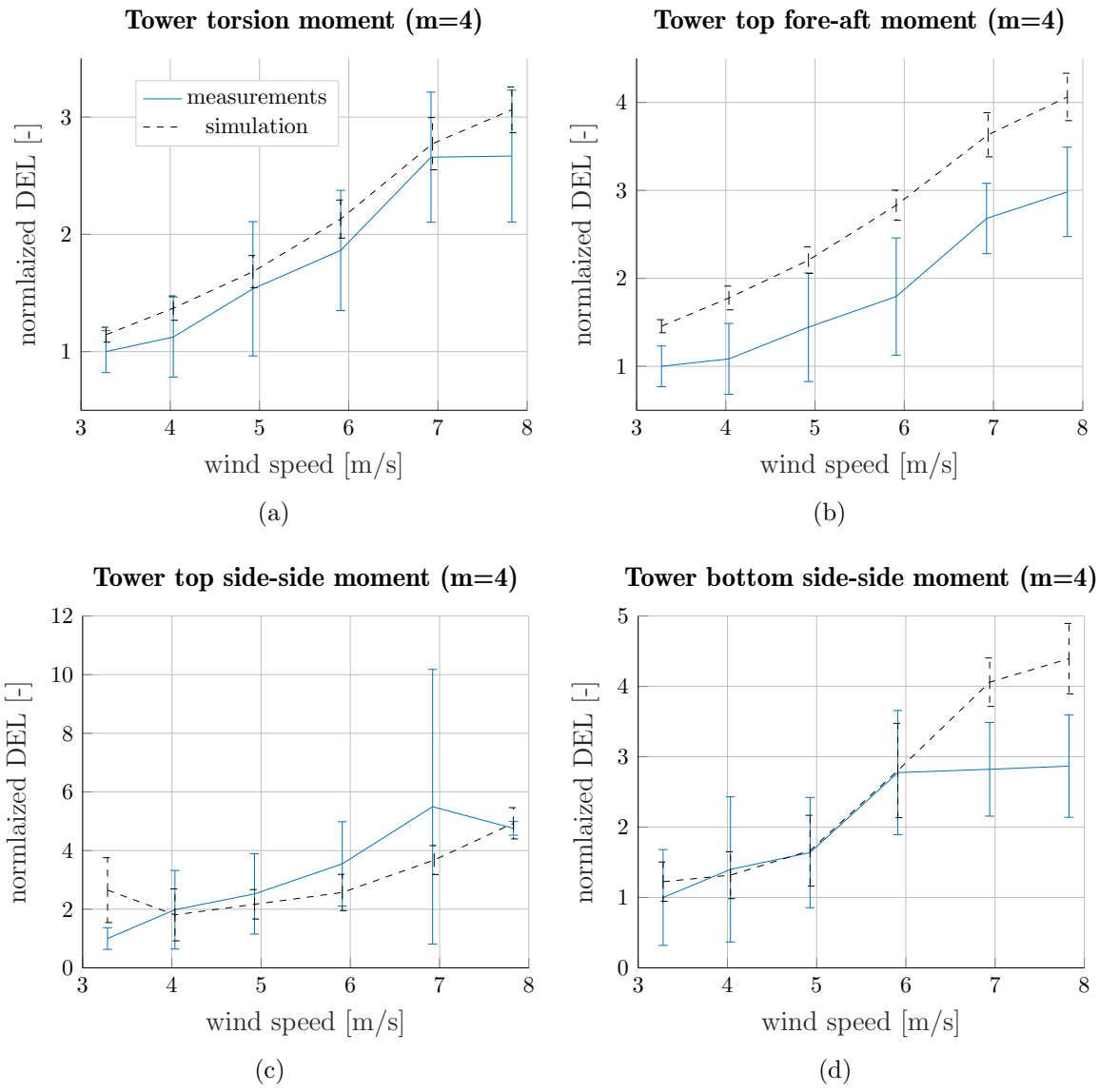

Figure A.8: Measured and simulated tower torsion **(a)**, tower top fore-aft moment **(b)**, tower top side-side moment **(c)** and tower bottom side-side moment **(d)** at WTG 5 at an ambient TI of 12 % and wake-free inflow.

Appendix B

Validation of wake models

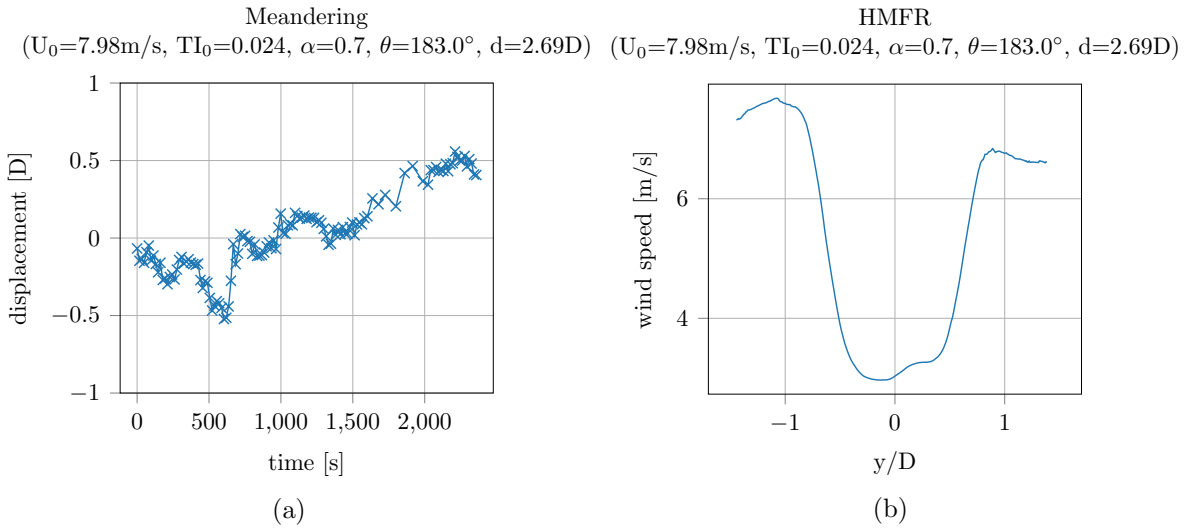

Figure B.1: Meandering time series **(a)** and wind speed deficit in the HMFR **(b)** at $2.69D$ downstream of the turbine (Reinwardt et al. 2020a).

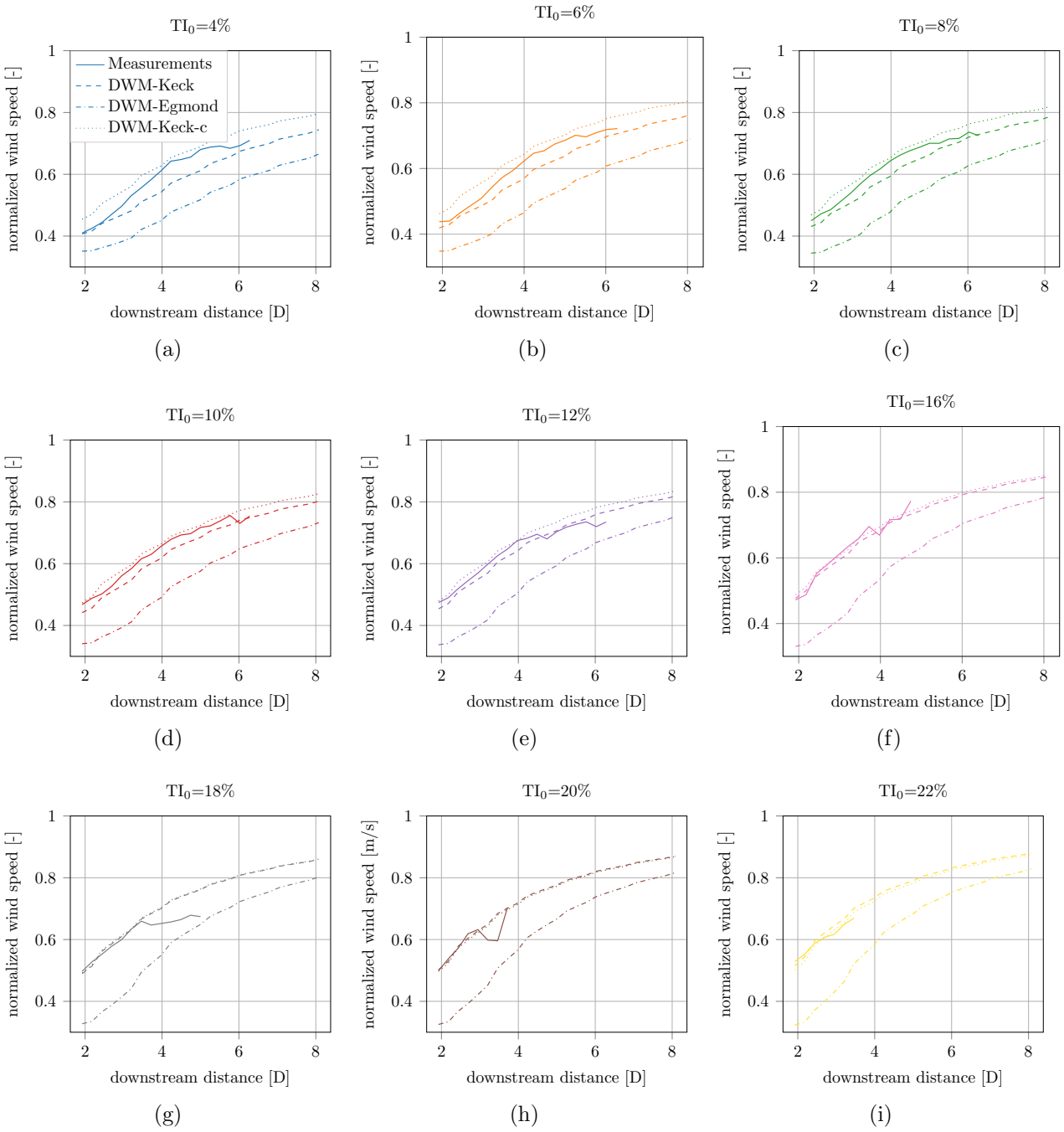

Figure B.2: Comparison of measurements and simulations of the rotor-averaged mean wind speed deficit in the HMFR for different turbulence intensities. The solid, the dashed and the dashed dotted line reflect the measurements, the results of the DWM-Keck model and those of the DWM-Egmond model, respectively. The recalibrated model is denoted DWM-Keck-c and depicted as a pointed line.

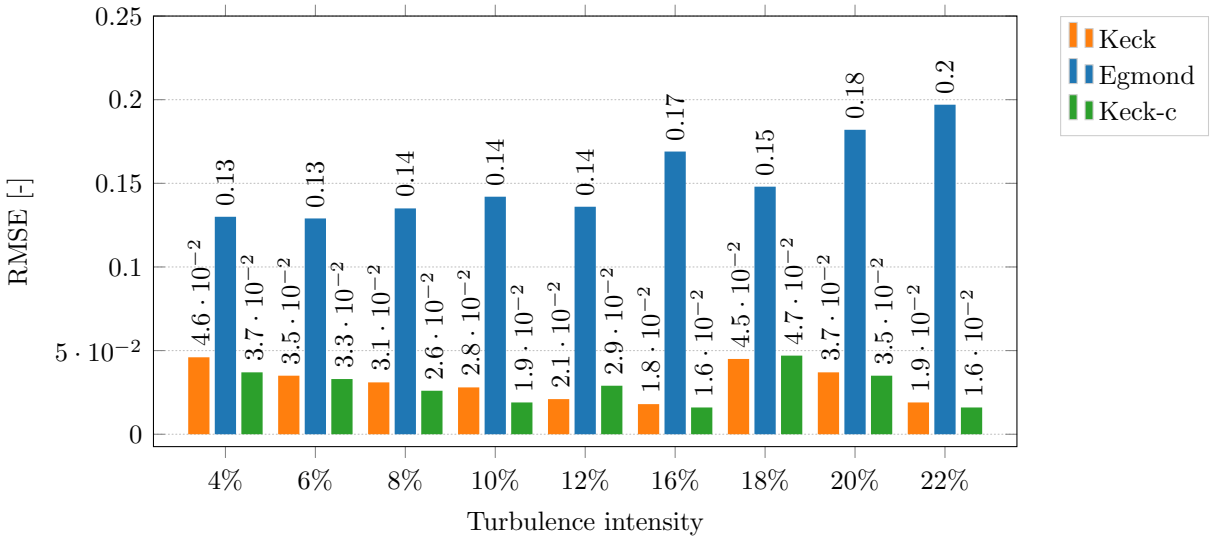

Figure B.3: RMSE between the lidar-measured and the simulated normalized rotor-averaged mean wind speed in the wake (Reinwardt et al. 2020a).

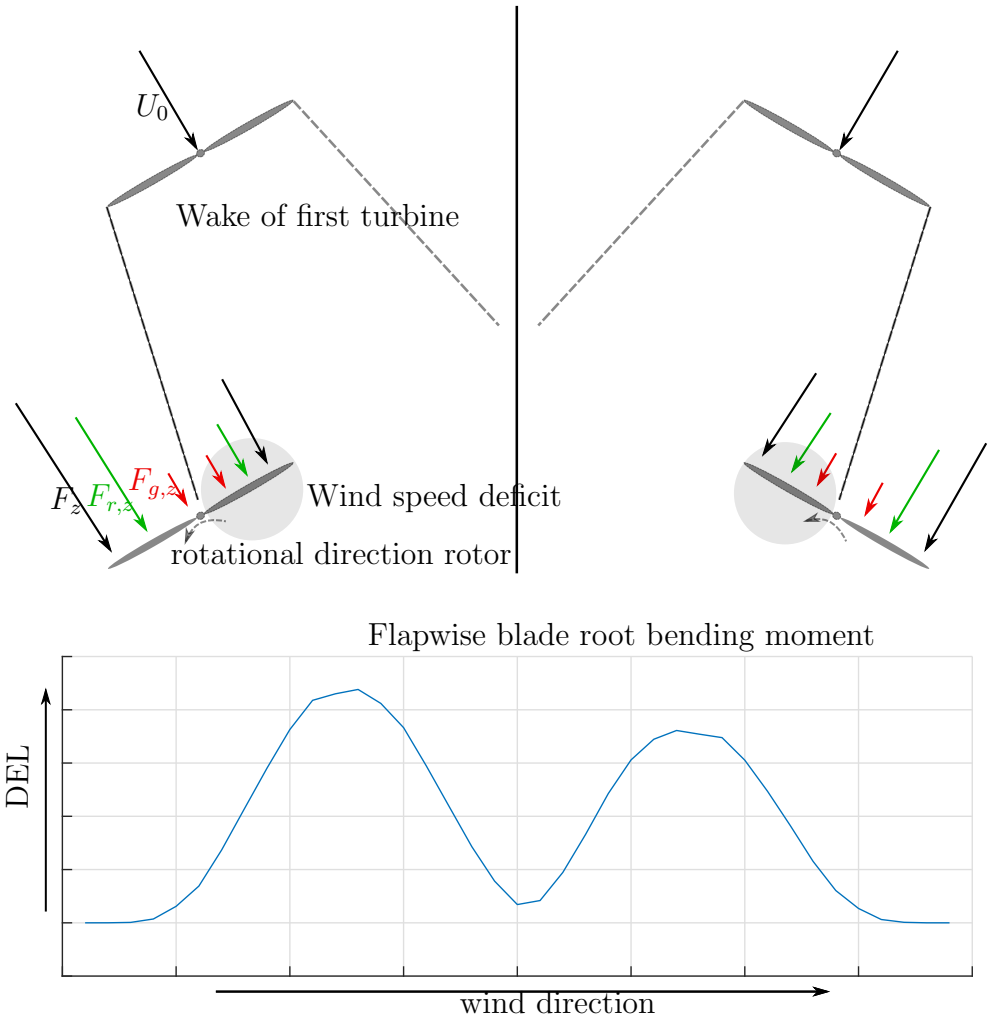

Figure B.4: Schematic illustration of the flapwise blade root bending moment in the rotating frame of reference. The aerodynamic force $F_{r,z}$, the gravitational force $F_{g,z}$ as well as the total force F_z perpendicular to the rotor plane at different wake situations are marked (Reinwardt et al. 2021).

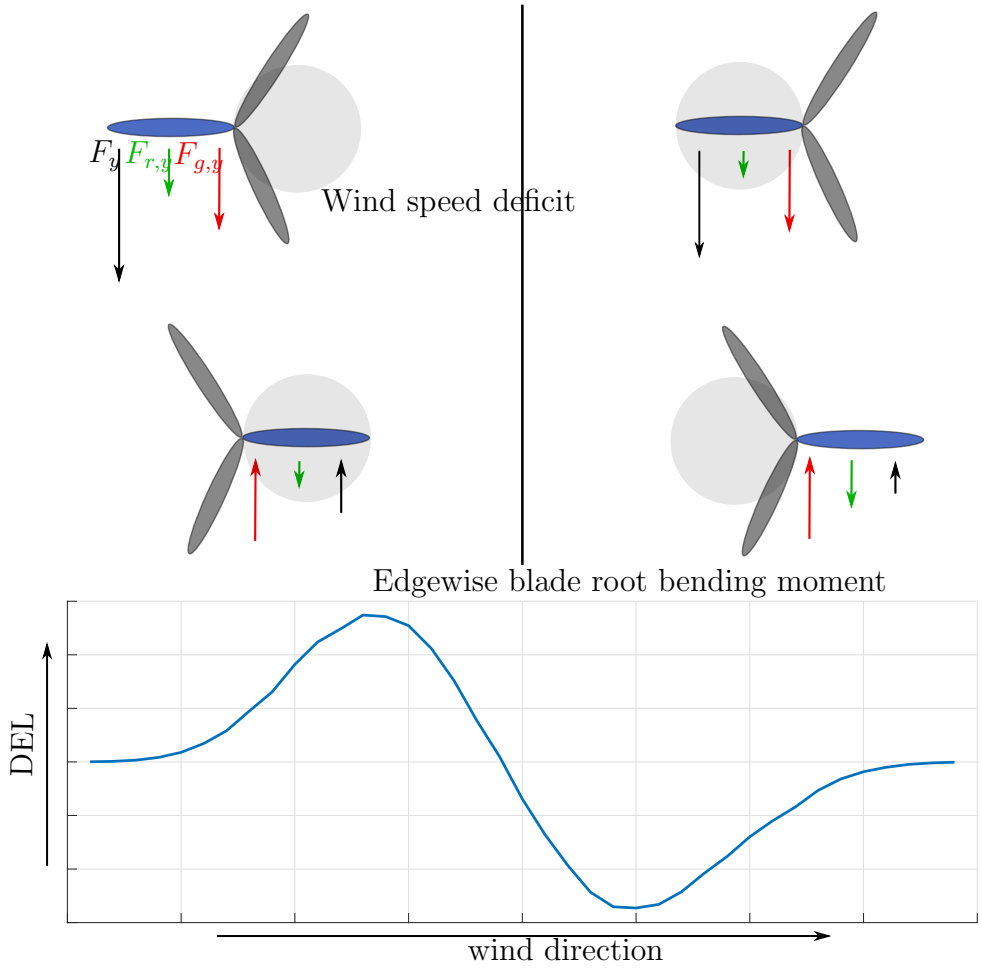

Figure B.5: Schematic illustration of the edgewise blade root bending moment in the rotating frame of reference. The aerodynamic force $F_{r,y}$, the gravitational force $F_{g,y}$ as well as the total force F_y in the rotor plane at different wake situations are marked (Reinwardt et al. 2021).

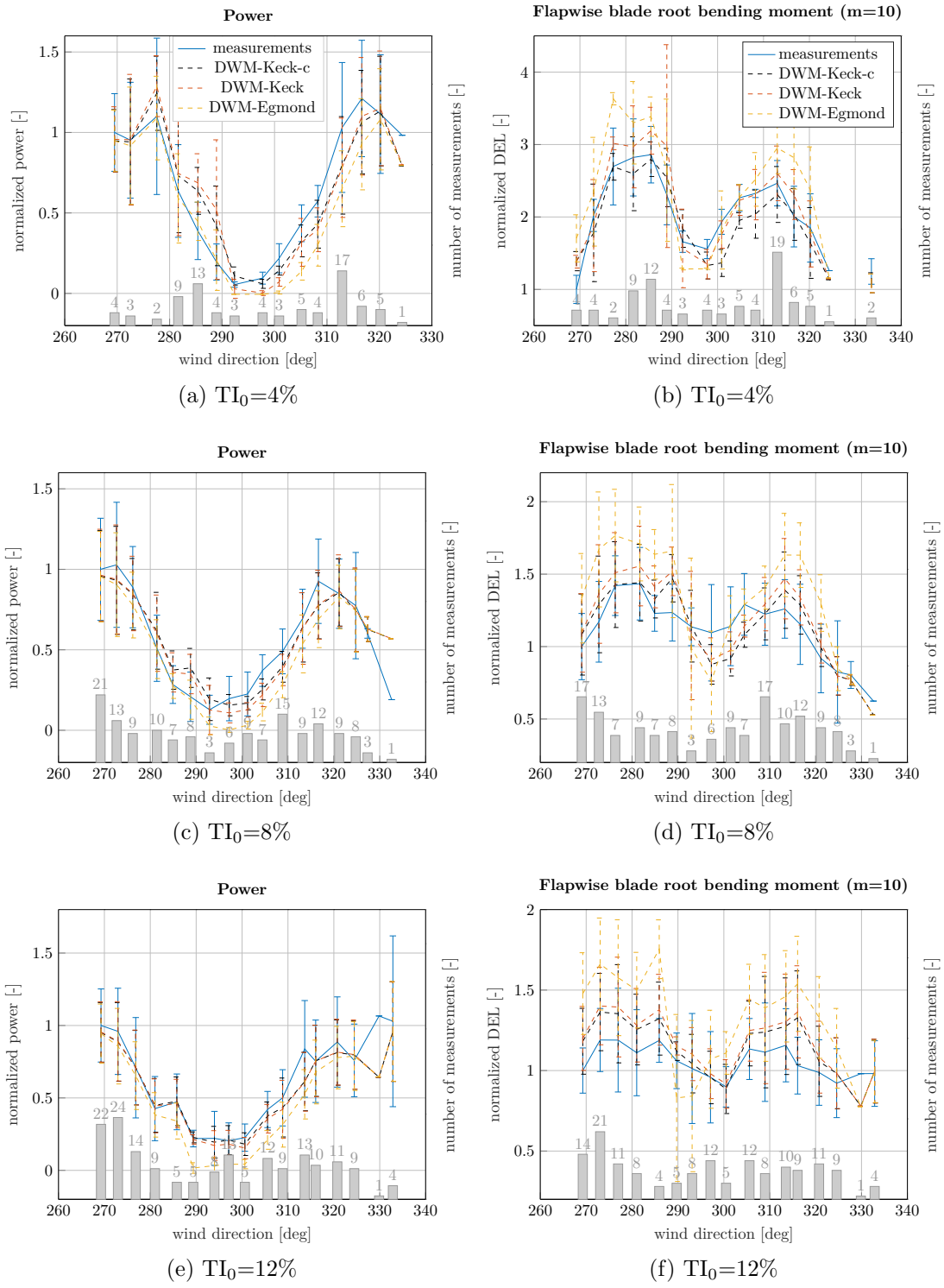

(a) TI_0=4% (b) TI_0=4%

(c) TI_0=8% (d) TI_0=8%

(e) TI_0=12% (f) TI_0=12%

Figure B.6: Measured and simulated power **(a)**, **(c)** and **(e)** as well as flapwise blade root bending moment **(b)**, **(d)** and **(f)** at an ambient wind speed of 6 m/s and an ambient TI of 4 % **(a)** and **(b)**, an ambient TI of 6 % **(c)** and **(d)**, and an ambient TI of 12 % **(e)** and **(f)** when WTG 2 is exposed to the wake of WTG 1. The number of measured 10-min time series in each wind direction bin is illustrated on the secondary axis (Reinwardt et al. 2021).

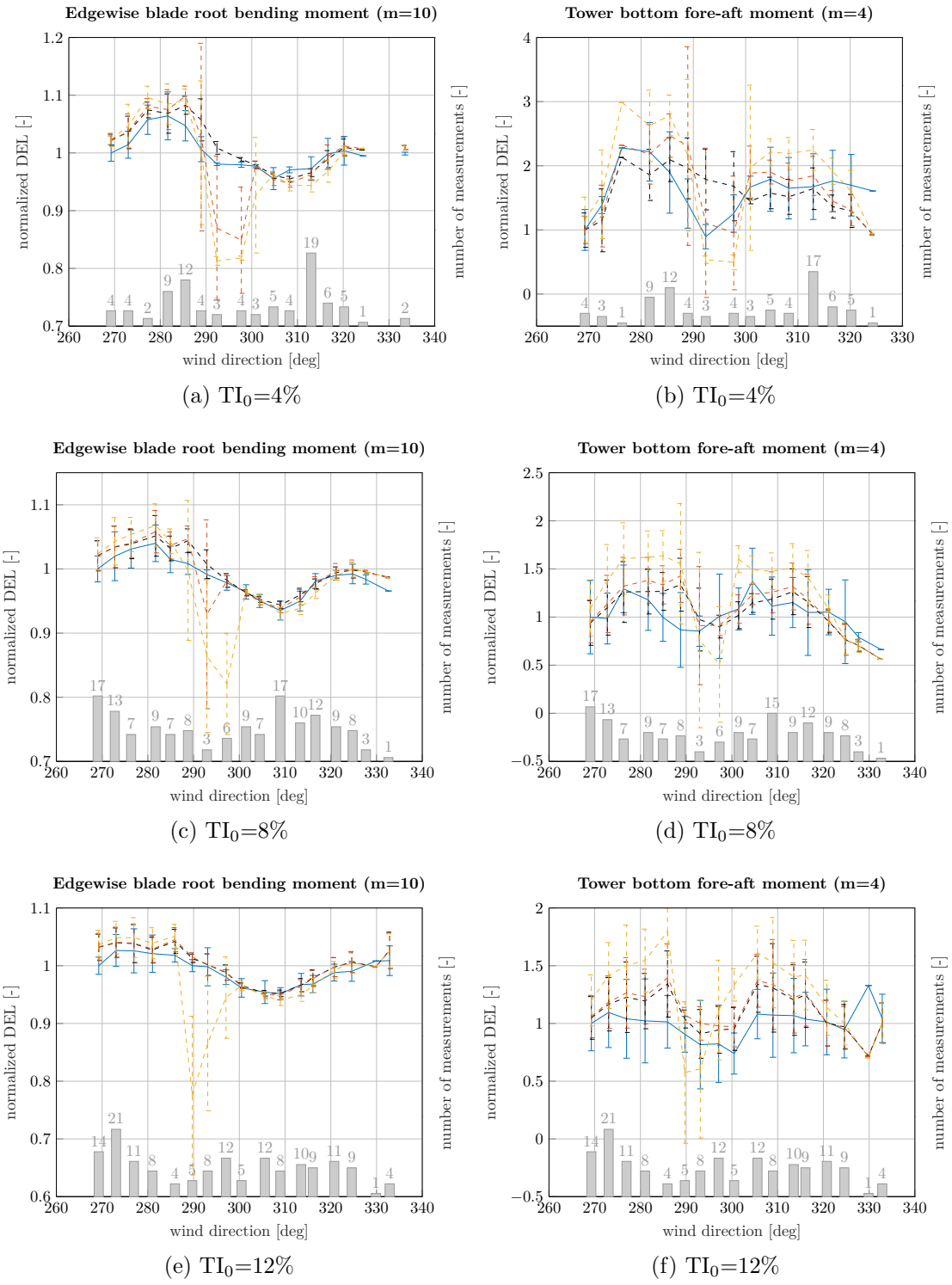

(a) TI_0=4% (b) TI_0=4%

(c) TI_0=8% (d) TI_0=8%

(e) TI_0=12% (f) TI_0=12%

Figure B.7: Measured and simulated edgewise blade root bending moment **(a)**, **(c)** and **(e)** as well as tower bottom fore-aft bending moment **(b)**, **(d)** and **(f)** at an ambient wind speed of 6 m/s and an ambient TI of 4 % **(a)** and **(b)**, an ambient TI of 6 % **(c)** and **(d)**, and an ambient TI of 12 % **(e)** and **(f)** when WTG 2 is exposed to the wake of WTG 1. The number of measured 10-min time series in each wind direction bin is illustrated on the secondary axis (Reinwardt et al. 2021).

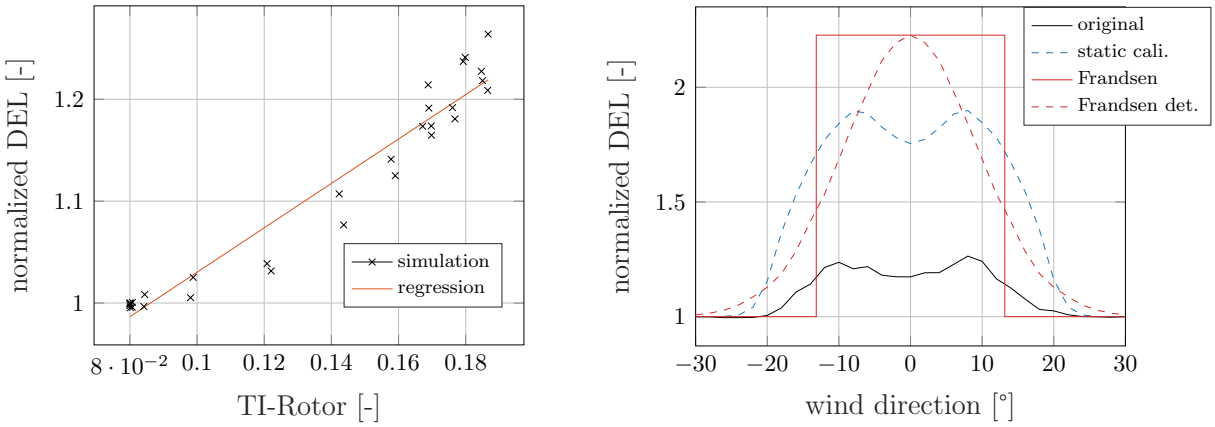

Figure B.8: Normalized main bearing fore-aft bending DEL over the rotor-averaged TI **(a)** and over the wind direction **(b)**. The DELs are calculated with a Wöhler coefficient of 14, an ambient wind speed of 8 m/s, an ambient TI of 8 %, and a downstream distance of $3.61D$.

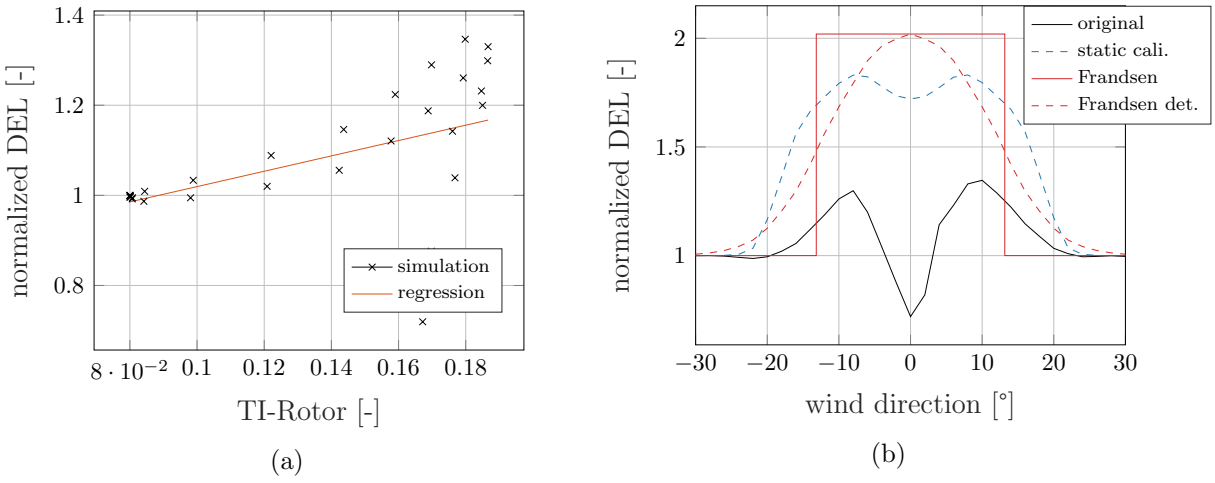

Figure B.9: Normalized main bearing torque DEL over the rotor-averaged TI **(a)** and over the wind direction **(b)**. The DELs are calculated with a Wöhler coefficient of 14, an ambient wind speed of 8 m/s, an ambient TI of 8 %, and a downstream distance of $3.61D$.

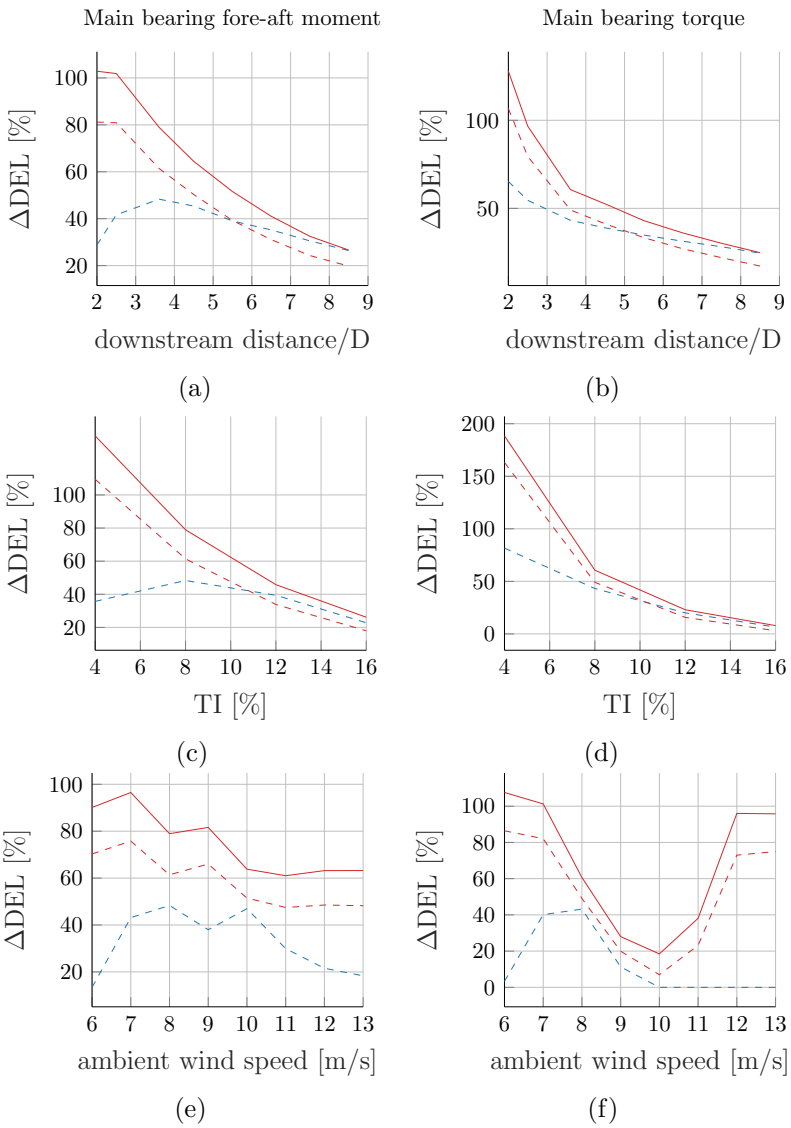

Figure B.10: DEL deviations of the static DWM and the Frandsen model with respect to the original DWM model. The simulations were carried out with an ambient wind speed of 8 m/s and an ambient TI of 8 % for varying downstream distances (**(a)** to **(c)**), for a fixed ambient wind speed of 8 m/s, but varying ambient TIs (**(d)** to **(f)**), and for a fixed ambient TI of 8 %, but varying ambient wind speeds (**(g)** to **(i)**), both of the latter at a downstream distance of $3.61D$.

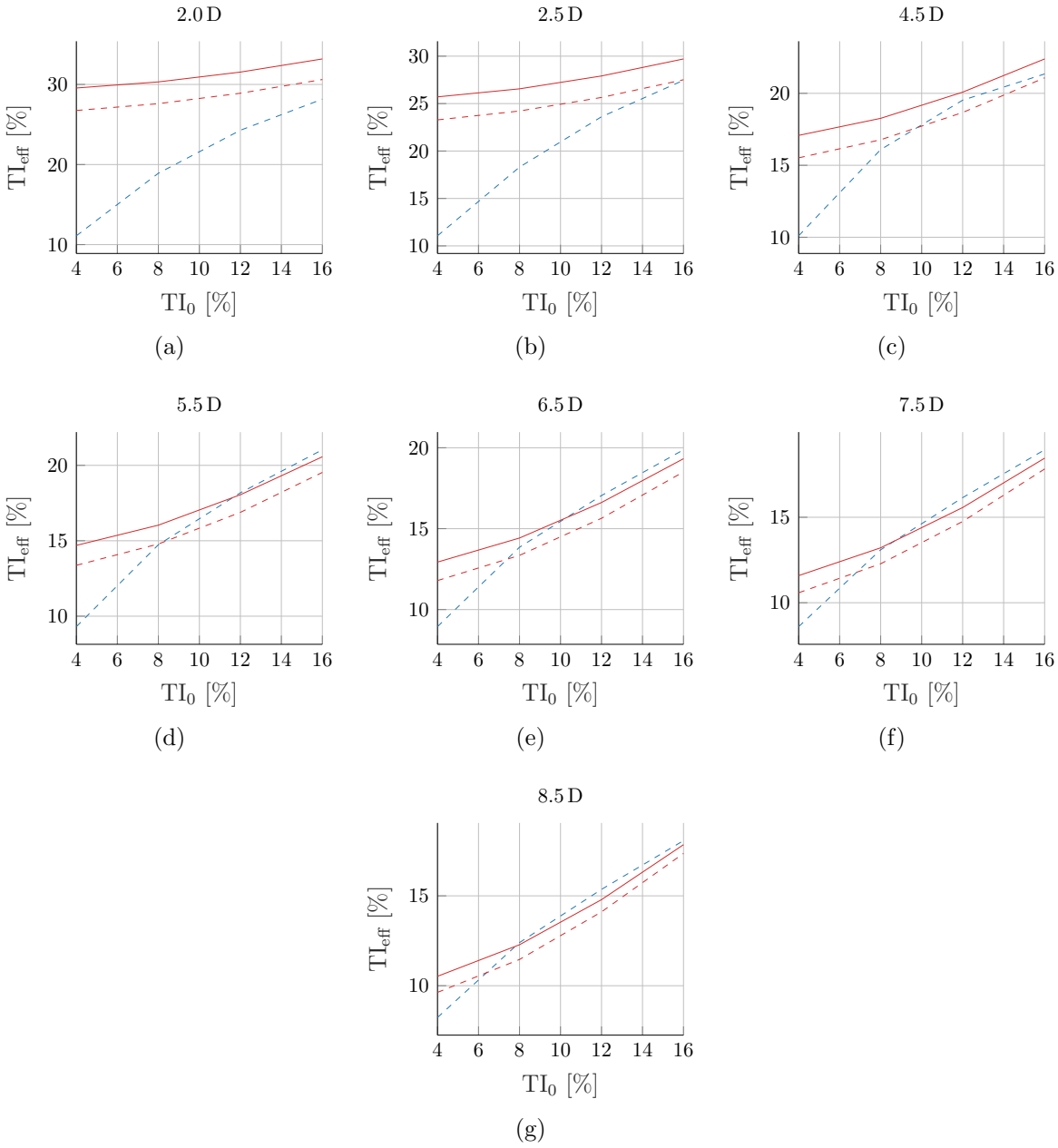

Figure B.11: Effective TI of the static DWM and the Frandsen models over the ambient TI. The simulations were carried out with an ambient wind speed of 8 m/s and a Wöhler coefficient of 14.

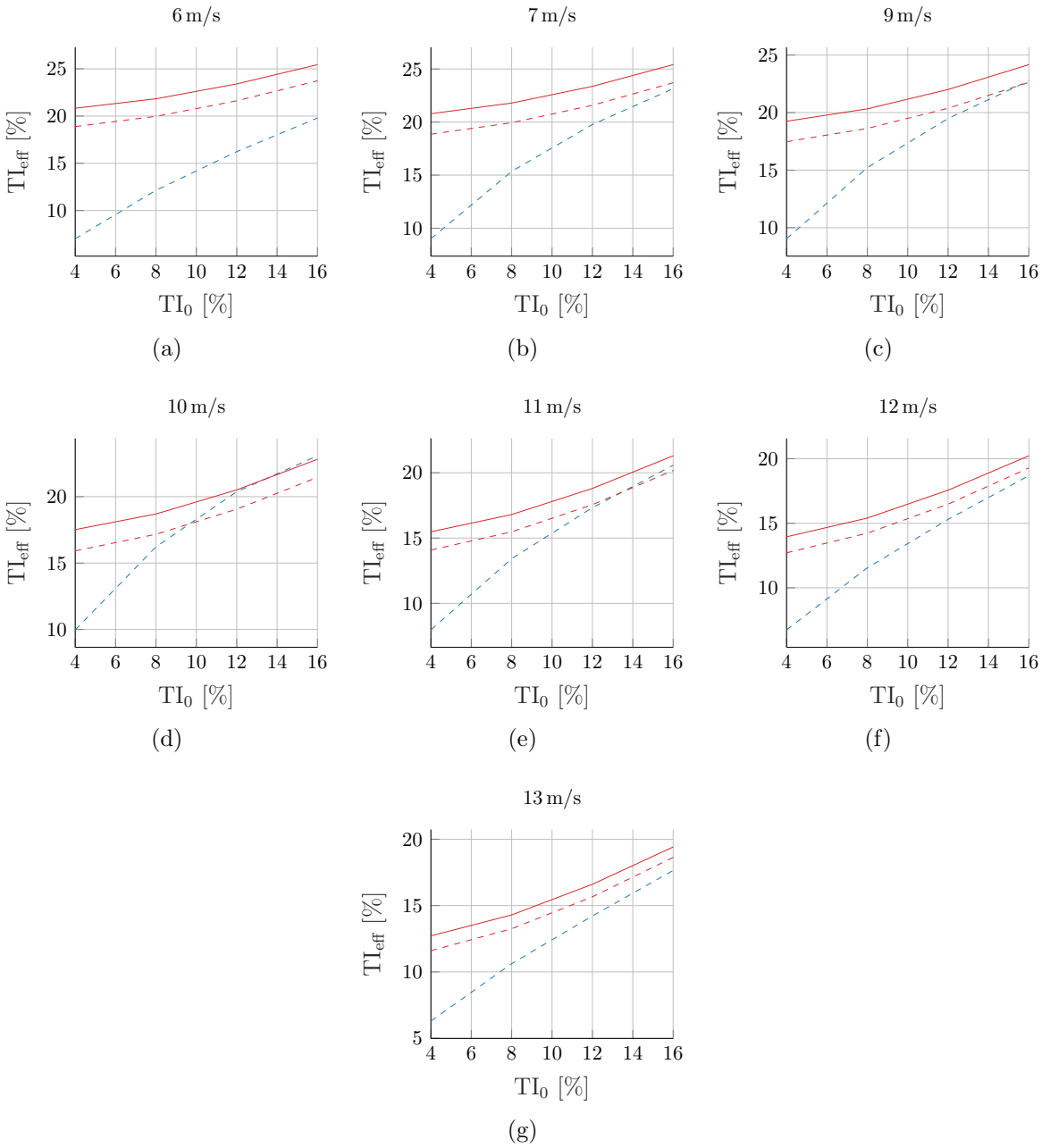

Figure B.12: Effective TI of the static DWM and the Frandsen models over the ambient TI at a downstream distance of 3.61 D. The simulations were carried out with a Wöhler coefficient of 14.

Bibliography

Ainslie, J. F. (1988). "Calculating the flowfield in the wake of wind turbines". In: *J. Wind Eng. Ind. Aerodyn.* 27, 213–224.

Arya, S. P. (1995). "Atmospheric boundary layer and its parameterization". In: *Wind Climate in Cities*. Ed. by J. E. Cermak, A. G. Davenport, E. J. Plate, and D. X. Viegas. Dordrecht: Springer Netherlands, 41–66. ISBN: 978-90-481-4485-3 978-94-017-3686-2. DOI: 10.1007/978-94-017-3686-2_3.

Barthelmie, R. J., O. Rathmann, S. T. Frandsen, K. S. Hansen, E. Politis, J. Prospathopoulos, K. Rados, D. Cabezón, W. Schlez, J. Phillips, A. Neubert, J. G. Schepers, and S. P. v. d. Pijl (July 1, 2007a). "Modelling and measurements of wakes in large wind farms". In: *Journal of Physics: Conference Series* 75, 012049. DOI: 10.1088/1742-6596/75/1/012049.

Barthelmie, R. J., S. T. Frandsen, M. N. Nielsen, S. C. Pryor, P.-E. Rethore, and H. E. Jørgensen (Nov. 2007b). "Modelling and measurements of power losses and turbulence intensity in wind turbine wakes at Middelgrunden offshore wind farm". In: *Wind Energy* 10 (6), 517–528. DOI: 10.1002/we.238.

Barthelmie, R. J. and L. E. Jensen (May 25, 2010). "Evaluation of wind farm efficiency and wind turbine wakes at the Nysted offshore wind farm". In: *Wind Energy* 13 (6), 573–586. DOI: 10.1002/we.408.

Barthelmie, R., K. Hansen, S. T. Frandsen, O. Rathmann, J. G. Schepers, W. Schlez, J. Phillips, K. Rados, A. Zervos, E. S. Politis, and P. K. Chaviaropoulos (2009). "Modelling and measuring flow and wind turbine wakes in large wind farms offshore". In: *Wind Energy* 12 (12), 431–444. DOI: 10.1002/we.348.

Bastankhah, M. and F. Porté-Agel (2014). "A new analytical model for wind-turbine wakes". In: *Renewable Energy* 70 (2014), 116–123.

Bergman, G., J. W. Wagenaar, and K. Boorsma (2016). *LAWINE instrumentation report*. Tech. rep. ECN-X–14-085. The Netherlands: Energy Research Center of the Netherlands (ECN).

Bingöl, F., J. Mann, and G. C. Larsen (Jan. 2010). "Light detection and ranging measurements of wake dynamics, part I: One-dimensional scanning". In: *Wind Energy* 13 (1), 51–61. DOI: 10.1002/we.352.

BMWI (2020). *Development of renewable energy in Germany 2019*. URL: https://www.erneuerbare-energien.de/EE/Redaktion/DE/Bilderstrecken/entwicklung-der-erneuerbaren-energien-in-deutschland-im-jahr-englisch.html1 (visited on 01/27/2021).

Burton, T. (2011). *Wind Energy Handbook*. Berlin, Heidelberg: Wiley. ISBN: 978-0-470-69975-1.

Chemnitz, I. (2021). *alaska/Wind*. URL: https://www.ifm-chemnitz.de/produkte/alaskamultibodydynamics/alaskawind/ (visited on 03/09/2021).

Cleve, J., M. Greiner, P. Enevoldsen, B. Birkemose, and L. Jensen (Mar. 2009). "Model-based analysis of wake-flow data in the Nysted offshore wind farm". In: *Wind Energy* 12 (2), 125–135. DOI: 10.1002/we.314.

Conti, D., N. Dimitrov, and A. Peña (2020). "Aero-elastic load validation in wake conditions using nacelle-mounted lidar measurements". In: *Wind Energy Science Discussions*, 1–31. DOI: 10.5194/wes-2020-8.

Dimitrov, N. (July 22, 2019). "Surrogate models for parameterized representation of wake-induced loads in wind farms". In: *Wind Energy* 22 (10), 1371–1389. DOI: 10.1002/we.2362.

Dimitrov, N., A. Borraccino, A. Peña, A. Natarajan, and J. Mann (Aug. 6, 2019). "Wind turbine load validation using lidar-based wind retrievals". In: *Wind Energy* 22 (11), 1512–1533. DOI: 10.1002/we.2385.

DTU (2021). *WAsP*. URL: https://www.wasp.dk/wasp (visited on 03/20/2021).

Duc, T., O. Coupiac, N. Girard, G. Giebel, and T. Göçmen (May 22, 2019). "Local turbulence parameterization improves the Jensen wake model and its implementation for power optimization of an operating wind farm". In: *Wind Energy Science* 4 (2), 287–302. DOI: 10.5194/wes-4-287-2019.

Emeis, S. (2013). *Wind Energy Meteorology*. Green Energy and Technology. Berlin, Heidelberg: Springer Berlin Heidelberg. ISBN: 978-3-642-30522-1 978-3-642-30523-8. DOI: 10.1007/978-3-642-30523-8.

Foken, T. (2016). *Angewandte Meteorologie: Mikrometeorologische Methoden*. 3. Auflage. OCLC: 945131917. Berlin Heidelberg: Springer Spektrum. 394 pp. ISBN: 978-3-642-25524-3 978-3-642-25525-0.

Frandsen, S., R. Barthelmie, S. Pryor, O. Rathmann, S. Larsen, J. Højstrup, and M. Thøgersen (2006). "Analytical modelling of wind speed deficit in large offshore wind farms". In: *Wind Energy* 9, 39–53. DOI: 10.1002/we.189.

Frandsen, S. (2007). "Turbulence and turbulence-generated structural loading in wind turbine clusters". PhD thesis. Technical University of Denmark. ISBN: 87-550-3458-6.

Garratt, J. (1994). *The Atmospheric Boundary Layer*. Cambridge Atmospheric and Space Science Series. Cambridge University Press. ISBN: 9780521467452.

Gaumond, M., P.-E. Rethore, A. Bechmann, S. Ott, G. C. Larsen, A. Peña, and K. S. Hansen (2012). "Benchmarking of wind turbine wake models in large offshore wind farms". In: *Proceedings of The Science of Making Torque from Wind Conference*. Oldenburg.

Gerke, N., I. Reinwardt, P. Dalhoff, M. Dehn, and W. Moser (June 2018). "Validation of turbulence models through SCADA data". In: *Journal of Physics: Conference Series* 1037, 072027. DOI: 10.1088/1742-6596/1037/7/072027.

Göçmen, T. and G. Giebel (2018). "Data-driven wake modelling for reduced uncertainties in short-term possible power estimation". In: *Journal of Physics: Conference Series* 1037, 072002. DOI: 10.1088/1742-6596/1037/7/072002.

González-Longatt, F., P. Wall, and V. Terzija (2012). "Wake effect in wind farm performance: Steady-state and dynamic behavior". In: *Renewable Energy* 39 (1), 329–338.

Hansen, M. O. L. (2008). *Aerodynamics of Wind Turbines*. 2nd ed. OCLC: ocm86172940. London: Earthscan. ISBN: 978-1-84407-438-9.

IEC 61400-1 Ed.4 (2019). *Wind energy generation systems - Part 1: Design requirements*. Guideline. International Electrotechnical Commission (IEC).

IEC 61400-12-1 (2017). *IEC 61400-12-1: Wind energy generation systems - Part 12-1: Power performance measurements of electricity producing wind turbines*. Guideline. International Electrotechnical Commission (IEC).

Jensen, N. O. (1983). *A note on wind generator interaction*. Tech. rep. Risø-M-2411(EN). Roskilde: Risø National Laboratory.

Jonkman, J. M., J. Annoni, G. Hayman, B. Jonkman, and A. Purkayastha (2017). "Development of FAST.Farm: A New Multi-Physics Engineering Tool for Wind-Farm Design and Analysis". In: *35th Wind Energy Symposium*. Grapevine, Texas: American Institute of Aeronautics and Astronautics. ISBN: 978-1-62410-456-5. DOI: 10.2514/6.2017-0454.

Kaimal, J. C. and J. J. Finnigan (1994). *Atmospheric Boundary Layer Flows: Their Structure and Measurement*. New York: Oxford University Press. ISBN: 978-0-19-506239-7.

Katic, I., J. Højstrup, and N. Jensen (1987). "A simple model for cluster efficiency". In: *EWEC'86. Proceedings. Vol. 1*. Ed. by W. Palz and E. Sesto. A. Raguzzi, 407–410.

Keck, R.-E. (2013). "A consistent turbulence formulation for the dynamic wake meandering model in the atmospheric boundary layer". PhD thesis. Technical University of Denmark.

Keck, R.-E. (June 23, 2014). "Validation of the standalone implementation of the dynamic wake meandering model for power production". In: *Wind Energy* 18 (9), 1579–1591.

Keck, R.-E., M. de Maré, M. J. Churchfield, S. Lee, G. Larsen, and H. A. Madsen (Nov. 2014). "On atmospheric stability in the dynamic wake meandering model". In: *Wind Energy* 17 (11), 1689–1710.

Kolmogorov, A. N. (1941a). "Dissipation of energy in the locally isotropic turbulence". In: *Comptes Rendus (Doklady) de l' Académie des Sciences de l'* XXXII (1), 16–18.

Kolmogorov, A. N. (1941b). "The local structure of turbulence in incompressible viscous fluid for very large Reynolds numbers". In: *Comptes Rendus (Doklady) de l' Académie des Sciences de l'* XXX (4), 16–18.

Larsen, G. C., H. A. Madsen, K. Thomsen, and T. J. Larsen (July 2008a). "Wake meandering: A pragmatic approach". In: *Wind Energy* 11 (4), 377–395. DOI: 10.1002/we.267.

Larsen, G. C. (2009). *A simple stationary semi-analytical wake model*. Tech. rep. Risø-R-1713(EN). Roskilde: Risø National Laboratory.

Larsen, G. C., H. A. Madsen, F. Bingöl, J. Mann, S. Ott, J. N. Sørensen, V. Okulov, N. Troldborg, M. Nielsen, K. Thomsen, T. J. Larsen, and R. Mikkelsen (June 2007). *Dynamic wake meandering modeling*. Tech. rep. Risø-R-1607(EN). Roskilde: Risø National Laboratory.

Larsen, G. C., H. A. Madsen, T. J. Larsen, and N. Troldborg (July 2008b). *Wake modeling and simulation*. Tech. rep. Risø-R-1653(EN). Roskilde: Risø National Laboratory for Sustainable Energy.

Larsen, T., G. Larsen, H. Aagaard Madsen, K. Thomsen, and S. Markkilde Petersen (2015). "Comparison of measured and simulated loads for the Siemens SWT 2.3 oper-

ating in wake conditions at the Lillgrund Wind Farm using HAWC2 and the dynamic wake meander model". In: *EWEA Annual Conference and Exhibition*.

Larsen, T. J., H. A. Madsen, G. C. Larsen, and K. S. Hansen (May 2013). "Validation of the dynamic wake meander model for loads and power production in the Egmond aan Zee wind farm". In: *Wind Energy* 16 (4), 605–624.

Luzzatto-Fegiz, P. (June 2018). "A one-parameter model for turbine wakes from the entrainment hypothesis". In: *Journal of Physics: Conference Series* 1037, 072019. DOI: 10.1088/1742-6596/1037/7/072019.

Machefaux, E., G. C. Larsen, N. Troldborg, M. Gaunaa, and A. Rettenmeier (Dec. 2015a). "Empirical modeling of single-wake advection and expansion using full-scale pulsed lidar-based measurements". In: *Wind Energy* 18 (12), 2085–2103. DOI: 10.1002/we.1805.

Machefaux, E., G. C. Larsen, N. Troldborg, K. S. Hansen, N. Angelou, T. Mikkelsen, and J. Mann (Aug. 2016). "Investigation of wake interaction using full-scale lidar measurements and large eddy simulation". In: *Wind Energy* 19 (8), 1535–1551. DOI: 10.1002/we.1936.

Machefaux, E., G. C. Larsen, and J. P. Murcia Leon (2015b). "Engineering models for merging wakes in wind farm optimization applications". In: *Journal of Physics: Conference Series* 625, 012037. DOI: 10.1088/1742-6596/625/1/012037.

Machefaux, E., G. C. Larsen, N. Troldborg, and A. Rettenmeier (2013). "Single wake meandering, advection and expansion - An analysis using an adapted pulsed lidar and CFD LES-ACL simulations". In: *Prodeedings of EWEA 2013 - European Wind Energy Conference & Exhibition*. European Wind Energy Association (EWEA).

Machefaux, E., N. Troldborg, G. Larsen, J. Mann, and H. Aagaard Madsen (2012). "Experimental and numerical study of wake to wake interaction in wind farms". In: *Proceedings of EWEA 2012 - European Wind Energy Conference & Exhibition*. Copenhagen: European Wind Energy Association (EWEA).

Machielse, L. A. H. (2007). *Measured wind and performance characteristics in the wake of 2.5MW turbines*. Tech. rep. ECN-X–06-130. Netherlands: Energy Research Center of the Netherlands (ECN).

Madsen, H. A., G. Larsen, and K. Thomsen (2005). "Wake flow characteristics in low ambient turbulence conditions". In: *Proceedings (CD-ROM)*. Copenhagen Offshore Wind.

Madsen, H. A., G. C. Larsen, T. J. Larsen, and N. Troldborg (Nov. 8, 2010). "Calibration and validation of the dynamic wake meandering model for implementation in an aeroelastic code". In: *J. Sol. Energy Eng.* 132 (4), 041014. DOI: https://doi.org/10.1115/1.4002555.

Mann, J. (1994). "The spatial structure of neutral atmospheric surface-layer turbulence". In: *Journal of Fluid Mechanics* 273, 141–168. DOI: 10.1017/S0022112094001886.

Mann, J. (1998). "Wind field simulation". In: *Probabilistic Engineering Mechanics* 13 (4), 269–282. DOI: https://doi.org/10.1016/S0266-8920(97)00036-2.

Méchali, M., R. Barthelmie, S. Frandsen, L. Jensen, and P.-E. Réthoré (2006). "Wake effects at Horns Rev and their influence on energy production". In: *Proceedings of the European Wind Energy Conference & Exhibition*. Athens.

Miner, M. A. (1945). "Cumulative damage in fatigue". In: *J. Appl. Mech. (ASME)* 12 (3), A159–A164. DOI: https://doi.org/10.1115/1.4009458.

Neunaber, I., M. Hölling, R. J. A. M. Stevens, G. Schepers, and J. Peinke (Oct. 15, 2020). "Distinct turbulent regions in the wake of a wind turbine and their inflow-dependent locations: The creation of a wake map". In: *Energies* 13 (20), 5392. DOI: 10.3390/en13205392.

Niayifar, A. and F. Porté-Agel (2015). "A new analytical model for wind farm power prediction". In: *Journal of Physics: Conference Series* 625, 012039. DOI: 10.1088/1742-6596/625/1/012039.

Nygaard, N. G. (2014). "Wakes in very large wind farms and the effect of neighbouring wind farms". In: *Journal of Physics: Conference Series* 524, 012162. DOI: 10.1088/1742-6596/524/1/012162.

Özdemir, H. and E. Bot (2018). "An advanced method for wind turbine wake modeling". In: *Wind Energy Symposium*. Florida. DOI: 10.2514/6.2018-0515.

Palmgren, A. G. (1924). "Die Lebensdauer von Kugellagern". In: *Zeitschrift des Vereines Deutscher Ingenieure (ZVDI)* 14, 339–341.

Peña, A., C. B. Hasager, J. Lange, J. Anger, M. Badger, F. Bingöl, O. Bischoff, J.-P. Cariou, F. Dunne, S. Emeis, M. Harris, M. Hofsäss, I. Karagali, J. Laks, S. Larsen, J. Mann, T. Mikkelsen, L. Y. Pao, M. Pitter, A. Rettenmeier, A. Sathe, F. Scanzani, D. Schlipf, E. Simley, C. Slinger, R. Wagner, and I. Würth (2013). *Remote Sensing for Wind Energy*. Tech. rep. E-Report-0029(EN). Roskilde: DTU Wind Energy, 308.

Poodt, M. J. S. and D. A. J. Wouters (2016). *On the added benefits of ground-based LiDAR for wind turbine load measurements*. Tech. rep. ECN-E–16-051. Netherlands: Energy Research Center of the Netherlands (ECN).

Quarton, D. C. and J. Ainslie (1989). "Turbulence in wind turbine wakes". In: *Wind Engineering* 14 (1), 15–23.

Quaschning, V. (2019). *Regenerative Energiesysteme: Technologie – Berechnung – Klimaschutz*. 10th ed. München: Carl Hanser Verlag GmbH & Co. KG. ISBN: 978-3-446-46113-0 978-3-446-46114-7. DOI: 10.3139/9783446461147.

Radaj, D. and M. Vormwald (2007). *Ermüdungsfestigkeit: Grundlagen für Ingenieure*. 3., neubearbeitete und erweiterte Auflage. OCLC: 255665882. Berlin: Springer. ISBN: 978-3-540-71458-3.

Rathmann, O., R. Barthelmie, and S. Frandsen (2006). "Turbine wake model for wind resource software". In: *Proceedings of the European Wind Energy Conference & Exhibition*. Athens.

Rathmann, O., S. Frandsen, and R. Barthelmie (2007). "Wake modelling for intermediate and large wind farms". In: *Proceedings of the European Wind Energy Conference & Exhibition*. Milan.

Reinwardt, I., N. Gerke, P. Dalhoff, D. Steudel, and W. Moser (June 2018). "Validation of wind turbine wake models with focus on the dynamic wake meandering model". In: *Journal of Physics: Conference Series* 1037, 072028. DOI: 10.1088/1742-6596/1037/7/072028.

Reinwardt, I., L. Schilling, P. Dalhoff, D. Steudel, and M. Breuer (2020a). "Dynamic wake meandering model calibration using nacelle-mounted lidar systems". In: *Wind Energy Science* 5 (2), 775–792. DOI: 10.5194/wes-5-775-2020.

Reinwardt, I., L. Schilling, D. Steudel, N. Dimitrov, P. Dalhoff, and M. Breuer (2021). "Validation of the dynamic wake meandering model with respect to loads and power production". In: *Wind Energy Science* 6 (2), 441–460. DOI: 10.5194/wes-6-441-2021.

Reinwardt, I., L. Schilling, P. Dalhoff, D. Steudel, and M. Breuer (2020b). "Extension of the DWM model towards a static model for site-specific load simulations". In: *Journal of Physics: Conference Series* 1618, 062007. DOI: 10.1088/1742-6596/1618/6/062007.

Sanderse, B. (2009). *Aerodynamics of wind turbine wakes*. Tech. rep. ECN-E-–09-016. Netherlands: Energy Research Center of the Netherlands (ECN).

Sathe, A., R. Banta, L. Pauscher, K. Vogstad, D. Schlipf, and S. Wylie (2015). *Estimating Turbulence Statistics and Parameters from Ground- and Nacelle-Based Lidar Measurements*. Tech. rep. Roskilde: IEA Wind.

Stull, R. (1988). *An Introduction to Boundary Layer Meteorology*. Atmospheric and Oceanographic Sciences Library. Springer Netherlands. ISBN: 9789027727695.

Thomsen, K. and P. Sørensen (Mar. 1999). "Fatigue loads for wind turbines operating in wakes". In: *Journal of Wind Engineering and Industrial Aerodynamics* 80 (1), 121–136. DOI: 10.1016/S0167-6105(98)00194-9.

Toft, H., L. Svenningsen, W. Moser, J. Sørensen, and M. Thøgersen (2016). "Assessment of wind turbine structural integrity using response surface methodology". In: *Engineering Structures* 106, 471–483. DOI: 10.1016/j.engstruct.2015.10.043.

Troldborg, N. and A. R. Meyer Forsting (Dec. 2017). "A simple model of the wind turbine induction zone derived from numerical simulations". In: *Wind Energy* 20 (12), 2011–2020. DOI: 10.1002/we.2137.

Trujillo, J.-J., F. Bingöl, G. C. Larsen, J. Mann, and M. Kühn (Jan. 2011). "Light detection and ranging measurements of wake dynamics. Part II: Two-dimensional scanning". In: *Wind Energy* 14 (1), 61–75. DOI: 10.1002/we.402.

Vasiljevi, N. (2014). "A time-space synchronization of coherent Doppler scanning lidars for 3D measurements of wind fields". PhD thesis. Technical University of Denmark. ISBN: 978-87-92896-62-9.

Veers, P. S. (Mar. 1988). *Three-Dimensional Wind Simulation*. Tech. rep. SAND88-0152(EN). Albuquerque, New Mexico and Livermore, California: Sandia National Laboratories.

Verhoef, H., v. d. A. Werff, and H. Oostrum (2009). *Comparative measurements between a Triton SODAR and Meteo Measurements at the EWTW, The Netherlands*. Tech. rep. ECN-X–09-104. Netherlands: Energy Research Center of the Netherlands (ECN).

Weitkamp, C. (2005). *Lidar: Range-Resolved Optical Remote Sensing of the Atmosphere*. en. Ed. by C. Weitkamp. Springer Series in Optical Sciences 102. New York: Springer. ISBN: 978-0-387-40075-4.

Zierath, J., R. Rachholz, and C. Woernle (July 2016). "Field test validation of Flex5, MSC.Adams, alaska/Wind and SIMPACK for load calculations on wind turbines: Field test validation of multibody codes for wind turbine simulation". In: *Wind Energy* 19 (7), 1201–1222. DOI: 10.1002/we.1892.